Advances in Industrial Control

Ali Bidram
Vahidreza Nasirian
Ali Davoudi
Frank L. Lewis

Cooperative Synchronization in Distributed Microgrid Control

AIC

Springer

Advances in Industrial Control

Series editors

Michael J. Grimble, Glasgow, UK
Michael A. Johnson, Kidlington, UK

More information about this series at http://www.springer.com/series/1412

Ali Bidram · Vahidreza Nasirian
Ali Davoudi · Frank L. Lewis

Cooperative Synchronization in Distributed Microgrid Control

Springer

Ali Bidram
Quanta Technology
Markham, ON
Canada

Vahidreza Nasirian
TeraDiode (United States)
Wilmington, MA
USA

Ali Davoudi
Department of Electrical Engineering
The University of Texas at Arlington
Arlington, TX
USA

Frank L. Lewis
The University of Texas at Arlington
Research Institute
Fort Worth, TX
USA

MATLAB® and Simulink® are registered trademarks of The MathWorks, Inc., 3 Apple Hill Drive, Natick, MA 01760-2098, USA, http://www.mathworks.com.

ISSN 1430-9491 ISSN 2193-1577 (electronic)
Advances in Industrial Control
ISBN 978-3-319-50807-8 ISBN 978-3-319-50808-5 (eBook)
DOI 10.1007/978-3-319-50808-5

Library of Congress Control Number: 2016959531

Printed on acid-free paper

This Springer imprint is published by Springer Nature
The registered company is Springer International Publishing AG
The registered company address is: Gewerbestrasse 11, 6330 Cham, Switzerland

To my lovely Maryam who has made my life meaningful.

Ali Bidram

To those whose unconditional love fueled my passions, and
will propel me toward ultimate summits of success. Particularly,
To my mother Fatemeh, and
To my lovely Bauran and Hasan

Vahidreza Nasirian

To Mehdi Khajian, whose untimely passing left the sharif-EE class of 2003 in a deep sorrow.

Ali Davoudi

To Galina, Roma, and Chris, who make every day exciting.

Frank L. Lewis

Series Editors' Foreword

The series *Advances in Industrial Control* aims to report and encourage technology transfer in control engineering. The rapid development of control technology has an impact on all areas of the control discipline. New theory, new controllers, actuators, sensors, new industrial processes, computer methods, new applications, new design philosophies…, new challenges. Much of this development work resides in industrial reports, feasibility study papers and the reports of advanced collaborative projects. The series offers an opportunity for researchers to present an extended exposition of such new work in all aspects of industrial control for wider and rapid dissemination.

In 2015, the *Advances in Industrial Control* series published the monograph *Voltage Control and Protection in Electrical Power Systems* by Sandro Corsi (ISBN 978-1-4471-6635-1, 2015). This was an authoritative, detailed and comprehensive study of how to design and implement voltage control systems in a national-scale electrical power grid. Some of the key concepts were a three-level control hierarchy and the decomposition of the grid into weakly interactive control regions. Each region was driven by "pilot" nodes or "leader" nodes and selected control generators that supported these nodes. The pilot nodes selected were those able strongly to influence or lead a set of surrounding buses. The decomposed structure for the three levels of the hierarchy was then used to construct the system controllers and to create an information network that provided the necessary system measurements.

This idea of leaders to influence or co-ordinate the behaviour of a set of neighbouring entities in a system is a feature of the present monograph *Cooperative Synchronization in Distributed Microgrid Control* by authors Ali Bidram, Vahidreza Nasirian, Ali Davoudi, and Frank L. Lewis, where the application domain this time is microgrid power systems. Microgrids are defined as small-scale local power systems that supply a small spatial area. Examples could be in a small geographical area such as a remote community or could be a self-contained facility such as a hospital, or a cruise liner. A reason for the current interest in microgrids is the widespread need to integrate and exploit different renewable sources of electric power into one system. There are two types of microgrid, AC microgrids and DC microgrids, both of which are analysed in the authors' monograph. The DC microgrid may receive more focus in the future as a way of dealing with localised sources of renewable energy and its storage using, for example, batteries.

What is particularly novel about the present monograph is the use of leadership and the regularisation of the behaviour of all the entities in a distributed multi-agent system. Chapter 3 in the monograph is a fascinating presentation that starts from group animal behaviour as in swarms of birds or shoals of fish and culminates in a theory for the co-ordinated control of a multi-agent system. It is this notion of entities, all becoming synchronised and moving together towards a common goal, that finds application in the electric power system field.

The analysis of microgrids is exhaustively reported in the monograph. This begins with modelling and a specification of the control objectives of AC and DC microgrids respectively. Subsequently the monograph focuses on three different aspects of AC microgrids: distributed control, Multi-objective adaptive distributed control and finally droop-free distributed control (Chaps. 4–6). Then the focus turns to the cooperative control and distributed assistive control of DC microgrids (Chaps. 7 and 8).

The monograph has a wealth of material on the power system aspects of microgrids and their coordinated control. The introduction to the field of multi-agent system control is very welcome and timely, but what distinguishes this monograph and makes it an excellent entry to the *Advances in Industrial Control* series is the demonstration of how these ideas can find use in a practical industrial application.

Michael J. Grimble
Michael A. Johnson
Industrial Control Centre
University of Strathclyde
Glasgow, Scotland, UK

Preface

This book studies the distributed control of microgrids. Microgrids are small-scale power networks that are exploited to supply local loads in small geographical spans. Microgrids have various applications such as remote villages, hospitals, universities and educational institutes, police stations, business and residential buildings, shipboard power systems, military bases, ships. The microgrid concept, with its local control and power quality support, potentially allows for reliable and predictable operation of renewable energy generators and for scalable addition of new generation and loads. Conventionally, microgrids are spanned on the traditional AC distribution networks that supply AC loads. These microgrids with AC electrical infrastructure are called AC microgrids. Recently, DC microgrids have also gained much attention due to their advantages. DC microgrids exploit a DC electrical infrastructure. This book applies techniques from distributed cooperative control of multi-agent dynamical systems to synchronization, power sharing, and load balancing problems arising in AC and DC electric power microgrids. Distributed networks of coupled dynamical systems have received much attention over the years because they occur in many different fields including biological and social systems, physics and chemistry, and computer science.

In Chap. 1, an introduction on microgrids and distributed control of multi-agent systems is provided. Chapter 2 introduces AC microgrid with focus on its control. An inverter-based distributed generator (DG) consists of primary power source (e.g., battery), voltage source converter (VSC) and the power, voltage and current control loops. The control loops assign and regulate the output voltage and the frequency of the VSC. The dynamics of the DG can be expressed in the form of a nonlinear state space equation. A systematic derivation for the relevant equations for primary control is given. A basic introduction to secondary and tertiary control is also given. Later, dynamic models are developed for voltage-controlled voltage source inverters (VCVSI) and current-controlled voltage source inverters (CCVSI). Finally, the objectives for primary and secondary controllers in DC microgrid are introduced.

Chapter 3 discusses distributed cooperative control of multi-agent systems. Graph theory is introduced which is used to represent the communication structure of a multi-agent-based system. Later, consensus in multi-agent systems is introduced, and it is shown how it can be used in multi-agent-regulating problems and multi-agent synchronization problem. A general analysis on multi-agent systems with variable graph structure and nodes with vector states is done. Finally, the concepts of synchronization are applied to electric circuits.

In Chap. 4, the design and principles of distributed secondary control of AC microgrids are discussed. The secondary control in microgrid is a tracking synchronization problem in which the leader node (one of the DGs) tracks the desired value, while the other nodes synchronize their outputs with that of the leader. For example, if it is desired to control the voltage of the microgrid, then the reference voltage is provided only to the leader node. The leader conveys its information to its neighbors who further convey their information to their neighbors. This chain of exchange of information ensures that all the DGs are aware of the reference voltage and their primary controller brings their voltages to the reference values. Similarly, the frequency of individual DGs can be synchronized. Chapter 4 provides a detailed information on how the concepts of cooperative control can be applied to solve the problem of voltage regulation and frequency synchronization in microgrids. Moreover, it is shown how the cooperative secondary frequency controller also shares the active power among the DGs based on their power ratings.

As mentioned before, the DGs are interfaced with microgrid via voltage source inverters. Depending upon the requirement, a VSI may be designed as voltage-controlled voltage source inverters or current-controlled voltage source inverters. The control structure of a VCVSI ensures regulated voltage and frequency, while the control in CCVSI regulates the active and reactive power delivery. In Chap. 5, a multi-objective distributed control framework is designed for AC microgrids. To achieve the multiple goals, secondary controller has two separate control layers: First control layer controls the VCVSIs which control the output voltage and frequency of the DGs, whereas second control layer controls the CCVSIs that manage the flow of active and reactive power. In addition to multi-objective distributed control framework, Chap. 5 discusses adaptive distributed voltage control techniques in AC microgrids. The adaptive distributed voltage control compensates for the nonlinear and uncertain dynamics of DGs and, hence, obviates the control design challenges caused by the nonlinear dynamics of DGs. The controller is fully independent of the DG parameters and the specification of the connector by which each DG is connected to the microgrid. Therefore, the controller can be deployed on any DG regardless of the DG parameters and the connector specifications, and its performance does not deteriorate by the change in DG parameters (e.g., due to aging and thermal effects). The adaptive voltage controller appropriately responds to the changes in the system operating condition, without any manual intervention, and adjusts the control parameters in real time.

Droop control, which is inspired from the governors in synchronous generators, are implemented virtually in inverter-based DGs. Droop control is popular due to its simplicity but it is ineffective in the presence of nonlinear loads, and its reactive power sharing ability is poor when there are unequal bus voltages. To address these issues, a droop-free distributed controller is designed for AC microgrids. To design a droop-free controller, each DG is equipped with a voltage regulator, reactive power regulator, and active power regulator. Each DG exchanges information of its voltage and normalized active and reactive power with their neighbors. The voltage regulator at a DG uses the voltage measurements (its own and neighbors) to estimate the grid voltage using a voltage estimator. This estimate is then compared against the required voltage, and the error is passed through a PI controller to synchronize the voltage to the required voltage. Similarly, using the principles of cooperative control, active and reactive power can be shared among all DGs based on their power ratings.

Similar to hierarchical control structure in AC microgrids (inspired by the traditional power grids), the same concept is implemented in DC microgrids. For a DC microgrid, the main objectives are global voltage regulation and proportional load sharing. These objectives can be met using similar control strategies that were employed in AC microgrids. The primary controller is augmented with a distributed secondary controller at each DG. The secondary controller consists of a voltage regulator and a current regulator. The voltage regulator estimates the grid voltage from the measurements of its neighbors and updates its voltage such that its voltage is equal to the voltage grid. When this process is performed at all DGs, voltage regulation is achieved. A noise-resilient voltage observer is designed such that it can estimate the grid voltage from the voltage information of a limited number of DGs. The voltage observer uses the principle of dynamic voting protocol to perform the voltage estimation. To ensure that the load is distributed proportionally, a current regulator compares its normalized currents with its neighbors and adjusts the current such that the normalized current of all DGs are equal. Equal normalized current of all DGs ensures that each DG is loaded based on its rating. The global dynamic model and details of the controller are provided in Chap. 7.

Chapter 8 discusses the utilization of power buffers to improve the stability of DC microgrids when the loads are volatile due to limited generational inertia and damping. Power buffer is a power electronic converter with a large storage component that can decouple the dynamics of distribution network and the load. During transients, the buffer can use its stored energy to supply the load and prevent the disturbance from reaching the distribution network. In traditional power grids, central storage units are used to balance the supply and demand, but they are slow and expensive. A power buffer, on the other hand, is fast and efficient and can be installed at the load terminal. Typically, power buffers are controlled individually to serve local loads, but their efficiency can further be improved if the buffers operate collectively to serve neighboring loads. To achieve a cooperative operation of power buffers, a communication module is provided that enables the buffers to exchange information with their neighbors. In this way, in case of load changes, the buffer at that node along with the neighboring buffers can supply the required load. This collective response from the buffers increases the damping of the microgrid.

Markham, ON, Canada — Ali Bidram
Wilmington, MA, USA — Vahidreza Nasirian
Arlington, TX, USA — Ali Davoudi
Fort Worth, TX, USA — Frank L. Lewis

Contents

Chapter 1
Introduction

Deregulation of the electric power industry imposes requirements for more responsive economic dispatch for dynamic balance between energy generation and loads. Concern about environmental impacts and shortages of fossil fuels have increased interest in clean and renewable energy generation, including wind power, photovoltaic, hydroelectric power, fuel cells, and microturbines. Wind energy and photovoltaic are among the most promising renewable energy resources, yet these sources are intermittent and unpredictable and cannot be used for reliable economic dispatch; they have low inertias and cannot provide power quality support for the grid. Microgrids are small-scale power networks that are exploited to supply local loads in small geographical spans. Microgrids have various applications such as remote villages, hospitals, universities and educational institutes, police stations, business and residential buildings, shipboard power systems, military bases, and ships. The microgrid concept, with its local control and power quality support, potentially allows for reliable and predictable operation of renewable energy generators, and for scalable addition of new generation and loads. Microgrids facilitate the reliable integration of renewable energy resources such as wind and solar generation and fuel cells through distributed generators (DGs). The microgrid operates on the idea of autonomous subsystems composed of small local areas with dedicated control systems that provide guaranteed power quality support to the distribution grid. The microgrid concept potentially enables high penetration of DGs without requiring redesign or reengineering of the distribution system itself, and was designed to lower the cost and improve the reliability of small-scale distribution systems. Current local control methods for microgrids do not always provide adequate power quality support for the grid or reliable power generation profiles for renewable energy sources [1–4].

Conventionally, microgrids are spanned on the traditional AC distribution networks that supply AC loads. These microgrids with AC electrical infrastructure are called AC microgrids. Recently, DC microgrids have also gained much attention due to their advantages. DC microgrids exploit a DC electrical infrastructure. Energy resources are integrated into the microgrid using various power electronics

A. Bidram et al., *Cooperative Synchronization in Distributed Microgrid Control*,
Advances in Industrial Control, DOI 10.1007/978-3-319-50808-5_1

devices. In AC microgrids, renewable energy resources are integrated to the grid through inverters while in DC microgrids, these resources are connected to the grid through DC–DC converters. In both cases, the power electronic converters are equipped with corresponding control circuits to meet the control objectives, such as active and reactive power flow and voltage and frequency control in AC microgrids, and power and voltage control in DC microgrids. This book discusses different distributed control strategies exploited in AC and DC microgrids.

AC microgrids exploit a hierarchical control structure that contains three main levels, namely primary, secondary, and tertiary control levels. The primary control operates at the fastest timescale and maintains voltage and frequency stability of the microgrid subsequent to the islanding process when switching from grid-connected mode. It is essential to provide independent active and reactive power sharing controls for the DGs in the presence of both linear and nonlinear loads. Moreover, the power sharing control avoids undesired circulating currents. The secondary control compensates for the voltage and frequency deviations caused by the operation of the primary controls and restores frequency and voltage synchronization. At the highest level and slowest timescale, the tertiary control manages the power flow between the microgrid and the main grid and facilitates an economically optimal operation.

The traditional secondary control of AC microgrids exploits a centralized control structure. Central controllers command globally on the gathered system-wide information and require a complex and in some cases two-way communication network that adversely affects system flexibility and configurability and increases the reliability concerns by posing single point of failure. The single point of failure means that by the failure of the central controller, the whole control system fails down. In this book, the distributed control structure is introduced to implement the secondary control of microgrids. A microgrid can be considered as a multi-agent system where its DGs are the energy nodes (agents). The distributed structure of the communication network improves the system reliability. In this control structure, the control protocols are distributed on all DGs. Therefore, the requirement for a central controller is obviated and the control system does not fail down subsequent to outage of a single unit.

Distributed networks of coupled dynamical systems have received much attention over the years because they occur in many different fields including biological and social systems, physics and chemistry, and computer science. Various terms are used in the literature for phenomena related to collective behavior on networks of systems, such as flocking, consensus, synchronization, formation, and rendezvous. The distributed cooperative control of multi-agent systems can be used to implement the secondary control of microgrids. The term "distributed" means that the controller requires a communication network by which each agent only receives the information of its neighboring agents. The term "cooperative" means that, in contrast to the competitive control, all agents act as one group toward a common synchronization goal and follow cooperative decisions. Distributed cooperative control of multi-agent systems is mainly categorized into the regulator synchronization problem and the tracking synchronization problem. In regulator synchronization problem, also called leaderless consensus, all agents synchronize to a common value that is not prescribed or controllable. In tracking synchronization problem, all agents synchronize to a leader node that acts as a command generator. Neighboring agents can communicate with each other. The leader is only connected to a small portion of the agents.

The secondary control of AC microgrids is similar to the tracking synchronization problem of a multi-agent system where the DG voltages and frequencies are required to track their nominal values. The dynamics of DGs in microgrids are nonlinear and nonidentical. Therefore, input–output feedback linearization is used to transform the nonlinear heterogeneous dynamics of DGs to linear dynamics. Input–output feedback linearization transforms the secondary voltage control to a second-order tracking synchronization problem. The secondary frequency control is transformed to a first-order synchronization problem using input–output feedback linearization. Based on the transformed dynamics, fully distributed voltage and frequency control protocols are derived for each DG. The proposed distributed controls are implemented through a sparse communication network, with only one-way communication links, where each DG requires its own information and the information of its neighbors.

In AC microgrids, DGs can be of rotating machinery or voltage source inverter (VSI)-based types. The control structure of a VSI may vary based on the control objectives such as voltage and frequency, or active and reactive powers. VCVSIs have internal voltage and current controller loops that facilitate the voltage and frequency controls of DG. However, in some DGs, the sole active and reactive power control may be of interest. This requirement can be satisfied through the current-controlled voltage source inverters (CCVSI). Up to this point, most of the presented secondary control schemes have only covered the voltage and frequency controls of VCVSIs. In this book, a two-layer control framework is introduced to implement the secondary control for an islanded microgrid containing both VCVSIs and CCVSIs. The first control layer deals with the voltage and frequency controls of VCVSIs. Additionally, the active and reactive powers of VCVSIs are allocated based on their active and reactive power ratings. The second control layer objectives are to control the active and reactive powers of CCVSIs. Each control layer is implemented through the distributed control of multi-agent systems.

The distributed secondary voltage control of AC microgrids can be made adaptive with respect to the changes in the DG parameters and microgrid operating conditions. The term adaptive refers to the following salient features of the proposed controller. The proposed controller compensates for the nonlinear and uncertain dynamics of DGs and, hence, obviates the control design challenges caused by the nonlinear dynamics of DGs. The controller is fully independent of the DG parameters and the specification of the connector by which each DG is connected to the microgrid. Therefore, the controller can be deployed on any DG regardless of the DG parameters and the connector specifications, and its performance does not deteriorate by the change in DG parameters (e.g., due to aging and thermal effects). The proposed controller appropriately responds to the changes in the system operating condition, without any manual intervention, and adjusts the control parameters in real time. Linear-in-parameter neural networks (NN) can be used to design an adaptive and distributed secondary voltage control. Neural networks are used to compensate for the uncertainties caused by the unknown dynamics of DGs. The NN weights are the control parameters and are calculated in real time. DGs are considered as agents that can communicate with each other through a communication network.

Although inverter-based AC microgrids have been prevalent, DC microgrids are currently emerging at distribution levels. The DC nature of emerging renewable energy sources (e.g., solar) or storage units (e.g., batteries and ultracapacitors) efficiently lends itself toward a DC microgrid paradigm that avoids redundant conversion stages. Many of the new loads are electronic DC loads (e.g., in data centers), and even some traditional AC loads, e.g., induction machines, can appear as DC loads when controlled by inverter-fed drive systems [5]. DC microgrids are also shown to have about two orders of magnitude more availability compared to their AC counterparts, thus making them ideal candidates for mission-critical applications [6]. Moreover, DC microgrids can overcome some disadvantages of AC systems, e.g., transformer inrush current, frequency synchronization, reactive power flow, and power quality issues. Given the desire for developing DC microgrids, control algorithms must be tailored to account for individual behavior of entities that form up a DC system, as well as their interactive behavior. Chapter 7 focuses on the development of distributed control techniques that are inspired by the operation of DC systems. They provide global voltage regulation and accurate load sharing through a minimal communication.

Proliferation of power electronics loads in DC distribution networks shifts the load consumption profiles from the traditional constant impedance loads to electronically driven loads with potentially volatile power profiles. Such fast-acting consumption patterns can destabilize the entire distribution network, given their weak nature due to the lack of damping and generational inertia [7, 8]. Hardware-centric approaches focus on placement of energy storage devices or power buffers to decouple the source, load, and distribution network dynamics (e.g., [9–11]). However, widespread utilization of these devices can be costly. Control-centric approaches are the alternative solutions. Chapter 8 studies a control approach that coordinates and groups power buffers across a DC microgrid. Information exchange in a distributed and sparse network enables power buffers to act globally, rather than locally.

References

1. Bidram A, Davoudi A (2012) Hierarchical structure of microgrids control system. IEEE Trans Smart Grid 3:1963–1976
2. Hatziargyriou N, Asano H, Iravani R, Marnay C (2007) Microgrids. IEEE Power Energ Mag 5:78–94
3. Lasseter RH (2002) Microgrid. In: Proceedings of IEEE power and energy society, vol 1. Winter meeting. New York, pp 305–308

4. Lopes JAP, Moreira CL, Madureira AG (2006) Defining control strategies for microgrids islanded operation. IEEE Trans Power Syst 21:916–924
5. Kwasinski A, Onwuchekwa CN (2011) Dynamic behavior and stabilization of DC Microgrids with instantaneous constant-power loads. IEEE Trans Power Electron 26:822–834
6. Kwasinski A (2011) Quantitative evaluation of dc microgrids availability: effects of system architecture and converter topology design choices. IEEE Trans Power Electron 26(3): 835–851
7. Sanchez S, Molinas M (2014) Degree of influence of system state transition on the stability of a dc microgrid. IEEE Trans Smart Grid 30:2535–2542
8. Farhadi M, Mohammed O (2015) Adaptive energy management in redundant hybrid DC microgrid for pulse load mitigation. IEEE Trans Smart Grid 6:54–62
9. Inthamoussou FA, Queralt JP, Bianchi FD (2013) Control of a supercapacitor energy storage system for microgrid applications. IEEE Trans Energy Convers 28:690–697
10. Xu G, Xu L, Morrow DJ, Chen D (2012) Coordinated dc voltage control of wind turbine with embedded energy storage system. IEEE Trans Energy Convers 27:1036–1045
11. Tummuru NR, Mishra MK, Srinivas S (2015) Dynamic energy management of hybrid energy storage system with high-gain PV converter. IEEE Trans Energy Convers 30:150–160

Chapter 2
Control and Modeling of Microgrids

In this chapter, the control objectives in AC and DC microgrids are discussed separately. This chapter brings together the existing AC and DC microgrid control schemes. Based on the desired control objectives, mathematical models are presented for DGs. These mathematical models are the key elements in designing control schemes for microgrids.

2.1 Control of AC Microgrids

In this section, first the control objectives in AC microgrids are elaborated. Then, based on these control objectives, the hierarchical control structure of AC microgrids is discussed. The hierarchical control structure contains three main levels, namely primary, secondary, and tertiary control levels. Finally, the dynamical model of distributed generators is elaborated. These dynamical models will be used in subsequent chapters to design distributed control protocols for microgrids.

2.1.1 Control Objectives in AC Microgrids

Microgrids can operate in two modes: grid-connected mode and islanded mode. The proper control of microgrid is a prerequisite for stable and economically efficient operation. The principal roles of the microgrid control structure are as follows [1–6]:

- Voltage and frequency regulation for both operating modes,
- Proper load sharing and DG coordination,
- Microgrid resynchronization with the main grid,
- Power flow control between the microgrid and the main grid,

A. Bidram et al., *Cooperative Synchronization in Distributed Microgrid Control*,
Advances in Industrial Control, DOI 10.1007/978-3-319-50808-5_2

- Optimizing the microgrid operating cost,
- Proper handling of transients and restoration of desired conditions when switching between modes.

These requirements are of different significances and timescales, thus requiring a hierarchical control structure to address each requirement at a different control hierarchy level. The microgrid hierarchical control strategy consists of three levels, namely primary, secondary, and tertiary controls, as shown in Fig. 2.1. The primary

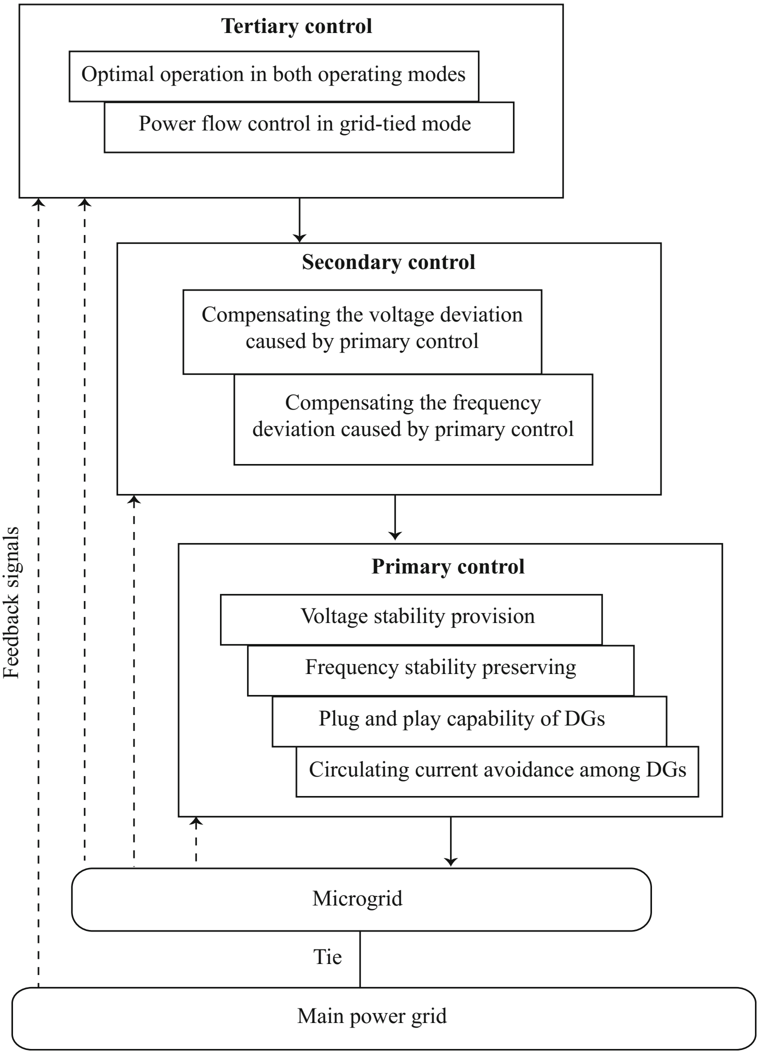

Fig. 2.1 Hierarchical control levels of a microgrid. © [2016] IEEE. Reprinted, with permission, from IEEE Transactions on Smart Grid [1]

control operates at the fastest timescale and maintains voltage and frequency stability of the microgrid subsequent to the islanding process when switching from grid-connected mode. It is essential to provide independent active and reactive power sharing controls for the DGs in the presence of both linear and nonlinear loads. Moreover, the power sharing control avoids undesired circulating currents. The primary control level includes fundamental control hardware, commonly referred to as zero level, which comprises internal voltage and current control loops of the DGs. The secondary control compensates for the voltage and frequency deviations caused by the operation of the primary controls and restores frequency and voltage synchronization. At the highest level and slowest timescale, the tertiary control manages the power flow between the microgrid and the main grid and facilitates an economically optimal operation [1, 7].

2.1.2 Primary Control Techniques in AC Microgrids

The primary control is designed to satisfy the following requirements:

- To stabilize the voltage and frequency: Subsequent to an islanding event, the microgrid may lose its voltage and frequency stability due to the mismatch between the power generated and consumed.
- To offer plug-and-play capability for DGs and properly share the active and reactive powers among them, preferably, without any communication links.
- To mitigate circulating currents that can cause overcurrent phenomenon in the power electronic devices and damage the DC-link capacitor.

The primary control provides the reference points for the real-time voltage and current control loops of DGs. These inner control loops are commonly referred to as zero-level control. The zero-level control is generally implemented in either active/reactive power (PQ) mode or voltage control mode [6].

In the PQ control mode, the DG active and reactive power delivery is regulated on the predetermined reference points, as shown in Fig. 2.2. The control strategy is implemented with a current-controlled voltage source inverter (CCVSI). In Fig. 2.2, H_1 controller regulates the DC-link voltage and the active power through adjusting the magnitude of the output active current of the converter, i_p. H_2 controller regulates the output reactive power by adjusting the magnitude of the output reactive current, i.e., i_q [6].

In the voltage control mode, the DG operates as a voltage-controlled voltage source inverter (VCVSI)where thereference voltage, v_o^*, is determined by the primary control, conventionally via droop characteristics [6], as shown in Fig. 2.3. The nested voltage and current control loops in the voltage control mode are shown in Fig. 2.4. This controller feeds the current signal as a feedforward term via a transfer function (e.g., virtualimpedance) [1].

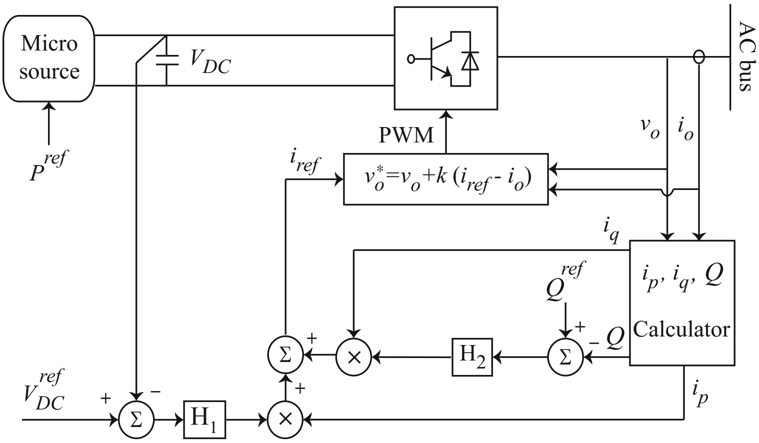

Fig. 2.2 PQ control mode with active and reactive power references. © [2016] IEEE. Reprinted, with permission, from IEEE Transactions on Smart Grid [1]

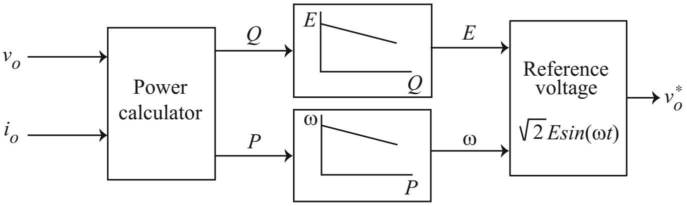

Fig. 2.3 Reference voltage determination for voltage control mode. © [2016] IEEE. Reprinted, with permission, from IEEE Transactions on Smart Grid [1]

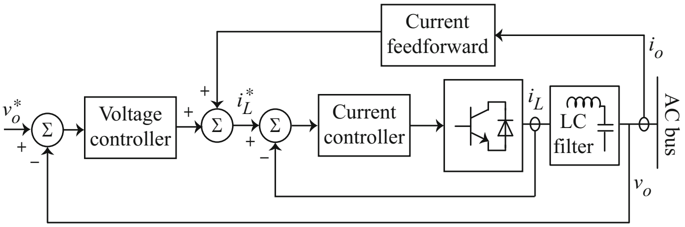

Fig. 2.4 Voltage and current control loops in voltage control mode. © [2016] IEEE. Reprinted, with permission, from IEEE Transactions on Smart Grid [1]

Power quality of small-scale islanded systems is of particular importance due to the presence of nonlinear and single-phase loads and the low inertia of the microgrid. To improve the power quality for a set of energy sources connected to a common bus, the control structure shown in Fig. 2.5 is used. In this figure, $H_{\mathrm{LPF}}(s)$ denotes the transfer function of a low-pass filter. Each converter has an independent

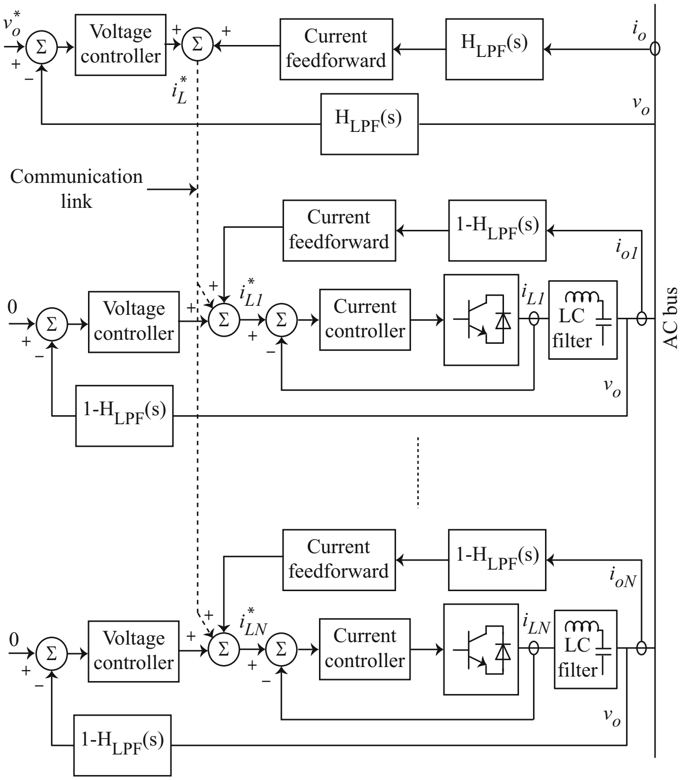

Fig. 2.5 Zero-level control loops for a set of energy sources connected to an AC bus. © [2016] IEEE. Reprinted, with permission, from IEEE Transactions on Smart Grid [1]

current control loop and a central voltage control loop that is adopted to distribute the fundamental component of the active and reactive powers among different sources. The reference point for the voltage controlloop is determined by the primary control. The individual current controllers ensure power quality by controlling the harmonic contents of the supplied currents to the common AC bus. The DG's control modes are usually implemented using the droop characteristic techniques [1, 8].

Droop Control. The droop control method has been referred to as independent, autonomous, and wireless control due to the elimination of intercommunication links between the converters. The conventional active power control (frequency droop characteristic) and reactive power control (voltage droop characteristic), those illustrated in Fig. 2.6, are used for voltage mode control. Principles of the conventional droop methods can be explained by considering an equivalent circuit of a VCVSI connected to an AC bus, as shown in Fig. 2.7. If switching ripples and high-frequency harmonics are neglected, the VCVSI can be modeled as an AC source, with the voltage of $E\angle\delta$. In addition, assume that the common AC bus

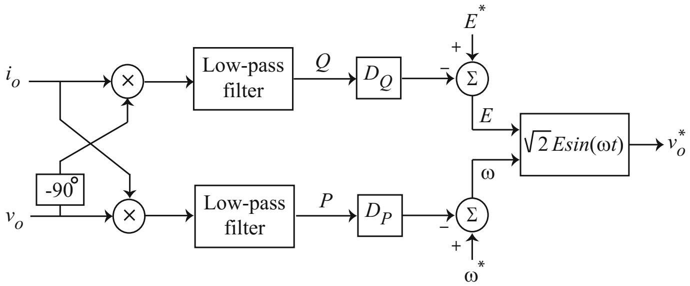

Fig. 2.6 Conventional droop method. © [2016] IEEE. Reprinted, with permission, from IEEE Transactions on Smart Grid [1]

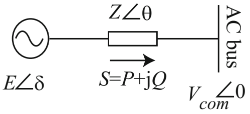

Fig. 2.7 Simplified diagram of a converter connected to the microgrid. © [2016] IEEE. Reprinted, with permission, from IEEE Transactions on Smart Grid [1]

voltage is $V_{\mathrm{com}}\angle 0$ and the converter output impedance and the line impedance are lumped as a single effective line impedance of $Z\angle\theta$. The complex power delivered to the common AC bus is calculated as

$$S = V_{\mathrm{com}} I^* = \frac{V_{\mathrm{com}} E\angle\theta - \delta}{Z} - \frac{V_{\mathrm{com}}^2\angle\theta}{Z}, \tag{2.1}$$

from which the real and reactive powers are achieved as

$$\begin{cases} P = \frac{V_{\mathrm{com}}E}{Z}\cos(\theta-\delta) - \frac{V_{\mathrm{com}}^2}{Z}\cos(\theta), \\ Q = \frac{V_{\mathrm{com}}E}{Z}\sin(\theta-\delta) - \frac{V_{\mathrm{com}}^2}{Z}\sin(\theta). \end{cases} \tag{2.2}$$

If the effective line impedance, $Z\angle\theta$, is assumed to be purely inductive, $\theta = 90°$, then (2.2) can be reduced to

$$\begin{cases} P = \frac{V_{\mathrm{com}}E}{Z}\sin\delta, \\ Q = \frac{V_{\mathrm{com}}E\,\cos\delta - V_{\mathrm{com}}^2}{Z}. \end{cases} \tag{2.3}$$

If the phase difference between the converter output voltage and the common AC bus, δ, is small enough, then $\sin\delta \approx \delta$ and $\cos\delta \approx 1$. Thus, one can apply the frequency and voltage droop characteristics to fine-tune the voltage reference of the VCVSI as shown in Fig. 2.6 based on

$$\begin{cases} \omega = \omega^* - D_P P, \\ E = E^* - D_Q Q, \end{cases} \tag{2.4}$$

where the primary control references E^* and ω^* are the DG output voltage RMS value and angular frequency at the no-load condition, respectively. The droop coefficients, D_P and D_Q, can be adjusted either heuristically or by tuning algorithms (e.g., particle swarm optimization [9]). In the former approach, D_P and D_Q are determined based on the converter power rating and the maximum allowable voltage and frequency deviations. For instance, in a microgrid with N DGs, corresponding D_P and D_Q should satisfy the following constraints [10, 11]

$$\begin{cases} D_{P1}P_{n1} = D_{P2}P_{n2} = \ldots = D_{PN}P_{nN} = \Delta\omega_{\max}, \\ D_{Q1}Q_{n1} = D_{Q2}Q_{n2} = \ldots = D_{QN}Q_{nN} = \Delta E_{\max}, \end{cases} \tag{2.5}$$

where $\Delta\omega_{\max}$ and $\Delta E_{\max}$ are the maximum allowable angular frequency and voltage deviations, respectively. P_{ni} and Q_{ni} are the nominal active and reactive powers of the ith DG.

During the grid-tied operation of microgrid, the DG voltage and angular frequency, E and ω, are enforced by the gird. The DG output active and reactive power references, P^{ref} and Q^{ref}, can hence be adjusted through E^* and ω^* [6] as

$$\begin{cases} P^{\text{ref}} = \frac{\omega^* - \omega}{D_P}, \\ Q^{\text{ref}} = \frac{E^* - E}{D_Q}. \end{cases} \tag{2.6}$$

Dynamic response of the conventional primary control, on the simplified system of Fig. 2.7, can be studied by linearizing (2.3) and (2.4). For instance, the linearized active power equation in (2.3) and frequency droop characteristic in (2.4) are

$$\begin{cases} \Delta P = G\Delta\delta, \\ \Delta\omega = \Delta\omega^* - D_P\Delta P. \end{cases} \tag{2.7}$$

where at the operating point of V_{com0}, E_0, and δ_0

$$G = \frac{V_{\text{com0}}E_0}{Z}\cos\delta_0, \tag{2.8}$$

and

$$\Delta\delta = \int \Delta\omega dt. \tag{2.9}$$

Therefore, the small-signal model for the active power control in (2.4) is

$$\Delta P(s) = \frac{G}{s + D_P G} \Delta\omega^*(s). \tag{2.10}$$

A similar procedure can be adopted to extract the small-signal model of the reactive power control.

The block diagram of the small-signal model for the active power control of (2.4) is demonstrated in Fig. 2.8. As shown in (2.10), time constant of the closed-loop control can only be adjusted by tuning D_P. On the other hand, as shown in (2.4), D_P also affects the DG frequency. Thus, a basic trade-off exists between the time constant of the control system and the frequency regulation.

As opposed to the active load sharing technique, the conventional droop method can be implemented with no communication links, and therefore, it is more reliable. However, it has some drawbacks as listed below:

- Since there is only one control variable for each droop characteristic, e.g., D_P for frequency droop characteristic, it is impossible to satisfy more than one control objectives. As an example, a design trade-off needs to be considered between the time constant of the control system and the voltage and frequency regulation [12, 13].
- The conventional droop method is developed assuming highly inductive effective impedance between the VCVSI and the AC bus. However, this assumption is challenged in microgrid applications since low-voltage transmission lines are mainly resistive. Thus, (2.3) is not valid for microgrid applications [11].
- As opposed to the frequency, the voltage is not a global quantity in the microgrid. Thus, the reactive power control in (2.4) may adversely affect the voltage regulation for critical loads.
- In case of nonlinear loads, the conventional droop method is unable to distinguish the load current harmonics from the circulating current. Moreover, the current harmonics distort the DG output voltage. The conventional droop method can be modified to reduce the total harmonic distortion (THD) of the output voltages [14, 15].

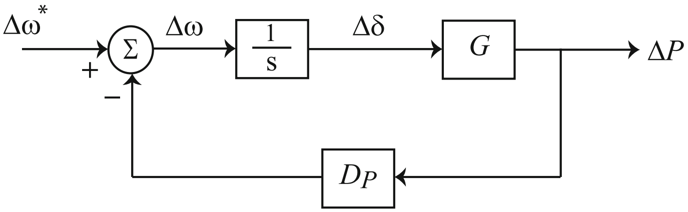

Fig. 2.8 Small-signal model of the conventional active power control. © [2016] IEEE. Reprinted, with permission, from IEEE Transactions on Smart Grid [1]

These potential drawbacks have been widely discussed in the literature. The proposed solutions are discussed next.

Adjustable Load Sharing Method. In this technique for improving droop control, the time constant of the proposed active and reactive power controllers can be adjusted without causing any impact on the DG voltage and frequency [12, 13]. The proposed active power controller uses the conventional controller in (2.4); however, the phase angle of the VCVSI, δ, in Fig. 2.7 is determined by

$$\delta = K_p \int \omega dt, \tag{2.11}$$

where K_p is an integral gain. Given (2.11), the small-signal model of the proposed controller can be derived as

$$\Delta P(s) = \frac{K_p G}{s + K_p D_P G} \Delta\omega^*(s), \tag{2.12}$$

where G is defined in (2.8). The block diagram of this model is illustrated in Fig. 2.9. The eigenvalue of the linearized control system of (2.12) is

$$\lambda = -K_p D_P G \tag{2.13}$$

Equation (2.13) shows this eigenvalue depends on the integral gain, K_p, and the droop coefficient, D_p. Therefore, the closed-loop time constant can be directly adjusted by tuning K_p. Since D_p is remained intact, the resulting frequency of the active power control in (2.4) will no longer be affected by the controller time constant adjustment.

Similarly, at the operating point of $V_{\text{com}0}$, E_0, and δ_0, the small-signal control for the reactive power control in (2.4) can be found by perturbing (2.3) and (2.4).

$$\Delta Q(s) = \frac{H}{1 + D_Q H} \Delta E^*(s), \tag{2.14}$$

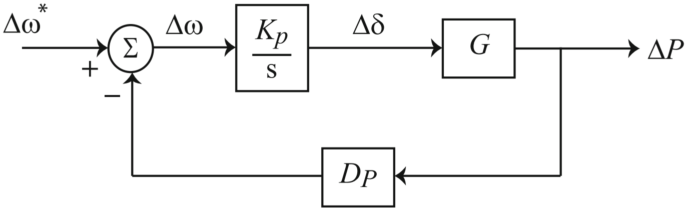

Fig. 2.9 The small-signal model of the adjustable active power control. © [2016] IEEE. Reprinted, with permission, from IEEE Transactions on Smart Grid [1]

where

$$H = \frac{V_{\text{com0}} \cos \delta_0}{Z}. \tag{2.15}$$

As shown in (2.14), ΔQ is a linear function of a reference signal, ΔE^*. Since H is a function of δ_0, line, and the operating point, performance of the conventional reactive power control in (2.4) tightly depends on the microgrid operational parameters. In the adjustable reactive power sharing method, an integral controller is used that regulates the common bus voltage in Fig. 2.7, V_{com}, to match a reference voltage, V_{ref} [12]

$$E = K_q \int (V_{\text{ref}} - V_{\text{com}}) \mathrm{d}t, \tag{2.16}$$

where K_q is the integral gain and

$$V_{\text{ref}} = E^* - D_Q Q. \tag{2.17}$$

In steady state, V_{com} and V_{ref} are equal. Moreover, the steady-state reactive power can be calculated as

$$Q = \frac{E^* - V_{\text{com}}}{D_Q}. \tag{2.18}$$

Thus, as opposed to (2.14) and (2.15), microgrid operational parameters will no longer affect the reactive power control. Additionally, voltage regulation of the common bus is guaranteed. The small-signal model for the proposed reactive power control is shown in Fig. 2.10 and is expressed by

$$\Delta Q(s) = \frac{k_q H}{s + k_q D_Q H} \Delta E^*(s) - \frac{k_q H}{s + k_q D_Q H} \Delta V_{\text{com}}(s) \tag{2.19}$$

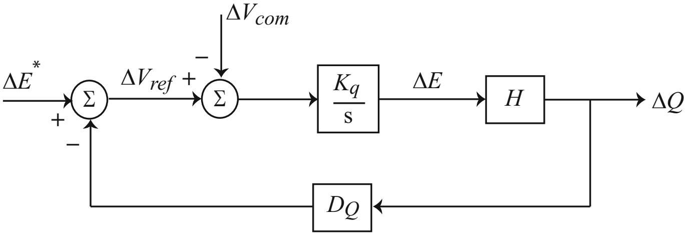

Fig. 2.10 The small-signal model of the adjustable reactive power control. © [2016] IEEE. Reprinted, with permission, from IEEE Transactions on Smart Grid [1]

The closed-loop transfer function of (2.19) is a function of both k_q and D_Q. Therefore, the dynamic response of the proposed reactive power control can be directly adjusted by k_q. Since D_Q is remained intact, the resulting voltage of the reactive power control in (2.4) will no longer be affected by the controller time constant adjustment.

VPD/FQB Droop Method. Low-voltage transmission lines are basically resistive. Thus, one can consider a resistive effective line impedance, i.e., $\theta = \theta^{\circ}$, and also can assume the δ to be small enough that $\sin\delta \approx \delta$. Considering these assumptions, (2.2) can be simplified as

$$\begin{cases} P \approx \frac{V_{\text{com}}E - V_{\text{com}}^2}{Z}, \\ Q \approx -\frac{V_{\text{com}}E}{Z}\delta. \end{cases} \tag{2.20}$$

Thus, the voltage-active power droop and frequency-reactive power boost (VPD/FQB) characteristics are alternatively considered [2]

$$\begin{cases} E = E^* - D_P P, \\ \omega = \omega^* + D_Q Q, \end{cases} \tag{2.21}$$

where E^* and ω^* are the output voltage amplitude and angular frequency of the DG at the no-load condition, respectively. D_P and D_Q are the droop and boost coefficients, respectively.

Droop and boost characteristics of VPD/FQB method are shown in Fig. 2.11. This approach offers an improved performance for controlling low-voltage microgrids with highly resistive transmission lines. However, it strongly depends on system parameters, and this dependency confines its application. Additionally, the VPD/FQB technique may face a malfunction in the presence of nonlinear loads and cannot guarantee the voltage regulation. Similar to the adjustable load sharing method, the VPD/FQB technique can be modified to adjust the controller time constant without causing voltage and frequency deviations. In the VPD control mode, the common bus voltage, V_{com}, is controlled to follow a reference voltage, V_{ref}.

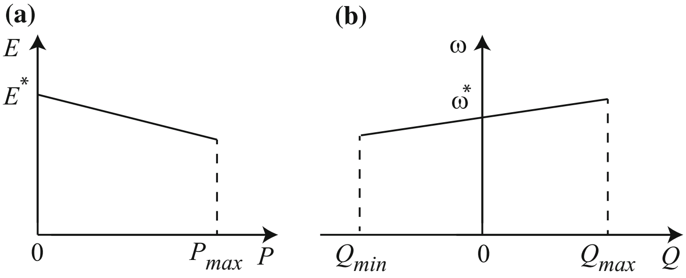

Fig. 2.11 Droop/boost characteristics for low-voltage microgrids: **a** voltage-active power droop characteristic and **b** frequency-reactive power boost characteristic. © [2016] IEEE. Reprinted, with permission, from IEEE Transactions on Smart Grid [1]

$$E = \left(K_{P1} + \frac{K_{I1}}{s}\right)(V_{\mathrm{ref}} - V_{\mathrm{com}}), \tag{2.22}$$

where

$$V_{\mathrm{ref}} = E^{*} - D_P P, \tag{2.23}$$

and K_{P1} and K_{I1} are the proportional and integral gains of the active power controller, respectively. In steady state,

$$V_{\mathrm{com}} = V_{\mathrm{ref}} = E^{*} - D_P P. \tag{2.24}$$

In the FQB control mode, δ is determined by another proportional–integral (PI) controller as

$$\delta = \left(K_{P2} + \frac{K_{I2}}{s}\right)\omega, \tag{2.25}$$

where K_{P2} and K_{I2} are the proportional and integral gains of the reactive power controller, respectively. In the modified VPD/FQB method, the time constants of the closed-loop controllers are directly adjusted by the proportional and integral gains, K_{P1}, K_{I1}, K_{P2}, and K_{I2}.

Virtual Frame Transformation Method. An orthogonal linear transformation matrix, $\mathbf{T}_{PQ}$, is used to transfer the active/reactive powers to a new reference frame where the powers are independent of the effective line impedance [16, 17]. For the system shown in Fig. 2.7, $\mathbf{T}_{PQ}$ is defined as

$$\begin{bmatrix} P' \\ Q' \end{bmatrix} = \mathbf{T}_{PQ}\begin{bmatrix} P \\ Q \end{bmatrix} = \begin{bmatrix} \sin\theta & -\cos\theta \\ \cos\theta & \sin\theta \end{bmatrix}\begin{bmatrix} P \\ Q \end{bmatrix}. \tag{2.26}$$

The transformed active and reactive powers, P' and Q', are then used in droop characteristics in (2.4). The block diagram of this technique is shown in Fig. 2.12.

Similarly, a virtual frequency/voltage frame transformation is defined as

$$\begin{bmatrix} \omega' \\ E' \end{bmatrix} = \mathbf{T}_{\omega E}\begin{bmatrix} \omega \\ E \end{bmatrix} = \begin{bmatrix} \sin\theta & \cos\theta \\ -\cos\theta & \sin\theta \end{bmatrix}\begin{bmatrix} \omega \\ E \end{bmatrix}, \tag{2.27}$$

where E and ω are calculated through the conventional droop equations in (2.4). The transformed voltage and frequency, E' and ω', are then used as reference values for the VCVSI voltage control loop [18]. The virtual frame transformation method decouples the active and reactive power controls. However, the applied transformation requires a prior knowledge of the effective line impedance. Moreover, the control method does not consider possible negative impacts of nonlinear loads, does not ensure a regulated voltage, and comprises a basic trade-off between the control loop time constant adjustment and voltage/frequency regulation.

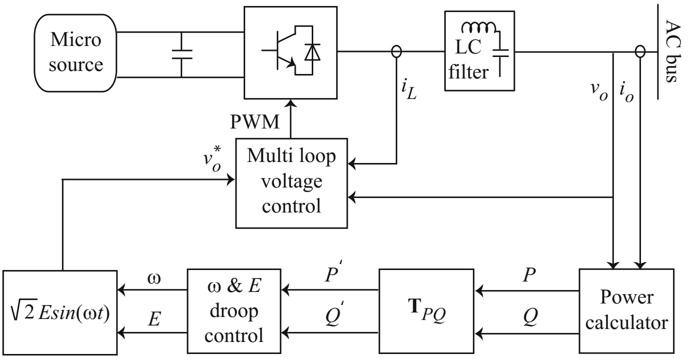

Fig. 2.12 Droop method with virtual power frame transformation. © [2016] IEEE. Reprinted, with permission, from IEEE Transactions on Smart Grid [1]

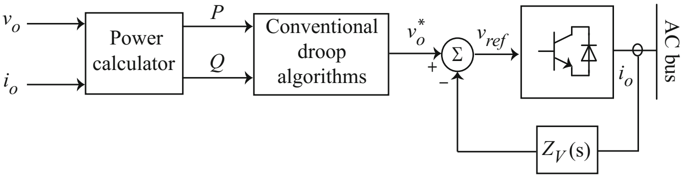

Fig. 2.13 Block diagram of the virtual output impedance method. © [2016] IEEE. Reprinted, with permission, from IEEE Transactions on Smart Grid [1]

Virtual Output Impedance. An intermediate control loop can be adopted to adjust the output impedance of the VCVSIs [19, 20]. In this control loop, as depicted in Fig. 2.13, the VCVSI output voltage reference, v_{ref}, is proportionally drooped with respect to the output current, i_{o}, i.e.,

$$v_{\text{ref}} = v_{\text{o}}^{*} - Z_V(s)i_o, \tag{2.28}$$

where $Z_V(s)$ is the virtual output impedance and v_{o}^{*} is the output voltage reference that is obtained by the conventional droop techniques in (2.4). If $Z_V(s) = sL_V$ is considered, a virtual output inductance is emulated for the VCVSI. In this case, the output voltage reference of the VCVSI is drooped proportional to the derivative of its output current. In the presence of nonlinear loads, the harmonic currents can be properly shared by modifying (2.28) as

$$v_{\text{ref}} = v_{\text{o}}^{*} - s\sum L_{Vh}I_h, \tag{2.29}$$

where I_h is the hth current harmonic and L_{Vh} is the inductance associated with I_h. L_{Vh} values need to be precisely set to effectively share the current harmonics.

Since the output impedance of the VCVSI is frequency dependent, in the presence of nonlinear loads, THD of the output voltage would be relatively high. This can be mitigated by using a high-pass filter instead of sL_V in (2.28)

$$v_{\text{ref}} = v_{\text{o}}^* - L_V \frac{s}{s+\omega_c} i_o \tag{2.30}$$

where ω_c is the cutoff frequency of the high-pass filter.

If the virtual impedance, Z_V, is properly adjusted, it can prevent the occurrence of current spikes when the DG is initially connected to the microgrid. This soft starting can be facilitated by considering a time-variant virtual output impedance as

$$Z_V(t) = Z_f - (Z_f - Z_i)e^{-t/T}, \tag{2.31}$$

where Z_i and Z_f are the initial and final values of the virtual output impedance, respectively. T is the time constant of the start-up process.

Most recently, the virtual output impedance method has been modified for voltage unbalance compensation, caused by the presence of unbalanced loads in the microgrid [12]. The block diagram of the modified virtual output impedance method is shown in Fig. 2.14. As is shown, the measured DG output voltage and current are fed into the positive and negative sequence calculator (PNSC). Outputs of the PNSC, i_{o}^+, i_{o}^-, v_{o}^+, and v_{o}^-, are used to find the positive and negative sequences of the DG active and reactive powers. The negative sequence of the reactive power, Q^-, is multiplied by the v_{o}^- and then a constant gain, G. The result is then used to find the voltage reference. The constant gain G needs to be fine-tuned to minimize the voltage unbalance without compromising the closed-loop stability [21].

The virtual output impedance method alleviates the dependency of the droop techniques on system parameters. Additionally, this control method properly operates in the presence of nonlinear loads. However, this method does not guarantee the voltage regulation, and adjusting the closed-loop time constant may result in an undesired deviation in the DG voltage and frequency.

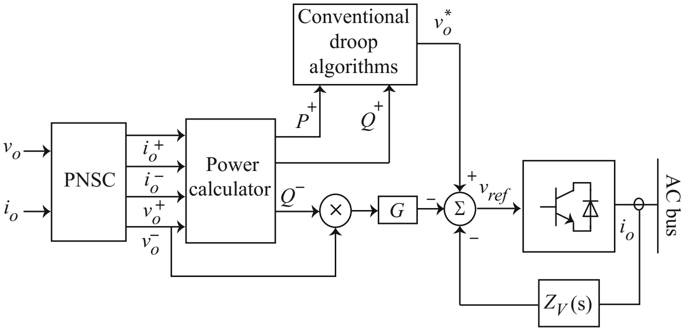

Fig. 2.14 Virtual output impedance with voltage unbalance compensator. © [2016] IEEE. Reprinted, with permission, from IEEE Transactions on Smart Grid [1]

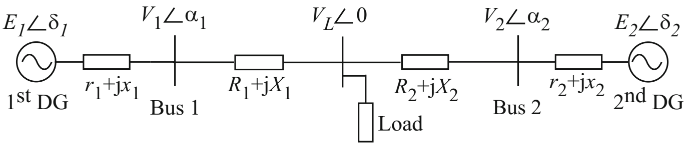

Fig. 2.15 A typical two-DG system. © [2016] IEEE. Reprinted, with permission, from IEEE Transactions on Smart Grid [1]

Adaptive Voltage Droop Control. In this method, two terms are added to the conventional reactive power control in (2.4). Additional terms are considered to compensate for the voltage drop across the transmission lines that deliver power from the DG to critical loads [11]. For a typical 2-DG system shown in Fig. 2.15, the voltages at first and second buses are

$$V_i\angle\alpha_i = E_i\angle\delta_i - (r_i + jx_i)(I_i\angle - \theta_i), \quad i = 1, 2, \tag{2.32}$$

where $I_i\angle - \theta_i$ is the output current of the ith DG. Using (2.4), one can write

$$V_i = E_i^* - D_{Qi}Q_i - r_iI_i\cos\gamma_i - x_iI_i\sin\gamma_i, \tag{2.33}$$

where $\gamma_i = \alpha_i + \theta_i$. The bus voltage of the ith DG can also be formulated in terms of its active and reactive powers, P_i and Q_i, as

$$V_i = E_i^* - D_{Qi}Q_i - \frac{r_iP_i}{E_i^*} - \frac{x_iQ_i}{E_i^*}. \tag{2.34}$$

The terms r_iP_i/E_i^* and x_iQ_i/E_i^* represent the voltage drop on the internal impedance $r_i + jx_i$. These terms can be incorporated in the conventional reactive power control of (2.4) to compensate for the voltage drops in the transmission lines as

$$E_i = E_i^* + \left(\frac{r_iP_i}{E_i^*} + \frac{x_iQ_i}{E_i^*}\right) - D_{Qi}Q_i \tag{2.35}$$

Although the reactive power control in (2.35) improves the voltage regulation of the farther buses, it is still dependent on the active power control in (2.4). This problem is resolved by adopting the voltage droop coefficient as a nonlinear function of active and reactive powers [11]

$$\begin{cases} E_i = E_i^* + (\frac{r_iP_i}{E_i^*} + \frac{x_iQ_i}{E_i^*}) - D_i(P_i, Q_i)Q_i, \\ D_i(P_i, Q_i) = D_{Qi} + m_{Qi}Q_i^2 + m_{Pi}P_i^2, \end{cases} \tag{2.36}$$

where D_{Qi}, m_{Qi}, and m_{Pi} are droop coefficients. The terms $m_{Qi}Q_i^2$ and $m_{Pi}P_i^2$ mitigate the negative impacts of the active power control and the microgrid parameters on the reactive power control.

The adaptive droop method is particularly desirable when the voltage regulation of some buses is not feasible. The higher-order terms in (2.36) significantly improve the reactive power sharing under heavy loading conditions. The potential disadvantage, however, is the required prior knowledge of the transmission line parameters [11]. This control method is not fully functional in the presence of nonlinear loads. Moreover, given the basics discussed for the adjustable load sharing method, adjusting the time constant may result in undesired deviations in DG voltage and frequency.

Signal Injection Method. In this approach, each DG injects a small AC voltage signal to the microgrid. Frequency of this control signal, ω_q, is determined by the output reactive power, Q, of the corresponding DG as

$$\omega_q = \omega_{q0} + D_Q Q, \tag{2.37}$$

where ω_{q0} is the nominal angular frequency of injected voltage signals and D_Q is the boost coefficient. The small real power transmitted through the signal injection is then calculated, and the RMS value of the output voltage of the DG, E, is accordingly adjusted as

$$E = E^* - D_P p_q, \tag{2.38}$$

where E^* is the RMS value of the no-load voltage of the DG and D_P is the droop coefficient. This procedure is repeated until all VCVSIs produce the same frequency for the control signal.

Here, this technique is elaborated for a system of two DGs shown in Fig. 2.15. It is assumed that D_Q is the same for both DGs. Initially, first and second DGs inject low-voltage signals to the system with the following frequencies:

$$\begin{cases} \omega_{q1} = \omega_{q0} + D_Q Q_1, \\ \omega_{q2} = \omega_{q0} + D_Q Q_2. \end{cases} \tag{2.39}$$

Assuming $Q_1 > Q_2$

$$\Delta\omega = \omega_{q1} - \omega_{q2} = D_Q(Q_1 - Q_2) = D_Q \Delta Q \tag{2.40}$$

The phase difference between the two voltage signals can be obtained as

$$\delta = \int \Delta\omega \mathrm{d}t = D_Q \Delta Q t. \tag{2.41}$$

Due to the phase difference between the DGs, a small amount of active power flows from one to the other. Assuming inductive output impedances for DGs, the transmitted active power from DG1 to DG2, p_{q1}, is

$$p_{q1} = \frac{V_{q1} V_{q2}}{x_1 + x_2 + X_1 + X_2} \sin \delta, \tag{2.42}$$

where V_{q1} and V_{q2} are the RMS values of the injected voltage signals. Moreover, the transmitted active power in reverse direction, from DG2 to DG1, p_{q2}, is

$$p_{q2} = -p_{q1}. \tag{2.43}$$

The DG voltages are adjusted as

$$\begin{cases} E_1 = E^* - D_P p_{q1}, \\ E_2 = E^* - D_P p_{q2}. \end{cases} \tag{2.44}$$

Herein, it is assumed that D_P is the same for both DGs. The difference between the DG output voltages is

$$\Delta E = E_1 - E_2 = -2 D_P p_{q1}. \tag{2.45}$$

Thus, one can write

$$\begin{cases} \Delta Q = A \Delta E, \\ A = 2V_L \frac{\sin \varphi}{|Z|} - V_L \frac{\sin(\varphi + \delta)}{|Z|}, \\ r_1 + R_1 + j(x_1 + X_1) = r_2 + R_2 + j(x_2 + X_2) = |Z| \angle \varphi, \end{cases} \tag{2.46}$$

where V_L is the load voltage. The block diagram of the proposed controller is shown in Fig. 2.16.

In the presence of nonlinear loads, parallel DGs can be controlled to participate in supplying current harmonics by properly adjusting the voltage loop bandwidth [22]. For that, first, frequency of the injected voltage is drooped based on the total distortion power, D

$$\begin{cases} \omega_d = \omega_{d0} - m D, \\ D = \sqrt{S^2 - P^2 - Q^2}, \end{cases} \tag{2.47}$$

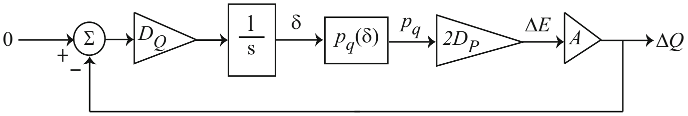

Fig. 2.16 Block diagram of the signal injection method for reactive power sharing. © [2016] IEEE. Reprinted, with permission, from IEEE Transactions on Smart Grid [1], [22]

where ω_{d0} is the nominal angular frequency of the injected voltage signals, m is the droop coefficient, and S is the DG nominal power. A procedure similar to (2.39)–(2.42) is adopted to calculate the power transmitted by the injected signal, p_d. The bandwidth of VCVSI voltage loop is adjusted as

$$\mathrm{BW} = \mathrm{BW}_0 - D_{\mathrm{bw}} p_d, \tag{2.48}$$

where BW_0 is the nominal bandwidth of the voltage loop and D_{bw} is the droop coefficient. The block diagram of the signal injection method is shown in Fig. 2.17.

Signal injection method properly controls the reactive power sharing and is not sensitive to variations in the line impedances [23]. It also works for linear and nonlinear loads and over various operating conditions. However, it does not guarantee the voltage regulation.

Nonlinear Load Sharing. Some have challenged the functionality of droop techniques in the presence of nonlinear loads [14, 15]. Two approaches for resolving this issue are discussed here. In the first approach [14], the DGs equally share the linear and nonlinear loads. For this purpose, each harmonic of the load current, I_h, is sensed to calculate the corresponding voltage droop harmonic, V_h, at the output terminal of the DG. The voltage harmonics are compensated by adding 90° leading signals, corresponding to each current harmonic, to the DG voltage reference. Therefore, the real and imaginary parts of the voltage droop associated with each current harmonic are

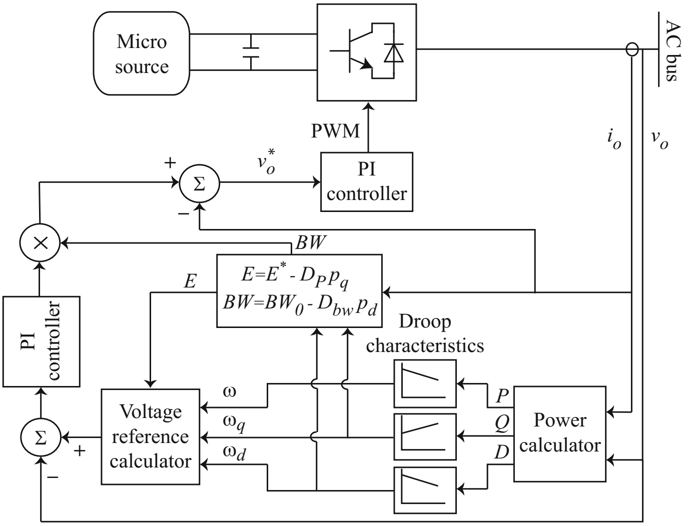

Fig. 2.17 Block diagram of the updated signal injection method. © [2016] IEEE. Reprinted, with permission, from IEEE Transactions on Smart Grid [1]

$$\begin{cases} \mathrm{Re}(V_h) = -k_h \mathrm{Im}(I_h), \\ \mathrm{Im}(V_h) = k_h \mathrm{Re}(I_h), \end{cases} \tag{2.49}$$

where k_h is the droop coefficient for the hth harmonic. As a result, the output voltage THD is significantly improved.

In the second approach, the conventional droop method is modified to compensate for the harmonics of the DG output voltage. These voltage harmonics are caused by the distorted voltage drop across the VCVSI output impedance and are due to the distorted nature of the load current [15]. As shown in Fig. 2.18, first, the DG output voltage and current are used to calculate the fundamental term and harmonics of the DG output active and reactive powers, (P_1, Q_1) and (P_h, Q_h), respectively. It is noteworthy that distorted voltage and current usually do not carry even harmonics, and thus, h is usually an odd number. P_1 and Q_1 are fed to the conventional droop characteristics in (2.4) to calculate the fundamental term, v_o^*, of the VCVSI voltage reference, v_{ref}. As shown in Fig. 2.18, to cancel out the output voltage harmonics, a set of droop characteristics are considered for each individual harmonic. Each set of droop characteristics determines an additional term to be included in the VCVSI output voltage reference, v_{ref}, to cancel the corresponding voltage harmonic. Each current harmonic, I_h, is considered as a constant current source, as shown in Fig. 2.19. In this figure, $E_h \angle \delta_h$ denotes a phasor for the corresponding voltage signal that is included in the voltage reference, v_{ref}. $Z_h \angle \theta_h$ represents the VCVSI output impedance associated with the hth current harmonic. The active and reactive powers delivered to the harmonic current source, P_h and Q_h, are

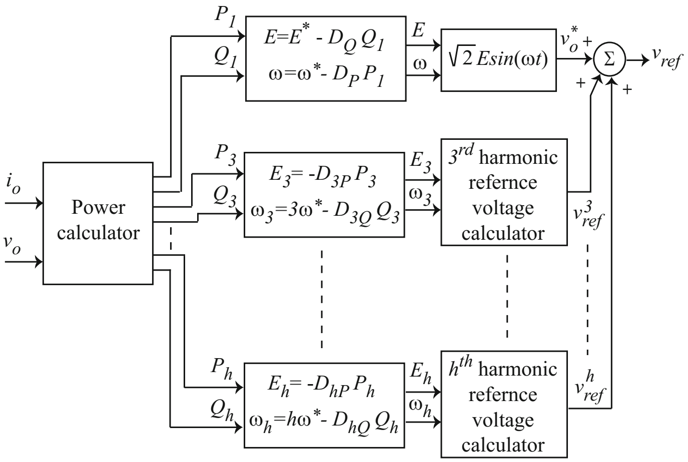

Fig. 2.18 Control block diagram for the harmonic cancelation technique. © [2016] IEEE. Reprinted, with permission, from IEEE Transactions on Smart Grid [1]

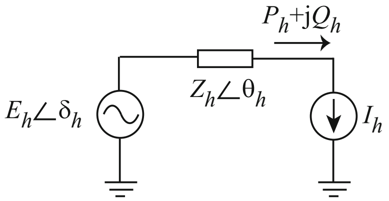

Fig. 2.19 *h*th harmonic equivalent circuit of a DG. © [2016] IEEE. Reprinted, with permission, from IEEE Transactions on Smart Grid [1]

$$\begin{cases} P_h = E_h I_h \cos\delta_h - Z_h I_h^2 \cos\theta_h, \\ Q_h = E_h I_h \sin\delta_h - Z_h I_h^2 \sin\theta_h. \end{cases} \tag{2.50}$$

When δ_h is small enough (i.e., $\sin(\delta_h) = \delta_h$), P_h and Q_h are roughly proportional to E_h and θ_h, respectively. Therefore, the following droop characteristics can be used to eliminate the *h*th DG output voltage harmonic

$$\begin{cases} \omega_h = h\omega^* - D_{hQ}Q_h, \\ E_h = -D_{hP}P_h, \end{cases} \qquad h \neq 1, \tag{2.51}$$

where ω^* is the rated fundamental frequency of the microgrid. D_{hP} and D_{hQ} are the droop coefficients. As is shown in Fig. 2.18, the harmonic reference voltage, v_{ref}^h, for eliminating the *h*th output voltage harmonic, can be formed with E_h and the phase angle generated from the integration of ω_h.

Primary control techniques are application specific and bring specific features. The active load sharing method provides tight current sharing and high power quality; however, it requires communication links and high-bandwidth control loops. On the other hand, the droop methods provide local controls without any communication infrastructures. The potential advantages and disadvantages of the conventional droop method and its modifications are outlined in Table 2.1, based on which the following statements can be concluded:

- System identification is required to find the line parameters for some techniques, e.g., adaptive voltage droop or virtual frame transformation methods.
- Modified droop techniques, excluding the ones for low-voltage microgrids, decouple the active and reactive power controls.
- Adjustable load sharing and adaptive voltage droop methods are the only techniques that offer voltage regulation.
- Nonlinear loads need to be accommodated with the complicated control techniques such as the virtual impedance, the signal injection, or the nonlinear load sharing methods to achieve a mitigated level of harmonics in the microgrid.

The adjustable load sharing is the only technique where the system time constant can be independently adjusted without affecting the DG voltage and frequency.

Table 2.1 The potential advantages and disadvantages of the discussed droop methods

Droop method	Potential advantages	Potential disadvantages
Conventional droop method	Simple implementation	Affected by the system parameters Only functional for highly inductive transmission lines Cannot handle nonlinear loads Voltage regulation is not guaranteed Adjusting the controller speed for the active and reactive power controllers can affect the voltage and frequency controls
Adjustable load sharing method	Adjusting the controller speed for the active and reactive power controllers without compromising the voltage and frequency controls Robust to the system parameter variations Improved voltage regulation	Cannot handle nonlinear loads
VPD/FQB droop method	Simple implementation Adjusting the controller speed for the active and reactive power controllers without compromising the voltage and frequency controls	Affected by the system parameters Only functional for highly resistive transmission lines Cannot handle nonlinear loads
Virtual frame transformation method	Simple implementation Decoupled active and reactive power controls	Cannot handle nonlinear loads The line impedances should be known a priori Adjusting the controller speed for the active and reactive power controllers can affect the voltage and frequency controls Voltage regulation is not guaranteed
Virtual output impedance	Simple implementation Not affected by the system parameters Functional for both linear and nonlinear loads Mitigates the harmonic distortion of the output voltage Can compensate for the unbalance of the DG output voltages	Adjusting the controller speed for the active and reactive power controllers can affect the voltage and frequency controls Voltage regulation is not guaranteed
Adaptive voltage droop method	Improved voltage regulation Not affected by the system parameters	Cannot handle nonlinear loads Adjusting the controller speed for the active and reactive power controllers can affect the voltage and frequency controls System parameters should be known a priori

(continued)

Table 2.1 (continued)

Droop method	Potential advantages	Potential disadvantages
Signal injection method	Functional for both linear and nonlinear loads Not affected by the system parameters	Complicated implementation Adjusting the controller speed for the active and reactive power controllers can affect the and frequency controls Voltage regulation is not guaranteed
Nonlinear load sharing techniques	Properly shares the current harmonics between the DGs and, consequently, cancels out the voltage harmonics	Affected by the system parameters Poor voltage regulation for the case of precise reactive power sharing Adjusting the controller speed for the active and reactive power controllers can affect the voltage and frequency controls

2.1.3 Secondary Control

Primary control, as discussed previously, may cause frequency and voltage deviations even in steady state. Although the energy storage devices can compensate for this deviation, they are unable to provide the power for load frequency control over the long term due to their short energy capacity. Primary control is implemented locally at each DG. The secondary control, as a centralized controller, restores the microgrid voltage and frequency and compensates for the deviations caused by the primary control. This level of the control hierarchy is designed to have slower dynamic response than that of the primary, which justifies decoupled dynamics analysis of the primary and the secondary control loops and facilitates their individual designs [1].

Figure 2.20 represents the block diagram of the conventional secondary control with a centralized control structure. As shown in this figure, frequency of the microgrid and the terminal voltage of a given DG are compared with the corresponding reference values, ω_{ref} and v_{ref}, respectively. Then, the error signals are processed by individual controllers as in (2.52); the resulting signals ($\delta\omega$ and δE) are sent to the primary controller of the DG to compensate for the frequency and voltage deviations [1, 24]

$$\begin{cases} \delta\omega = K_{P\omega}(\omega_{\text{ref}} - \omega) + K_{I\omega}\int(\omega_{\text{ref}} - \omega)dt + \Delta\omega_s, \\ \delta E = K_{PE}(v_{\text{ref}} - E) + K_{IE}\int(v_{\text{ref}} - E)dt, \end{cases} \tag{2.52}$$

where $K_{P\omega}$, $K_{I\omega}$, K_{PE}, and K_{IE} are the controller parameters. An additional term, $\Delta\omega_s$, is considered in frequency controller in (2.52) to facilitate synchronization of the microgrid to the main gird. In the islanded operating mode, this additional term is zero. However, during the synchronization, a PLL module is required to measure $\Delta\omega_s$. During the grid-tied operation, voltage and frequency of the main grid are considered as the references in (2.52).

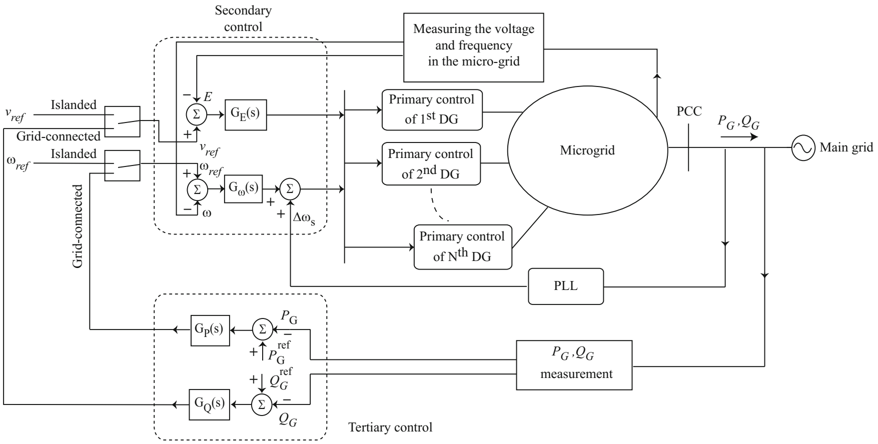

Fig. 2.20 Block diagram of the secondary and tertiary controls. © [2016] IEEE. Reprinted, with permission, from IEEE Transactions on Smart Grid [1]

Most recently, the potential function-based optimization technique has been suggested for secondary control [18]. In this method, a potential function is considered for each DG. This function is a scalar cost function that carries all the information on the DG measurements, constraints, and control objectives as

$$\varphi_j(x_j) = w^u \sum_{i=1}^{n_u} p_i^u(x_j) + w^c \sum_{i=1}^{n_c} p_i^c(x_j) + w^g p_j^g(x_j), \tag{2.53}$$

where φ_j is the potential function related to each DG and x_j comprises the measurements from the DG unit (e.g., voltage, current, and real and reactive powers). p_i^u denotes the partial potential functions that reflect the measurement information of the DG. p_i^c denotes the operation constraints that ensure the stable operation of microgrid. p_j^g is used to mitigate the DG measurements from the predefined set points. w^u, w^c, and w^g are the weighted factors for the partial potential functions.

The block diagram of the potential function-based technique is shown in Fig. 2.21. In this technique, when the potential functions approach their minimum values, the microgrid is about to operate at the desired states. Therefore, inside the optimizer in Fig. 2.21, set points of the DG are determined so as to minimize the potential functions and thus to meet the microgrid control objectives.

The potential function-based technique requires bidirectional communication infrastructure to facilitate data exchange from the DG to the optimizer (measurements) and vice versa (calculated set points). The data transfer links add propagation delays to the control signals. This propagation delay is tolerable, since the secondary controllers are slower than the primary ones.

The secondary control can also be designed to satisfy the power quality requirements, e.g., voltage balancing at critical buses [25]. The block diagram of the

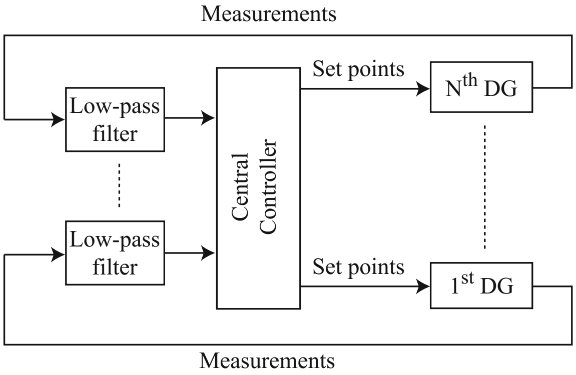

Fig. 2.21 The potential function-based technique block diagram. © [2016] IEEE. Reprinted, with permission, from IEEE Transactions on Smart Grid [1]

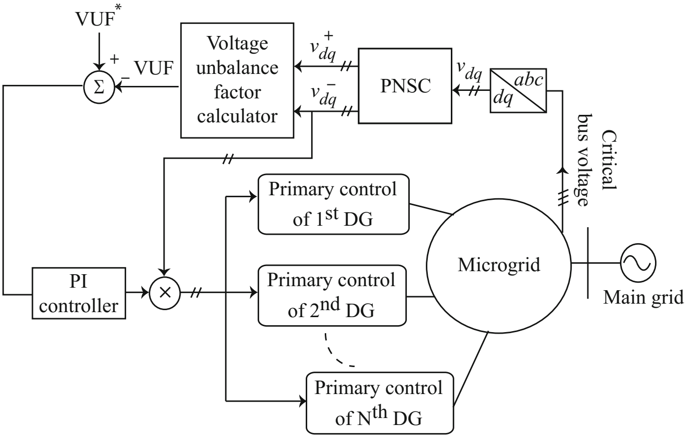

Fig. 2.22 Voltage unbalance compensation in the secondary control. © [2016] IEEE. Reprinted, with permission, from IEEE Transactions on Smart Grid [1]

voltage unbalance compensator is shown in Fig. 2.22. First, the critical bus voltage is transformed to the *d*-*q* reference frame. Once the positive and negative sequence voltages for both *d*- and *q*-axis are calculated, one can find the voltage unbalance factor (VUF) as

$$\mathrm{VUF} = 100\frac{\sqrt{(v_d^-)^2 + (v_q^-)^2}}{\sqrt{(v_d^+)^2 + (v_q^+)^2}}, \tag{2.54}$$

where v_d^+ and v_d^- are the positive and negative sequence voltages of the direct component and v_q^+ and v_q^- are the positive and negative sequence voltages of the quadrature component, respectively. As depicted in Fig. 2.22, the calculated VUF is compared with the reference value, VUF*, and the difference is fed to a PI controller. The controller output is multiplied by the negative sequence of the direct and quadrature voltage components, v_d^- and v_q^-, and the results are added to the references of DG voltage controllers to compensate for the voltage unbalance.

2.1.4 Tertiary Control

Tertiary control is the last control level in Fig. 2.1 and operates on the slowest timescale. It considers the economical concerns for optimal operation of the microgrid and manages the power flow between microgrid and main grid [7]. In the grid-tied mode, the power flow between microgrid and main grid can be managed by adjusting the amplitude and frequency of DG . The block diagram of this process is shown in Fig. 2.20. First, active and reactive output powers of the microgrid, P_G and Q_G, are measured. These quantities are then compared with the corresponding reference values, P_G^{ref} and Q_G^{ref}, to obtain the frequency and voltage references, ω_{ref} and v_{ref} based on

$$\begin{cases} \omega_{\mathrm{ref}} = K_{PP}(P_G^{\mathrm{ref}} - P_G) + K_{IP}\int (P_G^{\mathrm{ref}} - P_G)\mathrm{d}t, \\ v_{\mathrm{ref}} = K_{PQ}(Q_G^{\mathrm{ref}} - Q_G) + K_{IQ}\int (Q_G^{\mathrm{ref}} - Q_G)\mathrm{d}t, \end{cases} \tag{2.55}$$

where K_{PP}, K_{IP}, K_{PQ}, and K_{IQ} are the controller parameters [1]. ω_{ref} and v_{ref} are further used as the reference values to the secondary control, as in (2.52).

The tertiary control also provides an economically optimal operation, e.g., by using a gossiping algorithm. Generally, the economically optimal operation is satisfied if all the DGs operate at equal marginal costs (variation of the total cost with respect to the variation of the generated power), C_{opt} [26–29]. In the gossiping algorithm, initially, random output power set points, P_i^0 and P_j^0, are considered for the ith DG and its random gossiping partner, jth DG, respectively. Then, considering the prior knowledge about the marginal cost curves of the DGs, the optimal output power of the two DGs, P_i^{opt} and P_j^{opt}, is determined. At this time, each of the two DGs changes its output power to generate at the optimal point. The aforementioned procedure is illustrated in Fig. 2.23. The same procedure is repeated for other pairs of DGs until the whole DGs in the microgrid operate optimally. Additionally, evolutionary game theory-based techniques are proposed to facilitate the power management by local information and thus to simplify the required communication infrastructures.

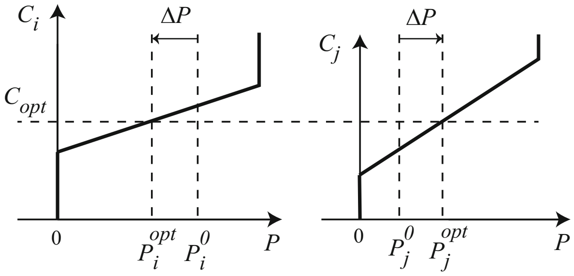

Fig. 2.23 Marginal cost function matching between two DGs. © [2016] IEEE. Reprinted, with permission, from IEEE Transactions on Smart Grid [1]

2.2 Dynamic Modeling of AC Microgrids

The microgrid control schemes employ the nonlinear dynamical model of DGs. In this section, the dynamical model of VCVSIs and CCVSIs is elaborated.

2.2.1 *Voltage-Controlled Voltage Source Inverters*

The block diagram of a voltage-controlled voltage source inverter (VCVSI)-based DG is shown in Fig. 2.24. It contains an inverter bridge, connected to a primary DC power source (e.g., photovoltaic panels or fuel cells). The control loops, including the power, voltage, and current controllers, adjust the output voltage and frequency

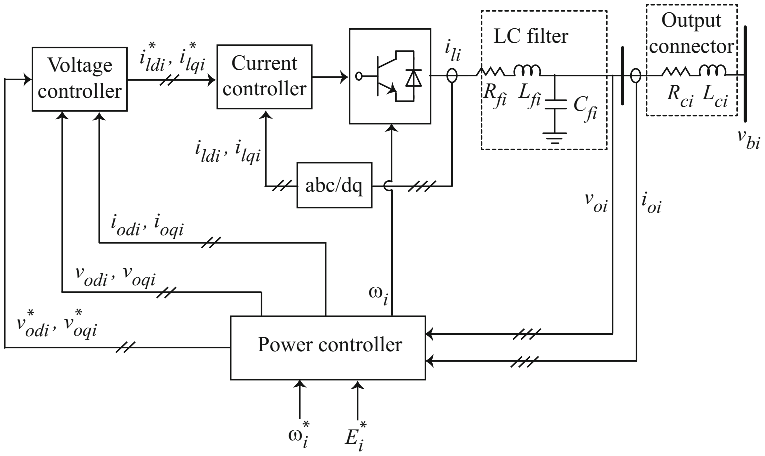

Fig. 2.24 Block diagram of an inverter-based DG. © [2016] IEEE. Reprinted, with permission, from IEEE Transactions on Power Systems [33]

of the inverter bridge [18, 24, 27]. Given the relatively high switching frequency of the inverter bridge, the switching artifacts can be safely neglected via average-value modeling. As stated in [9], DC bus dynamics can be safely neglected, assuming an ideal source from the DG side.

It should be noted that the nonlinear dynamics of each DG are formulated in its own *d*-*q* (direct–quadrature) reference frame. It is assumed that the reference frame of the *i*th DG is rotating at the frequency of ω_i. The reference frame of one DG is considered as the common reference frame with the rotating frequency of ω_{com}. The angle of the *i*th DG reference frame, with respect to the common reference frame, is denoted as δ_i and satisfies the following differential equation

$$\dot{\delta}_i = \omega_i - \omega_{\mathrm{com}}. \tag{2.56}$$

The power controller block, shown in Fig. 2.25, contains the droop technique in (2.4) and provides the voltage references v^*_{odi} and v^*_{oqi} for the voltage controller, as well as the operating frequency ω_i for the inverter bridge. Two low-pass filters with the cutoff frequency of ω_{ci} are used to extract the fundamental component of the output active and reactive powers, denoted as P_i and Q_i, respectively. The differential equations of the power controller can be written as

$$\dot{P}_i = -\omega_{\mathrm{ci}} P_i + \omega_{\mathrm{ci}} (v_{\mathrm{odi}} i_{\mathrm{odi}} + v_{\mathrm{oqi}} i_{\mathrm{oqi}}), \tag{2.57}$$

$$\dot{Q}_i = -\omega_{\mathrm{ci}} Q_i + \omega_{\mathrm{ci}} (v_{\mathrm{oqi}} i_{\mathrm{odi}} - v_{\mathrm{odi}} i_{\mathrm{oqi}}), \tag{2.58}$$

where v_{odi}, v_{oqi}, i_{odi}, and i_{oqi} are the direct and quadrature components of v_{oi} and i_{oi} in Fig. 2.24. As shown in Fig. 2.25, the primary voltage control strategy for each DG aligns the output voltage magnitude on the *d*-axis of the corresponding reference frame. Therefore,

$$\begin{cases} v^*_{\mathrm{odi}} = E^*_i - D_{Qi} Q_i, \\ v^*_{\mathrm{oqi}} = 0. \end{cases} \tag{2.59}$$

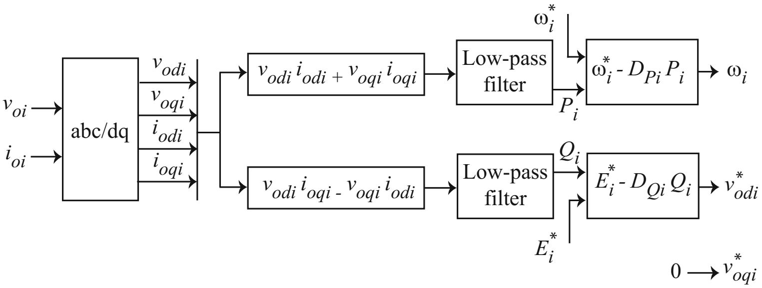

Fig. 2.25 Block diagram of the power controller. © [2016] IEEE. Reprinted, with permission, from IEEE Transactions on Power Systems [33]

The block diagram of the voltage controller is shown in Fig. 2.26. The differential algebraic equations of the voltage controller are written as

$$\dot{\phi}_{\mathrm{di}} = v^{*}_{\mathrm{odi}} - v_{\mathrm{odi}}, \tag{2.60}$$

$$\dot{\phi}_{\mathrm{qi}} = v^{*}_{\mathrm{oqi}} - v_{\mathrm{oqi}}, \tag{2.61}$$

$$i^{*}_{\mathrm{ldi}} = F_i i_{\mathrm{odi}} - \omega_b C_{fi} v_{\mathrm{oqi}} + K_{\mathrm{PV}i}(v^{*}_{\mathrm{odi}} - v_{\mathrm{odi}}) + K_{\mathrm{IVi}}\phi_{\mathrm{di}}, \tag{2.62}$$

$$i^{*}_{\mathrm{lqi}} = F_i i_{\mathrm{oqi}} + \omega_b C_{\mathrm{fi}} v_{\mathrm{odi}} + K_{\mathrm{PVi}}(v^{*}_{\mathrm{oqi}} - v_{\mathrm{oqi}}) + K_{\mathrm{IVi}}\phi_{\mathrm{qi}}, \tag{2.63}$$

where ϕ_{di} and ϕ_{qi} are the auxiliary state variables defined for PI controllers in Fig. 2.26 and ω_b is the nominal angular frequency. Other parameters are shown in Figs. 2.24 and 2.26.

The block diagram of the current controller is shown in Fig. 2.27. The differential algebraic equations of the current controller are written as

Fig. 2.26 Block diagram of the voltage controller. © [2016] IEEE. Reprinted, with permission, from IEEE Transactions on Power Systems [33]

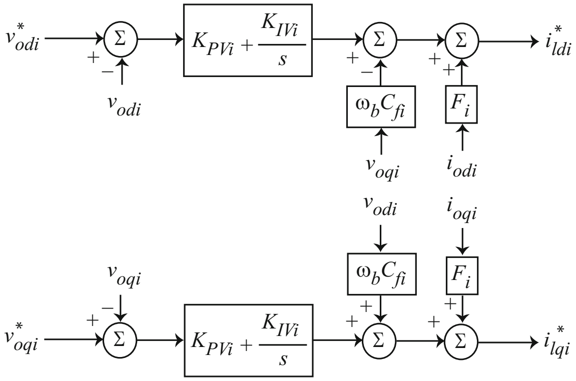

Fig. 2.27 Block diagram of the current controller. © [2016] IEEE. Reprinted, with permission, from IEEE Transactions on Power Systems [33]

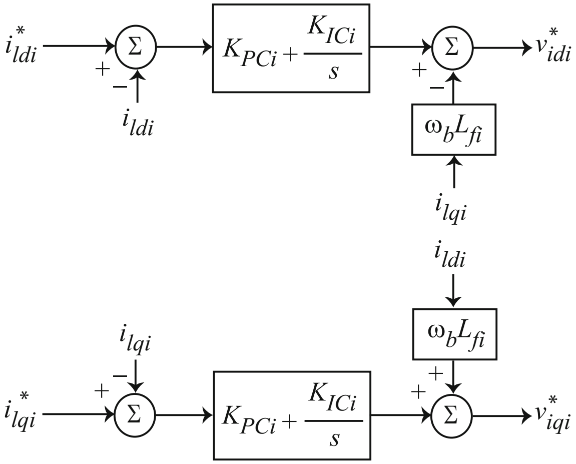

$$\dot{\gamma}_{\mathrm{di}} = i^*_{\mathrm{ldi}} - i_{\mathrm{ldi}}, \tag{2.64}$$

$$\dot{\gamma}_{\mathrm{qi}} = i^*_{\mathrm{lqi}} - i_{\mathrm{lqi}}, \tag{2.65}$$

$$v^*_{\mathrm{idi}} = -\omega_b L_{\mathrm{fi}} i_{\mathrm{lqi}} + K_{\mathrm{PCi}}(i^*_{\mathrm{ldi}} - i_{\mathrm{ldi}}) + K_{\mathrm{ICi}}\gamma_{\mathrm{di}}, \tag{2.66}$$

$$v^*_{\mathrm{iqi}} = \omega_b L_{\mathrm{fi}} i_{\mathrm{ldi}} + K_{\mathrm{PCi}}(i^*_{\mathrm{lqi}} - i_{\mathrm{lqi}}) + K_{\mathrm{ICi}}\gamma_{\mathrm{qi}}, \tag{2.67}$$

where γ_{di} and γ_{qi} are the auxiliary state variables defined for the PI controllers in Fig. 2.27. i_{ldi} and i_{lqi} are the direct and quadrature components of i_{li} in Fig. 2.24. Other parameters are shown in Figs. 2.24 and 2.27.

The differential equations for the output LC filter and output connector are as follows:

$$\dot{i}_{\mathrm{ldi}} = -\frac{R_{\mathrm{fi}}}{L_{\mathrm{fi}}} i_{\mathrm{ldi}} + \omega_i i_{\mathrm{lqi}} + \frac{1}{L_{\mathrm{fi}}} v_{\mathrm{idi}} - \frac{1}{L_{\mathrm{fi}}} v_{\mathrm{odi}}, \tag{2.68}$$

$$\dot{i}_{\mathrm{lqi}} = -\frac{R_{\mathrm{fi}}}{L_{\mathrm{fi}}} i_{\mathrm{lqi}} - \omega_i i_{\mathrm{ldi}} + \frac{1}{L_{\mathrm{fi}}} v_{\mathrm{iqi}} - \frac{1}{L_{\mathrm{fi}}} v_{\mathrm{oqi}}, \tag{2.69}$$

$$\dot{v}_{\mathrm{odi}} = \omega_i v_{\mathrm{oqi}} + \frac{1}{C_{\mathrm{fi}}} i_{\mathrm{ldi}} - \frac{1}{C_{\mathrm{fi}}} i_{\mathrm{odi}}, \tag{2.70}$$

$$\dot{v}_{\mathrm{oqi}} = -\omega_i v_{\mathrm{odi}} + \frac{1}{C_{\mathrm{fi}}} i_{\mathrm{lqi}} - \frac{1}{C_{\mathrm{fi}}} i_{\mathrm{oqi}}, \tag{2.71}$$

$$\dot{i}_{\mathrm{odi}} = -\frac{R_{\mathrm{ci}}}{L_{\mathrm{ci}}} i_{\mathrm{odi}} + \omega_i i_{\mathrm{oqi}} + \frac{1}{L_{\mathrm{ci}}} v_{\mathrm{odi}} - \frac{1}{L_{\mathrm{ci}}} v_{\mathrm{bdi}}, \tag{2.72}$$

$$\dot{i}_{\mathrm{oqi}} = -\frac{R_{\mathrm{ci}}}{L_{\mathrm{ci}}} i_{\mathrm{oqi}} - \omega_i i_{\mathrm{odi}} + \frac{1}{L_{\mathrm{ci}}} v_{\mathrm{oqi}} - \frac{1}{L_{\mathrm{ci}}} v_{\mathrm{bqi}}. \tag{2.73}$$

Equations (2.56)–(2.73) form the large-signal dynamical model of the ith DG. The large-signal dynamical model can be written in a compact form as

$$\begin{cases} \dot{x}_i = \mathbf{f}_i(x_i) + \mathbf{k}_i(x_i)\mathbf{D}_i + \mathbf{g}_i(x_i)u_i, \\ y_i = h_i(x_i), \end{cases} \tag{2.74}$$

where the state vector is

$$x_i = [\,\delta_i \quad P_i \quad Q_i \quad \phi_{\mathrm{di}} \quad \phi_{\mathrm{qi}} \quad \gamma_{\mathrm{di}} \quad \gamma_{\mathrm{qi}} \quad i_{\mathrm{ldi}} \quad i_{\mathrm{lqi}} \quad v_{\mathrm{odi}} \quad v_{\mathrm{oqi}} \quad i_{\mathrm{odi}} \quad i_{\mathrm{oqi}}\,]^T. \tag{2.75}$$

The term $\mathbf{D}_i = [\omega_{\mathrm{com}}\ v_{\mathrm{bdi}}\ v_{\mathrm{bqi}}]^T$ is considered as a known disturbance. The detailed expressions for $\mathbf{f}_i(x_i)$, $\mathbf{g}_i(x_i)$, and $\mathbf{k}_i(x_i)$ can be extracted from (2.56) to (2.73).

2.2.2 *Current-Controlled Voltage Source Inverters*

The block diagram of a current-controlled voltage source inverter (CCVSI)-based DG is shown in Fig. 2.28. It contains an inverter bridge, connected to a primary DC power source. The current controller adjusts the direct and quadrature terms of output current i_{oi}. As shown in Fig. 2.29, a control block is used to calculate the angle of the ith CCVSI reference frame with respect to the common reference frame α_i such that the quadrature term of output voltage v_{oqi} becomes zero. This control block is named as α_i calculator.

The block diagram of the current controller is shown in Fig. 2.30. The differential algebraic equations of the current controller are written as

$$\dot{\gamma}_{\mathrm{di}} = i_{\mathrm{drefi}} - i_{\mathrm{odi}}, \tag{2.76}$$

$$\dot{\gamma}_{\mathrm{qi}} = i_{\mathrm{qrefi}} - i_{\mathrm{oqi}}, \tag{2.77}$$

$$v_{\mathrm{idi}}^* = v_{\mathrm{odi}} - \omega_b L_{\mathrm{fi}} i_{\mathrm{oqi}} + K_{\mathrm{PCi}}(i_{\mathrm{drefi}} - i_{\mathrm{odi}}) + K_{\mathrm{ICi}}\gamma_{\mathrm{di}}, \tag{2.78}$$

$$v_{\mathrm{iqi}}^* = v_{\mathrm{oqi}} + \omega_b L_{\mathrm{fi}} i_{\mathrm{odi}} + K_{\mathrm{PCi}}(i_{\mathrm{qrefi}} - i_{\mathrm{oqi}}) + K_{\mathrm{ICi}}\gamma_{\mathrm{qi}}, \tag{2.79}$$

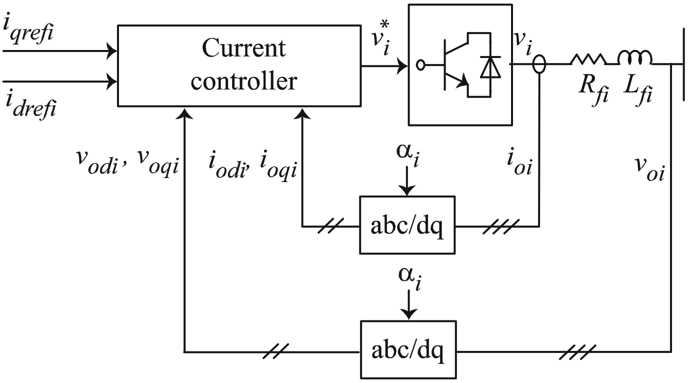

Fig. 2.28 Block diagram of a CCVSI. © [2016] IEEE. Reprinted, with permission, from IEEE Transactions on Industrial Informatics [34]

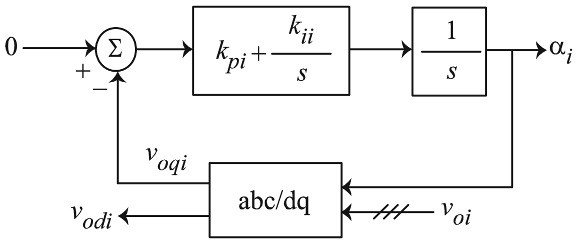

Fig. 2.29 Block diagram of α_i calculator. © [2016] IEEE. Reprinted, with permission, from IEEE Transactions on Industrial Informatics [34]

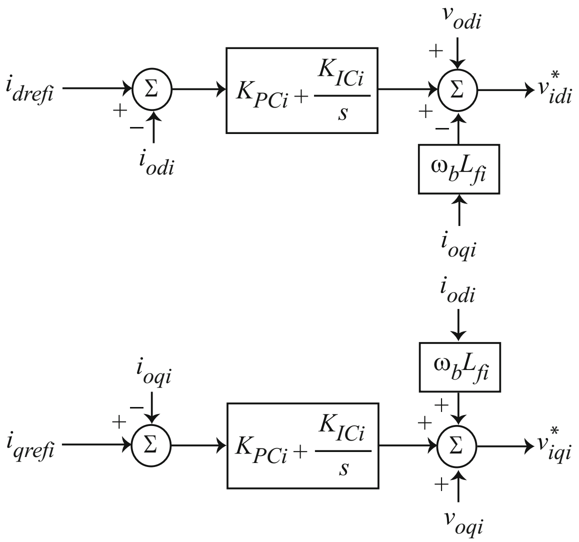

Fig. 2.30 Block diagram of the current controller for a CCVSI. © [2016] IEEE. Reprinted, with permission, from IEEE Transactions on Industrial Informatics [34]

where γ_{di} and γ_{qi} are the auxiliary state variables defined for the PI controllers in Fig. 4.4. i_{odi} and i_{oqi} are the direct and quadrature components of output current i_{oi} in Fig. 4.2. Other parameters are shown in Figs. 4.2 and 4.4. Assuming that the inverter bridge produces the demanded voltage, i.e., $v^*_{\mathrm{idi}} = v_{\mathrm{idi}}$ and $v^*_{\mathrm{iqi}} = v_{\mathrm{iqi}}$, the dynamics of output RL filter can be written as

$$\dot{i}_{\mathrm{odi}} = -\frac{R_{\mathrm{fi}}}{L_{\mathrm{fi}}} i_{\mathrm{odi}} + \omega_{\mathrm{com}} i_{\mathrm{oqi}} + \frac{1}{L_{\mathrm{fi}}} v_{\mathrm{idi}} - \frac{1}{L_{\mathrm{fi}}} v_{\mathrm{odi}}, \tag{2.80}$$

$$\dot{i}_{\mathrm{oqi}} = -\frac{R_{\mathrm{fi}}}{L_{\mathrm{fi}}} i_{\mathrm{oqi}} - \omega_{\mathrm{com}} i_{\mathrm{odi}} + \frac{1}{L_{\mathrm{fi}}} v_{\mathrm{iqi}} - \frac{1}{L_{\mathrm{fi}}} v_{\mathrm{oqi}}. \tag{2.81}$$

Equations (2.76)–(2.81) form the large-signal dynamical model of the ith CCVSI. The large-signal dynamical model can be written in a compact form as

$$\begin{cases} \dot{x}_{\mathrm{CCi}} = \mathbf{f}_{\mathrm{CCi}}(x_{\mathrm{CCi}}) + \mathbf{k}_{\mathrm{CCi}}(x_{\mathrm{CCi}})\mathbf{D}_{\mathrm{CCi}} + \mathbf{g}_{\mathrm{CCi}}(x_{\mathrm{CCi}})u_{\mathrm{CCi}} \\ y_{\mathrm{CCi}} = h_{\mathrm{CCi}}(x_{\mathrm{CCi}}) + d_{\mathrm{CCi}}u_{\mathrm{CCi}} \end{cases}, \tag{2.82}$$

where the state vector is

$$x_{\mathrm{CCi}} = \begin{bmatrix} \gamma_{\mathrm{di}} & \gamma_{\mathrm{qi}} & i_{\mathrm{odi}} & i_{\mathrm{oqi}} \end{bmatrix}^T. \tag{2.83}$$

The term $\mathbf{D}_{CCi} = [\omega_{\mathrm{com}}\ v_{\mathrm{odi}}]^T$ is considered as a known disturbance. The detailed expressions for $\mathbf{f}_{\mathrm{CCi}}(x_{\mathrm{CCi}})$, $\mathbf{g}_{\mathrm{CCi}}(x_{\mathrm{CCi}})$, and $\mathbf{k}_{\mathrm{CCi}}(x_{\mathrm{CCi}})$ can be extracted from (2.76) to (2.81).

2.3 Control of DC Microgrids

Although inverter-based AC microgrids have been prevalent, DC microgrids are currently emerging at distribution levels. The DC nature of emerging renewable energy sources (e.g., solar) or storage units (e.g., batteries and ultracapacitors) efficiently lends itself to a DC microgrid paradigm that avoids redundant conversion stages [30]. Many of the new loads are electronic DC loads (e.g., in data centers). Even some traditional AC loads, e.g., induction machines, can appear as DC loads when controlled by inverter-fed drive systems.

DC microgrids are also shown to have about two orders-of-magnitude more availability compared to their AC counterparts, thus making them ideal candidates for mission-critical applications [22, 31]. Moreover, DC microgrids can overcome some disadvantages of AC systems, e.g., transformer inrush current, frequency synchronization, reactive power flow, phase unbalance, and power quality issues [32].

2.3.1 Control Objectives

A DC microgrid is an interconnection of DC sources and DC load through a transmission/distribution network. Given the intermittent nature of electric loads, sources must be dynamically controlled to provide load power demand at any moment, while preserving a desired voltage at consumer terminals. Sources may reflect a variety of rated powers. It is desired to share the total load demand among these sources in proportion to their rated power; such load sharing approach is widely known as *proportional load sharing*. This approach prevents overstressing of sources and helps to span lifetime of the power-generating entities in the microgrid. While the source voltages are the sole variables controlling power flow, they must be tightly managed to also ensure a desirable voltage regulation.

2.3.2 Standard Control Technique

A hierarchical structure, illustrated in Fig. 2.31, is widely used to control DC sources. This structure includes primary, secondary, and tertiary levels, where the primary has the highest and the tertiary has the lowest [7].

A. *Primary Control*

This controller uses droop mechanism to handle proportional load sharing. Figure 2.32 explains the functionality of the primary controller for two sources with identical rated powers. Therein, a virtual resistance, R_D, is introduced to the output of each source. While the load sharing benefits from this virtual resistance, it is not a physical impedance and, thus, does not cause any power loss. In this stage, the voltage controllers inside each source follow the voltage reference generated by the droop mechanism, i.e.,

$$v_o^* = v_{\text{ref}} - R_D . i_o \tag{2.84}$$

where v_o^* is the reference voltage for the inner-loop voltage controller, R_D is the droop coefficient, v_{ref} is the rated voltage of the microgrid, and i_o is the output

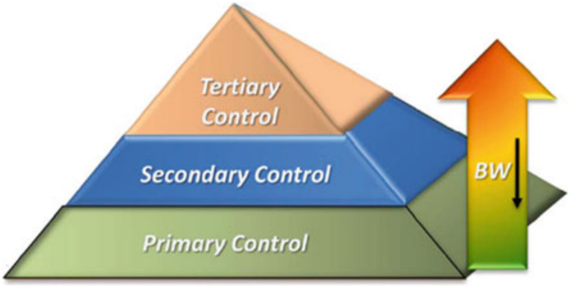

Fig. 2.31 Hierarchical control structure for DC systems. © [2017] IEEE. Reprinted, with permission, from IEEE Transactions on Industrial Electronics [7]

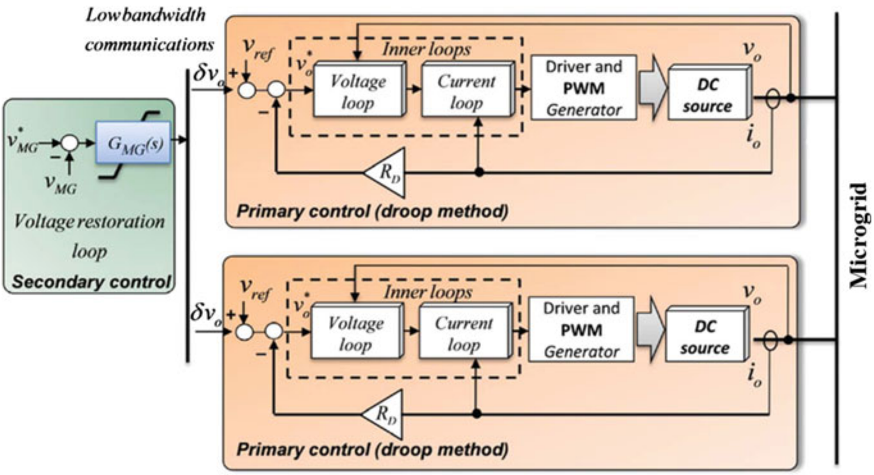

Fig. 2.32 Primary and secondary control algorithms. © [2017] IEEE. Reprinted, with permission, from IEEE Transactions on Industrial Electronics [7]

current of the source. In steady state, given low distribution line resistances, all terminal voltages converge to the same value. Given identical rated voltages used at all sources, one can conclude that the droop terms, $R_D.i_o$, will share identical values as well. This, equivalently, implies that the total load is shared among sources in inverse proportion to their droop coefficients. By choosing the droop coefficients in inverse proportion to the source power ratings, the droop mechanism will successfully manage proportional load sharing.

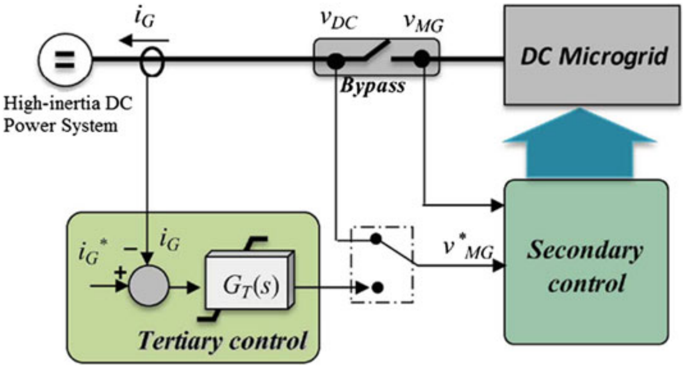

Fig. 2.33 Tertiary control for grid-connected operation. © [2017] IEEE. Reprinted, with permission, from IEEE Transactions on Industrial Electronics [7]

B. *Secondary Control*

Although the droop controller satisfies a desired load sharing, the droop term, $R_D.i_o$, leaves a voltage deviation from the rated voltage of, v_{ref}, all across the network. The secondary controller serves as voltage restoration here. As shown in Fig. 2.32, it senses the microgrid voltage and compares it with the desired voltage of v^*_{MG} through a controller, $G_{\mathrm{MG}}(s)$; the controller is usually a proportional–integral (PI) module. The controller generates a voltage correction term, δv_o, which is relayed to all sources. The sources then use $v_{\mathrm{ref}} + \delta v_o$ as the reference in the droop mechanism instead of the v_{ref} itself. The term δv_o boosts all voltages across the system until, within this closed-loop feedback control mechanism, all voltages be restored on the reference value of v^*_{MG}. It should be noted that v^*_{MG} and v_{ref} may not be the same values; however, they are usually equal.

C. *Tertiary Control*

Power generation in the microgrid may exceed the local power demand, particularly when the maximum power is to be absorbed from renewable energy sources. In such a case, the excess power will be transmitted directly to a high-inertia DC system or to the main AC grid through an inverter. On the other side, when locally generated power is short of the load demand, a high-inertia DC system or AC grid will provide power to fill up the need. Such bidirectional power exchange with a high-inertia system requires a separate controller called tertiary control. As demonstrated in Fig. 2.33, tertiary controller compares the power flow between the two power grids with a reference value of i^*_G and accordingly updates the reference voltage of the microgrid, v^*_{MG}. Generally, as v^*_{MG} increases, the DC microgrid sends out more power and vice versa.

References

1. Bidram A, Davoudi A (2012) Hierarchical structure of microgrids control system. IEEE Trans Smart Grid 3:1963–1976
2. Guerrero JM, Matas J, Vicuna LGD, Castilla M, Miret J (2007) Decentralized control for parallel operation of distributed generation inverters using resistive output impedance. IEEE Trans Ind Electron 54:994–1004
3. Guerrero JM, Vicuna LGD, Matas J, Castilla M, Miret J (2005) Output impedance design of parallel-connected UPS inverters with wireless load-sharing control. IEEE Trans Ind Electron 52:1126–1135
4. Katiraei F, Iravani MR, Lehn PW (2005) Microgrid autonomous operation during and subsequent to islanding process. IEEE Trans Power Del 20:248–257
5. Katiraei F, Iravani MR (2005) Power management strategies for a microgrid with multiple distributed generation units. IEEE Trans Power Syst 21:1821–1831
6. Lopes JAP, Moreira CL, Madureira AG (2006) Defining control strategies for microgrids islanded operation. IEEE Trans Power Syst 21:916–924
7. Guerrero JM, Vásquez JC, Matas J, Castilla M, Vicuña LGD, Castilla M (2011) Hierarchical control of droop-controlled AC and DC microgrids-A general approach toward standardization. IEEE Trans Ind Electron 58:158–172

8. Prodanović M, Green TC (2006) High-quality power generation through distributed control of a power park microgrid. IEEE Trans Ind Electron 53:1471–1482
9. Pogaku N, Prodanovic M, Green TC (2007) Modeling, analysis and testing of autonomous operation of an inverter-based microgrid. IEEE Trans Power Electron 22:613–625
10. Diaz G, Gonzalez-Moran C, Gomez-Aleixandre J, Diez A (2010) Scheduling of droop coefficients for frequency and voltage regulation in isolated microgrids. IEEE Trans Power Syst 25:489–496
11. Rokrok E, Golshan MEH (2010) Adaptive voltage droop method for voltage source inverters in an islanded multibus microgrid. IET Gen Trans Dist 4(5):562–578
12. Sao CK, Lehn W (2005) Autonomous load sharing of voltage source inverters. IEEE Trans Power Del 20:1009–1016
13. Sao CK, Lehn W (2008) Control and power management of converter fed microgrids. IEEE Trans Power Syst 23:1088–1098
14. Borup U, Blaabjerg F, Enjeti PN (2001) Sharing of nonlinear load in parallel-connected three-phase converters. IEEE Trans Ind Appl 37:1817–1823
15. Zhong QC (2013) Harmonic droop controller to reduce the voltage harmonics of inverters. IEEE Trans Ind Electron 60:936–945
16. Li Y, Li YW (2009) Virtual frequency-voltage frame control of inverter based low voltage microgrid. In: Proceedings of IEEE Electrical Power and Energy Conference, 2009, pp 1–6
17. Li Y, Li YW (2011) Power management of inverter interfaced autonomous microgrid based on virtual frequency-voltage frame. IEEE Trans Smart Grid 2:30–40
18. Li Y, Vilathgamuwa DM, Loh PC (2004) Design, analysis, and real-time testing of a controller for multibus microgrid system. IEEE Trans Power Electron 19:1195–1204
19. Guerrero JM, Matas J, Vicuna LGD, Castilla M, Miret J (2006) Wireless-control strategy for parallel operation of distributed generation inverters. IEEE Trans Ind Electron 53:1461–1470
20. Yao W, Chen M, Matas J, Guerrero JM, Qian Z (2011) Design and analysis of the droop control method for parallel inverters considering the impact of the complex impedance on the power sharing. IEEE Trans Ind Electron 58:576–588
21. Mehrizi-Sani A, Iravani R (2010) Potential-function based control of a microgrid in islanded and grid-connected models. IEEE Trans Power Syst 25:1883–1891
22. Kwasinski A (2011) Quantitative evaluation of dc Microgrids availability: effects of system architecture and converter topology design choices. IEEE Trans Power Electron 26(3):835–851
23. Tuladhar A, Jin H, Unger T, Mauch K (2000) Control of parallel inverters in distributed AC power systems with consideration of line impedance effect. IEEE Trans Ind Appl 36:131–138
24. Ilic MD, Liu SX (1996) Hierarchical power systems control: Its value in a changing industry. Springer, London
25. Savaghebi M, Jalilian A, Vasquez J, Guerrero J (2012) Secondary control scheme for voltage unbalance compensation in an islanded droop- controlled microgrid. IEEE Trans. Smart Grid 3:797–807
26. Barklund E, Pogaku N, Prodanovic´ M, Hernandez-Aramburo C, Green TC (2008) Energy management in autonomous microgrid using stability-constrained droop control of inverters. IEEE Trans Power Electron 23:2346–2352
27. Pantoja A, Quijano N (2011) A population dynamics approach for the dispatch of distributed generators. IEEE Trans Ind Electron 58:4559–4567
28. Tanabe T et al (2007) Optimized operation and stabilization of microgrids with multiple energy resources. In: Proceedings of 7th International Conference on Power Electronics, 2007, pp 74–78
29. Vanthournout K, Brabandere KD, Haesen E, Driesen J, Deconinck G, Belmans R (2005) Agora: Distributed tertiary control of distributed resources. In: Proceedings of 15th Power Systems Computation Conference, 2005, pp 1–7
30. Chen YK, Wu YC, Song CC, Chen YS (2013) Design and implementation of energy management system with fuzzy control for dc Microgrid systems. IEEE Trans Power Electron 28(4):1563–1570

31. Ikebe H (2003) Power systems for telecommunications in the IT age. In: Proceedings of IEEE INTELEC, 2003, pp 1–8
32. Balog RS, Weaver W, Krein PT (2012) The load as an energy asset in a distributed dc Smartgrid architecture. IEEE Trans Smart Grid 3:253–260
33. Bidram A, Davoudi A, Lewis FL, Guerrero JM (2013) Distributed cooperative secondary control of microgrids using feedback linearization. IEEE Trans Power Systems 28 (3):3462–3470
34. Bidram A, Davoudi A, Lewis F (2014) A multi-objective distributed control framework for islanded microgrids. IEEE Trans Ind Inform 10:1785–1798

Chapter 3
Introduction to Multi-agent Cooperative Control

This book applies techniques from distributed cooperative control of multi-agent dynamical systems to synchronization, power sharing, and load balancing problems arising in electric power microgrids. This chapter presents the background and fundamental ideas needed for the book in cooperative control of multi-agent systems. For more information see [1].

Distributed networks of coupled dynamical systems have received much attention over the years because they occur in many different fields including biological and social systems, physics and chemistry, and computer science. Various terms are used in literature for phenomena related to collective behavior on networks of systems, such as flocking, consensus, synchronization, formation, and rendezvous.

In the past few decades, an increasing number of industrial, commercial, and consumer applications have called for the coordination of multiple interconnected dynamical agents. Research on synchronized behaviors of networked cooperative systems, or multi-agent systems, and on distributed decision algorithms has received extensive attention due to their widespread applications in spacecraft, unmanned air vehicles (UAVs) [2], multi-vehicle systems [3], mobile robots, multipoint surveillance [4], sensor networks [5], networked autonomous teams, and so on. See [4, 6] for surveys of engineering applications of cooperative multi-agent control systems.

This chapter outlines the fundamental ideas used in the rest of the book to develop analysis and design methods for cooperative control of multi-agent dynamical systems on graphs. These ideas are detailed in [1]. The chapter starts by presenting an overview of synchronization behavior in nature and social systems. It is seen that distributed decisions made by each agent in a group based only on the information locally available to it from its neighbors can result in collective synchronized motion of an overall group. Mechanisms are given by which decisions can be made locally by each agent and informed leaders can guide collective behaviors by interacting directly with only a few agents. These ideas are extended to achieve synchronization mechanisms in physical oscillators and rotating synchronous generators in interconnected electric power systems. The idea of a

A. Bidram et al., *Cooperative Synchronization in Distributed Microgrid Control*,
Advances in Industrial Control, DOI 10.1007/978-3-319-50808-5_3

communication graph that models the information flows in a multi-agent group is introduced. The dependence of collective behaviors of a group on the type of information flow allowed between its agents is emphasized. Simple dynamical systems on communication graphs are presented, and simple distributed control protocols given to direct their collective behavior. Such protocols are used in the rest of the book for synchronization, voltage sharing, and load balancing in electric power microgrids.

3.1 Synchronization in Nature, Social Systems, and Coupled Oscillators

This section presents an overview of synchronization behavior in nature and social systems. It is seen that distributed decisions made by each agent in a group based on the information locally available to it by observing only its nearest neighbors can result in collective synchronized motion of an overall group. Distributed control mechanisms are given by which decisions can be made locally by each agent and informed leaders can guide collective behaviors by interacting directly with only a few agents. These mechanisms occurring in nature can be tailored to provide synchronization and collective performance objectives in engineered systems and electric power networks. More information is given in [1].

The ability to coordinate multiple intercommunicating agents is important in many real-world decision tasks where it is necessary for agents to exchange information with each other. Distributed local decision and control algorithms are desirable and appear in many situations due to their computational simplicity, flexibility, and robustness to the loss of single agents. Applications of synchronization and distributed coordination of multi-agent systems have been observed in the evolution of distributed cooperation in social groups, synchronization in coupled dynamical oscillators, biological synchronization, and social networks. It has been observed that distributed decision using local neighbor responses can accurately model the panic behavior of crowds during emergency building evacuation. Synchronization and local distributed control mechanisms have been observed in the spread of infectious diseases in structured populations and in metabolic stability in random genetic nets. More details are given in [1].

3.1.1 Synchronization in Animal Motion in Collective Groups

The collective synchronized motions of animal social groups are among the most beautiful sights in nature [7]. Collective motions allow the group to achieve what the individual cannot. Benefits of aggregate motion include defense from predators, social and mating advantages, and group foraging for food [8]. Each individual has its own inclinations and motions, yet the aggregate motion makes the group appear to be a single entity with its own laws of motion, psychology, and responses to external events. Flocks of birds, schools of fish, and herds of animals are aggregate entities that take on an existence of their own due to the collective motion instincts of their individual members [9]. In collective motion situations, the important entity becomes the group, not the individual. Such synchronized and responsive motion makes one think of choreographed motions in a dance, yet they are a product not of planned scripts, but of simple instantaneous decisions and responses by individual members [7, 10].

3.1.1.1 Distributed Local Neighborhood Protocols for Synchronization

To reproduce the collective motion of an animal group in computer animation has been a challenge. It would be impossible to script the motion of each individual using planned motions or trajectories. Analysis of groups based on social behaviors is complex, yet the individuals in collectives appear to follow simple rules that make their motion efficient, responsive, and practically instantaneous. The cumulative motion of animal groups can be programmed in computer animation by endowing each individual with the same few rules that allow it to respond to the situations it encounters. The responses of the individuals accumulate to produce the combined motion of the group.

In large social groups, each individual is aware only of the motions of its immediate neighbors. The field of perceptual awareness of the individual changes for different types of animal groups and in different motion scenarios. The collective synchronized motion of large groups can be captured by using a few simple rules governing the behavior of the individuals based on the observed behaviors of their neighbors. Individual motions in a group are the result of the balance of two opposing behaviors: a desire to stay close to the group, and a desire to avoid collisions with other individuals. Reynolds [9] has captured the tendencies governing the motions of individuals through his three rules. These rules depend on the motions of the neighbors of each individual in the group.

Reynolds' Rules [9]

1. Collision avoidance: avoid collisions with neighbors
2. Velocity matching: match speed and direction of motion with neighbors
3. Flock centering: stay close to neighbors.

There are many mechanisms for implementing Reynolds' rules in dynamical systems control of importance is the definition of an individual's "neighborhood".

Consider motion in R^2 and define $(p_i(t), q_i(t))$ as the position of node i in the (x, y) plane. Define the state of agent i as $x_i = [p_i \;\; q_i]^{\mathrm{T}} \in R^2$.

Define the distance between nodes i and j as

$$r_{ij} = |x_j - x_i| = \sqrt{(p_j - p_i)^2 + (q_j - q_i)^2} \tag{3.1}$$

Agents seek to attract to their neighbors according to the third rule. To see how this can be implemented mathematically define an interaction radius ρ and the interaction neighborhood by $N_i = \{j : r_{ij} \le \rho\}$. If agent i is within a distance of ρ from agent j, it seeks to approach agent j to stay close to its neighbors. It is noted that radius ρ is different for different animal groups and different vehicles. Moreover, for some groups, such as flocks of birds in migration, the collision and interaction neighborhoods are not circular.

The dynamics used to simulate the individual group members can be very simple, yet realistic results are obtained. Consider agent motion in 2-D described by the dynamics

$$\dot{x}_i = u_i \tag{3.2}$$

with states $x_i = [p_i \;\; q_i]^{\mathrm{T}} \in R^2$. This is a simple point-mass dynamics with velocity control inputs $u_i = [u_{pi} \;\; u_{qi}]^{\mathrm{T}} \in R^2$.

A suitable law for flock centering is given by

$$u_i = \sum_{j \in N_i} a_{ij}(x_j - x_i) \tag{3.3}$$

which causes agent i to turn toward other agents inside the interaction neighborhood N_i. The flock centering gain $a_{ij} \ge 0$ is nonzero only if agent j is in the interaction neighborhood of agent i. If a_{ij} is large, then agent i seeks more vigorously to approach agent j. The flock centering protocol can be written in terms of the components of velocity as

$$\dot{p}_i = u_{pi} = \sum_{j \in N_i / N_i^c} a_{ij}(p_j - p_i) \tag{3.4}$$

$$\dot{q}_i = u_{qi} = \sum_{j \in N_i / N_i^c} a_{ij}(q_j - q_i) \tag{3.5}$$

The control protocols (3.3)–(3.5) are known as *cooperative local voting protocols* because each agent seeks to make the difference between his state and those of his neighbors equal to zero. That is, each agent seeks to achieve consensus with its neighbors. These protocols are *distributed* in the sense that they depend only on the local neighbor information as allowed by the communication graph topology.

An alternative protocols for flock centering is given by

$$u = \sum_{j \in N_i} a_{ij} \frac{(x_j - x_i)}{r_{ij}} = \sum_{j \in N_i} a_{ij} \frac{(x_j - x_i)}{|x_j - x_i|} \tag{3.6}$$

which is normalized by dividing by the distance between agents. Note that the sum is over components of a unit vector. Therefore, this law prescribes a desired direction of motion and results in motion of uniform velocity. By contrast, the law (3.3) gives velocities that are smaller if one is closer to one's neighbors.

Alternative methods to local cooperative protocols for implementing Reynolds' rules include potential field approaches [11, 12]. Potential field methods include approaches for obstacle avoidance and goal seeking and are intimately related to the topics in this section.

3.1.2 Leadership in Animal Groups on the Move

We have seen that information can be transferred only locally between individual neighboring members of animal groups, yet this results in collective synchronized motions of the whole group. Local motion control protocols are based on a few simple rules that are followed by all individuals. However, in many situations, the whole group must move toward some goal, such as along migratory routes or toward food sources. In these cases, only a few informed individuals may have pertinent information about the required directions of motion.

Some species have evolved specialized mechanisms for conveying information about location and direction of goals. One example is the waggle dance of the honeybee that recruits hive members to visit food sources. Mechanisms of information transfer in groups involve questions such as how information about required motion directions, originally held by only a few informed individuals, can propagate through an entire group by simple mechanisms that are the same for every individual [8, 13]. It is shown by [8] that only a small percentage of the individuals in a group need be directly aware of the location of the goal. If the group is connected in the sense that information can eventually propagate through the graph from one individual to any other, then a small percentage of informed individuals can influence the motions of the entire swarm to align to the goal state location.

These ideas are formalized mathematically in Sect. 3.3.2 about multi-agent synchronization to the trajectory of a leader node who can be directly observed by only a few agents.

3.1.3 Synchronization in Coupled Oscillators and Electric Power Systems

Coupled dynamical oscillators occur in many fields of research, including chemistry, physics, electrical engineering, and biology [7, 10, 14]. In 1995, Vicsek et al. [15] reported interesting results of collective behaviors of self-driven particles in phase transition. They showed that by using nearest neighbor interaction rules, all agents eventually move in the same direction.

Kuramoto [14] analyzed local coupling in populations of chemical oscillators to study waves and turbulence. He showed that there is a critical information coupling coefficient above which coupled oscillators synchronize. Interconnected Kuramoto oscillators have the dynamics

$$\dot{\theta}_i = \omega_i + \frac{K}{N}\sum_j \sin(\theta_j - \theta_i) \tag{3.7}$$

with oscillation frequency ω_i and coupling gain K [10]. The oscillators are said to synchronize if $\dot{\theta}_i(t) - \dot{\theta}_j(t) \to 0$ as $t \to \infty\ \forall i,j$. It is seen that these systems are interconnected by terms not in $(\theta_j - \theta_i)$ as in (3.3), but by terms like $\sin(\theta_j - \theta_i)$.

Kuramoto took the oscillation frequencies as distributed about a mean value according to a probability density function. He showed that there is a coupling gain K below which the oscillators remain incoherent, i.e., do not synchronize. Above this gain, the incoherent state becomes unstable, and the oscillators split into two groups those with oscillation frequencies close to the mean synchronize to a mean frequency $\bar{\theta}$, while the others drift relative to this group.

In [16], synchronization is studied using the Lyapunov function $V = \frac{1}{2}\dot{\theta}^{\mathrm{T}}\dot{\theta}$, with $\theta = [\theta_1 \ldots \theta_N]^{\mathrm{T}}$. It is shown that $\dot{V} = -\frac{K}{N}\sum_{i,j}\cos(\theta_i - \theta_j)(\dot{\theta}_i - \dot{\theta}_j)^2$. It is shown that above some value for the coupling gain, and if the initial phase differences are in a certain compact set, the oscillators converge to the mean frequency $\bar{\omega} = \frac{1}{N}\sum\limits_i \omega_i$.

The ideas of synchronization in Kuramoto oscillators can be applied to synchronization in electric power systems. The basic swing equations for rotating synchronous electric generators are given for the ith generator as (assuming the lossless case) by

$$\begin{aligned} \dot{\omega}_i &= -D_i\omega_i + \frac{\omega_{i0}}{M_i}P_{mi} - E_i^2 G_{ii} - P_{ei} \\ &= -D_i\omega_i + \frac{\omega_{i0}}{M_i}P_{mi} - E_i^2 G_{ii} - E_i \sum_{j\in N_i} E_j Y_{ij}\sin(\delta_i - \delta_j) \end{aligned} \tag{3.8}$$

$$\dot{E}_i = -a_i E_i + u_i + b_i \sum_{j \in N_i} E_j \cos(\delta_i - \delta_j) \tag{3.9}$$

with frequency $\omega_i = \dot{\delta}_i$, mechanical power P_{mi}, electrical power P_{ei}, and admittance Y_{ij} capturing the networked interconnection structure between generators. A frequency equilibrium is characterized by frequency synchronization $\omega_i = \omega_j,\ \forall i,j$ and balanced power flow $Q_i(\delta_i) = P_{mi} - P_{ei} - E_i^2 G_{ii} = 0,\ \ \forall i$. In [17] it was shown that these interconnected systems are generalized Kuramoto oscillators, and conditions for synchronization to a common frequency are given.

Ortega [18] used a nonlinear passivity-based approach for general lossy systems. Partial differential equations were solved for the controls, which have the form

$$u_i = k_1 E_i - k_2 \omega_i - b_i \sum_{j \in N_i} E_j \cos(\delta_i - \delta_j) + \sum_{j \in N_i} k_{ij} \omega_j \tag{3.10}$$

where k_{ij} are nonlinear functions. It is seen that these controls are given not by terms not in $(\delta_j - \delta_i)$ as in (3.3), but by terms like $\cos(\delta_j - \delta_i)$.

3.2 Communication Graphs for Interconnected Systems

Local synchronization protocols such as those just discussed capture very well the dynamics of intercoupled biological and animal groups, dynamical oscillators in chemistry and physics, and interconnected electric power systems. These protocols depend on the awareness of each individual of his neighbors. We have seen that the information flow between members of a social group is instrumental in determining the motion of the overall group. In this book, we are concerned with the behaviors and interactions of dynamical systems that are interconnected by the links of a communication network. The fundamental control issues concern how the graph topology interacts with the local feedback control protocols of the agents to produce overall behaviors of the interconnected nodes.

The communication network interconnecting the dynamical systems can be modeled as a graph with directed edges corresponding to the allowed flow of information between the systems. See [1, 19, 20] for more information. The systems are modeled as the nodes in the graph and are sometimes called agents. We call this the study of multi-agent dynamical systems on graphs.

A *graph* is a pair $G = (V, E)$ with $V = \{v_1, \ldots, v_N\}$ a set of N nodes or vertices and E a set of edges or arcs. Elements of E are denoted as (v_i, v_j) which is termed an edge or arc from v_i to v_j, and represented as an arrow with tail at v_i and head at v_j. The edges represent the allowed flow of information in the graph. We assume the graph is simple, i.e., $(v_i, v_i) \notin E,\ \forall i$ no self-loops, and no multiple edges between the same pairs of nodes. Edge (v_i, v_j) is said to be outgoing with respect to node v_i and incoming with respect to v_j; node v_i is termed the parent and v_j the child. The in-degree of v_i is the number of edges having v_i as a head. The out-degree of a node v_i is the number of edges having v_i as a tail. The set of (in-) neighbors of a node v_i is $N_i = \{v_j : (v_j, v_i) \in E\}$, i.e., the set of nodes with edges incoming to v_i. The number of neighbors $|N_i|$ of node v_i is equal to its in-degree.

If the in-degree equals the out-degree for all nodes $v_i \in V$, the graph is said to be *balanced*. If $(v_i, v_j) \in E \Rightarrow (v_j, v_i) \in E, \ \forall i, j$, the graph is said to be *bidirectional;* otherwise, it is termed a directed graph or digraph. Associate with each edge $(v_j, v_i) \in E$, a weight $a_{ij} \geq 0$. Note the order of the indices in this definition. One has $a_{ij} > 0$ only if there is an edge from node j to node i. A graph is said to be *undirected* if $a_{ij} = a_{ji}, \ \forall i, j$, that is, if it is bidirectional and the weights of edges (v_i, v_j) and (v_j, v_i) are the same.

A directed path is a sequence of nodes $v_0, v_1, \ldots, v_r$ such that $(v_i, v_{i+1}) \in E, \ i \in \{0, 1, \ldots, r-1\}$. Node v_i is said to be connected to node v_j, if there is a directed path from v_i to v_j. The distance from v_i to v_j is the length of the shortest path from v_i to v_j. Graph G is said to be strongly connected if v_i, v_j are connected for all distinct nodes $v_i, v_j \in V$. For bidirectional and undirected graphs, if there is a directed path from v_i to v_j, then there is a directed path from v_j to v_i, and the graph is called simply "connected".

If a graph is not connected, it is disconnected. A *component* of an undirected graph is a connected subgraph that is not connected to the remainder of the graph.

Information in social networks only travels directly between immediate neighbors in a graph, as decreed by the nonzero edge weights a_{ij}. Nevertheless, if a graph is connected, then this locally transmitted information travels finally to every agent in the graph.

A (directed) tree is a connected digraph where every node except one, called the root, has in-degree equal to one. A spanning tree of a digraph is a directed tree formed by graph edges that connects all the nodes of the graph. A graph is said to have a spanning tree if a subset of the edges forms a directed tree. This is equivalent to saying that all nodes in the graph are reachable from a single (root) node by following the edge arrows. A graph may have multiple spanning trees. Define the root set or leader set of a graph as the set of nodes that are the roots of all spanning trees. If a graph is strongly connected it contains at least one spanning tree. In fact, if a graph is strongly connected, then all nodes are root nodes (Fig. 3.2).

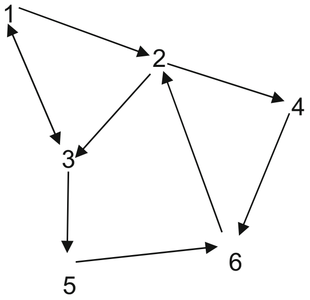

Fig. 3.1 A directed graph

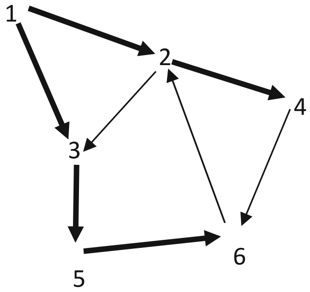

Fig. 3.2 A spanning tree for the graph in Fig. 3.1 with root node 1

3.2.1 Graph Matrices–Algebraic Graph Theory

Graph structure and properties can be studied by examining the properties of certain matrices associated with the graph. This is known as algebraic graph theory [19, 20].

Given the edge weights a_{ij}, a graph can be represented by an adjacency or connectivity matrix $A = [a_{ij}]$ with weights $a_{ij} > 0$ if $(v_j, v_i) \in E$ and $a_{ij} = 0$ otherwise. Note that $a_{ii} = 0$. Define the weighted in-degree of node v_i as the ith row sum of A

$$d_i = \sum_{j=1}^{N} a_{ij} \tag{3.11}$$

and the weighted out-degree of node v_i as the ith column sum of A

$$d_i^o = \sum_{j=1}^{N} a_{ji} \tag{3.12}$$

The adjacency matrix A of an undirected graph is symmetric, $A = A^{\mathrm{T}}$. A graph is said to be (*weight*) *balanced* if the weighted in-degree equals the weighted out-degree for all i. If all the nonzero edge weights are all equal to 1, this is the same as the definition of balanced graph. An undirected graph is weight balanced, since if $A = A^{\mathrm{T}}$ and then the ith row sum equals the ith column sum. We may be loose at times and refer to node v_i simply as node i, and refer simply to in-degree, out-degree, and the balanced property, without the qualifier “weight”, even for graphs having non-unity weights on the edges.

Graph Laplacian Matrix. Define the diagonal in-degree matrix $D = \mathrm{diag}\{d_i\}$ and the (weighted) graph Laplacian matrix $L = D - A$. Note that L has all row sums equal to zero. Many properties of a graph may be studied in terms of its graph Laplacian. In fact, we shall see that the Laplacian matrix is of extreme importance in the study of dynamical multi-agent systems on graphs. The eigenvalues of L specify many properties of the underlying graph topology.

3.3 Cooperative Control of Multi-agent Systems on Communication Graphs

The main interest of this book is cooperative control of multi-agent dynamical electric power systems interconnected by a communication graph topology. The links of the graph represent the allowed information flow between the systems. In cooperative control systems on graphs, there are intriguing interactions between the individual agent dynamics and the topology of the communication graph. The graph topology may severely limit the possible performance of any control laws used by the agents. Moreover, in cooperative control on graphs, all the control protocols must be distributed in the sense that the control law of each agent is only allowed to depend on information from its immediate neighbors in the graph topology. If enough care is not shown in the design of the local agent control laws, the individual agent dynamics may be stable, but the networked systems on the graph may exhibit undesirable behaviors.

In cooperative control, each agent is endowed with its own state variable and dynamics. A fundamental problem in multi-agent dynamical systems on graph is the design of distributed protocols that guarantee consensus or synchronization in the sense that the states of all the agents reach the same value. The states could represent vehicle headings or positions, estimates of sensor readings in a sensor network, oscillation frequencies, frequencies and voltages in an electric power network, and so on.

The principles of cooperative multi-agent systems that we have discussed in this chapter have been developed by many researchers. Distributed decision and parallel computation algorithms were studied and developed in [21]. The field of cooperative control for multi-agent systems was started in earnest with the two seminal papers in 2003 [22] and 2004 [23]. Early work was furthered in [24–27]. In the development of cooperative control theory, work was generally done initially for simple systems including first-order integrator dynamics in continuous time and discrete time. Then, results were established for second-order systems and higher-order dynamics. Applications were made to vehicle formation control and graphs with time-varying topologies and communication delays. See [28–33].

Early work focused on reaching consensus or synchronization of networks of anonymous dynamical systems, where all agents have the same role. This is known as the leaderless consensus problem or the cooperative regulator problem. Later work focused on synchronization to the dynamics of a leader or root node which generates a command target trajectory. This is the controlled consensus problem or the cooperative tracker.

3.3.1 Consensus and the Cooperative Regulator Problem

Given dynamical systems at each node i with state $x_i(t)$, we wish to find controllers that make all the states the same, specified as follows.

Definition 3.1 (*Consensus-The Cooperative Regulator Problem*) Find a distributed control protocol for each agent i that drives all states to the same constant steady-state values $x_i(t) \to x_j(t) \to \text{const}, \ \forall i, j$. This value is known as a consensus value.

The control protocols are required to be *distributed* in that the control for agent i is only allowed to depend on the state of agent i and its neighbors $j \in N_i$ in the graph topology.

Consider the case where all N nodes of the graph G have scalar first-order single-integrator dynamics

$$\dot{x}_i = u_i \tag{3.13}$$

with $x_i, u_i \in R$. This corresponds to endowing each node or agent with a memory.

Consider the local control protocols for each agent i

$$u_i = \sum_{j \in N_i} a_{ij}(x_j - x_i) \tag{3.14}$$

with a_{ij} the graph edge weights. This control is distributed in that it only depends on the immediate neighbors $j \in N_i$ of node i in the graph topology. This is known as a *local voting protocol,* since the control input of each node depends on the difference between its state and all its neighbors. Note that if these states are all the same, then $\dot{x}_i = u_i = 0$. In fact, it will be seen that, under certain graph connectivity conditions, this protocol indeed drives all states to the same consensus value.

In the control protocol (3.14), there are only appearances of the states of node i and its neighbors. There is no external reference input. Therefore, this distributed controller is known as a *cooperative regulator.*

We wish to show that protocol (3.14) solves the consensus problem and to determine the consensus value reached. Write the closed-loop dynamics as

$$\dot{x}_i = \sum_{j \in N_i} a_{ij}(x_j - x_i) \tag{3.15}$$

$$\dot{x}_i = -x_i \sum_{j \in N_i} a_{ij} + \sum_{j \in N_i} a_{ij} x_j = -d_i x_i + \begin{bmatrix} a_{i1} & \dots & a_{iN} \end{bmatrix} \begin{bmatrix} x_1 \\ \vdots \\ x_N \end{bmatrix} \tag{3.16}$$

with d_i the in-degree. Define the global state vector $x = [x_1 \ \dots \ x_N]^{\mathrm{T}} \in R^N$ and the diagonal matrix of in-degrees $D = \mathrm{diag}\{d_i\}$. Then the global dynamics are given by

$$\dot{x} = -Dx + Ax = -(D - A)x \tag{3.17}$$

$$\dot{x} = -Lx \tag{3.18}$$

With $L = D - A$ the Laplacian matrix. Note that the global control input vector $u = [u_1 \ldots u_N]^T \in R^N$ is given by

$$u = -Lx \tag{3.19}$$

It is seen that, using the local voting protocol (3.14), the closed-loop dynamics (3.18) depends on the graph Laplacian matrix L. We shall now see how the evolution of first-order integrator dynamical systems on graphs depends on the graph properties through the Laplacian matrix. The eigenvalues λ_i of L are instrumental in this analysis [1]. Order the eigenvalues of L in increasing magnitude as $\{\lambda_1, \lambda_2, \ldots, \lambda_N\}$, with N the number of nodes in the graph.

Note that the Laplacian matrix is $L = D - A$ and as such has row sum equal to zero. Therefore, $L\underline{1} = 0$, with $\underline{1} = [1 \quad 1 \quad \ldots \quad 1]^T$ the vector of ones. Therefore, the first eigenvalue of L is $\lambda_1 = 0$ with a right eigenvalue of $v_1 = \underline{1}$. It is known that the eigenvalues of L all have nonnegative real parts [1]. It may have several eigenvalues at zero, and the remainder of the eigenvalues has positive real parts. If the graph has a spanning tree, the only eigenvalue at zero is λ_1, and all other eigenvalues of L have positive real parts [1].

The dynamics given by (3.18) has a system matrix of $-L$, and hence has eigenvalues in the open left-half plane. At steady-state, according to (3.18) one has

$$0 = -Lx_{ss} \tag{3.20}$$

Therefore, the steady-state global state is in the nullspace of L. If the graph has a spanning tree, then $\lambda_1 = 0$ and all other eigenvalues of L have positive real parts. Then, (3.18) is a Type-1 system, and all states reach constant steady-state values. Since $L\underline{1} = 0$, (3.20) becomes $0 = -cL\underline{1}$, and all agents reach the same consensus value of c.

The next result formalizes the consensus properties of the distributed control protocols (3.14).

Theorem 3.1 (Cooperative Regulation for First-order Systems) *The cooperative regulator protocol* (3.14) *guarantees consensus of the single-integrator dynamics* (3.13) *if and only if the graph has a spanning tree. Then, all node states come to the same steady-state values* $x_i = x_j = c,\ \forall i,j$. *The consensus value is given by*

$$c = \sum_{i=1}^{N} p_i x_i(0) \tag{3.21}$$

where $w_1 = [p_1 \quad \ldots \quad p_N]^T$ *is the normalized left eigenvector of the Laplacian L for* $\lambda_1 = 0$. *That is* $w_1^T L = 0,\ \|w_1\| = 1$. *Finally, consensus is reached with a time constant given by*

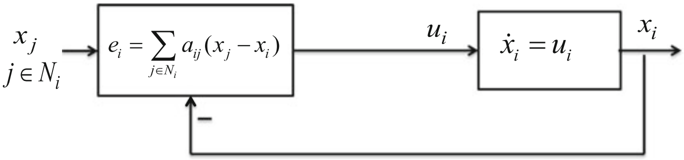

Fig. 3.3 Multi-agent cooperative regulator

$$\tau = 1/\mathrm{Re}\{\lambda_2\} \tag{3.22}$$

with λ_2 the second eigenvalue of L, known as the Fiedler eigenvalue.

Proof: [1] Figure 3.3 shows the cooperative regulator controller. It is the same as the single-agent regulator, except that now each agent must take into account the states $x_j(t)$ of its neighbors in determining its error. This is formalized by defining the *local neighborhood consensus error* as

$$e_i = \sum_{j \in N_i} a_{ij}(x_j - x_i) \tag{3.23}$$

According to the theorem, if the graph has a spanning tree, then $e_i(t) \to 0, \forall i$ if and only if the consensus problem is solved, that is, $x_i(t) \to x_j(t) \to \text{const}, \ \forall i, j.$

It is important to note that in the single-agent regulator problem, the state goes to zero. By contrast, in the multi-agent cooperative regulator problem, the states go to constant values that depend on the initial conditions of all agents in the graph, as per (3.21). This is a consequence of the interrelation in interconnected multi-agent systems between the control protocols (3.14) and the communication graph topology, as captured in the eigenvalues of the Laplacian matrix L.

3.3.2 Synchronization and the Cooperative Tracker Problem

Consider now the situation in Fig. 3.4 which depicts a leader or target node with state $x_0(t)$. Now, one desires to find controllers that make all the states synchronize to the leader's state, specified as follows.

Definition 3.2 (*Synchronization-The Cooperative Tracker Problem*) Find a distributed control protocol for each agent i that drives all states to the state of the leader node, $x_i(t) \to x_0(t), \ \forall i.$

This is known as the synchronization or *cooperative tracker problem*. There has been much discussion of the terms "consensus" and "synchronization" in the literature, with ancillary terms appearing such as "leaderless consensus" and "synchronization with or without leader." This is cleared up by using simply the terms "cooperative regulator" and "cooperative tracker".

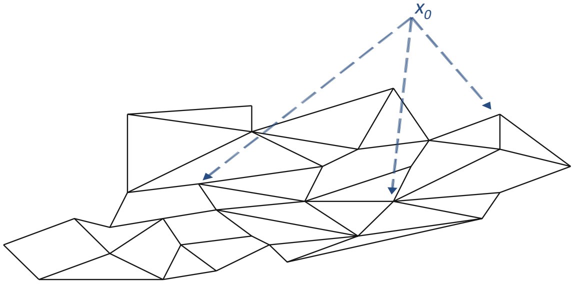

Fig. 3.4 Communication graph with leader node x_0

To solve this problem for the first-order integrator dynamics (3.13), consider the distributed cooperative tracker protocols

$$u_i = \sum_{j \in N_i} a_{ij}(x_j - x_i) + g_i(x_0 - x_i) \tag{3.24}$$

with a_{ij} the graph edge weights. In this protocol, the gains $g_i \geq 0$ are known as pinning gains. One has $g_i > 0$ only if node i has a direct edge from the leader node. As depicted in Fig. 3.4, the intent is that only a small percentage of nodes has $g_i > 0$, and hence has direct access to the leader's state. Nevertheless, we shall now see that under certain graph connectivity conditions, this protocol indeed solves the cooperative tracker problem.

Write the closed-loop dynamics as

$$\dot{x}_i = \sum_{j \in N_i} a_{ij}(x_j - x_i) + g_i(x_0 - x_i) \tag{3.25}$$

$$\begin{aligned} \dot{x}_i &= -x_i \sum_{j \in N_i} a_{ij} + \sum_{j \in N_i} a_{ij}x_j + g_i x_0 - g_i x_i \\ &= -(d_i + g_i)x_i + \begin{bmatrix} a_{i1} & \dots & a_{iN} \end{bmatrix} \begin{bmatrix} x_1 \\ \vdots \\ x_N \end{bmatrix} + g_i x_0 \end{aligned} \tag{3.26}$$

with d_i the in-degree. Define the global state vector $x = [x_1 \dots x_N]^{\mathrm{T}} \in R^N$, the diagonal matrix of in-degrees $D = \mathrm{diag}\{d_i\}$, and the diagonal pinning gain matrix $G = \mathrm{diag}\{g_i\}$. Then the global dynamics are given by

$$\dot{x} = -(D + G)x + Ax = -(D + G - A)x + G\underline{x}_0 \tag{3.27}$$

$$\dot{x} = -(L + G)x + G\underline{x}_0 \tag{3.28}$$

where $\underline{x}_0 = \underline{1}x_0 = \begin{bmatrix} x_0 & \dots & x_0 \end{bmatrix}^{\mathrm{T}}$.

The properties of the cooperative tracker protocol (3.24) depend on the graph properties through the pinned Laplacian matrix ($L + G$). The eigenvalues λ_i of ($L + G$) are instrumental in this analysis [1].

To analyze the behavior of the cooperative tracker, define the tracker synchronization errors

$$\delta_i(t) = x_0(t) - x_i(t) \tag{3.29}$$

and the global tracking error vector $\delta = [\,\delta_1 \quad \ldots \quad \delta_N\,]$, with N the number of agents. Assume the leader node dynamics are

$$\dot{x}_0 = 0 \tag{3.30}$$

Then the global synchronization error dynamics is

$$\begin{aligned} \dot{\delta}(t) &= \dot{\underline{x}}_0(t) - \dot{x}(t) \\ &= (L + G)x - G\underline{x}_0 \end{aligned} \tag{3.31}$$

However, since $L\underline{1} = 0$, one has $L\underline{x}_0 = 0$ and

$$\dot{\delta} = (L + G)x - (L + G)\underline{x}_0 = -(L + G)\delta \tag{3.32}$$

Hence, the global synchronization error goes to zero if ($L + G$) is stable. The next theorem gives the conditions.

Theorem 3.2 (Cooperative Tracking for First-order Systems) *The cooperative tracking protocol* (3.24) *guarantees tracking of the single-integrator dynamics* (3.13) *if and only if the graph has a spanning tree. Then,* $x_i(t) \to x_0(t),\ \forall i$.

Proof: [1] The proof uses the fact that, if the graph has a spanning tree, all eigenvalues of ($L + G$) have positive real parts, so that (3.32) is a stable system.

Figure 3.5 shows the cooperative tracker. It is the same as the single-agent tracker, except that now each agent must take into account the states $x_j(t)$ of its neighbors in determining its error, and the state of the leader node if $g_i > 0$. This is formalized by defining the *local neighborhood tracking error* as

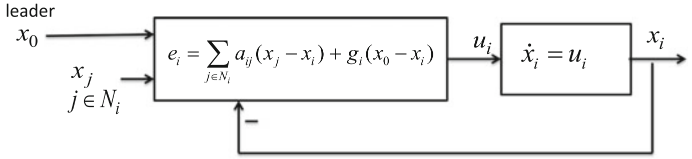

Fig. 3.5 Multi-agent cooperative tracker

$$e_i = \sum_{j \in N_i} a_{ij}(x_j - x_i) + g_i(x_0 - x_i) \tag{3.33}$$

According to the theorem, if the graph has a spanning tree, then $e_i(t) \to 0, \forall i$ if and only if the consensus problem is solved, that is, $\delta_i(t) = x_0(t) - x_i(t) \to 0 \ \forall i$.

3.3.3 More General Agent Dynamics and Vector States

The preceding results can be extended to more general agent dynamics, including vector states and general state variable dynamics.

3.3.3.1 Vector States

We have presented cooperative regulator results for scalar first-order integrator dynamics (3.13), that is

$$\dot{x}_i = u_i \tag{3.34}$$

with scalar $x_i, u_i \in R$. Suppose now that the states and controls are vectors so that $x_i, u_i \in R^n$. Then the preceding developments can be extended using the idea of Kronecker product [34].

Consider two matrices $A \in R^{p \times q}, B \in R^{s \times t}$, denote $A = [a_{ij}]$. The (*left*) Kronecker product is given as

$$A \otimes B = [a_{ij}B] \in R^{ps \times qt} \tag{3.35}$$

For vector states, the integrator dynamics are treated as follows. If the state and input are vectors, then the step from (3.16) to (3.17) cannot be taken, for note that the states in (3.16) are vectors. Therefore, every element in D and A in (3.17) and (3.18) must be multiplied by the $n \times n$ identity matrix I. This yields

$$\dot{x} = -((D - A) \otimes I)x = -(L \otimes I)x \tag{3.36}$$

Theorem 3.1 remains valid.

For the cooperative tracker, Eqs. (3.28) and (3.32) must be replaced, respectively, by

$$\dot{x} = -((L + G) \otimes I)x + (G \otimes I)\underline{x}_0 \tag{3.37}$$

$$\dot{\delta} = -((L + G) \otimes I)\delta \tag{3.38}$$

Theorem 3.2 remains valid.

3.3.3.2 General State Variable Agent Dynamics

Consider N agents interconnected on a communication graph having general linear time-invariant state variable dynamics

$$\dot{x}_i = Ax_i + Bu_i \tag{3.39}$$

with vector states and controls $x_i \in R^n, u_i \in R^m$. Consider the local neighborhood tracking errors (3.33) and the distributed cooperative tracker protocols

$$u_i = cKe_i = cK\left(\sum_{j\in N_i} a_{ij}(x_j - x_i) + g_i(x_0 - x_i)\right) \tag{3.40}$$

with K a state variable feedback gain matrix and $c > 0$ a coupling gain. The closed-loop dynamics are

$$\dot{x}_i = Ax_i + cBK\left(\sum_{j\in N_i} a_{ij}(x_j - x_i) + g_i(x_0 - x_i)\right) \tag{3.41}$$

Define the global state vector $x = \mathrm{vec}\{x_i\} \equiv \begin{bmatrix} x_1^{\mathrm{T}} & x_2^{\mathrm{T}} & \dots & x_N^{\mathrm{T}} \end{bmatrix}^{\mathrm{T}} \in R^{nN}$ and the leader's global vector as $\underline{x}_0 = \mathrm{vec}\{x_0\} \equiv (\underline{1} \otimes x_0) = \begin{bmatrix} x_0^{\mathrm{T}} & x_0^{\mathrm{T}} & \dots & x_0^{\mathrm{T}} \end{bmatrix}^{\mathrm{T}} \in R^{nN}$. Then using a development like (3.26), the global closed-loop dynamics are seen to be

$$\dot{x} = [(I_N \otimes A) - c((L+G) \otimes BK)]x \; + \; c((L+G) \otimes BK)\underline{x}_0 \tag{3.42}$$

Assume the leader's dynamics are

$$\dot{x}_0 = Ax_0 \tag{3.43}$$

Then the global error dynamics are

$$\dot{\delta} = [(I_N \otimes A) - c((L+G) \otimes BK)]\delta \tag{3.44}$$

There are many methods for selecting c and K to guarantee synchronization to the leader's state. One result is the following from [35].

Theorem 3.3 (Cooperative Tracking for State Variable Multi-agent Systems) *Consider multi-agent dynamics* (3.39) *with distributed controls* (3.40)*. Suppose that* (A, B) *is stabilizable. Select positive definite design matrices* $Q = Q^{\mathrm{T}} \in \mathbb{R}^{n\times n}$ *and* $R = R^{\mathrm{T}} \in \mathbb{R}^{m\times m}$*, Design the feedback control gain K as*

$$K = R^{-1}B^{\mathrm{T}}P, \tag{3.45}$$

where P is the unique positive definite solution of the control algebraic Riccati equation (*ARE*))

$$0 = A^{\mathrm{T}}P + PA + Q - PBR^{-1}B^{\mathrm{T}}P. \tag{3.46}$$

Then under Assumption 1, the synchronization error dynamics (*9*) *is asymptotically stable if the coupling gain*

$$c \geq \frac{1}{2\underline{\lambda}_R} \tag{3.47}$$

with $\underline{\lambda}_R = \min_{i \in \mathcal{N}} \mathrm{Re}(\lambda_i)$.

Proof: [35] Note that this design has two parts, a local design procedure based on (3.45), (3.46) to select the gain matrix K, and a global design condition (3.47) based on the graph topology to select the coupling gains c. The graph topology is captured here in terms of $\underline{\lambda}_R = \min_{i \in \mathcal{N}} \mathrm{Re}(\lambda_i)$, the eigenvalue with smallest real part. Note that (3.47) and (3.22) employ the same object $\underline{\lambda}_R = \min_{i \in \mathcal{N}} \mathrm{Re}(\lambda_i) = \mathrm{Re}(\lambda_2)$.

This theorem highlights an important factor about controls design for multi-agent systems on communication graphs. Namely, the communication graph topology must be taken into account in the design of local controllers. To wit, consider the local agent dynamics (3.39) with the local controls $u_i = -Kx_i$. Then, the closed-loop local dynamics are $\dot{x}_i = (A - BK)u_i$. These dynamics are stabilized by the gain computed using the ARE design (3.45), (3.46). However, if these dynamics are now linked together using a communication graph, the interconnected closed-loop dynamics are (3.41), which are influenced by the neighbors states x_j, $j \in N_i$. These interconnected dynamics can be unstable if the condition (3.47) does not hold.

Therefore, in multi-agent systems, the local controls design must take into account the graph topology up front, or stability cannot be guaranteed. The graph topology is captured here in terms of $\underline{\lambda}_R = \min_{i \in \mathcal{N}} \mathrm{Re}(\lambda_i)$, the eigenvalue with smallest real part.

3.4 Time-Varying Edge Weights and Switched Graphs

The results in this chapter so far are for the case of graphs with fixed constant edge weights a_{ij}. In many applications, however, the edge weights are time varying, such as when communication links fade and the channel gains a_{ij} change, or when links are temporarily lost so that $a_{ij} = 0$. Dynamically changing interaction topologies have been studied in [22, 23, 25, 36]. The following results allow the extension of Theorems 3.1 and 3.2 to the case of time-varying edge weights and switched graphs.

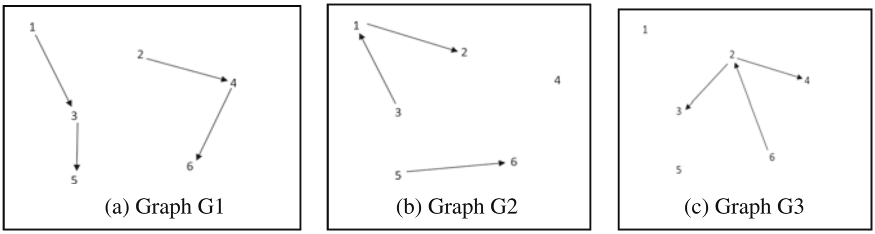

(a) Graph G1 (b) Graph G2 (c) Graph G3

Fig. 3.6 Three disconnected graphs whose union is strongly connected

Examine Fig. 3.6, which shows three directed communication graphs, none of which is strongly connected or has a spanning tree. Their union, however, is strongly connected. If the nodes represent dynamical agents, the graphs could represent the communication topology at three subsequent times. Though at no time are all the agents strongly connected, over the complete time period all nodes will eventually communicate with each other.

Consider a finite set of digraphs $\{G_p, p = 1, P\}$. The set is said to be jointly strongly connected if the union of its members is strongly connected. The set is said to jointly have a spanning tree if the union of its members has a spanning tree.

Consider the dynamics (3.13) with distributed protocols (3.14). We wish to allow the graph interactions to vary with time. Consider a finite set of possible graph topologies $\{G_p : p = 1, \ldots, P\}$ with G_p having adjacency matrix A_p, in-degree matrix D_p, and Laplacian L_p. Let

$$\dot{x} = -L_\sigma x \tag{3.48}$$

with $\sigma(t) \in \{1, 2, \ldots, P\}$ a switching signal whose value at time t indicates which graph describes the current topology at time t. Let $t_0, t_1, \ldots$ be the times at which $\sigma(t)$ switches and let $t_{i+1} - t_i > \tau$ for some fixed dwell time $\tau > 0$.

The next result from [36] shows when the distributed local protocols (3.14) deliver consensus on switched graph topologies. In connection with this proof, the importance of the setup in here is that the Laplacians are constant between switchings, and $t_j - t_{j-1} > \tau$ for some fixed dwell time $\tau > 0$ so that the number of graphs in any bounded time interval is finite.

Theorem 3.4 (Continuous-Time Consensus on Changing Graph Topologies) *Consider the dynamics* (3.13) *and protocols* (3.14) *on switched graphs. Let the graphs switch at times* $t_0, t_1, \ldots$. *Assume there exists an infinite sequence of contiguous, nonempty, bounded time intervals* $[t_{i_j}, t_{i_{j+1}})$, $j = 1, 2, \ldots$ *starting at* $t_{i_1} = t_0 = 0$, *such that the union of graphs over each interval has a spanning tree. Then consensus is reached and*

$$x_{ss} = 1c \tag{3.49}$$

for some consensus value c.

This theorem states that if there exists an infinite sequence of contiguous, nonempty, bounded time intervals over each of which the set of graphs jointly has a spanning tree, then consensus is reached. Note, however, that the consensus value c in Theorem 3.2 is not the same as (3.21) and depends on the switching times and individual graph topologies at each time instant.

Results similar to this hold for cooperative tracking Theorem 3.2, and for the case when the graph weights are time varying between switching times [36].

References

1. Lewis FL, Zhang H, Hengster-Movric K, Das A (2014) Cooperative control of multi-agent systems: optimal and adaptive design approaches. Springer, Berlin
2. Wang X, Yadav V, Balakrishnan S (2007) Cooperative UAV formation flying with obstacle/collision avoidance. IEEE Trans Contr Syst Technol 15(4):672–679
3. Murray R (2007) Recent research in cooperative control of multivehicle systems. J Dyn Syst Meas Control 129(5):571–583
4. Cruz D, McClintock J, Perteet B, Orqueda O, Cao Y, Fierro R (2007) Decentralized cooperative control—a multivehicle platform for research in networked embedded systems. IEEE Control Syst Mag 27(3):58–78
5. Chen J, Cao X, Cheng P, Xiao Y, Sun Y (2010) Distributed collaborative control for industrial automation with wireless sensor and actuator networks. IEEE Trans Ind Electron 57 (12):4219–4230
6. Defoort M, Floquet T, Kokosy A, Perruquetti W (2008) Sliding-mode formation control for cooperative autonomous mobile robots. IEEE Trans Ind Electron 55(11):3944–3953
7. Strogatz SH, Stewart I (1993) Coupled oscillators and biological synchronization. Sci Am 269 (6):102–109
8. Couzin ID, Krause J, Franks NR, Levin SA (2005) Effective leadership and decision-making in animal groups on the move. Nature 533:513–516
9. Reynolds CW (1987) Flocks, Herds, and schools: a distributed behavioral model. In: Stone MC (ed) Proc. SIGGRAPH 87, Computer Graphics, vol 21(4), pp 25–34
10. Strogatz SH (2000) From Kuramoto to Crawford: exploring the onset of synchronization in populations of coupled oscillators. Physica D 143:1–20
11. Leonard NE, Fiorelli E (2001) Virtual leaders, artificial potentials, and coordinated control of groups. Proc. IEEE Conf Decis Control 2968–2973
12. Gazi V, Passino KM (2004) Stability analysis of social foraging swarms. IEEE Trans Syst, Man, and Cybern-Part B: Cybern 34(1):539–557
13. Wang W, Slotine J (2006) A theoretical study of different leader roles in networks. IEEE Trans Autom Control 51(7):1156–1161
14. Kuramoto Y (1984) Chemical oscillations, waves, and turbulence. Springer, Berlin
15. Vicsek T, Czir´ok A, Ben-Jacob E, Cohen I, Shochet O (1995) Novel type of phase transition in a system of self-driven particles. Phys Rev Lett 75(6):1226–1229
16. Chopra N, Spong MW (2005) On synchronization of Kuramoto Oscillators. Proc. IEEE CDC
17. Dorfler F, Bullo F (2010) Transient stability analysis in power networks and synchronization of non-uniform Kuramoto oscillators. In: Proc. American Control Conference. Baltimore, MD, pp 930–937

18. Ortega R, Galaz M, Astolfi A, Sun Y (2005) Transient stabilization of multimachine power systems with nontrivial transfer conductances. IEEE Trans Autom Control 50(1):60–75
19. Diestel R (2000) Graph theory. Springer, New York
20. Godsil C, Royle GF (2001) Algebraic graph theory. Springer, New York
21. Bertsekas D, Tsitsiklis JN (1997) Parallel and distributed computation: numerical methods. Athena Scientific, Belmont, MA
22. Jadbabaie A, Lin J, Morse A (2003) Coordination of groups of mobile autonomous agents using nearest neighbor rules. IEEE Trans Autom Control 48(6):988–1001
23. Olfati-Saber R, Murray R (2004) Consensus problems in networks of agents with switching topology and time-delays. IEEE Trans Autom Control 49(9):1520–1533
24. Fax J, Murray R (2004) Information flow and cooperative control of vehicle formations. IEEE Trans Autom Control 49(9):1465–1476
25. Ren W, Beard R (2005) Consensus seeking in multiagent systems under dynamically changing interaction topologies. IEEE Trans Autom Control 50(5):655–661
26. Moreau L (2005) Stability of multiagent systems with time-dependent communication links. IEEE Trans Autom Control 50(2):169–182
27. Ren W, Beard R, Atkins E (2005) A survey of consensus problems in multi-agent coordination. Proc Am Control Conf, Portland, OR, pp 1859–1864
28. Han J, Li M, Guo L (2006) Soft control on collective behavior of a group of autonomous agents by a shill agent. J Syst Sci Complex 19:54–62
29. Ren W, Beard R, Atkins E (2007) Information consensus in multivehicle cooperative control. IEEE Control Syst Mag 27(2):71–82
30. Ren W, Moore K, Chen Y (2007) High-order and model reference consensus algorithms in cooperative control of multivehicle systems. J Dyn Syst Meas Control 129(5):678–688
31. Olfati-Saber R, Fax J, Murray R (2007) Consensus and cooperation in networked multi-agent systems. Proc IEEE 95(1):215–233
32. Zhu W, Cheng D (2010) Leader-following consensus of second-order agents with multiple time-varying delays. Automatica 46(12):1994–1999
33. Ren W, Cao C (2011) Distributed coordination of multi-agent networks: emergent problems, models, and issues. Springer, London
34. Brewer J Kronecker products and matrix calculus in system theory. IEEE Trans Circuits Syst 25(9):772–781
35. Zhang H, Lewis FL, Das Abhijit (2011) Optimal design for synchronization of cooperative systems: state feedback, observer and output feedback. IEEE Trans Automatic Control 56 (8):1948–1952
36. Ren W, Beard RW (2008) Distributed consensus in multi-vehicle cooperative control. Springer, London

Chapter 4
Distributed Control of AC Microgrids

The traditional secondary control of microgrids discussed in Chap. 2 exploits a centralized control structure. Central controllers command globally based on gathered system-wide information and require a complex [10, 12] and in some cases two-way communication network [14]. All DGs are commanded by communications from a single central controller. This adversely affects system flexibility and configurability and increases reliability concerns by posing a single point of failure. The single point of failure means that if the central controller fails, the whole control system fails. In this chapter, distributed control structure is used to implement the secondary control of microgrids. A microgrid can be considered as a multi-agent system where its DGs are the energy nodes (agents). Figure 4.1 shows a distributed communication structure that takes advantage of the multi-agent environment for a microgrid system with DGs as agents. A distributed structure of the communication network improves the system reliability. In this control structure, the control protocols are distributed on all DGs. Therefore, the requirement for a central controller is obviated and the control system does not fail down subsequent to outage of a single unit.

In this chapter, we take advantage of the graph theory notions and distributed control methods in Chap. 3 to design improved, distributed, and sparse communication networks for microgrids. The distributed cooperative control of multi-agent systems can be used to implement the secondary control of microgrids. The term "distributed" means that the controller utilizes a communication network by which each agent only receives information from its neighboring agents. The term "cooperative" means that, in contrast to the competitive control, all agents act as one group toward a common synchronization goal and follow cooperative decisions. Distributed cooperative control of multi-agent systems was detailed in Chap. 3 and is mainly categorized into the regulator synchronization problem and the tracking synchronization problem. In the regulator synchronization problem, also called leaderless consensus, all agents synchronize to a common value that is not prescribed or controllable. In the tracking synchronization problem, all agents synchronize to a leader node that acts as a command generator. Neighboring agents can

A. Bidram et al., *Cooperative Synchronization in Distributed Microgrid Control*,
Advances in Industrial Control, DOI 10.1007/978-3-319-50808-5_4

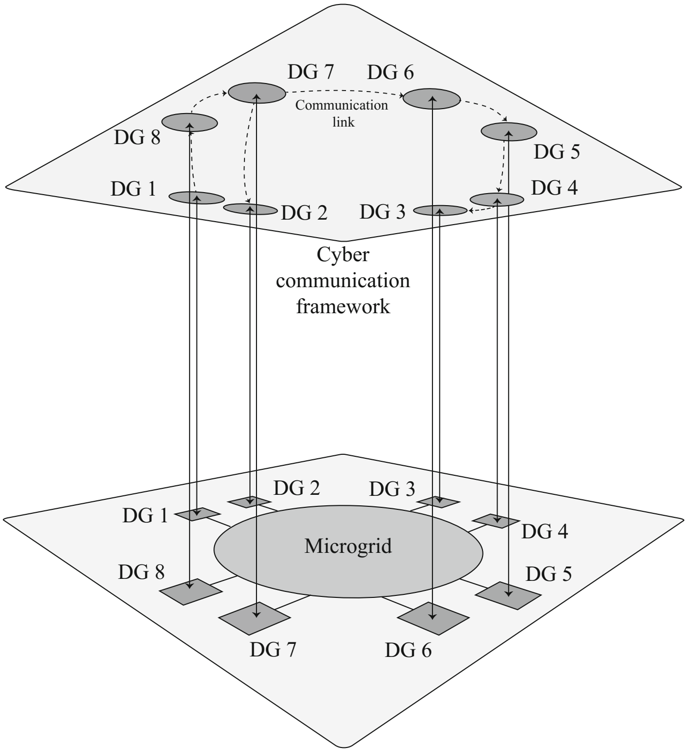

Fig. 4.1 Multi-agent environment for a microgrid system with DGs as agents [4]. © [2016] IEEE. Reprinted, with permission, from IEEE transactions on energy conversion [19]

communicate with each other. The leader is only connected to a small portion of the agents [9, 11, 12, 15].

The secondary control of microgrids is similar to the tracking synchronization problem of a multi-agent system where the DG voltages and frequencies are required to track their prescribed nominal values. The dynamics of DGs in microgrids are nonlinear and nonidentical. Therefore, a method known as input–output feedback linearization [16] is used here to transform the nonlinear heterogeneous dynamics of DGs to linear dynamics. Input–output feedback linearization transforms the secondary voltage control problem to a second-order multi-agent tracking synchronization problem. On the other hand, the secondary frequency control is transformed to a first-order multi-agent tracking synchronization problem using input–output feedback linearization. Based on the transformed dynamics, fully distributed voltage and frequency control protocols are derived for each DG. The proposed distributed controls are implemented through a sparse communication network, with only one-way communication links, where each DG requires only its own information and the information of its neighbors.

4.1 Distributed Secondary Frequency Control

In this section, distributed cooperative control techniques for multi-agent systems as discussed in Chap. 3 are used to design secondary frequency controllers for microgrids. A method known as input–output feedback linearization [16] can be used as shown here to transform the nonlinear heterogeneous dynamics of DGs to linear dynamics. Once input–output feedback linearization is applied, the secondary frequency control leads to a first-order multi-agent synchronization problem. Fully distributed frequency control protocols are derived for each DG that synchronizes the DG frequencies to the prescribed nominal value. The proposed secondary frequency control is implemented through a sparse communication network. The communication network is modeled by a digraph. Each DG requires only its own information and information from its neighbors on the digraph. This leads to a sparse distributed communication structure that only requires one-way communication links and is more reliable than centralized secondary frequency controls.

According to Chap. 2, the nonlinear dynamics of a VCVSI can be written as

$$\begin{cases} \dot{\mathbf{x}}_i = \mathbf{f}_i(\mathbf{x}_i) + \mathbf{k}_i(\mathbf{x}_i)\mathbf{D}_i + \mathbf{g}_i(\mathbf{x}_i)u_i \\ y_i = h_i(\mathbf{x}_i) + d_i u_i \end{cases}, \tag{4.1}$$

Detailed expressions for $\mathbf{f}_i(\mathbf{x}_i)$, $\mathbf{g}_i(\mathbf{x}_i)$, $h_i(\mathbf{x}_i)$, $d_i(\mathbf{x}_i)$, and $\mathbf{k}_i(\mathbf{x}_i)$ are adopted from the nonlinear VCVSI model presented in Chap. 2.

As discussed in Chap. 2, the primary control is usually implemented as a local controller at each DG by the droop technique. Droop technique prescribes a desired relation between the frequency and the active power, and between the voltage amplitude and the reactive power. The primary frequency control is

$$\omega_i = \omega_i^* - D_{Pi} P_i, \tag{4.2}$$

where ω_i^* is the primary frequency control reference and D_{Pi} is the frequency active power droop coefficient. The secondary frequency control chooses ω_i^* such that the angular frequency of each DG synchronizes to its nominal value, i.e., $\omega_i \to \omega_{\text{ref}}$. For secondary frequency control, $y_i = \omega_i$ and $u_i = \omega_i^*$. Therefore, the output $y_i(t)$ is related to the input $u_i(t)$ by the nonlinear function $h_i(x_i)$ and d_i. The difficulties associated with the nonlinear nature of the dynamics can be overcome by using the following procedure.

Differentiate the output of each agent to obtain

$$\dot{y}_i = L_{\mathbf{f}_i} h_i + L_{\mathbf{g}_i} h_i u_i + d_i \dot{u}_i, \tag{4.3}$$

where $L_{\mathbf{f}} h = \frac{\partial h}{\partial \mathbf{x}} \mathbf{f}(\mathbf{x})$ denotes Lie derivative [16].

Define the auxiliary control v_i as

$$v_i = L_{\mathbf{f}_i} h_i + L_{\mathbf{g}_i} h_i u_i + d_i \dot{u}_i. \tag{4.4}$$

Then, the control input u_i satisfies the nonlinear state variable equation

$$d_i \dot{u}_i = -L_{\mathbf{g}_i} h_i u_i - L_{\mathbf{f}_i} h_i + v_i. \tag{4.5}$$

Equation (4.5) allows direct computation of the control input u_i in terms of v_i. It is noted that the state-space equation (5) guarantees that the control input u_i is differentiable.

Equation (4.4) defines the input–output feedback linearization that results in the first-order linear systems

$$\dot{y}_i = v_i, \ \forall i. \tag{4.6}$$

Using this input–output feedback linearization, the dynamics of each agent are decomposed into the first-order dynamical system in (4.6) and a set of internal dynamics [16]

$$\dot{\mu}_i = W_i(y_i, \mu_i), \ \forall i, \tag{4.7}$$

where $\mu_i \in \mathbb{R}^{n_i}$ represents the internal dynamics.

Preliminaries of Graph Theory. Graph theory was discussed in Chap. 3 and is reviewed here. The communication network of a multi-agent cooperative system can be modeled by a directedgraph (digraph). A digraph is usually expressed as $Gr = (V_G, E_G, A_G)$ with a non-empty finite set of N nodes $V_G = \{v_1, v_2, \ldots, v_N\}$, a set of edges or arcs $E_G \subset V_G \times V_G$, and the associated adjacency matrix $A_G = [a_{ij}] \in R^{N \times N}$. In a microgrid, DGs are considered as the nodes of the communication digraph. The edges of the corresponding digraph of the communication network denote the communication links.

An edge from node j to node i is denoted by (v_j, v_i), which means that node i receives the information from node j. a_{ij} is the weight of edge (v_j, v_i), and $a_{ij} > 0$ if $(v_j, v_i) \in E_G$, otherwise $a_{ij} = 0$. Node i is called a neighbor of node j if $(v_i, v_j) \in E_G$. The set of neighbors of node j is denoted as $N_j = \{i \mid (v_i, v_j) \in E_G\}$. For a digraph, if node i is a neighbor of node j, then node j can get information from node i, but not necessarily vice versa. The in-degree matrix is defined as $D = \mathrm{diag}\{d_i\} \in R^{N \times N}$ with $d_i = \sum_{j \in N_i} a_{ij}$. The Laplacian matrix is defined as $L = D - A_G$. A direct path from node i to node j is a sequence of edges, expressed as $\{(v_i, v_k), (v_k, v_l), \ldots, (v_m, v_j)\}$. A digraph is said to have a spanning tree, if there is a root node with a direct path from that node to every other node in the graph [15].

To solve the synchronization problem for the systems in (4.6), cooperative team objectives can be expressed in terms of the local neighborhood tracking error $e_{yi} \in R$

$$e_{yi} = \sum_{j \in N_i} a_{ij}(y_i - y_j) + b_i(y_i - y_0). \tag{4.8}$$

The pinning gain $b_i \geq 0$ is nonzero only for the nodes that are directly connected to the leader node y_0. It is assumed that b_i is nonzero for at least one node. The nodes for which $b_i \neq 0$ are referred to as the pinned or controlled nodes.

From (4.8), the global neighborhood error vector for the graph Gr is written as

$$e_y = (L+B)\left(y - \underline{y}_0\right) \equiv (L+B)\delta_y, \tag{4.9}$$

where the global variables are defined as $y = [\,y_1 \quad y_2 \quad \cdots \quad y_N\,]^T \in R^N$, $e_y = \left[\,e_{y1} \quad e_{y2} \quad \cdots \quad e_{yN}\,\right]^T \in R^N$, and $\underline{y}_0 = \mathbf{1}_N \otimes y_0 \in R^N$, with $\mathbf{1}_N$ the vector of ones with the length of N. The Kronecker product is $\otimes$ [7]. $B \in R^{N \times N}$ is a diagonal matrix with diagonal entries equal to the pinning gains b_i. The global disagreement vector is δ_y.

Remark 4.1 Note that the global disagreement vector δ_y is a global vector that cannot be computed locally at each node. In this chapter, to achieve a fully distributed control structure, the local neighborhood tracking error in (4.8) is used to solve the synchronization problem.

Definition 4.1 The global neighborhood error in (4.9) is uniformly ultimately bounded (UUB) if there exists a compact set $\Omega \subset \mathbb{R}^N$ such that $\forall e_y(t_0) \in \Omega$ there exists a bound Bo and a time $t_f(Bo, e_y(t_0))$, both independent of t_0, such that $\left\|e_y(t)\right\| \leq Bo,\ \forall t > t_0 + t_f$ [20].

Definition 4.2 The agent outputs $y_i(t)$ are cooperative UUB with respect to the leader node output $y_0(t)$ if there exists a compact set $\Omega \subset \mathbb{R}$ such that $\forall (y_i(t_0) - y_0(t_0)) \in \Omega$ there exists a bound Bo and a time $t_f(Bo, (y_i(t_0) - y_0(t_0)))$, both independent of t_0, such that $\|y_i(t_0) - y_0(t_0)\| \leq Bo,\ \forall t > t_0 + t_f$ [20].

Assumption 4.1 The vector $\dot{\underline{y}}_0 = \mathbf{1}_N \otimes \dot{y}_0$ is bounded so that $\left\|\dot{\underline{y}}_0\right\| \leq Y_M$, for some finite bound Y_M that is generally unknown.

Lemma 4.1 [6]. *Let the digraph Gr have a spanning tree and $b_i \neq 0$ for at least one root node. Assume that the zero dynamics of each node $\dot{\mu}_i = W_i(0, \mu_i)$, $\forall i$ are asymptotically stable. Let the auxiliary control v_i in (4.5) be chosen as*

$$v_i = -ce_{yi}, \tag{4.10}$$

where the scalar $c > 0$ and e_{yi} is in (4.8). Then, the global neighborhood error e_y in (4.9) is UUB with the practical bound in (4.17). Moreover, the agent outputs $y_i(t)$ are cooperative UUB with respect to the leader node output $y_0(t)$ and all nodes synchronize to $y_0(t)$.

Proof From (4.10), the global input vector v is

$$v = \begin{bmatrix} v_1 & v_2 & \cdots & v_N \end{bmatrix}^T = -ce_y. \tag{4.11}$$

Consider the Lyapunov function candidate

$$V = \frac{1}{2} e_y^T P e_y, \quad \text{where } P = \operatorname{diag}\{1/w_i\}, \tag{4.12}$$

where w_i are the elements of a vector w that satisfies $(L + B)w = \mathbf{1}_N$. Since the digraph Gr has a spanning tree and $k_i \neq 0$ for at least one root node, $L + B$ is non-singular and a unique solution exists for w [15].

Differentiating (4.12) and using (4.9) yield

$$\dot{V} = e_y^T P(L+B)(\dot{y} - \dot{\underline{y}}_0) = e_y^T P(L+B)(v - \dot{\underline{y}}_0). \tag{4.13}$$

Defining $A \equiv L + B$, and placing (4.11) into (4.13) yields

$$\dot{V} = \frac{-c}{2} e_y^T (PA + A^T P) e_y - e_y^T PA\dot{\underline{y}}_0. \tag{4.14}$$

From [15], $Q \equiv PA + A^T P$ is positive definite. Therefore, $\frac{c}{2} e_y^T Q e_y \geq \frac{c}{2} \underline{\sigma}(Q) \left\| e_y \right\|^2$, and hence,

$$\frac{-c}{2} e_y^T Q e_y \leq \frac{-c}{2} \underline{\sigma}(Q) \left\| e_y \right\|^2. \tag{4.15}$$

where $\underline{\sigma}(\cdot)$ is the minimum singular value of a matrix. According to (4.15) and Assumption 4.1,

$$\dot{V} \leq \frac{-c}{2} \underline{\sigma}(Q) \left\| e_y \right\|^2 + \left\| e_y \right\| \overline{\sigma}(P) \overline{\sigma}(A) Y_M, \tag{4.16}$$

where $\overline{\sigma}(\cdot)$ is the maximum singular value of a matrix. $\dot{V} \leq 0$ if

$$\left\| e_y \right\| \geq \frac{\overline{\sigma}(P) \overline{\sigma}(A) Y_M}{\frac{c}{2} \underline{\sigma}(Q)}. \tag{4.17}$$

Equation (4.17) shows that the derivative of Lyapunov function in (4.16) is negative outside a compact set around origin with the radius of $\overline{\sigma}(P)\overline{\sigma}(A)Y_M / \frac{c}{2}\underline{\sigma}(Q)$. This demonstrates that any trajectory of $e_y(t)$ beginning in this compact set evolves completely within this compact set. Therefore, according to the standard Lyapunov theorem extension, $e_y(t)$ is UUB. According to (4.9), if the graph has a spanning tree, then $L + B$ is non-singular and $\left\| \delta_y \right\| \leq \left\| e_y \right\| / \underline{\sigma}(L+B)$. Therefore, the global disagreement vector δ_y is UUB, and hence, $y_i(t)$ are cooperative UUB with respect to $y_0(t)$ (The term cooperative UUB is defined in Definition 4.2). If the zero dynamics $\dot{\mu}_i = W_i(0, \mu_i)$, $\forall i$ are asymptotically stable, then (4.6) and (4.10) are asymptotically stable [16]. This completes the proof. □

Remark 4.2 Lemma 4.1 only focuses on proving the local stability of (4.6) and (4.10) by assuming the local asymptotically stability of internal dynamics in (4.7). It should be noted that the local asymptotically stability of zero dynamics $\dot{\mu}_i = W_i(0, \mu_i)$, $\forall i$ proves the local asymptotically stability of internal dynamics [16].

Remark 4.3 If $\dot{y}_0 = 0$, then, the error bound in (4.17) is zero and the global disagreement vector is asymptotically stable. Note that the error bound (4.17) can be made small by increasing the control gain c. In practical systems, making the error bound exactly equal to zero may be unrealistic if there are unknown disturbances or unknown leader motions. In such cases, exact synchronization cannot be achieved. The purpose of this chapter is to make the synchronization errors small in the presence of unknown leader node velocity. Definitions 4.1 and 4.2 define a synchronization concept that is close enough to realistic situations.

Remark 4.4 Suppose that $Y_M = 0$, Eq. (4.16) yields

$$\dot{V} \leq \frac{-c}{2}\underline{\sigma}(Q)\left\|e_y\right\|^2 \leq \frac{-c}{2}\frac{\underline{\sigma}(Q)}{\overline{\sigma}(P)}V \equiv -2\alpha V, \tag{4.18}$$

From (4.18), one can write

$$V(t) \leq \exp(-2\alpha t)V(t_0), \tag{4.19}$$

where exp(.) is the exponential function. From (4.12) and (4.19),

$$\frac{1}{2}\underline{\sigma}(P)\left\|e_y(t)\right\|^2 \leq \frac{1}{2}\overline{\sigma}(P)\exp(-2\alpha t)\left\|e_y(t_0)\right\|^2, \tag{4.20}$$

or equivalently

$$\left\|e_y(t)\right\| \leq \sqrt{\frac{\overline{\sigma}(P)}{\underline{\sigma}(P)}}\exp(-\alpha t)\left\|e_y(t_0)\right\|. \tag{4.21}$$

Equation (4.21) shows that the global neighborhood error $e_y(t)$ goes to zero with the time constant $1/\alpha$. Since $\alpha = \frac{-c}{2}\frac{\underline{\sigma}(Q)}{\overline{\sigma}(P)}$, the synchronization speed of the system can be adjusted by c.

4.2 Distributed Secondary Frequency and Power Control

As discussed in the previous section, the secondary frequency control chooses ω_i^* such that the angular frequency of each DG synchronizes to a prescribed nominal angular frequency, i.e., $\omega_i \to \omega_{\mathrm{ref}}$, where $\omega_{\mathrm{ref}} = 2\pi f_{\mathrm{ref}}$. The nominal frequency of the microgrid is f_{ref} and can be equal to 50 or 60 Hz. In addition to frequency synchronization, there is a second important control objective for secondary control. Namely, the secondary frequency control can also be used to share the active power equally among DGs based on their ratings, i.e., the DG output powers satisfy the following equality

$$D_{P1}P_1 = \cdots = D_{PN}P_N. \tag{4.22}$$

Since the active power droop coefficients D_{Pi} are chosen based on the active power rating of DGs, $P_{\max i}$, (4.22), is equivalent to

$$\frac{P_1}{P_{\max 1}} = \cdots = \frac{P_N}{P_{\max N}}. \tag{4.23}$$

Therefore, the secondary frequency control must also guarantee (4.22) or (4.23). For the secondary frequency control, the outputs and inputs of the dynamical model of DG are $y_i = \omega_i$ and $u_i = \omega_i^*$, respectively.

In this section, the distributed cooperative control of multi-agent systems will be adopted to develop the secondary frequency control with a distributed structure. The block diagram of VCVSI is shown in Fig. 4.2. The proposed secondary frequency control exploits the following relationship between the output active power of each DG and its angular frequency. The output active power of each DG can be written as

$$P_i = \frac{|v_{oi}||v_{bi}|}{X_{ci}} \sin(\delta_i) \equiv h_i \sin(\delta_i), \tag{4.24}$$

where δ_i is the angle of the DG reference frame with respect to the common reference frame.v_{oi}, v_{bi}, and $X_{ci} = \omega_i L_{ci}$ are shown in Fig. 4.2. The term h_i can be assumed to be constant since the amplitude of v_{oi} and v_{bi} changes slightly around the nominal voltage. Since X_{ci} is typically small, δ_i is small, and hence, $\sin(\delta_i)$ is approximately equal to δ_i. Considering these assumptions and differentiating (4.24) yields

$$\dot{P}_i = h_i(\omega_i - \omega_{\mathrm{com}}), \tag{4.25}$$

Equation (4.25) provides a direct relationship between the differentiated output power of DGs and their angular frequencies with respect to the angular frequency of microgrid. The global form of (4.25) can be written as

$$\dot{P} = h(\omega - \underline{\omega}_{\mathrm{com}}), \tag{4.26}$$

where $h = \mathrm{diag}\{h_i\}$ and $\underline{\omega}_{\mathrm{com}} = \mathbf{1}_N \otimes \omega_{\mathrm{com}}$.

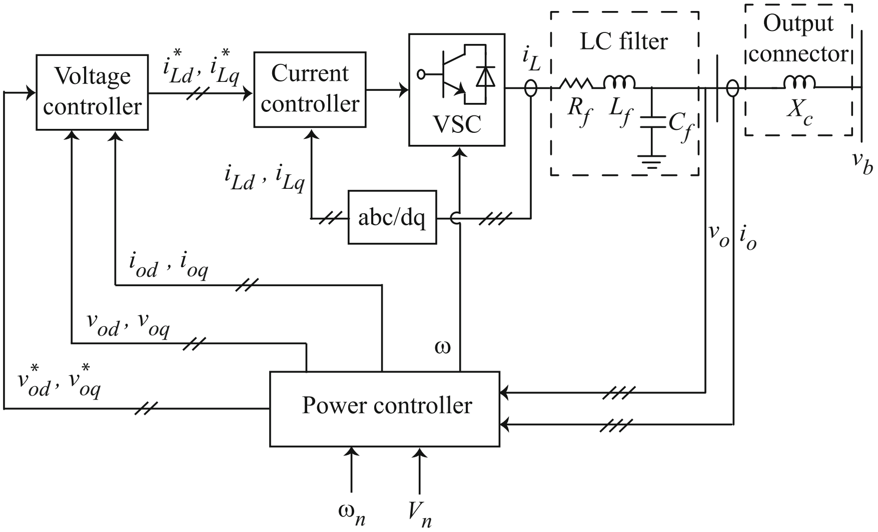

Fig. 4.2 The block diagram of a VCVSI. © [2016] IEEE. Reprinted, with permission, from IEEE transactions on power systems [4]

4.2.1 Distributed Cooperative Control Protocol for Frequency and Active Power Sharing

This section shows how to achieve two secondary control objectives using a single distributed control protocol at each DG. The distributed cooperative control protocol is designed to synchronize the frequency of DGs, ω_i, to the reference frequency, ω_{ref}, while also sharing the active power equally among DGs based on their power ratings as stated in (4.22).

Applying input–output feedback linearization by differentiating the frequency droop characteristic in (4.2) yields

$$\dot{\omega}_i^* = \dot{\omega}_i + D_{Pi}\dot{P}_i = u_i, \tag{4.27}$$

where u_i is an auxiliary control to be designed. Equation (4.27) is a dynamic system for computing the control input ω_i^* from u_i. The auxiliary control should be designed such that DG frequencies synchronize to the reference frequency ω_{ref}, and (4.22) is satisfied. According to (4.27), the secondary frequency control of a microgrid including N DGs is transformed to a synchronization problem for a first-order and linear multi-agent system

$$\begin{cases} \dot{\omega}_1 + D_{P1}\dot{P}_1 = u_1, \\ \dot{\omega}_2 + D_{P2}\dot{P}_2 = u_2, \\ \vdots \\ \dot{\omega}_N + D_{PN}\dot{P}_N = u_N. \end{cases} \tag{4.28}$$

To achieve synchronization, it is assumed that DGs can communicate with each other through the prescribed communication digraph Gr. The auxiliary controls u_i are chosen based on each DG's own information and the information of its neighbors in the communication digraph as

$$u_i = -c_f\left(\sum_{j \in N_i} a_{ij}(\omega_i - \omega_j) + \ b_i(\omega_i - \omega_{\text{ref}}) + \sum_{j \in N_i} a_{ij}(D_{Pi}P_i - D_{Pj}P_j)\right), \tag{4.29}$$

where $c_f \in R$ is the coupling gain. It is assumed that the pinning gain $b_i \geq 0$ is nonzero for only one DG that has the reference frequency ω_{ref}.

The global control input u is written as

$$u = -c_f((L+B)(\omega - \underline{\omega}_{\text{ref}}) + LD_P P), \tag{4.30}$$

where $\omega = \begin{bmatrix} \omega_1 & \omega_2 & \cdots & \omega_N \end{bmatrix}^T$, $\underline{\omega}_{\text{ref}} = \mathbf{1}_N \otimes \omega_{\text{ref}}$, with $\mathbf{1}_N$ the vector of ones with the length of N,$D_P = \text{diag}\{D_{Pi}\}$, and $P = \begin{bmatrix} P_1 & P_2 & \cdots & P_N \end{bmatrix}^T$. The Kronecker product is $\otimes$. $B \in \mathbb{R}^{N \times N}$ is a diagonal matrix with diagonal entries equal to the pinning gains b_i. The global form of dynamics in (4.28) can be written as

$$\dot{\omega} + D_P\dot{P} = -c_f((L+B)(\omega - \underline{\omega}_{\text{ref}}) + LD_P P). \tag{4.31}$$

The term $(L+B)(\omega - \underline{\omega}_{\text{ref}})$ is defined as the global neighborhood tracking error e. The term $\omega - \underline{\omega}_{\text{ref}}$ is defined as the global disagreement vector, δ.

Lemma 4.2 [15]. *Zero is a simple eigenvalue of L if and only if the directed graph has a spanning tree. Moreover,* $L\mathbf{1}_N = 0$, *with* $\mathbf{1}_N$ *being the vector of ones with the length of N.*

Lemma 4.3 [19]. *Let the digraph Gr have a spanning tree and* $b_i \neq 0$ *for at least oneroot node. Then,* $L + B$ *is a non-singular M-matrix. Additionally,*

$$\|\delta\| \leq \|e\| / \sigma_{\min}(L+B), \tag{4.32}$$

where $\sigma_{\min}(L+B)$ *is the minimum singular value of* $L+B$, *and* $e = 0$ *if and only if* $\delta = 0$.

In the following, it is assumed that the DG for which $b_i \neq 0$ is labeled as DG 1.

Lemma 4.4 [5]. *Let the digraph Gr have a spanning tree and* $b_i \neq 0$ *for only one DG placed as a root node of digraph Gr. Let the auxiliary control* u_i *be chosen as* *in* (4.29). *Then, the DG frequencies* ω_i *synchronize to* ω_{ref}, *and the active power among DGs is shared based on their power ratings satisfying* (4.23).

Proof In the steady state, the left sides of (4.31) and (4.26) are equal to zero. Setting the left side of (4.26) equal to zero yields

$$\omega = \underline{\omega}_{\text{com}}. \tag{4.33}$$

Equation (4.33) shows that all the DG frequencies synchronize to the microgrid frequency in steady state. Therefore, according to Lemma 4.2,

$$L\omega = 0. \tag{4.34}$$

Setting the left side of (4.31) equal to zero, and considering (4.34) yields

$$LD_P P + B(\omega - \underline{\omega}_{\text{ref}}) = 0. \tag{4.35}$$

The commensurate form of (4.35) can be written as

$$\begin{bmatrix} \sum\limits_{j=1:N} a_{1j} & -a_{12} & \cdots & -a_{1N} \\ -a_{21} & \sum\limits_{j=1:N} a_{2j} & \cdots & -a_{2N} \\ \vdots & \vdots & \ddots & \vdots \\ -a_{N1} & -a_{N2} & \cdots & \sum\limits_{j=1:N} a_{Nj} \end{bmatrix} \begin{bmatrix} D_{P1}P_1 \\ D_{P2}P_2 \\ \vdots \\ D_{PN}P_N \end{bmatrix} + \begin{bmatrix} b_1(\omega_1 - \omega_{\text{ref}}) \\ 0 \\ \vdots \\ 0 \end{bmatrix} = 0, \tag{4.36}$$

that equivalently yields (4.37) and (4.38).

$$a_{12}(D_{P1}P_1 - D_{P2}P_2) + \cdots + a_{1N}(D_{P1}P_1 - D_{PN}P_N) + b_1(\omega_1 - \omega_{ref}) = 0, \tag{4.37}$$

$$(\bar{L} + \bar{B})\left(\begin{bmatrix} D_{P2}P_2 \\ D_{P3}P_3 \\ \vdots \\ D_{PN}P_N \end{bmatrix} - \begin{bmatrix} D_{P1}P_1 \\ D_{P1}P_1 \\ \vdots \\ D_{P1}P_1 \end{bmatrix} \right) = 0, \tag{4.38}$$

where

$$\bar{L} = \begin{bmatrix} \sum\limits_{j=1:N} a_{2j} & -a_{23} & \cdots & -a_{2N} \\ -a_{32} & \sum\limits_{j=1:N} a_{3j} & \cdots & -a_{3N} \\ \vdots & \vdots & \ddots & \vdots \\ -a_{N2} & -a_{N3} & \cdots & \sum\limits_{j=1:N} a_{Nj} \end{bmatrix}, \tag{4.39}$$

$$\bar{B} = \begin{bmatrix} -a_{21} & 0 & \cdots & 0 \\ 0 & -a_{31} & \cdots & 0 \\ \vdots & \vdots & \ddots & \vdots \\ 0 & 0 & \cdots & -a_{N1} \end{bmatrix}. \tag{4.40}$$

Equation (4.38) shows that the set $\{D_{P1}P_1, D_{P2}P_2, \ldots, D_{PN}P_N\}$ can be considered on a communication digraph with $D_{P1}P_1$ as the leader node. All nodes have access to the leader $D_{P1}P_1$ through the matrix $\bar{B}$ in (4.40). Since the original digraph Gr has a spanning tree with $D_{P1}P_1$ as the root node, at least one of the diagonal terms in $\bar{B}$ is nonzero. Therefore, exploiting Lemma 4.3 shows that all $D_{Pi}P_i$ synchronize to a common value in the steady state which satisfies (4.22), or, equivalently, (4.23). Additionally, according to (4.37), having all $D_{Pi}P_i$ synchronized to a common value shows that ω_1 synchronizes to ω_{ref}, and hence, according to (4.33), all DG frequencies synchronize to ω_{ref}. This completes the proof. □

The block diagram of the secondary frequency control based on the distributed cooperative control is shown in Fig. 4.3. As shown in this figure, the control input ω_i^* is written as

$$\omega_i^* = \int u_i \mathrm{d}t. \tag{4.41}$$

The coupling gain c_f has a direct impact on the convergence speed of the proposed frequency control. The proposed secondary frequency control can admit both time-invariant and time-variant communication networks. In the case of time-invariant communication networks, according to the results of the Lemma 4.4, the communication topology should be a graph containing a spanning tree in which the secondary control of each DG only requires information about that DG and its immediate neighbors in the communication graph. Therefore, the communication

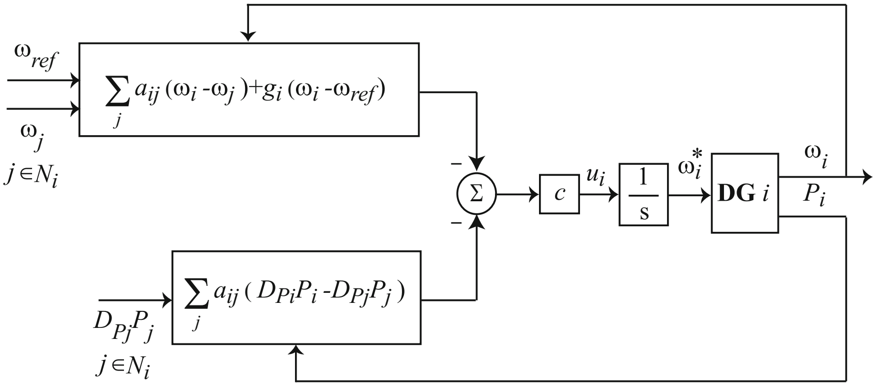

Fig. 4.3 The block diagram of the distributed secondary frequency control. © [2016] IEEE. Reprinted, with permission, from IEEE control systems magazine [20]

requirements for implementing the proposed control with a time-invariant communication network are rather mild.

In the case of time-variant communication structure, the communication network is piecewise constant (i.e., the adjacency matrix A_G changes intermittently at pre-specified time instants.). Therefore, the secondary frequency control is robust against data loss and communication link failures.

4.2.2 Case Studies

The effectiveness of the proposed secondary frequency control is verified by simulating an islanded microgrid in MATLAB. The reference value for the microgrid frequency $f_{\text{ref}} = \omega_{\text{ref}}/2\pi$ is set as 50 Hz. The coupling gain c_f is set to 400. Figure 4.4 illustrates the single-line diagram of the microgrid test system. This microgrid consists of four DGs. The lines between buses are modeled as series RL branches. The specifications of the DGs, lines, and loads are summarized in Table 4.1. It is assumed that DGs communicate with each other through the communication digraph depicted in Fig. 4.5. This communication topology is chosen based on the geographical location of DGs. The associated adjacency matrix of the digraph in Fig. 4.5 is

$$A_G = \begin{bmatrix} 0 & 0 & 0 & 0 \\ 1 & 0 & 0 & 0 \\ 0 & 1 & 0 & 0 \\ 1 & 0 & 0 & 0 \end{bmatrix}. \tag{4.42}$$

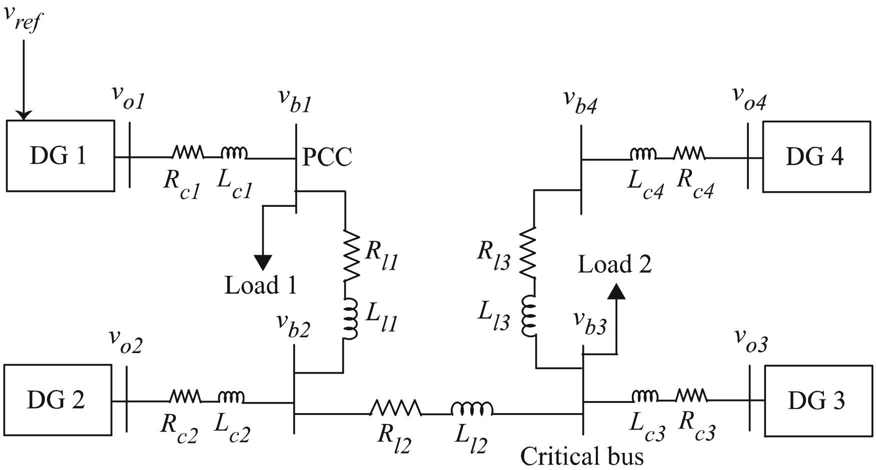

Fig. 4.4 Single-line diagram of the microgrid test system. © [2016] IEEE. Reprinted, with permission, from IEEE control systems magazine [20]

Table 4.1 Specifications of the microgrid test system

DGs	DG 1 & 2 (45 kVA rating)		DG 3 & 4 (34 kVA rating)			
	m_P	9.4×10^{-5}	m_P	12.5×10^{-5}		
	n_Q	1.3×10^{-3}	n_Q	1.5×10^{-3}		
	R_c	0.03 Ω	R_c	0.03 Ω		
	L_c	0.35 mH	L_c	0.35 mH		
	R_f	0.1 Ω	R_f	0.1 Ω		
	L_f	1.35 mH	L_f	1.35 mH		
	C_f	50 μF	C_f	50 μF		
	K_{PV}	0.1	K_{PV}	0.05		
	K_{IV}	420	K_{IV}	390		
	K_{PC}	15	K_{PC}	10.5		
	K_{IC}	20,000	K_{IC}	16,000		
Lines	Line 1		Line 2		Line 3	
	R_{l1}	0.23 Ω	R_{l2}	0.35 Ω	R_{l3}	0.23 Ω
	L_{l1}	318 μH	L_{l2}	1847 μH	L_{l3}	318 μH
Loads	Load 1		Load 2			
	P_{L1} (per phase)	12 kW	P_{L2} (per phase)	15.3 kW		
	Q_{L1} (per phase)	12 kVAr	Q_{L2} (per phase)	7.6 kVAr		

DG 1 is the only DG that is connected to the leader node with the pinning gain $b_1 = 1$.

It is assumed that the microgrid is islanded from the main grid at $t = 0$, and the secondary frequency control is applied at $t = 0.6$ s. Figure 4.6 shows frequencies and output powers of DGs before and after applying the secondary frequency control. As shown in Fig. 4.6a, once the primary control is applied, DG operating frequencies all go to a common value that is the operating frequency of microgrid. However, the secondary frequency control returns the operating frequency of microgrid to its nominal value after 0.3 s. Figure 4.6b shows that the all DG output powers satisfy (4.22) and (4.23), and are set according to the power rating of DGs.

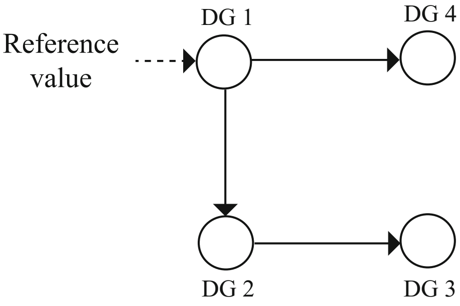

Fig. 4.5 Topology of the communication digraph. © [2016] IEEE. Reprinted, with permission, from IEEE control systems magazine [20]

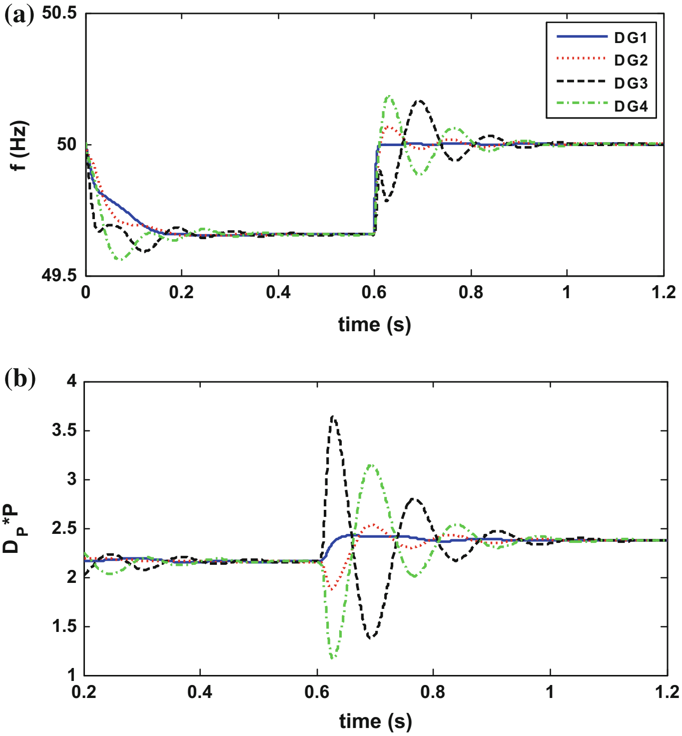

Fig. 4.6 The secondary frequency control with $c_f = 400$ and $f_{\text{ref}} = 50$ Hz: **a** DG frequencies and **b** DG active power ratios. © [2016] IEEE. Reprinted, with permission, from IEEE control systems magazine [20]

The coupling gain c_f has a direct impact on the synchronization speed of the secondary frequency control. To show this impact, the coupling gain is decreased from 400 to 40 in the following case study. Figure 4.7 shows the simulation results when the coupling gain c_f is set to 40. It is assumed that the microgrid is islanded from the main grid at $t = 0$, and the secondary frequency control is applied at $t = 0.6$ s. Compared with the simulation results in Fig. 4.7, smaller value of the coupling gain c_f decreases the frequency control synchronization speed.

To show the effectiveness of the proposed distributed frequency control, another round of simulations are performed using a time-varying communication network, shown in Fig. 4.8. The communication digraph in Fig. 4.8a models the communication network at the time interval [(0.6 + 0.15 k) s, (0.6 + 0.15 k) + 0.05 s], for $k = 0, 1, \ldots$ The communication digraph in Fig. 4.8b models the communication network at the time interval [(0.65 + 0.15 k) s, (0.65 + 0.15 k) + 0.05 s], for $k = 0, 1, \ldots$ The communication digraph in Fig. 4.8c models the communication network at the time interval [(0.7 + 0.15 k) s, (0.7 + 0.15 k) + 0.05 s], for $k = 0, 1, \ldots$ It is seen that over each 0.15 s period, the sequential completeness condition is satisfied.

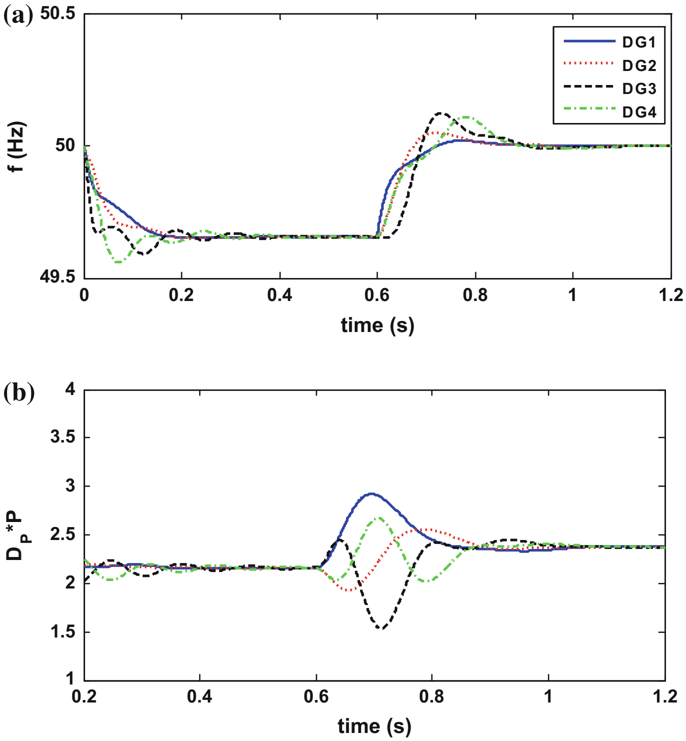

Fig. 4.7 The secondary frequency control with $c_f = 40$ and $f_{\mathrm{ref}} = 50$ Hz: **a** DG frequencies and **b** DG active power ratios. © [2016] IEEE. Reprinted, with permission, from IEEE control systems magazine [20]

As shown in Fig. 4.9a, once the primary control is applied, DG operating frequencies all go to a common value that is the operating frequency of microgrid. However, the secondary frequency control returns the operating frequency of microgrid to its nominal value. Figure 4.9b shows that the all DG output powers satisfy (4.22) and (4.23), and are set according to the power rating of DGs. These results verify the effectiveness of the proposed secondary frequency control when a time-varying communication network is used.

4.3 Distributed Secondary Voltage Control of AC Microgrids

The secondary voltage control restores the microgridoperating voltage to the nominal voltage subsequent to disturbances such as the islanding process. The dynamics of DGs in a microgrid are nonlinear and may be nonidentical. The

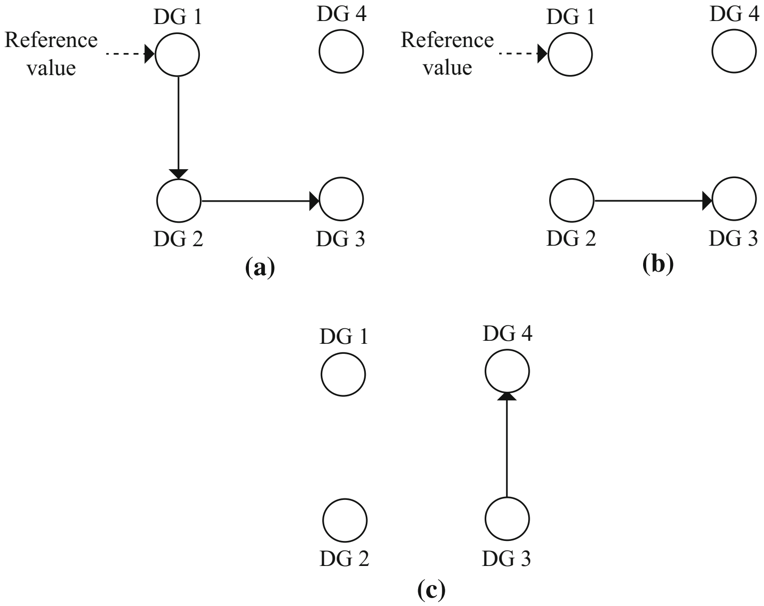

Fig. 4.8 Topologies of the time-varying communication network. © [2016] IEEE. Reprinted, with permission, from IEEE control systems magazine [20]

secondary voltage control resembles the tracking synchronization problem of a multi-agent system with nonlinear and nonidentical dynamics. Therefore, to design a distributed secondary voltage control, the tracking synchronization problem for a nonlinear and nonidentical multi-agent system must be solved [3]. The multi-agent cooperative techniques from Chap. 3 will be used here. Distributed cooperative control for multi-agent systems with nonlinear or nonidentical dynamics has been recently introduced in the literature [3]. In this chapter, a method known as input–output feedback linearization [16] is used to solve this problem. Input–output feedback linearization transforms the nonlinear and heterogeneous dynamics of DGs to linear dynamics. Thus, the secondary voltage control is transformed to a second-order multi-agent tracking synchronization problem. The Lyapunov technique is then adopted to derive fully distributed control protocols for each DG.

This section is organized as follows. First, the dynamical model of inverter-based DGs is presented. Then, input–output feedback linearization is adopted to design a secondary voltage control based on distributed cooperative control. Finally, the proposed secondary control is verified using a microgrid test system.

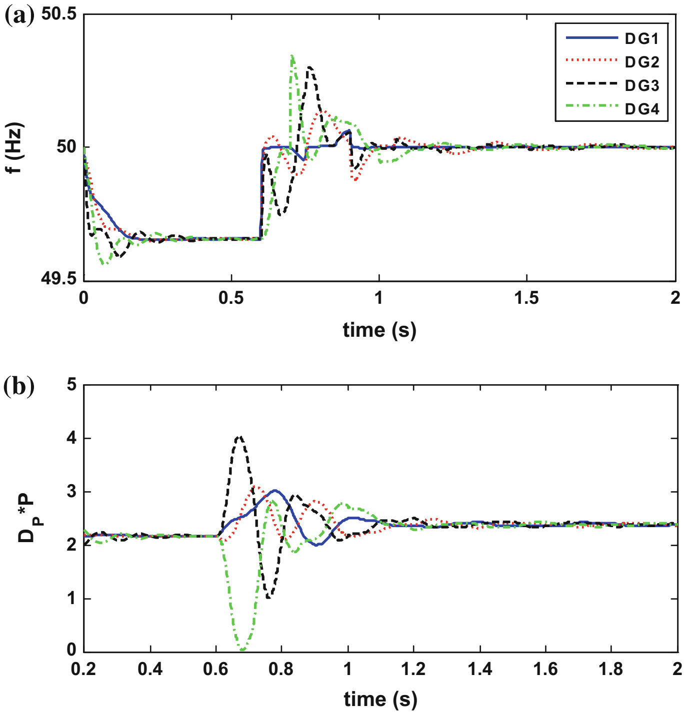

Fig. 4.9 The secondary frequency control with time-varying communication network: **a** DG frequencies and **b** DG active power ratios. © [2016] IEEE. Reprinted, with permission, from IEEE control systems magazine [20]

4.3.1 Secondary Voltage Control Objectives

The large-signal dynamical model can be written in a compact form as

$$\begin{cases} \dot{x}_i = \mathbf{f}_i(x_i) + \mathbf{k}_i(x_i)\mathbf{D}_i + \mathbf{g}_i(x_i)u_i, \\ y_i = h_i(x_i), \end{cases} \tag{4.43}$$

where the state vector is

$$x_i = [\,\delta_i \quad P_i \quad Q_i \quad \phi_{di} \quad \phi_{qi} \quad \gamma_{di} \quad \gamma_{qi} \quad i_{ldi} \quad i_{lqi} \quad v_{odi} \quad v_{oqi} \quad i_{odi} \quad i_{oqi}\,]^T. \tag{4.44}$$

The term $\mathbf{D}_i = [\omega_{\text{com}} \ v_{bdi} \ v_{bqi}]^T$ is considered as a known disturbance. The detailed expressions for $\mathbf{f}_i(x_i)$, $\mathbf{g}_i(x_i)$, and $\mathbf{k}_i(x_i)$ can be extracted from the dynamical model of VCVSIs explained in Chap. 2.

The secondary voltage control selects voltage reference, E_i^*, in the primary voltage control such that the terminal voltage amplitude of each DG approaches its reference value, i.e., $v_{o,\,\text{magi}} \to v_{\text{ref}}$. If v_{ref} is set to the nominal voltage of microgrid v_{nominal}, the output voltage magnitude of VCVSIs synchronizes to the nominal voltage of microgrid. However, v_{ref} can be chosen such that the voltage magnitude of a critical bus of microgrid synchronizes to v_{nominal}. In this case, v_{ref} is defined by

$$v_{\text{ref}} = k_{\text{pc}}(v_{\text{nominal}} - v_{\text{c,mag}}) + k_{\text{ic}} \int (v_{\text{nominal}} - v_{\text{c,mag}})\mathrm{d}t, \tag{4.45}$$

where $v_{c,\,\text{mag}}$ is the critical bus voltage magnitude and k_{pc} and k_{ic} are the control gains.

Since the amplitude of the DG output voltage is

$$v_{o,\,\text{magi}} = \sqrt{v_{odi}^2 + v_{oqi}^2} \tag{4.46}$$

and v_{oqi} is set to zero by the primary control as stated in Chap. 2, the synchronization of the voltage amplitude can be achieved by choosing the control input E_i^* such that $v_{odi} \to v_{\text{ref}}$. Therefore, for the secondary voltage control, the output and control input are set to $y_i = v_{odi}$ and $u_i = E_i^*$, respectively.

4.3.2 Distributed Secondary Voltage Control Using Feedback Linearization

A microgrid resembles a nonlinear and heterogeneous multi-agent system as discussed in Chap. 3, where each DG is an agent. The secondary control of microgrids is a tracking synchronization problem, where all DGs try to synchronize their terminal voltage amplitude to prespecified reference values. For this purpose, each DG only needs to communicate with its neighbors on the communication network. The required communication network can be modeled by a communication graph.

In this section, first, a preliminary on the graph theory is presented. Then, the secondary voltage control is implemented through input–output feedback linearization and distributed cooperative control of multi-agent systems. Finally, the communication network requirements for the proposed secondary voltage control are discussed.

Cooperative Secondary Voltage Control Based on Feedback Linearization and Tracking Synchronization. As previously discussed, the secondary voltage control chooses appropriate control inputs E_i^* in the primary voltage control to synchronize the voltage magnitudes of DGs $v_{o,\,\text{magi}}$ to the reference voltage v_{ref}. The synchronization of the voltage magnitudes of DGs $v_{o,\,\text{magi}}$ is equivalent to synchronizing the direct term of output voltages v_{odi}. Therefore, the secondary voltage control should choose u_i in (4.43) such that $y_i \to y_0, \forall i$, where $y_0 \equiv v_{\text{ref}}$.

Since the dynamics of DGs in a microgrid are nonlinear and might not be all identical, input–output feedback linearization can be used to facilitate the secondary voltage control design. In input–output feedback linearization, a direct relationship between the dynamics of the output y_i (or equivalently v_{odi}) and the control input u_i (or equivalently E_i^*) is generated by repetitively differentiating y_i with respect to time.

For the dynamics of the ith DG in (4.43), the direct relationship between the y_i and u_i is generated after the second derivative of the output y_i

$$\ddot{y}_i = L_{\mathbf{F}_i}^2 h_i + L_{\mathbf{g}_i} L_{\mathbf{F}_i} h_i u_i, \tag{4.47}$$

where

$$\mathbf{F}_i(x_i) = \mathbf{f}_i(x_i) + \mathbf{k}_i(x_i)\mathbf{D}_i. \tag{4.48}$$

$L_{\mathbf{F}_i} h_i$ is the Lie derivative [16] of h_i with respect to $\mathbf{F}_i$ and is defined by $L_{\mathbf{F}_i} h_i = \nabla h_i \mathbf{F}_i = \frac{\partial(h_i)}{\partial \mathbf{x}_i}\mathbf{F}_i . L_{\mathbf{F}_i}^2 h_i$ is defined by $L_{\mathbf{F}_i}^2 h_i = L_{\mathbf{F}_i}(L_{\mathbf{F}_i} h_i) = \frac{\partial(L_{\mathbf{F}_i} h_i)}{\partial \mathbf{x}_i}\mathbf{F}_i$.

An auxiliary control v_i is defined as

$$v_i = L_{\mathbf{F}_i}^2 h_i + L_{\mathbf{g}_i} L_{\mathbf{F}_i} h_i u_i. \tag{4.49}$$

Equations (4.47) and (4.49) result in the second-order linear system

$$\ddot{y}_i = v_i, \ \forall i. \tag{4.50}$$

By choosing appropriate v_i, the synchronization for y_i is provided. The control input u_i is implemented by v_i as

$$u_i = (L_{\mathbf{g}_i} L_{\mathbf{F}_i} h_i)^{-1}(-L_{\mathbf{F}_i}^2 h_i + v_i). \tag{4.51}$$

In the following, the procedure for designing appropriate v_i is elaborated. First, Eq. (4.50) and the first derivative of y_i are written as

$$\begin{cases} \dot{y}_i \equiv y_{i,1}, \\ \dot{y}_{i,1} = v_i, \end{cases} \forall i. \tag{4.52}$$

or equivalently

$$\dot{\mathbf{y}}_i = \mathbf{A}\mathbf{y}_i + \mathbf{B}v_i, \ \forall i \tag{4.53}$$

where $\mathbf{y}_i = [y_i \quad y_{i,1}]^T$, $\mathbf{B} = [0 \quad 1]^T$, and $\mathbf{A} = \begin{bmatrix} 0 & 1 \\ 0 & 0 \end{bmatrix}$.

Using input–output feedback linearization, the nonlinear dynamics of each DG in (4.43) are transformed to (4.53) and a set of internal dynamics. The commensurate reformulated dynamics of the reference generator can be expressed as

$$\dot{\mathbf{y}}_0 = \mathbf{A}\mathbf{y}_0, \tag{4.54}$$

where $\mathbf{y}_0 = \begin{bmatrix} y_0 & \dot{y}_0 \end{bmatrix}^T$. It should be noted that since $y_0 = v_{\text{ref}}$ is constant, $\dot{y}_0 = 0$.

It is assumed that DGs can communicate with each other through a communication network described by the digraph *Gr*. Based on the digraph *Gr*, the *i*th DG may need to transmit $\mathbf{y}_i$ in (4.53) through the communication network. It is assumed that only one DG has the access to the reference $\mathbf{y}_0$ in (4.54) by a weight factor known as the pinning gain b_i. The secondary voltage control problem is to find a distributed v_i in (4.51) such that $\mathbf{y}_i \longrightarrow \mathbf{y}_0, \forall i$. To solve this problem, the cooperative team objectives are expressed in terms of the local neighborhood tracking error

$$\mathbf{e}_i = \sum_{j \in N_i} a_{ij}(\mathbf{y}_i - \mathbf{y}_j) + \ b_i(\mathbf{y}_i - \mathbf{y}_0), \tag{4.55}$$

where a_{ij} denotes the elements of the communication digraph adjacency matrix. The pinning gain b_i is nonzero for one DG.

For a microgrid including *N* DGs, the global error vector for graph *Gr* is written from (4.55) as

$$\mathbf{e} = ((L + B) \otimes I_2)(\mathbf{Y} - \mathbf{Y}_0) \equiv ((L + B) \otimes I_2)\boldsymbol{\delta}, \tag{4.56}$$

where $\mathbf{Y} = [\mathbf{y}_1^T \mathbf{y}_2^T \ldots \mathbf{y}_N^T]^T$, $\mathbf{e} = [\mathbf{e}_1^T \mathbf{e}_2^T \ldots \mathbf{e}_N^T]^T$, $\mathbf{Y}_0 = \mathbf{1}_N \mathbf{y}_0$ ($\mathbf{1}_N$ is the vector of ones with the length of N.), $B = \text{diag}\{b_\text{i}\}$, I_2 is the identity matrix with two rows and two columns, and $\boldsymbol{\delta}$ is the global disagreement vector. The Kronecker product is shown as $\otimes$ [7]. $\dot{\mathbf{Y}}$ can be written as

$$\dot{\mathbf{Y}} = (I_N \otimes \mathbf{A})\mathbf{Y} + (I_N \otimes \mathbf{B})\mathbf{v}, \tag{4.57}$$

where $\mathbf{v} = [v_1 v_2 \ \ldots \ v_N]^T$ is the global auxiliary control vector. $\dot{\mathbf{Y}}_0$ can be written as

$$\dot{\mathbf{Y}}_0 = (I_N \otimes \mathbf{A})\mathbf{Y}_0. \tag{4.58}$$

The following definitions and lemmas are required for designing the auxiliary controls v_i.

Definition 4.3 [9]. (**A**, **B**) are stabilizable if there exists a matrix S such that all eigenvalues of **A**-**B**S have a strictly negative real part.

Definition 4.4 [12]. A matrix is Hurwitz if all of its eigenvalues have a strictly negative real part.

Definition 4.5 [12]. A symmetric matrix P is positive definite if $x^T P x$ is positive for all nonzero column vector x, and $x^T P x$ is zero only for $x = 0$.

Lemma 4.5 [20]. *Let* ($\mathbf{A}$, $\mathbf{B}$) *be stabilizable. Let the digraph Gr have a spanning tree and* $b_i \neq 0$ *for one DG placed on a root node of the digraph Gr . Let* λ_i ($i \in \{1, 2, \ldots, N\}$) *be the eigenvalues of* $L + B$*. The matrix*

$$\mathbf{H} = I_N \otimes \mathbf{A} - c(L+B) \otimes \mathbf{B}K \tag{4.59}$$

with $c \in R$ *and* $K \in R^{1\times2}$ *is Hurwitz if and only if all the matrices* $\mathbf{A} - c\lambda_i\mathbf{B}K$, $\forall i \in \{1, 2, \ldots, N\}$ *are Hurwitz.*

Lemma 4.6 [20]. *Let* ($\mathbf{A}$, $\mathbf{B}$) *be stabilizable and matrices* $Q = Q^T$ *and* $R = R^T$ *be positive definite. Let feedback gain K be chosen as*

$$K = R^{-1}\mathbf{B}^T P_1, \tag{4.60}$$

where P_1 *is the unique positive-definite solution of the control algebraic Riccati equation* (*ARE*)

$$\mathbf{A}^T P_1 + P_1\mathbf{A} + Q - P_1\mathbf{B}R^{-1}\mathbf{B}^T P_1 = 0. \tag{4.61}$$

Then, all the matrices $\mathbf{A}-c\lambda_i\mathbf{B}K$, $\forall i \in \{1, 2,\ldots, N\}$ *are Hurwitz if* $c \geq \frac{1}{2\lambda_{\min}}$, *where* $\lambda_{\min} = \min_{i\in\mathcal{N}} \mathrm{Re}(\lambda_i)$ ($\mathrm{Re}(\lambda_i)$ *denotes the real part of* λ_i*.*

Lemma 4.7 [4]. *Let the digraph Gr have a spanning tree and* $b_i \neq 0$ *for one DG placed on a root node of the digraph Gr. It is assumed that the internal dynamics of each DG are asymptotically stable. Let the auxiliary control* v_i *in* (4.51) *be*

$$v_i = -cK\mathbf{e}_i, \tag{4.62}$$

where $c \in R$ *is the coupling gain, and* $K \in R^{1\times2}$ *is the feedback control vector. Then, all* $\mathbf{y}_i$ *in* (4.53) *synchronize to* $\mathbf{y}_0$ *in* (4.54), *and hence, the direct term of DG output voltages* v_{odi} *synchronizes to* v_{ref}, *if K is chosen as in* (4.60) *and*

$$c \geq \frac{1}{2\lambda_{\min}}, \tag{4.63}$$

where $\lambda_{\min} = \min_{i\in\mathcal{N}} \mathrm{Re}(\lambda_i)$.

Proof Consider the Lyapunov function candidate

$$V = \frac{1}{2}\boldsymbol{\delta}^T P_2 \boldsymbol{\delta}, \quad P_2 = P_2^T,\ P_2 > 0, \tag{4.64}$$

where $\boldsymbol{\delta}$ is the global disagreement vector in (4.56). Then,

$$\dot{V} = \boldsymbol{\delta}^T P_2 \dot{\delta} = \boldsymbol{\delta}^T P_2\left(\dot{\mathbf{Y}} - \dot{\mathbf{Y}}_0\right) = \boldsymbol{\delta}^T P_2((I_N \otimes \mathbf{A})\boldsymbol{\delta} + (I_N \otimes \mathbf{B})\mathbf{v}). \tag{4.65}$$

The global auxiliary control $\mathbf{v}$ can be written as

$$\mathbf{v} = -c(I_N \otimes K)((L+B) \otimes I_2)\boldsymbol{\delta}. \tag{4.66}$$

Placing (4.66) into (4.65) yields

$$\dot{V} = \boldsymbol{\delta}^T P_2 (I_N \otimes \mathbf{A} - c(L+B) \otimes \mathbf{B}K)\boldsymbol{\delta} \equiv \boldsymbol{\delta}^T P_2 \mathbf{H}\delta. \tag{4.67}$$

From Lemmas 4.5 and 4.6, $\mathbf{H}$ is Hurwitz. Therefore, given any positive real number β, the positive-definite matrix P_2 can be chosen such that the following Lyapunov equation holds,

$$P_2\mathbf{H} + \mathbf{H}^T P_2 = -\beta I_{2N}, \tag{4.68}$$

Placing (4.68) in (4.67) yields

$$\dot{V} = \boldsymbol{\delta}^T P_2 \mathbf{H}\delta = \frac{1}{2}\boldsymbol{\delta}^T (P_2\mathbf{H} + \mathbf{H}^T P_2)\boldsymbol{\delta} = -\frac{\beta}{2}\boldsymbol{\delta}^T I_{2N}\boldsymbol{\delta}. \tag{4.69}$$

Equation (4.69) shows that $\dot{V} \leq 0$. Therefore, the global disagreement vector $\boldsymbol{\delta}$, (4.50), and (4.62) are asymptotically stable and all $\mathbf{y}_i$ in (4.53) synchronize to $\mathbf{y}_0$ in (4.54). Hence, the direct term of DG output voltages v_{odi} synchronizes to v_{ref}. If the internal dynamics are asymptotically stable, then they are all bounded. This completes the proof. □

The block diagram of secondary voltage control based on distributed cooperative control is shown in Fig. 4.10. As seen, the control input E_i^* is implemented using (4.51). Choosing the coupling gain c and the feedback control vector K based on (4.60) and (4.63) ensures the asymptotic stability of the controller. Moreover, these controller parameters can adjust the response speed of the secondary voltage control.

The Required Sparse Communication Topology for Secondary Control. The proposed secondary voltage control must be supported by a local communication network. The communication network can be implemented by the TCP/IP communication protocol with optical fiber links [18]. For the microgrids with a small geographical span, the communication network can also be implemented by CAN bus, PROFIBUS, and SERCOS communication protocols [2]. The settling time of the secondary control can be up to one minute [14]. Therefore, the communication network operates much faster than the secondary control. The sampling time of the secondary control can be chosen much larger than the sampling time of the communication network. It should be noted that communication links contain an intrinsic delay. Since the timescale of the secondary control is large enough, the communication link delays can be safely assumed to zero [4]. The proposed secondary voltage control can admit both time-invariant and time-variant communication networks.

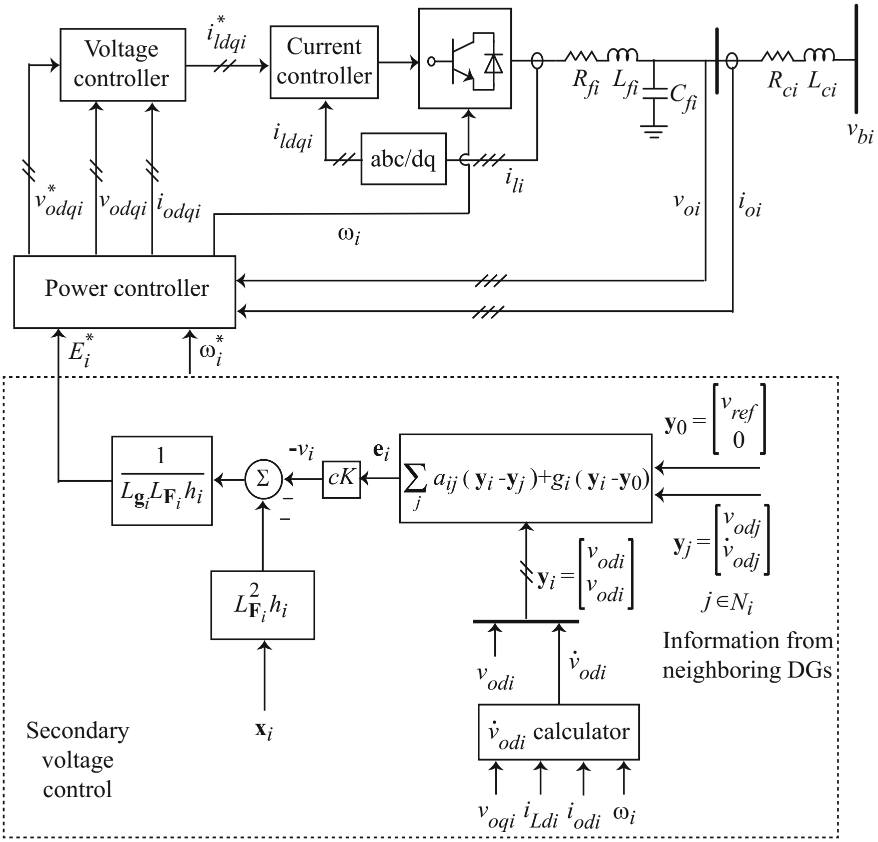

Fig. 4.10 The block diagram of the proposed secondary voltage control. © [2016] IEEE. Reprinted, with permission, from IEEE transactions on power systems [4]

In the case of time-invariant communication networks, the adjacency matrix A_G is fixed. According to the results of the Lemma 4.7, the communication topology should be a graph containing a spanning tree in which the secondary control of each DG only requires information about that DG and its immediate neighbors in the communication graph. Therefore, the communication requirements for implementing the proposed control with a time-invariant communication network are rather mild. However, the implemented secondary control may not be robust against communication link failures or data loss. Given the physical structure of the microgrid, it is not difficult to select a graph with a spanning tree that connects all the DGs in an optimal fashion. Such optimal connecting graphs can be designed using operations research or assignment problem solutions [1, 8]. The optimization criteria can include minimal lengths of the communication links, maximal use of existing communication links, and minimal number of links.

Alternatively, time-variant communication structure can be exploited to increase the secondary control reliability. In this communication structure, each DG can send its own information to the neighboring DGs intermittently. The communication network is piecewise constant (i.e., the adjacency matrix A_G changes intermittently at prespecified time instants.). Therefore, the secondary control is robust against data loss and communication link failures. According to [7], a time-variant communication network can provide the synchronization if the sequential completeness condition is satisfied. The sequential completeness condition means that, with the infinite sequence of finite intervals, the resulting graph over each finite interval must contain a spanning tree.

4.3.3 Case Studies

The microgrid shown in Fig. 4.4 is used to verify the effectiveness of the proposed secondary control. The specifications of the DGs, lines, and loads are summarized in Table 4.1. The simulation results are extracted by modeling the dynamical equations of microgrid in MATLAB.

It is assumed that DGs communicate with each other through the communication digraph depicted in Fig. 4.5. This communication topology is chosen based on the geographical location of DGs. DG 1 is the only DG connected to the leader node with the pinning gain of $b_1 = 1$.

In the following, first, the effectiveness of the proposed secondary voltage control is shown for three different reference voltage values. Then, the effects of the algebraic Riccati equation) parameters on the transient response of the controller are studied. Finally, the effectiveness of the proposed voltage control is verified when a time-varying communication network is used.

Simulation Results for Different Reference Voltage Values. In this section, the coupling gain in (4.62) is $c = 4$ which satisfies (4.63). The solution of the algebraic Riccati equation in (4.61) is used to calculate the feedback control vector K in (4.62). The algebraic Riccati equation parameters are chosen as $Q = \begin{bmatrix} 50000 & 0 \\ 0 & 1 \end{bmatrix}$ and $R = 0.01$. The resulting feedback control vector is $K = [2236\ 67.6]$. It is assumed that the microgrid is islanded from the main grid at $t = 0$, and the secondary control is applied at $t = 0.6$ s. It should be noted that the secondary control level always exists as a supervisory control level and takes actions in the event of disturbances. However, to highlight the effectiveness of the proposed secondary control, it is assumed that the secondary control is applied with a delay. Figure 4.11a–c show the simulation results

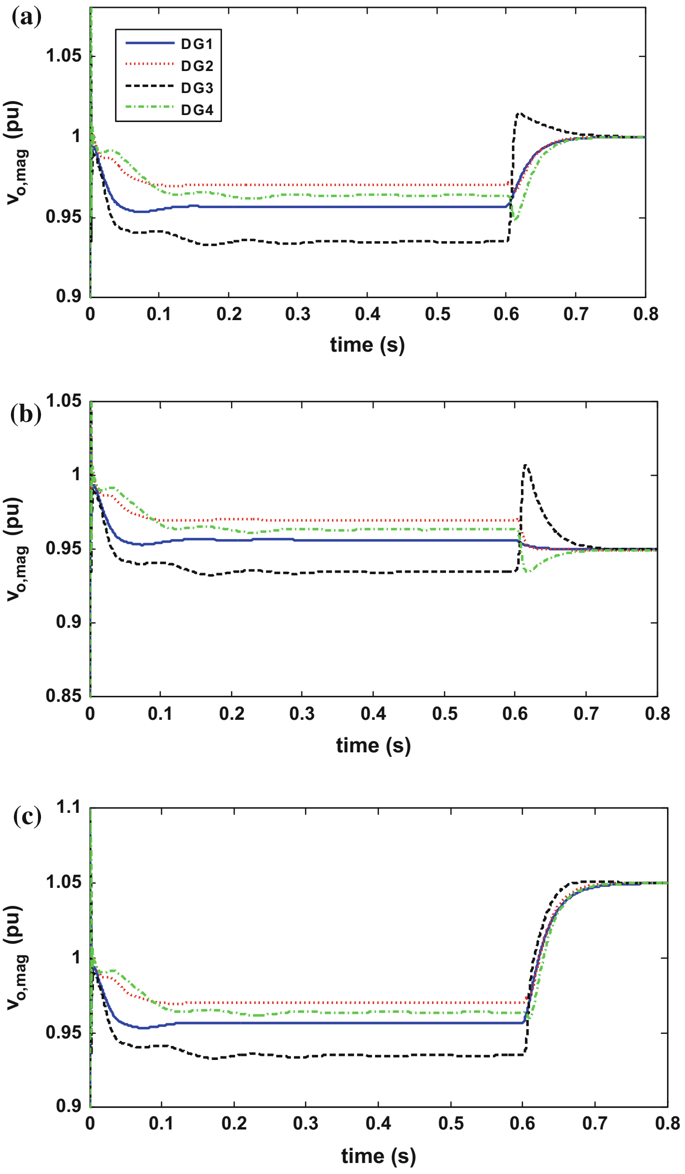

Fig. 4.11 DG output voltage magnitudes for **a** $v_{\mathrm{ref}} = 1$ pu, **b** $v_{\mathrm{ref}} = 0.95$ pu, and **c** $v_{\mathrm{ref}} = 1.05$ pu. © [2016] IEEE. Reprinted, with permission, from IEEE transactions on power systems [4]

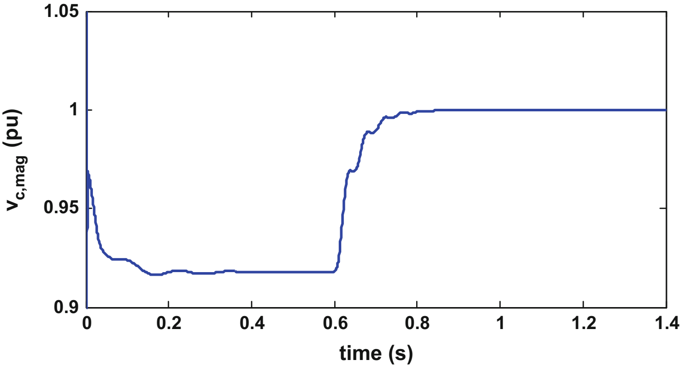

Fig. 4.12 Critical bus voltage magnitude. © [2016] IEEE. Reprinted, with permission, from IEEE transactions on power systems [4]

when the reference voltage value is set to 1, 0.95, and 1.05 pu, respectively. As seen, while the primary control keeps the voltage amplitudes stable, the secondary control returns all terminal voltage amplitudes to the prespecified reference values in 0.2 s.

The Secondary voltage control secondary voltage control can also be defined to control the voltage magnitude of the critical bus shown in Fig. 4.12. In this case, v_{ref} is chosen according to (4.45), where $v_{c,\ \mathrm{mag}}$ in (4.45) denotes the voltage magnitude of the critical bus. v_{nominal} in (4.45) is set to 1 pu. k_{pc} and k_{ic} in (4.45) are set to 4 and 100, respectively. As shown in Fig. 4.12, the secondary control is applied at t = 0.6 s and returns the voltage magnitude of critical bus to v_{nominal} in less than 0.3 s.

The Effect of Algebraic Riccati Equation (ARE) Parameters on the Transient Response. To show the effect of the ARE parameters on the response speed of the secondary voltage control, two different cases are considered. The reference value for the terminal voltage of DGs is set to 1 pu. In the first case, ARE parameters are set as $Q = \begin{bmatrix} 1000 & 0 \\ 0 & 1 \end{bmatrix}$ and $R = 0.01$. Compared with the case studied in Fig. 4.11a, the element in the first row and column of matrix Q, which directly affects the control of v_{odi}, is smaller. Figure 4.13a shows the DG output voltage magnitudes before and after applying the secondary control. As seen, the terminal voltage amplitudes synchronize to 1 pu after 0.3 s. Therefore, with a smaller Q, the secondary voltage control is slower than the case studied in Fig. 4.5a.

In the second case, the ARE parameters are set as $Q = \begin{bmatrix} 50000 & 0 \\ 0 & 1 \end{bmatrix}$ and $R = 5$. Compared with the case studied in Fig. 4.11a, R is larger. Figure 4.13b shows the

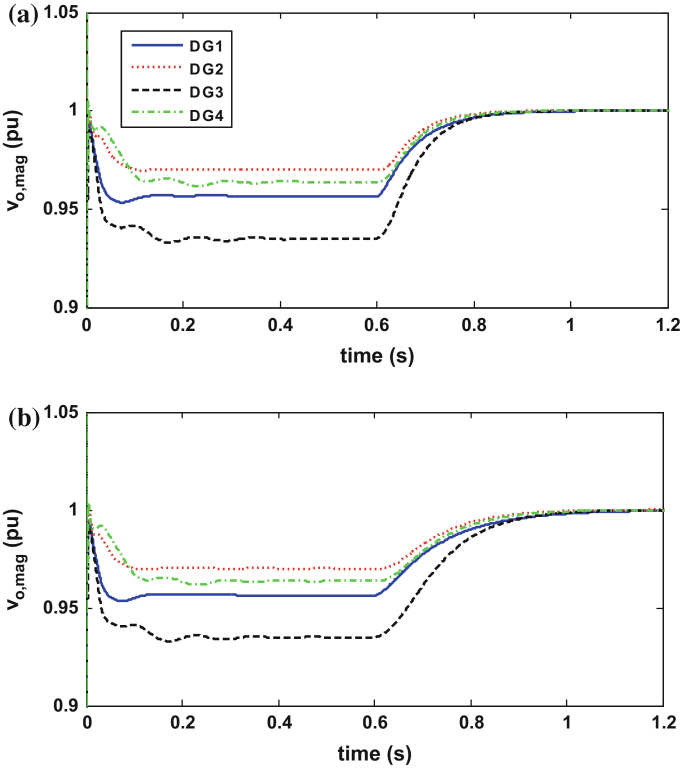

Fig. 4.13 DG output voltage magnitudes with the following control parameters: **a** $Q = \begin{bmatrix} 1000 & 0 \\ 0 & 1 \end{bmatrix}$ and $R = 0.01$, **b** $Q = \begin{bmatrix} 50000 & 0 \\ 0 & 1 \end{bmatrix}$ and $R = 5$. © [2016] IEEE. Reprinted, with permission, from IEEE transactions on power systems [4]

DG output voltage magnitudes before and after applying the secondary control. As seen, the terminal voltage amplitudes converge to 1 pu after 0.5 s. Therefore, with a larger R, the secondary voltage control is slower than the case studied in Fig. 4.11a. **The Effect of Time-varying Communication Networks on the Performance of the Distributed Secondary Voltage Control**. In this section, it is assumed that the microgrid is islanded from the main grid at $t = 0$, and the voltage control is applied at $t = 0.6$ s. However, the distributed voltage control is associated with time-varying communication networks. The Reference voltage reference voltage is set to $v_{\text{ref}} = 1$ pu. Figure 4.8 shows the three communication network structures that are used in simulation. Each structure is adopted at a specific time interval. The communication digraph in Fig. 4.8a models the communication network at the time

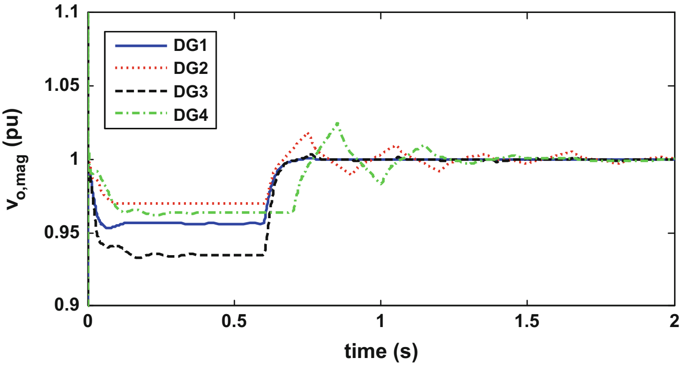

Fig. 4.14 DG output voltage magnitudes with time-varying communication network. © [2016] IEEE. Reprinted, with permission, from IEEE transactions on power systems [4]

interval [(0.6 + 0.15 *k*) s, (0.6 + 0.15 *k*) + 0.05 s], for $k = 0, 1, \ldots$ The communication digraph in Fig. 4.8b models the communication network at the time interval [(0.65 + 0.15 *k*) s, (0.65 + 0.15 *k*) + 0.05 s], for $k = 0, 1, \ldots$ The communication digraph in Fig. 4.8c models the communication network at the time interval [(0.7 + 0.15 *k*) s, (0.7 + 0.15 *k*) + 0.05 s], for $k = 0, 1, \ldots$ It is seen that over each 0.15 s period, the sequential completeness condition is satisfied. As shown in Fig. 4.14, while the primary control keeps the voltage amplitudes stable, the secondary control returns all terminal voltage amplitudes to v_{ref}. This simulation result verifies the effectiveness of the proposed voltage control in the case of time-varying communication networks and communication link failures.

4.4 Distributed Secondary Voltage and Reactive Power Control of AC Microgrids

As discussed in previous section, the distributed voltage control chooses appropriate control inputs V_{ni} to synchronize the voltage magnitudes of VCVSIs $v_{o,\ \mathrm{magi}}$ to the reference voltage v_{ref}. As an additional control objective, it can also be used to allocate the output reactive power of VCVSIs based on their reactive power ratings. According to the VCVSI nonlinear model described in Chap. 2, synchronizing the voltage magnitudes, $v_{o,\ \mathrm{magi}}$, is the same as synchronizing the direct term of output voltages v_{odi}.

Differentiating the voltage droop characteristic yields

$$\dot{V}_{ni} = \dot{v}_{odi} + n_{Qi}\dot{Q}_i = v_{vi}, \tag{4.70}$$

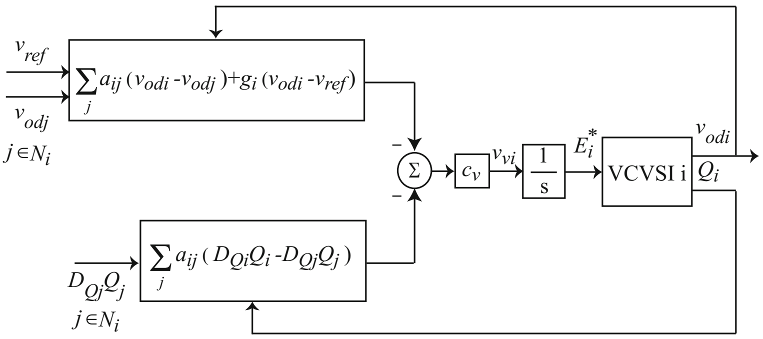

Fig. 4.15 The block diagram of the distributed voltage control in layer 1. © [2016] IEEE. Reprinted, with permission, from IEEE transactions on industrial informatics [21]

where v_{vi} is the auxiliary control input. Equation (4.70) computes the control input V_{ni} from v_{vi} as

$$V_{ni} = \int v_{vi} \mathrm{d}t. \tag{4.71}$$

According to (4.70), the voltage control of a microgrid including N_V VCVSIs can be transformed to a synchronization problem for a linear and first-order multi-agent system

$$\begin{cases} \dot{v}_{od1} + n_{Q1}\dot{Q}_1 = v_{v1} \\ \dot{v}_{od2} + n_{Q2}\dot{Q}_2 = v_{v2} \\ \vdots \\ \dot{v}_{odN_V} + n_{QN_V}\dot{Q}_{N_V} = v_{vN_V} \end{cases}. \tag{4.72}$$

To achieve synchronization, it is assumed that VCVSIs can communicate with each other through the prescribed communication digraph Gr. The auxiliary control v_{vi} is chosen based on each VCVSI's voltage magnitude and reactive power information, and the voltage magnitude and reactive power information of its neighbors on the communication digraph as

$$\begin{aligned} v_{vi} = & -c_{vi}\left(\sum_{j \in N_i} a_{ij}(v_{odi} - v_{odj}\right) + g_i(v_{odi} - v_{\mathrm{ref}}) \\ & + \sum_{j \in N_i} a_{ij}(n_{Qi}Q_i - n_{Qj}Q_j)), \end{aligned} \tag{4.73}$$

where c_{vi} is the control gains. It is assumed that the pinning gain $g_i \geq 0$ is nonzero for, at least, one VCVSI that has the reference voltage, v_{ref}, information. A procedure similar to that used for the frequency control of VCVSIs can be used to show the effectiveness of the auxiliary control v_{vi} in (4.73). The block diagram of the distributed voltage control is shown in Fig. 4.15.

References

1. Ahuja RK, Magnanti TL, Orlin JB (1993) Network flows: theory, algorithms, and applications. Prentice Hall, Englewood Cliffs
2. Bassi E, Benzi F, Lusetti L, Buja GS (1995) Communication protocols for electrical drives. In: Proceedings of the 21st international conference on industrial electronics (IECON), pp 706–711
3. Bidram A, Davoudi A (2012) Hierarchical structure of microgrids control system. IEEE Trans Smart Grid 3:1963–1976
4. Bidram A, Davoudi A, Lewis FL, Guerrero JM (2013) Distributed cooperative secondary control of microgrids using feedback linearization. IEEE Trans Power Syst 28:3462–3470
5. Bidram A, Davoudi A, Lewis FL, Qu Z (2013) Secondary control of microgrids based on distributed cooperative control of multi-agent systems. IET Gener Transm Distrib 7:822–831
6. Bidram A, Lewis FL, Davoudi A (2014) Synchronization of nonlinear heterogeneous cooperative systems using input–output feedback linearization. Automatica 50:2578–2585
7. Brewer JW (1978) Kronecker products and matrix calculus in system theory. IEEE Trans Circuits Syst 25:772–781
8. Burkard R, Dell'Amico M, Martello S (2009) Assignment problems. SIAM, Philadelphia
9. Fax J, Murray R (2004) Information flow and cooperative control of vehicle formations. IEEE Trans Autom Control 49:1465–1476
10. Guerrero JM, Vásquez JC, Matas J, Castilla M, Vicuña LGD, Castilla M (2011) Hierarchical control of droop-controlled AC and DC microgrids—a general approach toward standardization. IEEE Trans Ind Electron 58:158–172
11. Hui Q, Haddad W (2008) Distributed nonlinear control algorithms for network consensus. Automatica 42:2375–2381
12. Jadbabaie A, Lin J, Morse AS (2003) Coordination of groups of mobile autonomous agents using nearest neighbor rules. IEEE Trans Autom Control 48:988–1001
13. Mehrizi-Sani A, Iravani R (2010) Potential-function based control of a microgrid in islanded and grid-connected models. IEEE Trans Power Syst 25:1883–1891
14. Qu Z (2009) Cooperative control of dynamical systems: applications to autonomous vehicles. Springer, New York
15. Slotine JJE, Li W (2009) Applied nonlinear control. Prentice-Hall, New Jersey
16. Yang Q, Barria JA, Green TC (2011) Communication infrastructures for distributed control of power distribution networks. IEEE Trans Industr Inf 7:316–327
17. Zhang H, Lewis FL (2012) Adaptive cooperative tracking control of higher-order nonlinear systems with unknown dynamics. Automatica 48:1432–1439

18. Zhang H, Lewis FL, Das A (2011) Optimal design for synchronization of cooperative systems: State feedback, observer, and output feedback. IEEE Trans Autom Control 56:1948–1952
19. Bidram A, Davoudi A, Lewis FL, Ge SS (2014) Distributed adaptive voltage control of inverter-based microgrids. IEEE Trans Energy Convers 29:862–872
20. Bidram A, Lewis F, Davoudi A (2014) Distributed control systems for small-scale power networks: using multiagent cooperative control theory. IEEE Control Systems 34(6):56–77.
21. Bidram A, Davoudi A, Lewis F (2014) A multi-objective distributed control framework for islanded microgrids. IEEE Trans Ind Inform 10:1785–1798.

Chapter 5
Multi-objective and Adaptive Distributed Control of AC Microgrids

This chapter discusses the advanced methods for distributed control of AC microgrids. First, a two-layer control framework that implements the secondary control for an islanded microgrid containing both VCVSIs and CCVSIs is discussed. The first control layer deals with the voltage and frequency control of VCVSIs. The second control layer objectives are to control the active and reactive powers of CCVSIs. Each control layer is implemented through the distributed control of multi-agent systems. Then, a distributed and adaptive secondary voltage control method is discussed. The proposed controller compensates for the nonlinear and uncertain dynamics of DGs and, hence, obviates the control design challenges caused by the nonlinear dynamics of DGs. The controller is fully independent of the DG parameters. Therefore, the controller can be deployed on any DG regardless of the DG parameters and the connector specifications, and its performance does not deteriorate by the change in DG parameters (e.g., due to aging and thermal effects). The discussed controller appropriately responds to the changes in the system operating condition, without any manual intervention, and adjusts its control parameters in real time.

5.1 Multi-objective and Two-Layer Control Framework for AC Microgrids

As discussed in Chap. 2, the control structure of a VSI may vary based on the control objectives such as voltage and frequency, or active and reactive powers. In Chap. 4, distributed control structures for islanded microgrids with voltage-controlled voltage source inverters (VCVSIs) were proposed. VCVSIs have internal voltage and current controller loops that facilitate the voltage control and frequency control of DG. However, in some DGs, the sole active and reactive power controls may be of interest. This requirement can be satisfied through the current-controlled

A. Bidram et al., *Cooperative Synchronization in Distributed Microgrid Control*, Advances in Industrial Control, DOI 10.1007/978-3-319-50808-5_5

voltage source inverters (CCVSIs). CCVSIs possess an internal current controller that controls the direct and quadrature components of the VSI output current which in turn facilitates the active and reactive power controls of DG. Microturbines and fuel cells are dispatchable power sources, and their associated voltage source inverter can operate as a CCVSI to adjust their generated power by the microgrid operator. Solar panels and wind turbine generators are intermittent power sources. The uncertainty and intermittency in the generated power are a big hassle to exploit wind and solar power sources as dispatchable DGs. Energy storage systems (e.g., batteries) can be exploited to compensate for the intermittency in the generated power of wind and solar power sources. Doing so, solar panels and wind turbine generators can also be exploited as dispatchable power sources.

A microgrid is able to operate in both grid-connected and islanded modes. In the grid-connected mode, the main grid dictates the microgrid voltage and frequency. In this mode, the DG control objectives are defined as active and reactive power, and hence, they can be exploited as CCVSIs. The microgrid can switch to the islanded mode due to the preplanned scheduling or unplanned disturbances. Subsequent to the islanding process, microgrid loses the voltage and frequency support by the main gird as well as the active and reactive power balance between the total power generation and consumption. Therefore, some DGs are required to switch to the VCVSI structure to provide a fast voltage and frequency support and compensate for the mismatch between the power generation and consumption. In this chapter, it is assumed that some DGs remain in the CCVSI mode subsequent to islanding process [1].

The VCVSIs are equipped with the primary control to maintain the voltage and frequency stability of the microgrid. As discussed in Chap. 2, primary control avoids voltage and frequency instability by keeping these values in prespecified ranges. Coordinated control of the primary local controllers can be achieved by the active and reactive power droop techniques as

$$\begin{cases} \omega_i = \omega_i^* - D_{Pi} P_i, \\ v_{o,\mathrm{magi}}^* = E_i^* - D_{Qi} Q_i. \end{cases} \tag{5.1}$$

$v_{o,\mathrm{magi}}^*$ is the reference value for the output voltage magnitude that is provided for the internal voltage control loop of VCVSI. ω_i is the angular frequency of the VCVSI dictated by the primary control. P_i and Q_i are the measured active power and reactive power at the DG's terminal. D_{Pi} and D_{Qi} are the droop coefficients. E_i^* and ω_i^* are the primary control references. The droop coefficients are selected based on the active and reactive power ratings of each VCVSI.

The primary control provides a fast voltage and frequency support for the microgrid; however, it might not return the microgrid to the normal operating conditions, and an additional control is required to restore the voltage and frequency. This functionality is provided by the secondary control, which compensates for the voltage and frequency deviations caused by the primary control. The secondary control operates with a longer time frame than primary control and adjusts the control inputs of VCVSIs and CCVSIs to restore the voltage and frequency of microgrid to their nominal values.

In this chapter, a two-layer control framework is presented to implement the secondary control for an islanded microgrid with both VCVSIs and CCVSIs. The first layer, namely *control layer 1*, controls the VCVSIs. The second layer, namely *control layer 2*, controls CCVSIs. The distributed control of multi-agent systems is used to implement each control layer. Each control layer is associated with a limited and sparse communication network. Figure 5.1 shows the two-layer microgrid control framework along with the communication networks. The communication topology for each layer should be a graph containing a spanning tree in which the implemented controller at each DG only requires information about that DG and its direct neighbors in the communication graph. Given the physical structure of the microgrid, it is not difficult to select a graph with a spanning tree that connects all DGs in an optimal fashion. Such optimal connecting graphs can be designed using operations research or assignment problem solutions. The optimization criteria can include minimal lengths of the communication links, maximal use of existing communication links, and minimal number of links.

The *control layer 1* provides a framework to control VCVSIs in a distributed manner. This control layer has two main control parts, namely frequency control and voltage control. Frequency control chooses ω_i^* such that the angular frequency of each VCVSI synchronizes to its nominal value, i.e., $\omega_i \rightarrow \omega_{\text{ref}}$. Additionally, it allocates the VCVSI output active powers according to

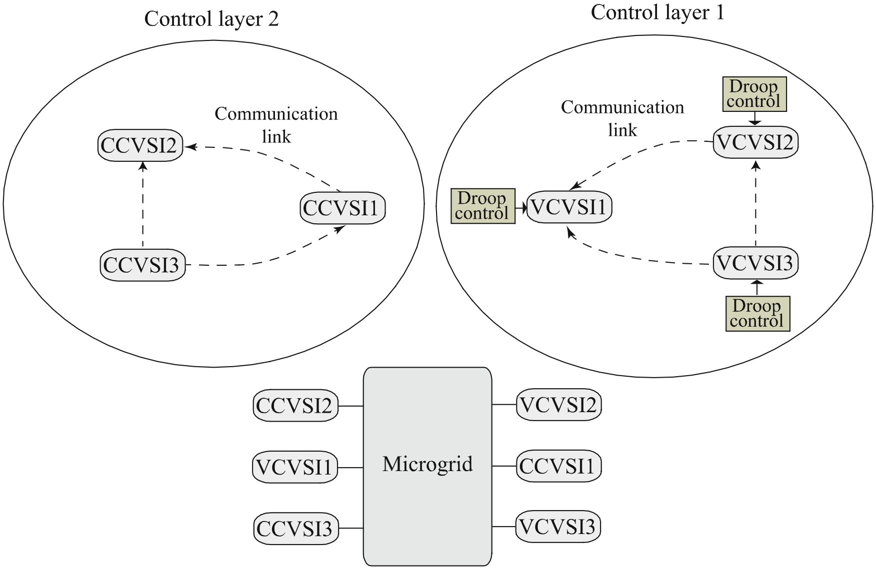

Fig. 5.1 The comprehensive distributed control of microgrids with two control layers. © [2016] IEEE. Reprinted, with permission, from IEEE Transactions on Industrial Informatics [1]

$$\frac{P_1}{P_{\max 1}} = \cdots = \frac{P_{N_V}}{P_{\max N_V}}, \tag{5.2}$$

where N_V is the number of VCVSIs in the islanded microgrid. $P_{\max i}$ denotes the active power rating of ith VCVSI. Since the active droop coefficients D_{Pi} are chosen based on the active power ratings of VCVSIs, (5.2) is equivalent to

$$D_{P1}P_1 = \cdots = D_{PN_V}P_{N_V}. \tag{5.3}$$

The voltage control selects E_i^* in (5.1) such that the output voltage amplitudes of VCVSIs $v_{o,\mathrm{magi}}$ return to the reference voltage, i.e., $v_{o,\mathrm{magi}} \to v_{\mathrm{ref}}$. If v_{ref} is set to the nominal voltage of microgrid v_{nominal}, the output voltage magnitude of VCVSIs synchronizes to the nominal voltage of microgrid. However, v_{ref} can be chosen such that the voltage magnitude of a critical bus of microgrid synchronizes to v_{nominal}.

The other objective of the voltage control can be defined as allocating the VCVSI output reactive powers according to

$$\frac{Q_1}{Q_{\max 1}} = \cdots = \frac{Q_{N_V}}{Q_{\max N_V}}, \tag{5.4}$$

where N_V is the number of VCVSIs in the islanded microgrid. $Q_{\max i}$ denotes the reactive power rating of ith VCVSI. Since the reactive droop coefficients D_{Qi} are chosen based on the reactive power ratings of VCVSIs, (5.4) is equivalent to

$$D_{Q1}Q_1 = \cdots = D_{QN_V}Q_{N_V}. \tag{5.5}$$

The voltage droop characteristic in (5.1) is designed assuming a fully inductive microgrid. Therefore, (5.4) and (5.5) can be exactly satisfied in fully inductive microgrids, and hence, small amount of mismatches among reactive power ratios can be observed in noninductive microgrids.

While the *control layer 1* is active to control the voltage and frequency of microgrid by tuning VCVSIs, the *control layer 2* objectives for CCVSIs are to control the active and reactive powers of CCVSIs. The CCVSIs should provide active and reactive power supports for VCVSIs by compensating a portion of the consumed active and reactive powers in the microgrid. Doing so, the VCVSIs can generate less active and reactive powers and save their active and reactive power capacities to provide a fast voltage and frequency control for future disturbances. The *control layer 2* sets the control inputs of CCVSIs such that their output active and reactive powers satisfy

$$\frac{P_1}{P_{\max 1}} = \cdots = \frac{P_{Nc}}{P_{\max Nc}} = \alpha_P, \tag{5.6}$$

$$\frac{Q_1}{Q_{\max 1}} = \cdots = \frac{Q_{N_C}}{Q_{\max N_C}} = \alpha_Q, \tag{5.7}$$

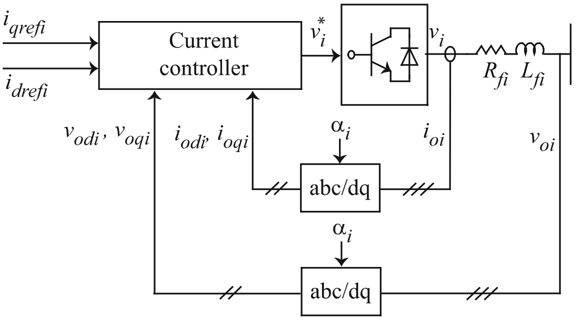

Fig. 5.2 The block diagram of a CCVSI. © [2016] IEEE. Reprinted, with permission, from IEEE Transactions on Industrial Informatics [1]

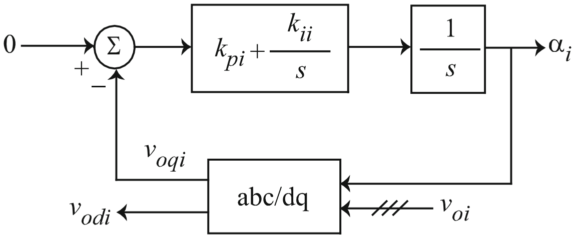

Fig. 5.3 The block diagram of α_i calculator. © [2016] IEEE. Reprinted, with permission, from IEEE Transactions on Industrial Informatics [1]

where N_C is the number of CCVSIs in the islanded microgrid. $P_{\max i}$ and $Q_{\max i}$ denote the active and reactive power ratings of ith CCVSIs. α_P and α_Q are pre-specified active and reactive power ratio references. Equations (5.6) and (5.7) show that the active and reactive powers of CCVSIs must be allocated based on their active and reactive power ratings.

Dynamical Model of CCVSIs: The block diagram of a CCVSI-based DG is shown in Fig. 5.2. It contains an inverter bridge, connected to a primary DC power source. The current controller adjusts the direct and quadrature terms of output current i_{oi}. As shown in Fig. 5.3, a control block is used to calculate the angle of the ith CCVSI reference frame with respect to the common reference frame α_i such that the quadrature term of output voltage v_{oqi} becomes zero [2]. This control block is named as α_i calculator.

The block diagram of the current controller is shown in Fig. 5.4. The differential algebraic equations of the current controller are written as

$$\dot{\gamma}_{di} = i_{\mathrm{dref}i} - i_{odi}, \tag{5.8}$$

$$\dot{\gamma}_{qi} = i_{\mathrm{qref}i} - i_{oqi}, \tag{5.9}$$

$$v_{idi}^* = v_{odi} - \omega_b L_{fi} i_{oqi} + K_{PCi}\left(i_{\mathrm{dref}i} - i_{odi}\right) + K_{ICi}\gamma_{di}, \tag{5.10}$$

$$v_{iqi}^* = v_{oqi} - \omega_b L_{fi} i_{odi} + K_{PCi}\left(i_{\mathrm{qref}i} - i_{oqi}\right) + K_{ICi}\gamma_{qi}, \tag{5.11}$$

where γ_{di} and γ_{qi} are the auxiliary state variables defined for the PI controllers in Fig. 5.4. i_{odi} and i_{oqi} are the direct and quadrature components of output current i_{oi} in Fig. 5.2. Other parameters are shown in Figs. 5.2 and 5.4. Assuming that the inverter bridge produces the demanded voltage, i.e., $v_{idi}^{*} = v_{idi}$ and $v_{iqi}^{*} = v_{iqi}$, the dynamics of output RL filter can be written as

$$\dot{i}_{odi} = -\frac{R_{fi}}{L_{fi}} i_{odi} + \omega_{\text{com}} i_{oqi} + \frac{1}{L_{fi}} v_{idi} - \frac{1}{L_{fi}} v_{odi}, \tag{5.12}$$

$$\dot{i}_{oqi} = -\frac{R_{fi}}{L_{fi}} i_{oqi} - \omega_{\text{com}} i_{odi} + \frac{1}{L_{fi}} v_{iqi} - \frac{1}{L_{fi}} v_{oqi}. \tag{5.13}$$

Equations (2.76)–(2.81) form the large-signal dynamical model of the *i*th CCVSI. The large-signal dynamical model can be written in a compact form as

$$\begin{cases} \dot{x}_{CCi} = \mathbf{f}_{CCi}(x_{CCi}) + \mathbf{k}_{CCi}(x_{CCi})\mathbf{D}_{CCi} + \mathbf{g}_{CCi}(x_{CCi})u_{CCi} \\ y_{CCi} = h_{CCi}(x_{CCi}) + d_{CCi}u_{CCi} \end{cases}, \tag{5.14}$$

where the state vector is

$$x_{CCi} = \begin{bmatrix} \gamma_{di} & \gamma_{qi} & i_{odi} & i_{oqi} \end{bmatrix}^T. \tag{5.15}$$

The term $\mathbf{D}_{CCi} = [\omega_{com} v_{odi}]^T$ is considered as a known disturbance. The detailed expressions for $\mathbf{f}_{CCi}(x_{CCi})$, $\mathbf{g}_{CCi}(x_{CCi})$, and $\mathbf{k}_{CCi}(x_{CCi})$ can be extracted from (2.76) to (2.81).

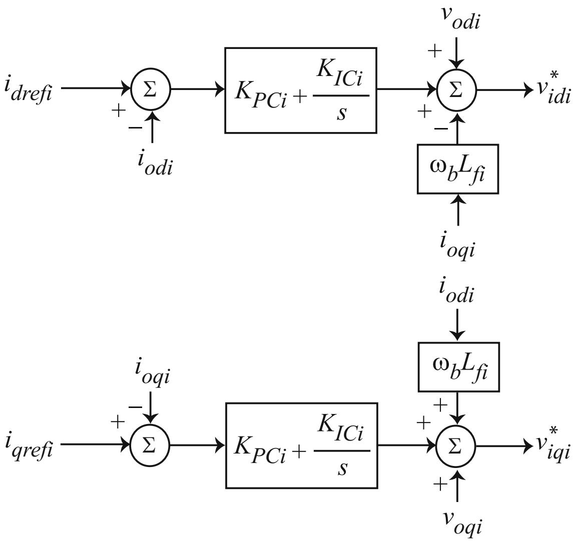

Fig. 5.4 The block diagram of the current controller for a CCVSI. © [2016] IEEE. Reprinted, with permission, from IEEE Transactions on Industrial Informatics [1]

The active and reactive powers of CCVSI can be written as

$$P_i = v_{odi} i_{odi} + v_{oqi} i_{oqi}, \tag{5.16}$$

$$Q_i = v_{oqi} i_{odi} - v_{odi} i_{oqi}. \tag{5.17}$$

Since the α_i of each CCVSI is chosen such that v_{oqi} becomes zero, the output active and reactive powers P_i and Q_i in (5.16) and (5.17) can be written as

$$P_i = v_{odi} i_{odi}, \tag{5.18}$$

$$Q_i = -v_{odi} i_{oqi}. \tag{5.19}$$

Therefore, $P_i/P_{\max i}$ and $Q_i/Q_{\max i}$ can be tuned by controlling i_{odi} and i_{oqi}. Since i_{odi} is controlled by $i_{d\text{ref}i}$, the output and control input in (2.82) are set to $y_{CCi} = \frac{P_i}{P_{\max i}}$ and $u_{CCi} = i_{d\text{ref}i}$ for the active power control. Since i_{oqi} is controlled by $i_{q\text{ref}i}$, the output and control input in (2.82) are set to $y_{CCi} = \frac{Q_i}{Q_{\max i}}$ and $u_{CCi} = i_{q\text{ref}i}$ for the reactive power control.

In the following, the control design procedure for VCVSIs and CCVSIs is elaborated.

5.1.1 Control Layer 1: Frequency Control and Voltage Control of VCVSIs

Frequency Control of VCVSIs: The distributed frequency control is to synchronize all of VCVSI frequencies to the nominal frequency. Additionally, it should allocate the output active power of VCVSIs based on their active power ratings; i.e., it should satisfy (5.2) and (5.3). In Chap. 4, the design procedure of the frequency control was elaborated.

Voltage Control of VCVSIs: In Chap. 4, the sole voltage control of VCVSI was discussed. In this chapter, the voltage and reactive power control of VCVSIs are considered. Therefore, the goal of voltage control is to choose appropriate control inputs E_i^* in (5.1) to synchronize the voltage magnitudes of VCVSIs $v_{o,\text{mag}i}$ to the reference voltage v_{ref} and allocate the output reactive power of VCVSIs based on their reactive power ratings; i.e., it satisfies (5.4) and (5.5). It should be noted that the voltage droop characteristic in (5.1) is designed assuming a microgrid with inductive transmission lines. Therefore, small mismatches among reactive power ratios and voltage magnitudes can be observed in microgrids where the transmission lines are not fully inductive.

As discussed in Chap. 4, the synchronization of the voltage magnitudes of VCVSIs, $v_{o,\text{mag}i}$, is equivalent to synchronizing the direct term of output voltages v_{odi}. To facilitate the simultaneous control of VCVSIs' voltage and reactive power, the fast dynamics of internal voltage and current controller are neglected. Doing so, one can write $v^*_{o,\mathrm{magi}} = v_{odi}$. Considering this fact, the differentiated voltage droop characteristic in (5.1) is

$$\dot{E}^*_i = \dot{v}_{odi} + D_{Qi}\dot{Q}_i = v_{vi}, \tag{5.20}$$

where v_{vi} is an auxiliary control to be designed. Equation (5.20) is a dynamic system for computing the control input E^*_i from v_{vi}. The auxiliary control should be designed such that VCVSI voltage magnitudes synchronize to the reference voltage v_{ref}, and (5.4) is satisfied. According to (5.20), the voltage control of a microgrid including N_V VCVSIs is transformed to a synchronization problem for a first-order and linear multi-agent system

$$\begin{cases} \dot{v}_{od1} + D_{Q1}\dot{Q}_1 = v_{v1}, \\ \dot{v}_{od2} + D_{Q2}\dot{Q}_2 = v_{v2}, \\ \vdots \\ \dot{v}_{odN_V} + D_{QN_V}\dot{Q}_{N_V} = v_{vN_V}. \end{cases} \tag{5.21}$$

To achieve synchronization, it is assumed that VCVSIs can communicate with each other through the prescribed communication digraph Gr. The auxiliary controls v_{vi} are chosen based on each VCVSI's own information and the information of its neighbors in the communication digraph as

$$v_{vi} = -c_v\left(\sum_{j\in N_i} a_{ij}(v_{odi} - v_{odj}) + b_i(v_{odi} - v_{\mathrm{ref}}) + \sum_{j\in N_i} a_{ij}(D_{Qi}Q_i - D_{Qj}Q_j)\right), \tag{5.22}$$

where $c_v \in R$ is the coupling gain. It is assumed that the pinning gain $b_i \geq 0$ is nonzero for one VCVSI that has the reference voltage v_{ref} information. Lemma 4.4 can be used to show that the auxiliary control in (5.22) synchronizes all VCVSI voltage amplitudes to v_{ref} and shares the output reactive power of VCVSIs based on their reactive power ratings. The reference voltage v_{ref} can be set to the nominal voltage of the microgrid to synchronize the VCVSI voltage magnitudes to the nominal voltage or can be chosen to control the voltage magnitude of a critical bus of microgrid.

The block diagram of the proposed voltage control is shown in Fig. 5.5. As shown in this figure, the control input E^*_i is written as

$$E^*_i = \int v_{vi}\mathrm{d}t. \tag{5.23}$$

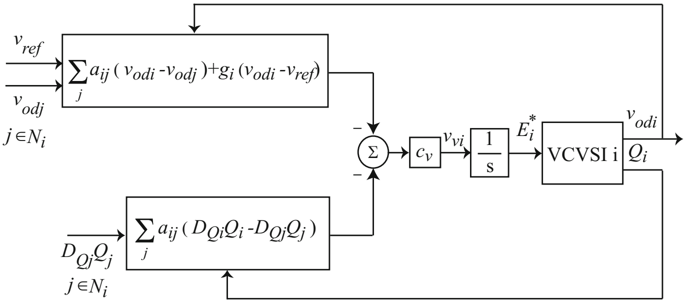

Fig. 5.5 The block diagram of the voltage control in the control layer 1. © [2016] IEEE. Reprinted, with permission, from IEEE Transactions on Industrial Informatics [1]

5.1.2 Control Layer 2: Active and Reactive Power Controls of CCVSIs

Active Power Control of CCVSIs: Subsequent to the islanding process, the active power of CCVSIs is required to be allocated based on their active power ratings which satisfy (5.6). Since the angle of the ith CCVSI reference frame with respect to the common reference frame α_i is chosen such that the quadrature term of output voltage v_{oqi} becomes zero, the output active power P_i can be tuned by controlling the direct term of output current i_{odi} in Fig. 5.2. Since i_{odi} is controlled by $i_{\mathrm{dref}i}$, the output and control input in (2.82) are set to $y_{CCi} = \frac{P_i}{P_{\mathrm{max}i}}$ and $u_{CCi} = i_{\mathrm{dref}i}$ for the active power control.

Input–output feedback linearization is used to generate a direct relationship between the output y_{CCi} and input u_{CCi}. According to (5.18), the derivative of P_i can be written as

$$\dot{P}_i = \dot{v}_{odi} i_{odi} + v_{odi} \dot{i}_{odi} \tag{5.24}$$

Replacing $\dot{i}_{odi}$ by (2.80) and dividing both sides of (5.24) by $P_{\mathrm{max}i}$ yield

$$\dot{y}_{CCi} = \frac{\dot{v}_{odi} i_{odi}}{P_{\mathrm{max}i}} + \frac{v_{odi}}{P_{\mathrm{max}i}}\left(-\frac{R_{fi}}{L_{fi}} i_{odi} + \omega_{\mathrm{com}} i_{oqi} + \frac{1}{L_{fi}} v_{idi} - \frac{1}{L_{fi}} v_{odi}\right). \tag{5.25}$$

Replacing v_{idi} by (2.78) yields

$$\dot{y}_{CCi} = M_{Pi}(\mathbf{x}_{CCi}) + N_{Pi}(\mathbf{x}_{CCi}) u_{CCi}, \tag{5.26}$$

where

$$\begin{aligned} M_{Pi}(\mathbf{x}_{CCi}) = {} & \frac{v_{odi}}{P_{\max i}}\left(-\frac{R_{fi}}{L_{fi}}i_{odi} + \omega_{\text{com}} i_{oqi} - \frac{1}{L_{fi}}v_{odi}\right) \\ & + \frac{v_{odi}}{P_{\max i}L_{fi}}\left(v_{odi} - \omega_b L_{fi} i_{oqi} - K_{PCi} i_{odi} + K_{ICi}\gamma_{di}\right) + \frac{\dot{v}_{odi} i_{odi}}{P_{\max i}}, \end{aligned} \tag{5.27}$$

and

$$N_{Pi}(\mathbf{x}_{CCi}) = \frac{v_{odi} K_{PCi}}{P_{\max i} L_{fi}}. \tag{5.28}$$

An auxiliary control $v_{Pi}$is defined as

$$v_{Pi} = M_{Pi}(\mathbf{x}_{CCi}) + N_{Pi}(\mathbf{x}_{CCi}) u_{CCi}. \tag{5.29}$$

Therefore, (5.26) and (5.29) result in a first-order regulator synchronization problem with the following linear system dynamics

$$\dot{y}_{CCi} = v_{Pi}, \ \forall i. \tag{5.30}$$

By choosing appropriate v_{Pi}, the synchronization for y_{CCi} is provided. The control input u_{CCi} is implemented by v_{Pi} as

$$u_{CCi} = \left(N_{Pi}(\mathbf{x}_{CCi})\right)^{-1}\left(-M_{Pi}(\mathbf{x}_{CCi}) + v_{Pi}\right). \tag{5.31}$$

The auxiliary controls v_{Pi} are chosen based on each CCVSI's own information and the information of its neighbors in the communication digraph as

$$v_{Pi} = -c_P\left(\sum_{j\in N_i} a_{ij}\left(\frac{P_i}{P_{\max i}} - \frac{P_j}{P_{\max j}}\right) + b_i\left(\frac{P_i}{P_{\max i}} - \alpha_P\right)\right), \tag{5.32}$$

where $c_P \in R$ is the coupling gain. It is assumed that the pinning gain $b_i \geq 0$ is nonzero for one CCVSI that has the reference active power ratio α_P. The block diagram of the proposed active power control is shown in Fig. 5.6. In the following, the Lyapunov technique is used to show the effectiveness of the proposed active power control protocol in (5.32). The global active power neighborhood tracking error is defined as $e_P = \begin{bmatrix} e_{P1} & e_{P2} & \cdots & e_{PN_C} \end{bmatrix}^T = (L+G)(\underline{P} - \underline{\alpha}_P)$, where $\underline{P} = \begin{bmatrix} \frac{P_1}{P_{\max 1}} & \frac{P_2}{P_{\max 2}} & \cdots & \frac{P_{N_C}}{P_{\max N_C}} \end{bmatrix}^T$ and $\underline{\alpha}_P = \mathbf{1}_{N_C} \otimes \alpha_P$. The global active power auxiliary control input $v_P = \begin{bmatrix} v_{P1} & v_{P2} & \cdots & v_{PN_C} \end{bmatrix}^T$ is defined as

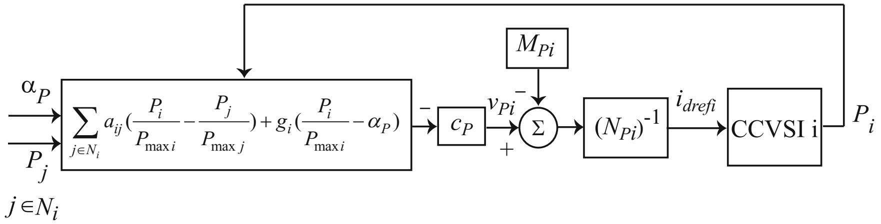

Fig. 5.6 The block diagram of the active power control in the control layer 2. © [2016] IEEE. Reprinted, with permission, from IEEE Transactions on Industrial Informatics [1]

$$v_P = \begin{bmatrix} v_{P1} & v_{P2} & \cdots & v_{PN_C} \end{bmatrix}^T = -c_P e_P. \tag{5.33}$$

Consider the Lyapunov function candidate

$$V = \frac{1}{2} e_P^T P e_P, \tag{5.34}$$

where $P = \text{diag}\{1/w_i\}$, w_i are the elements of a vector w that satisfies $(L+G)w = \mathbf{1}_N$. Since the digraph $\mathcal{G}$ has a spanning tree and $k_i \neq 0$ for at least one root node, $L + G$ is non-singular and a unique solution exists for w.

Differentiating (5.34) yields

$$\dot{V} = e_P^T P(L+G)v_P. \tag{5.35}$$

Defining $A \equiv L+G$ and placing (5.33) into (5.33) yield

$$\dot{V} = \frac{-c_P}{2} e_P^T (PA + A^T P) e_P. \tag{5.36}$$

From [3], $Q \equiv PA + A^T P$ is positive definite. Therefore, $\frac{c_P}{2} e_P^T Q e_P \geq \frac{c_P}{2} \sigma_{\min}(Q) \|e_P\|^2$, and hence,

$$\frac{-c_P}{2} e_P^T Q e_P \leq \frac{-c_P}{2} \sigma_{\min}(Q) \|e_P\|^2. \tag{5.37}$$

According to (5.37),

$$\dot{V} \leq \frac{-c_P}{2} \underline{\sigma}(Q) \|e_P\|^2 \leq 0. \tag{5.38}$$

Equation proves that the global neighborhood tracking error asymptotically goes to zero, and hence, according to Lemma 4.3, the distributed control protocols in (5.32) synchronize all $P_i/P_{\max i}$ to α_P.

Reactive Power Control of CCVSIs: Subsequent to the islanding process, the reactive power of CCVSIs should be shared based on their reactive power ratings that satisfy (5.7). Since the angle of the ith CCVSI reference frame with respect to the common reference frame α_i is chosen such that the quadrature term of output voltage v_{oqi} becomes zero, the output reactive power Q_i can be tuned by controlling the quadrature term of output current i_{oqi} in Fig. 5.2. Since i_{oqi} is controlled by $i_{q\mathrm{ref}i}$, the output and control input in (2.82) are set to $y_{CCi} = \frac{Q_i}{Q_{\max i}}$ and $u_{CCi} = i_{q\mathrm{ref}i}$ for the reactive power control.

Input–output feedback linearization is used to generate a direct relationship between the output y_{CCi} and input u_{CCi}. According to (5.19), the derivative of Q_i can be written as

$$\dot{Q}_i = -\dot{v}_{odi} i_{oqi} - v_{odi} \dot{i}_{oqi} \tag{5.39}$$

Replacing $\dot{i}_{oqi}$ by (2.81) and dividing both sides of (5.39) by $Q_{\max i}$ yield

$$\dot{y}_{CCi} = -\frac{\dot{v}_{odi} i_{oqi}}{Q_{\max i}} - \frac{v_{odi}}{Q_{\max i}}\left(-\frac{R_{fi}}{L_{fi}} i_{oqi} - \omega_{\mathrm{com}} i_{odi} + \frac{1}{L_{fi}} v_{iqi} - \frac{1}{L_{fi}} v_{oqi}\right). \tag{5.40}$$

Replacing *times* by (2.79) yields

$$\dot{y}_{CCi} = M_{Qi}(\mathbf{x}_{CCi}) + N_{Qi}(\mathbf{x}_{CCi}) u_{CCi}, \tag{5.41}$$

where

$$\begin{aligned} M_{Qi}(\mathbf{x}_{CCi}) = & -\frac{\dot{v}_{odi} i_{oqi}}{Q_{\max i}} - \frac{v_{odi}}{Q_{\max i}}\left(-\frac{R_{fi}}{L_{fi}} i_{oqi} - \omega_{\mathrm{com}} i_{odi} - \frac{1}{L_{fi}} v_{oqi}\right) \\ & -\frac{v_{odi}}{Q_{\max i} L_{fi}}\left(v_{oqi} + \omega_b L_{fi} i_{odi} - K_{PCi} i_{oqi} + K_{ICi} \gamma_{qi}\right), \end{aligned} \tag{5.42}$$

and

$$N_{Qi}(\mathbf{x}_{CCi}) = -\frac{v_{odi} K_{PCi}}{Q_{\max i} L_{fi}}. \tag{5.43}$$

An auxiliary control v_{Qi} is defined as

$$v_{Qi} = M_{Qi}(\mathbf{x}_{CCi}) + N_{Qi}(\mathbf{x}_{CCi}) u_{CCi}. \tag{5.44}$$

Therefore, (5.41) and (5.44) result in a first-order regulator synchronization problem with the following linear system dynamics

$$\dot{y}_{CCi} = v_{Qi}, \forall i. \tag{5.45}$$

By choosing appropriate v_{Qi}, the synchronization for y_{CCi} is provided. The control input u_{CCi} is implemented by v_{Qi} as

$$u_{CCi} = (N_{Qi}(\mathbf{x}_{CCi}))^{-1}(-M_{Qi}(\mathbf{x}_{CCi}) + v_i). \tag{5.46}$$

The auxiliary controls v_{Qi} are chosen based on each CCVSI's own information and the information of its neighbors in the communication digraph as

$$v_{Qi} = -c_Q\left(\sum_{j\in N_i} a_{ij}\left(\frac{Q_i}{Q_{\max i}} - \frac{Q_j}{Q_{\max j}}\right) + b_i\left(\frac{Q_i}{Q_{\max i}} - \alpha_Q\right)\right), \tag{5.47}$$

where $c_Q \in R$ is the coupling gain. It is assumed that the pinning gain $b_i \geq 0$ is nonzero for one CCVSI that has the reference reactive power ratio α_Q. The block diagram of the proposed reactive power control is shown in Fig. 5.7. The same procedure explained for active power control of CCVSIs can be used to show that all of $\frac{Q_i}{Q_{\max i}}$ synchronize to a α_Q and (5.7) is satisfied.

5.1.3 *Case Studies*

Simulation Results for the Microgrid Test System in Fig. 5.8. The effectiveness of the proposed control schemes is verified by simulating an islanded microgrid in MATLAB. Figure 5.8 shows the single-line diagram of the microgrid test system. This microgrid consists of seven DGs including three VCVSIs (DGs 1, 5, and 7) and four CCVSIs (DGs 2, 3, 4, and 6). The lines between buses are modeled as series RL branches. The specifications of the DGs, lines, and loads are summarized in Tables 5.1, 5.2, and 5.3. k_{pi} and k_{ii} in Fig. 5.3 are set to 285 and 142,500, respectively. The nominal line-to-line voltage and frequency of the microgrid are 380 V and 50 Hz, respectively. In the following, the simulation results are provided for three different cases, namely *Case* 1, *Case* 2, and *Case* 3. In *Cases* 1 and 2, a fixed communication network is exploited. In *Case* 3, the two-layer control framework is implemented through a time-varying communication network.

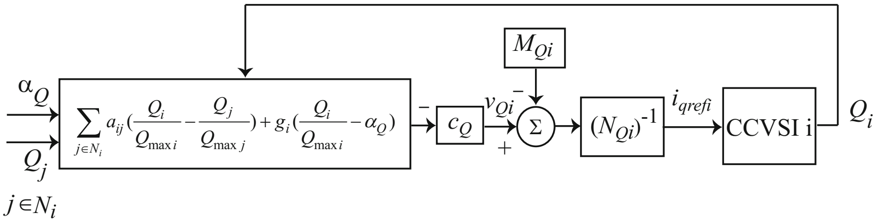

Fig. 5.7 The block diagram of the reactive power control in the control layer 2. © [2016] IEEE. Reprinted, with permission, from IEEE Transactions on Industrial Informatics [1]

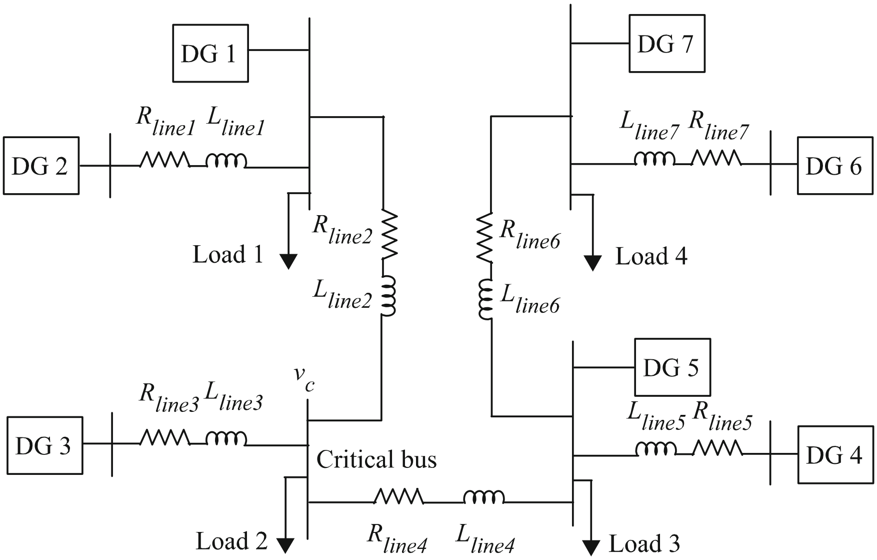

Fig. 5.8 Single-line diagram of the microgrid test system. © [2016] IEEE. Reprinted, with permission, from IEEE Transactions on Industrial Informatics [1]

Table 5.1 Specifications of DGs for microgrid test system in Fig. 4.8

	DG 1 and 3		DG 2	
VCVSIs	m_P	18.8×10^{-5}	m_P	25×10^{-5}
	n_Q	2.6×10^{-3}	n_Q	3×10^{-3}
	R_c	0.03 Ω	R_c	0.03 Ω
	L_c	0.35 mH	L_c	0.35 mH
	R_f	0.1 Ω	R_f	0.1 Ω
	L_f	1.35 mH	L_f	1.35 mH
	C_f	50 μF	C_f	50 μF
	K_{PV}	0.1	K_{PV}	0.05
	K_{IV}	420	K_{IV}	390
	K_{PC}	15	K_{PC}	10.5
	K_{IC}	20,000	K_{IC}	16,000
CCVSIs	DG 4 and 5		DG 6 and 7	
	R_f	0.23 Ω	R_f	0.35 Ω
	L_f	318 μH	L_f	1847 μH
	K_{PC}	10.5	K_{PC}	10.5
	K_{IC}	16,000	K_{IC}	16,000
	$P_{\max}$	1500 W	$P_{\max}$	2000 W
	$Q_{\max}$	1000 W	$Q_{\max}$	1200 W

Table 5.2 Specifications of *lines* for microgrid test system in Fig. 4.8

Line 1, 3, 5, 7		Line 2, 4, 6	
R_{line}	0.23 Ω	R_{line}	0.35 Ω
L_{line}	318 μH	L_{line}	1847 μH

Table 5.3 Specifications of loads for microgrid test system in Fig. 4.8

	Load 1	Load 2	Load 3	Load 4
R (per phase)	30 Ω	20 Ω	25 Ω	25 Ω
X (per phase)	15 Ω	10 Ω	10 Ω	15 Ω

It is assumed that VCVSIs and CCVSIs communicate with each other through the communication digraphs depicted in Fig. 5.9a, b, respectively. These communication topologies are chosen based on the geographical location of DGs. The associated adjacency matrix of the digraphs in Fig. 5.9a, b, namely A_{G1} and A_{G2}, are

$$A_{G1} = \begin{bmatrix} 0 & 0 & 0 \\ 1 & 0 & 0 \\ 1 & 0 & 0 \end{bmatrix}, \tag{5.48}$$

and

$$A_{G2} = \begin{bmatrix} 0 & 0 & 0 & 0 \\ 1 & 0 & 0 & 0 \\ 1 & 0 & 0 & 0 \\ 1 & 0 & 0 & 0 \end{bmatrix}, \tag{5.49}$$

respectively. DG 1 is the only VCVSI that knows the voltage and frequency reference values and is connected to the leader node with the pinning gain $b_1 = 1$. DG 4 is the only CCVSI that knows the reference value of active and reactive power ratios α_P and α_Q with the pinning gain $b_1 = 1$. The coupling gains c_f and c_v are set to 30. The coupling gains c_P and c_Q in (5.32) and (5.47) are set to 30.

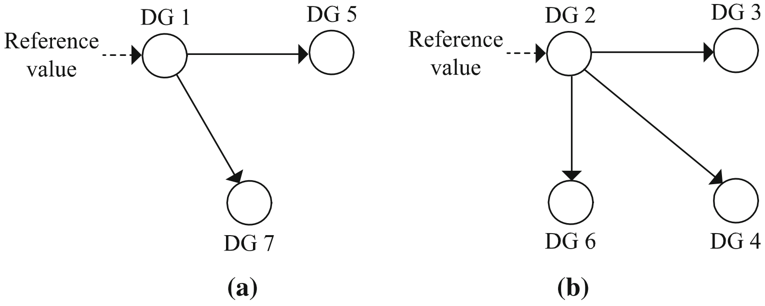

Fig. 5.9 Topology of the communication digraph for **a** control layer 1 and **b** control layer 2. © [2016] IEEE. Reprinted, with permission, from IEEE Transactions on Industrial Informatics [1]

In the first case, namely *Case* 1, the reference frequency and voltage $f_{ref} = \omega_{ref}/2\pi$ and v_{ref} are set to 50 Hz and 1 pu, respectively. The reference active and reactive power ratios are set to $\alpha_P = 0.4$ and $\alpha_Q = 0.3$, respectively. It should be noted that the proposed control framework always exists as a supervisory control level and takes actions in the event of disturbances. However, to highlight the effectiveness of the proposed controls, it is assumed that the microgrid is islanded from the main grid at$t = 0$, and the secondary control is applied at $t = 0.7$ s. Figure 5.10a shows the VCVSIs' frequencies. As shown in this figure, the frequency control of control layer 1 returns all VCVSIs' frequencies to 50 Hz. Figure 5.10b shows the ratio of the active powers of VCVSIs with respect to their active power ratings, or equivalently $D_{Pi}P_i$. As shown in this figure, the proposed frequency control satisfies (5.3). Figure 5.11a shows the VCVSIs' terminal voltage amplitudes. As shown in this figure, the voltage control of control layer 1 returns all VCVSIs' terminal voltage amplitudes to a close vicinity of 1 pu. Figure 5.11b shows the ratio of the reactive powers of VCVSIs with respect to their reactive power ratings, or equivalently $D_{Qi}Q_i$. Since the microgrid test bed is not fully inductive, small mismatches among the DG reactive power ratios are observed. Figure 5.12a shows the ratio of the active powers of CCVSIs with respect to their active power ratings. As shown in this figure, the control layer 2 returns all of the active power ratios to the reference ratio and satisfies (5.6). Figure 5.12b shows the ratio of the reactive powers of CCVSIs with respect to their reactive power ratings.

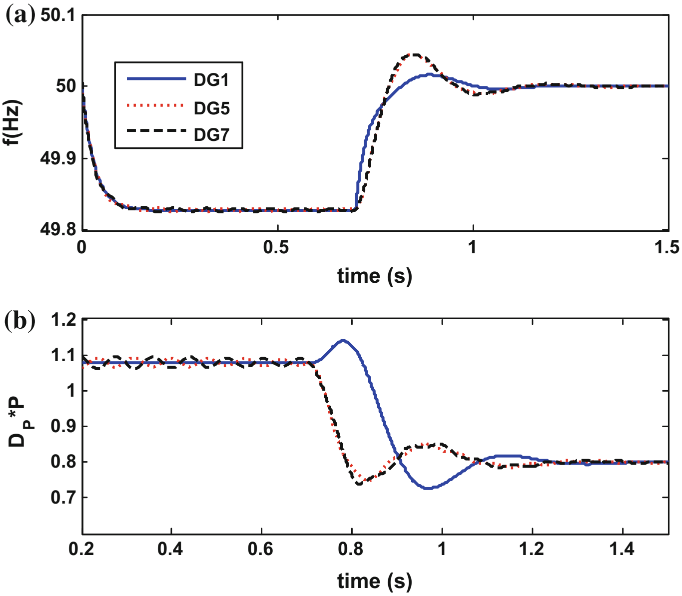

Fig. 5.10 Frequency control of control layer 1 in *Case* 1: **a** VCVSI frequencies and **b** VCVSI active power ratios $D_{Pi}P_i$. © [2016] IEEE. Reprinted, with permission, from IEEE Transactions on Industrial Informatics [1]

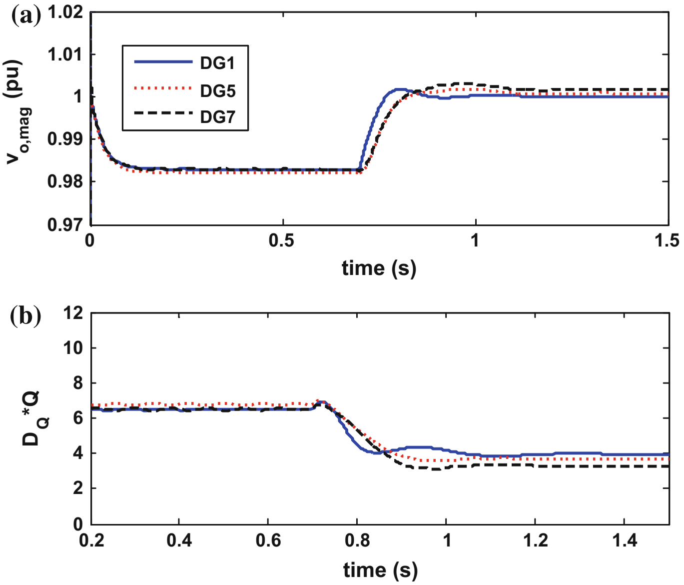

Fig. 5.11 Voltage control of control layer 1 in *Case* 1: **a** VCVSI output voltage magnitudes and **b** VCVSI reactive power ratios $D_{Qi}Q_i$. © [2016] IEEE. Reprinted, with permission, from IEEE Transactions on Industrial Informatics [1]

As shown in this figure, the control layer 2 returns all of the reactive power ratios to the reference ratio and satisfies (5.7). As shown in Fig. 5.12, CCVSIs provide active and reactive power supports for VCVSIs by compensating a portion of the active and reactive powers required for voltage and frequency restoration. Therefore, once the secondary control is applied, VCVSIs generate less active and reactive powers, as shown in Figs. 4.10b and 4.11b.

In the second case, namely *Case* 2, it is assumed that the reference frequency $f_{\text{ref}} = 50$ Hz and the reference active and reactive power ratios are set to $\alpha_P = 0.6$ and $\alpha_Q = 0.6$, respectively. However, the aim of the voltage control of control layer 1 is to control the voltage of the critical bus, as shown in Fig. 5.8. The microgrid gets islanded from the main grid at $t = 0$, and the secondary control is applied at $t = 0.7$ s. Figure 5.13a shows the VCVSIs' frequencies. As shown in this figure, the frequency control of control layer 1 returns all VCVSIs' frequencies to 50 Hz. Figure 5.13b shows the ratio of the active powers of VCVSIs with respect to their active power ratings. As shown in this figure, the proposed frequency control shares the active power among VCVSIs based on their active power ratings. Figure 5.14a shows the critical bus voltage amplitude. As shown in this figure, the voltage control of control layer 1 returns the critical bus voltage amplitude to 1 pu. Figure 5.14b shows the ratio of the reactive powers of VCVSIs with respect to their reactive power ratings. As shown in this figure, the proposed voltage control satisfies (5.4). Figure 5.15a shows the ratio of the active powers of CCVSIs with

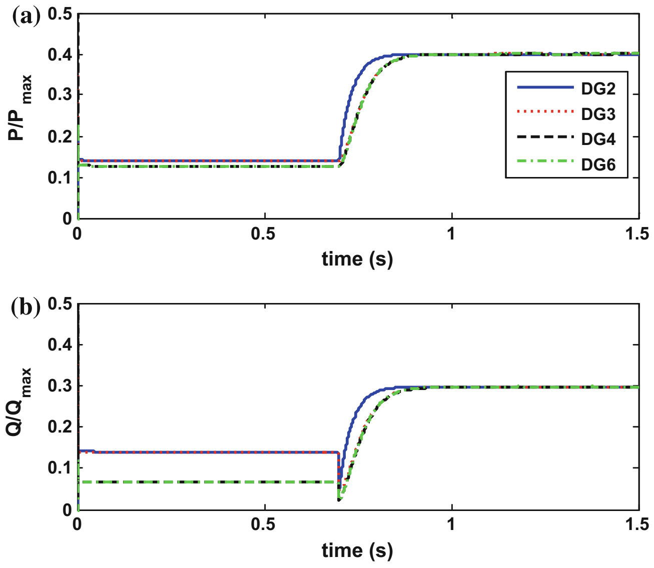

Fig. 5.12 Active and reactive power controls of control layer 2 in *Case* 1: **a** CCVSI active power ratios $P_i/P_{\mathrm{max}i}$ and **b** CCVSI reactive power ratios $Q_i/Q_{\mathrm{max}i}$. © [2016] IEEE. Reprinted, with permission, from IEEE Transactions on Industrial Informatics [1]

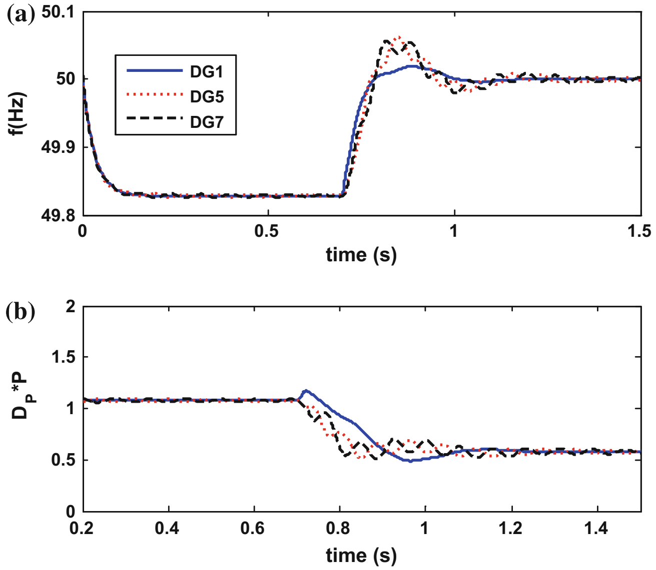

Fig. 5.13 Frequency control of control layer 1 in *Case* 2: **a** VCVSI frequencies and **b** VCVSI active power ratios $D_{Pi}P_i$. © [2016] IEEE. Reprinted, with permission, from IEEE Transactions on Industrial Informatics [1]

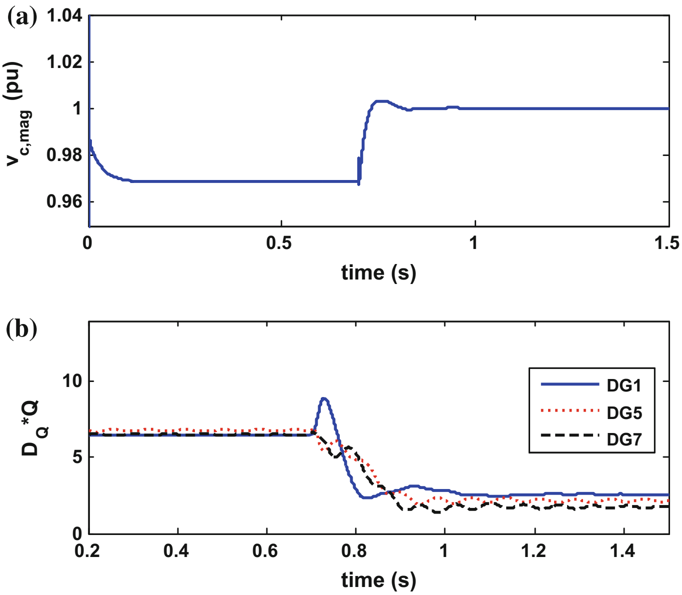

Fig. 5.14 Voltage control of control layer 1 in *Case* 2: **a** critical bus voltage magnitude and **b** VCVSI reactive power ratios $D_{Qi}Q_i$. © [2016] IEEE. Reprinted, with permission, from IEEE Transactions on Industrial Informatics [1]

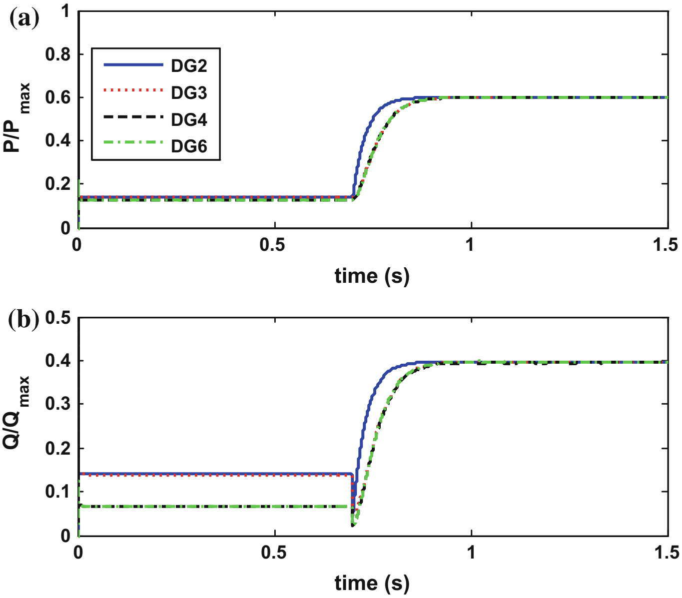

Fig. 5.15 Active and reactive power controls of control layer 2 in *Case* 2: **a** CCVSI active power ratios P_i/P_{maxi} and **b** CCVSI reactive power ratios Q_i/Q_{maxi}. © [2016] IEEE. Reprinted, with permission, from IEEE Transactions on Industrial Informatics [1]

respect to their active power ratings. As shown in this figure, control layer 2 returns all of the active power ratios to the reference ratio and satisfies (5.6). Figure 5.15b shows the ratio of the reactive powers of CCVSIs with respect to their reactive power ratings. As shown in this figure, the control layer 2 returns all of the reactive power ratios to the reference ratio and satisfies (5.7). Compared to *Case* 1, greater α_P and α_Q are chosen for control layer 2, and hence, VCVSIs generate less active and reactive powers, as shown in Figs. 5.13b and 5.14b.

In *Case* 3, it is assumed that the microgrid is islanded from the main grid at $t = 0$, and the frequency control is applied at $t = 0.7$ s. However, as opposed to *Case* 1, the distributed control framework is associated with time-varying communication networks. Figure 5.16 shows the three communication network structures that are used in simulation. Each structure is adopted at a specific time interval. The communication digraph in Fig. 5.16(a) models the communication network at the time interval $[(0.7 + 0.15\,k)$ s, $(0.7 + 0.15\,k) + 0.05$ s], for

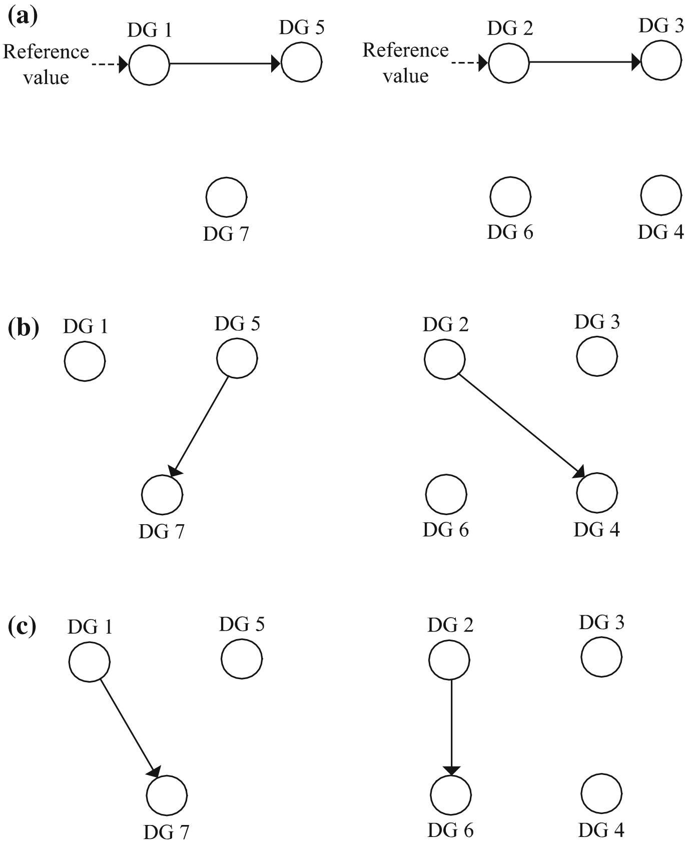

Fig. 5.16 Communication digraphs for the time-varying communication network in *Case* 3. © [2016] IEEE. Reprinted, with permission, from IEEE Transactions on Industrial Informatics [1]

$k = 0,1,\ldots$. The communication digraph in Fig. 5.16(b) models the communication network at the time interval [(0.75 + 0.15 k) s, (0.75 + 0.15 k) + 0.05 s], for $k = 0,1,\ldots$. The communication digraph in Fig. 5.16c models the communication network at the time interval [(0.8 + 0.15 k) s, (0.8 + 0.15 k) + 0.05 s], for $k = 0,1$, … It is seen that over the each 0.15-s period, the sequential completeness condition is satisfied. As shown in Fig. 5.17a, the control layer 1 returns all VCVSI frequencies to 50 Hz. Figure 5.17b shows the active powers multiplied by the active power droop coefficients, i.e., $D_{Pi}P_i$, for VCVSIs. As seen, the frequency control satisfies the equality in (5.4). Figure 5.18a shows the terminal voltage amplitude of VCVSIs, where they are all returned to 1 pu. Figure 5.18b shows the reactive powers of VCVSIs multiplied by the reactive power droop coefficients, i.e., $D_{Qi}Q_i$. As seen, the voltage control satisfies the equality in (5.6). Figure 4.19a, b shows the ratio of the active and reactive powers of CCVSIs with respect to their rated active and reactive powers. The control layer 2 returns all active and reactive power ratios to the reference ratios and satisfies (5.6) and (5.7). These simulation results verify the effectiveness of the proposed control framework in the case of time-varying communication networks and communication link failures.

Simulation Results for the IEEE 34-Bus Test Feeder. Figure 5.20 shows the single-line diagram of the modified IEEE 34-bus test feeder. Six DGs including three VCVSIs (DGs 1, 2, and 3) and three CCVSIs (DGs 4, 5, and 6) are connected to the test feeder. This feeder is converted to a balanced feeder by averaging the line parameters. The specification of lines is provided in [4]. The specifications of the DGs and loads are summarized in Tables 5.4 and 5.5. The control coefficients k_{pi} and k_{ii} in Fig. 5.3 are set to 285 and 142500, respectively. The nominal frequency and line-to-line voltage are set to 60 Hz and 24.9 kV, respectively. DGs are connected to the feeder through six Y-Y, 480 V/24.9 kV, and 400 kVA transformers with the series impedance of $0.03 + j0.12$ pu. It is assumed that VCVSIs and CCVSIs communicate through the communication digraphs depicted in Fig. 4.21a, b, respectively. DG 1 is the only VCVSI that knows the voltage and frequency reference values and is connected to the leader node with the pinning gain $b_1 = 1$. DG 4 is the only CCVSI that knows the reference value of active and reactive power ratios α_P and α_Q with the pinning gain $b_1 = 1$. The control gains c_f, c_v, c_P, and c_Q are all set to 30.

The reference frequency and voltage f_{ref} and v_{ref} are set to 60 Hz and 1 pu, respectively. The reference active and reactive power ratios are set to $\alpha_P = 0.7$ and $\alpha_Q = 0.6$. The test feeder is connected to the main grid at bus 800, as shown in Fig. 5.20. The test feeder is islanded from the main grid at $t = 0$, resembling an islanded microgrid. The secondary control is applied at $t = 0.7$ s. As shown in Fig. 5.22a, the control layer 1 returns all VCVSI frequencies to 60 Hz. Figure 5.22b shows the active powers multiplied by the active power droop coefficients, i.e., $D_{Pi}P_i$, for VCVSIs. As seen, the frequency control satisfies the equality in (5.4). Figure 5.23a shows the terminal voltage amplitude of VCVSIs, where they are all returned to 1 pu. Figure 5.23b shows the reactive powers of VCVSIs multiplied by the reactive power droop coefficients, i.e., $D_{Qi}Q_i$. As seen, the voltage

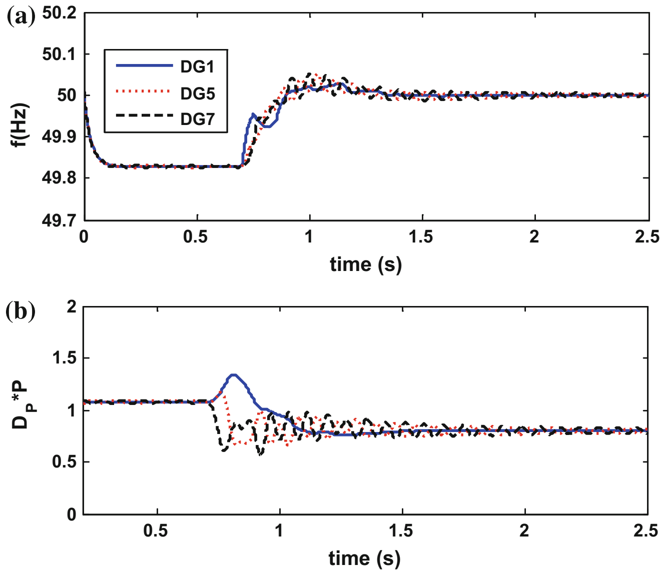

Fig. 5.17 Frequency control using control layer 1 in *Case* 3: **a** VCVSI frequencies and **b** VCVSI active power ratios $D_{Pi}P_i$. © [2016] IEEE. Reprinted, with permission, from IEEE Transactions on Industrial Informatics [1]

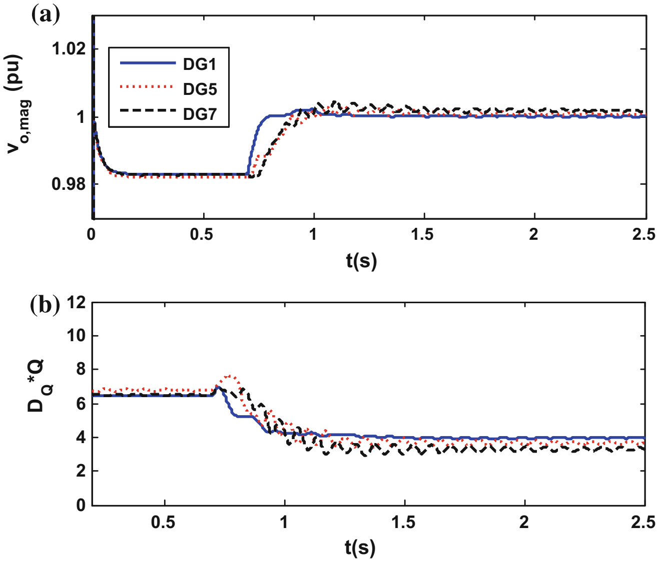

Fig. 5.18 Voltage control using control layer 1 in *Case* 3: **a** critical bus voltage magnitude and **b** VCVSI reactive power ratios $D_{Qi}Q_i$. © [2016] IEEE. Reprinted, with permission, from IEEE Transactions on Industrial Informatics [1]

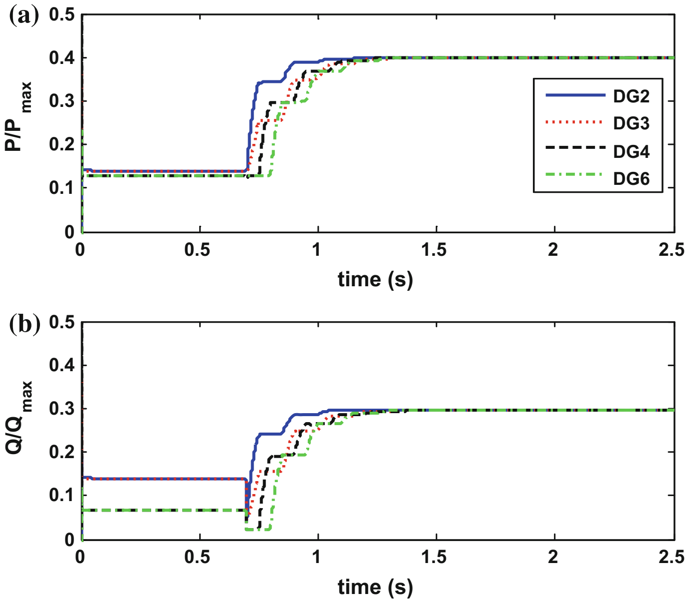

Fig. 5.19 Active and reactive power control using control layer 2 in *Case* 3: **a** CCVSI active power ratios P_i/P_{maxi} and **b** and CCVSI reactive power ratios Q_i/Q_{maxi}. © [2016] IEEE. Reprinted, with permission, from IEEE Transactions on Industrial Informatics [1]

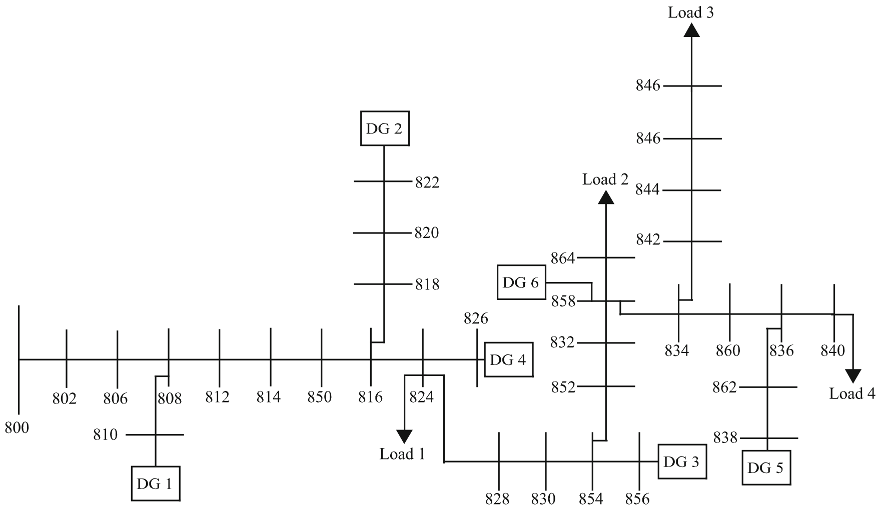

Fig. 5.20 Single-line diagram of modified IEEE 34-bus test feeder. © [2016] IEEE. Reprinted, with permission, from IEEE Transactions on Industrial Informatics [1]

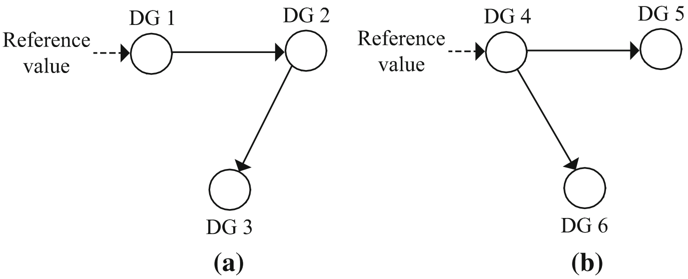

Fig. 5.21 Communication digraphs for IEEE 34-bus test feeder: **a** VCVSIs and **b** CCVSIs. © [2016] IEEE. Reprinted, with permission, from IEEE Transactions on Industrial Informatics [1]

Table 5.4 Specifications of DGs for IEEE 34-bus test feeder

	DG 1 and 2		DG 3	
VCVSIs	m_P	5.64×10^{-5}	m_P	7.5×10^{-5}
	n_Q	5.2×10^{-4}	n_Q	6×10^{-4}
	R_c	0.03 Ω	R_c	0.03 Ω
	L_c	0.35 mH	L_c	0.35 mH
	R_f	0.1 Ω	R_f	0.1 Ω
	L_f	1.35 mH	L_f	1.35 mH
	C_f	50 µF	C_f	50 µF
	K_{PV}	0.1	K_{PV}	0.05
	K_{IV}	420	K_{IV}	390
	K_{PC}	15	K_{PC}	10.5
	K_{IC}	20,000	K_{IC}	16,000
CCVSIs	DG 4 and 5		DG 6	
	R_f	0.2 Ω	R_f	0.35 Ω
	L_f	340 µH	L_f	1900 µH
	K_{PC}	11	K_{PC}	11
	K_{IC}	16,000	K_{IC}	16,000
	$P_{\max}$	35 kW	$P_{\max}$	30 kW
	$Q_{\max}$	32 kVAr	$Q_{\max}$	30 kVAr

Table 5.5 Specifications of loads for IEEE 34-bus test feeder

	Load 1 (Ω)	Load 2 (Ω)	Load 3 (Ω)	Load 4 (Ω)
R (per phase)	30	20	25	25
X (per phase)	15	10	10	15

control tries to share the reactive power among VCVSIs based on their reactive power ratings; however, since the transmission lines are not purely inductive, small mismatches among the DG reactive power ratios are observed. Figure 5.24a shows the ratio of the active powers of CCVSIs with respect to their rated active powers. The control layer 2 returns all active power ratios to the reference ratio and satisfies

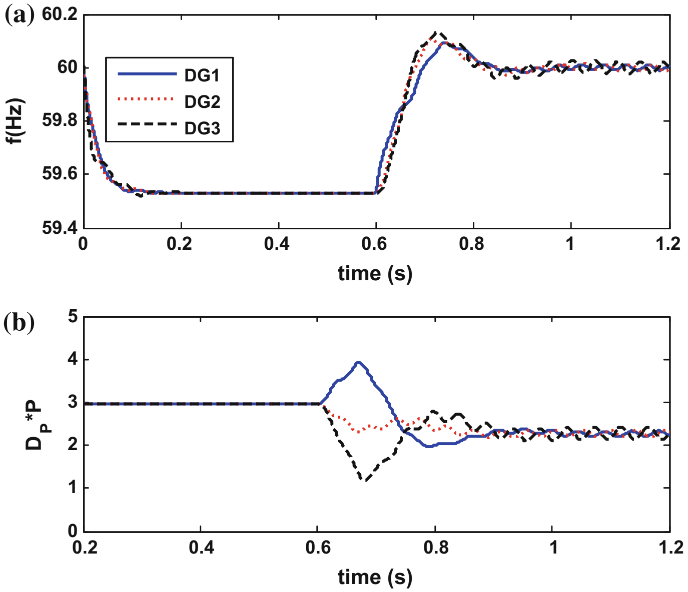

Fig. 5.22 Frequency control for IEEE 34-bus test feeder: **a** VCVSI frequencies and **b** VCVSI active power ratios $D_{Pi}P_i$.© [2016] IEEE. Reprinted, with permission, from IEEE Transactions on Industrial Informatics [1]

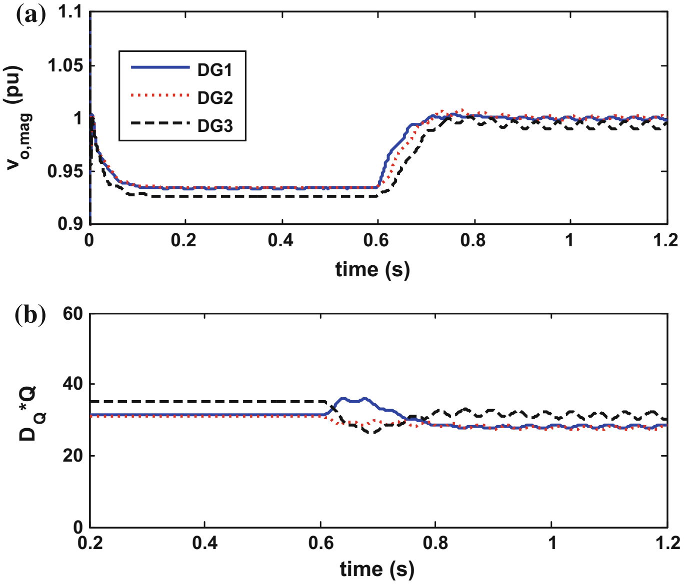

Fig. 5.23 Voltage control for IEEE 34-bus test feeder: **a** VCVSI output voltage magnitudes and **b** VCVSI reactive power ratios $D_{Qi}Q_i$. © [2016] IEEE. Reprinted, with permission, from IEEE Transactions on Industrial Informatics [1]

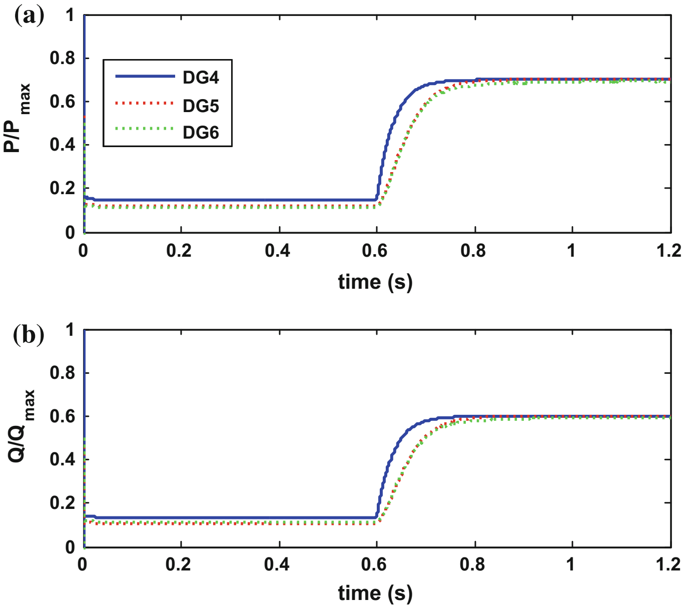

Fig. 5.24 Active and reactive power controls for IEEE 34-bus test feeder: **a** CCVSI active power ratios P_i/P_{maxi} and **b** CCVSI reactive power ratios Q_i/Q_{maxi}. © [2016] IEEE. Reprinted, with permission, from IEEE Transactions on Industrial Informatics [1]

(5.6). Figure 5.24b shows the ratio of the reactive powers of CCVSIs with respect to their reactive power ratings. As seen, the control layer 2 returns the reactive power ratios to the reference ratio and satisfies (5.7).

5.2 Adaptive and Distributed Voltage Control for AC Microgrids

This section extends the distributed secondary voltage control proposed in Chap. 4 and proposes an adaptive and distributed secondary voltage control for microgrids with inverter-based DGs. The term adaptive [5–8] refers to the following salient features of the proposed controller:

- The proposed controller compensates for the nonlinear and uncertain dynamics of DGs and, hence, obviates the control design challenges caused by the nonlinear dynamics of DGs.
- The controller is fully independent of the DG parameters and the specification of the connector by which each DG is connected to the microgrid. Therefore, the controller can be deployed on any DG regardless of the DG parameters and the

connector specifications, and its performance does not deteriorate by the change in DG parameters (e.g., due to aging and thermal effects).

- The proposed controller appropriately responds to the changes in the system operating condition, without any manual intervention, and adjusts the control parameters in real time.

Linear-in-parameter neural networks (NNs) are used to design an adaptive and distributed secondary voltage control. Neural networks are used to compensate for the uncertainties caused by the unknown dynamics of DGs [5]. The NN weights are the control parameters and are calculated in real time. DGs are considered as agents that can communicate with each other through a communication network. This communication network is modeled by a directed graph (digraph). It is assumed that the DG nonlinear dynamical model and parameters are unknown. The Lyapunov technique is adopted to derive fully distributed control protocols for each DG.

According to Chap. 2, the nonlinear dynamics of a VCVSI can be written as

$$\begin{cases} \dot{\mathbf{x}}_i = \mathbf{f}_i(\mathbf{x}_i) + \mathbf{k}_i(\mathbf{x}_i)\mathbf{D}_i + \mathbf{g}_i(\mathbf{x}_i)u_i \\ y_i = h_i(\mathbf{x}_i) + d_i u_i \end{cases} \tag{5.50}$$

Detailed expressions for $\mathbf{f}_i(\mathbf{x}_i)$, $\mathbf{g}_i(\mathbf{x}_i)$, $h_i(\mathbf{x}_i)$, $d_i(\mathbf{x}_i)$, and $\mathbf{k}_i(\mathbf{x}_i)$ are adopted from the nonlinear VCVSI model presented in Chap. 2.

The dynamics of inverter-based DGs are nonlinear. In this chapter, input–output feedback linearization and neural networks are used to compensate for the nonlinear dynamics of DGs. As discussed in Chap. 4, in input–output feedback linearization, a direct relationship between the dynamics of the output y_i (or equivalently v_{odi}) and the control input u_i (or equivalently E_i^*) is generated by repetitively differentiating y_i with respect to time. For the dynamics of the ith DG, the direct relationship between the y_i and u_i is generated after the second derivative of the output y_i. This direct relationship was calculated in Chap. 4 and can be written as:

$$\ddot{y}_i = L_{\mathbf{F}_i}^2 h_i + L_{\mathbf{g}_i} L_{\mathbf{F}_i} h_i u_i, \tag{5.51}$$

The commensurate reformulated dynamics of each DG can be written as

$$\begin{cases} \dot{y}_{i,1} \equiv y_{i,2}, \\ \dot{y}_{i,2} = f_i(x_i) + g_i(x_i)u_i, \end{cases} \quad \forall i, \tag{5.52}$$

where $y_i \equiv y_{i,1}$, $f_i(x_i) \equiv L_{\mathbf{F}_i}^2 h_i$, and $g_i(x_i) \equiv L_{\mathbf{g}_i} L_{\mathbf{F}_i} h_i$.

Remark 5.1 The function $g_i(x_i)$ is equal to $\frac{1}{L_{fi}C_{fi}}$. Therefore, a positive constant g_{0i} exists such that $\left|\frac{d}{dt}(1/g_i(x_i))\right| \leq g_{0i}$.

Using the input–output feedback linearization, each agent dynamics are decomposed into the second-order dynamical system in (5.52) and a set of internal dynamics. It should be noted that since $y_0 = v_{\text{ref}}$ is constant, $\dot{y}_0 = 0$. Define

$Y_i = [\,y_{i,1} \quad y_{i,2}\,]^T$ and $Y_0 = [\,y_{0,1} \quad y_{0,2}\,]^T = [\,v_{\text{ref}} \quad 0\,]^T$. The secondary voltage control is solved if a distributed u_i in (5.52) is found such that $Y_i \to Y_0$, $\forall i$. To design a controller independent of DG parameters, it is assumed that the nonlinear dynamics of DGs and, hence, functions $f_i(x_i)$ and $g_i(x_i)$ are unknown. Therefore, NNs should be exploited to design an adaptive control that compensates for the nonlinear and uncertain functions $f_i(x_i)$ and $g_i(x_i)$.

In this section, first, the sliding mode error is introduced. Then, the sliding mode errors are used to design adaptive and distributed secondary controls for each DG using the Lyapunov function technique.

Sliding Mode Error: For each DG, the cooperative team objective is expressed in terms of the local neighborhood tracking error

$$e_{i,m} = \sum_{j\in N_i} a_{ij}(y_{i,m} - y_{j,m}) + \ b_i(y_{i,m} - y_{0,m}), \tag{5.53}$$

where a_{ij} is the weight of the edge by which the jth DG is connected to the ith DG, and b_i is the pinning gain by which the ith DG is connected to the leader node. For the secondary voltage control, the leader node contains the information of the voltage reference, i.e., $Y_0 = [\,y_{0,1} \quad y_{0,2}\,]^T = [\,v_{\text{ref}} \quad 0\,]^T$. It should be noted that only a small portion of DGs need to be pinned to the leader node. Define $e_i = [\,e_{i,1} \quad e_{i,2}\,]^T$, $\delta_{i,m} = y_{i,m} - y_{0,m}$, $\delta_i = Y_i - Y_0$(δ_i is called the local disagreement vector, and Y_0 is considered as the leader node dynamics.), $\mathbf{e} = [\,e_1 \quad e_2 \quad \cdots \quad e_N\,]^T$, and $\boldsymbol{\delta} = [\,\delta_1 \quad \delta_2 \quad \cdots \quad \delta_N\,]^T$. The global neighborhood tracking error $\mathbf{e}$ can be written as

$$\mathbf{e} = (L + B)\boldsymbol{\delta}, \tag{5.54}$$

where $B = \text{diag}\{b_i\}$.

The sliding mode error r_i for each DG is defined as

$$r_i = \lambda_1 e_{i,1} + \lambda_2 e_{i,2}. \tag{5.55}$$

The parameters λ_i are chosen such that the polynomial $\lambda_1 + \lambda_2 s$ is Hurwitz. Therefore, on the sliding surface $r_i = 0$, e_i exponentially goes to zero. The derivative of the sliding mode error can be written as

$$\dot{r}_i = \lambda_1 e_{i,2} + \sum_{j\in N_i} a_{ij}(f_i + g_i u_i - f_j - g_j u_j) + b_i(f_i + g_i u_i). \tag{5.56}$$

Defining $d_i = \sum_{j\in N_i} a_{ij}$, (5.56) can be reformulated as

$$\dot{r}_i = \lambda_1 e_{i,2} + (d_i + b_i)(f_i + g_i u_i) - \sum_{j\in N_i} a_{ij}(f_j + g_j u_j). \tag{5.57}$$

Define

$$E_{i,1} = [\, e_{i,1} \quad e_{i,2} \,] \equiv e_i^T, \tag{5.58}$$

$$\Lambda = \begin{bmatrix} 0 & 1 \\ -\lambda_1 & -\lambda_2 \end{bmatrix}, \tag{5.59}$$

then,

$$\dot{E}_{i,1} = E_{i,1}\Lambda^T + r_i. \tag{5.60}$$

Note that Λ is Hurwitz. Therefore, given any symmetric and positive-definite matrix P_i, a positive real number β_i exists such that

$$\Lambda^T P_i + P_i \Lambda = -\beta_i I, \tag{5.61}$$

where I is the identity matrix.

5.2.1 The Adaptive and Distributed Controller Design

The energy function

$$V_{ri} = \frac{1}{2}\frac{r_i^2}{g_i} \tag{5.62}$$

is considered [9]. This function is later used to design the adaptive control input u_i. The energy function V_{ri} will be used to develop a Lyapunov function. The developed Lyapunov function will be exploited to prove that the designed control input synchronizes the output voltage magnitudes of DGs. The adaptive control input u_i should be chosen such that the derivative of the developed Lyapunov function be locally negative definite.

Differentiating V_{ri} and replacing $\dot{r}_i$ from (5.57) yield

$$\begin{aligned} \dot{V}_{ri} = {} & \frac{1}{2}\left(-g_{i0} + \frac{-\dot{g}_i}{g_i^2}\right) r_i^2 + r_i g_i^{-1}\left(-\sum_{j \in N_i} a_{ij}(f_j + g_j u_j)\right) \\ & + r_i g_i^{-1}\left(\lambda_1 e_{i,2} + (d_i + b_i)(f_i + g_i u_i) + \frac{g_i g_{i0} r_i}{2}\right), \end{aligned} \tag{5.63}$$

or equivalently

$$\dot{V}_{ri} = \frac{1}{2}\left(-g_{i0} + \frac{-\dot{g}_i}{g_i^2}\right) r_i^2 + r_i\bar{f}_i + r_i\bar{g}_i + r_i(d_i + b_i)u_i, \tag{5.64}$$

where

$$\bar{f}_i = \frac{\lambda_1 e_{i,2} + (d_i + b_i)f_i}{g_i} + \frac{g_{i0} r_i}{2} \tag{5.65}$$

is a function of the local information available at the *i*th DG, and

$$\bar{g}_i = -\frac{\sum_{j \in N_i} a_{ij}(f_j + g_j u_j)}{g_i} \tag{5.66}$$

is a function of the state variables of the *i*th DG and the state variables of its neighboring DGs on the communication digraph.

To facilitate the adaptive control design, NNs are used to compensate for the nonlinear dynamics of $\bar{f}_i$ and $\bar{g}_i$ in (5.65) and (5.66) instead of the functions f_i and g_i in (5.52). The unknown nonlinear function $\bar{f}_i$ is approximated on a prescribed compact set $\Omega_{\bar{f}}$ by the linear-in-parameter NN [6]

$$\bar{f}_i = W_{\bar{f}_i}^T \phi_{\bar{f}_i}(e_{i,1}, e_{i,2}, x_i) + \varepsilon_{\bar{f}_i}, \tag{5.67}$$

where the NN weight vector is $W_{\bar{f}_i} \in R^{l_{\bar{f}_i}}$, $\varepsilon_{\bar{f}_i}$ is the NN estimation error, and $\phi_{\bar{f}_i} \in R^{l_{\bar{f}_i}}$ consists of a set of $l_{\bar{f}_i}$ basis functions. The NN structure is shown in Fig. 5.25a. As shown in this figure, $e_{i,1}$, $e_{i,2}$, and x_i are the NN inputs and $\hat{W}_{\bar{f}_i}^T \phi_{\bar{f}_i}$ is the NN output. The estimations of weight vectors are denoted as $\hat{W}_{\bar{f}_i}$. The error of the NN weights is defined as $\tilde{W}_{\bar{f}_i}^T = \hat{W}_{\bar{f}_i}^T - W_{\bar{f}_i}^T$. The unknown nonlinear function $\bar{g}_i$ is approximated by linear-in-parameter NNs

$$\bar{g}_i = W_{\bar{g}i}^T \phi_{\bar{g}_i}(x_i, r_{-i}, x_{-i}, \hat{W}_{\bar{f}_{-i}}, \hat{W}_{\bar{g}_{-i}}) + \varepsilon_{\bar{g}_i}, \tag{5.68}$$

where the NN weight vector is $W_{\bar{g}_i} \in R^{l_{\bar{g}_i}}$,$\varepsilon_{\bar{g}_i}$ is the NN estimation error, and $\phi_{\bar{g}_i} \in R^{l_{\bar{g}_i}}$ consists of a set of $l_{\bar{g}_i}$basis functions. The NN structure is shown in Fig. 5.25b. As shown in this figure, x_i, r_{-i}, x_{-i}, $\hat{W}_{\bar{f}_{-i}}$, and $\hat{W}_{\bar{g}_{-i}}$ are the NN inputs and $\hat{W}_{\bar{g}_i}^T \phi_{\bar{g}_i}$ is the NN output. The estimations of weight vectors are denoted as $\hat{W}_{\bar{g}_i}$. The terms $r_{-i}, x_{-i}, \hat{W}_{\bar{f}_{-i}}$, and $\hat{W}_{\bar{g}_{-i}}$ are the sliding mode error, states, and the NN estimated weight vectors of the neighbors of *i*th DG on the communication digraph, respectively. The error of the NN weights is defined as $\tilde{W}_{\bar{g}_i}^T = \hat{W}_{\bar{g}_i}^T - W_{\bar{g}_i}^T$.

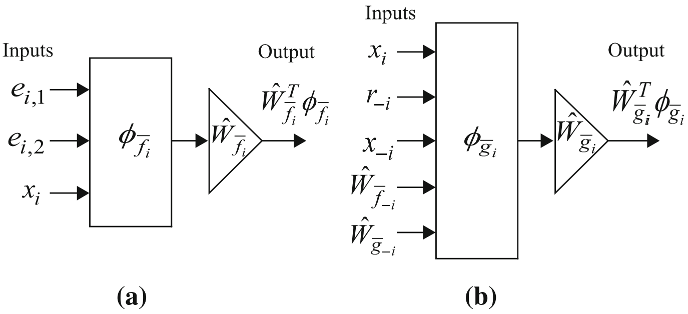

Fig. 5.25 NN structure for estimating (**a**) $\bar f_i$ and (**b**) $\bar g_i$. © [2016] IEEE. Reprinted, with permission, from IEEE Transactions on Energy Conversion [5]

Remark 5.2 Considering Stone–Weierstrass approximation theorem [10], positive numbers $W_{\bar f_i}^M$, $\varepsilon_{\bar f_i}^M$, $W_{\bar g_i}^M$, and $\varepsilon_{\bar g_i}^M$ exist such that $\left|W_{\bar f_i}\right| \le W_{\bar f_i}^M$, $\left|\varepsilon_{\bar f_i}\right| \le \varepsilon_{\bar f_i}^M$, $\left|W_{\bar g_i}\right| \le W_{\bar g_i}^M$, and $\left|\varepsilon_{\bar g_i}\right| \le \varepsilon_{\bar g_i}^M$.

Definition 5.1 The Y_i are cooperative uniformly ultimately bounded (UUB) with respect to Y_0 if there exists a compact set $\Omega \subset R^r$ such that $\forall (Y_i(t_0) - Y_0(t_0)) \in \Omega$, there exists a bound B and a time $t_f(B, (Y_i(t_0) - Y_0(t_0)))$, both independent of t_0, where $\|Y_i(t_0) - Y_0(t_0)\| \le B$, $\forall t > t_0 + t_f$ [5].

Lemma 5.1 The commensurate reformulated dynamics of DGs in (5.52) are considered. Let the digraph Gr contain a spanning tree and $b_i \neq 0$ for at least one root node. It is assumed that the internal dynamics are asymptotically stable. Supposed that the control inputs are chosen as [5]

$$u_i = -c_i r_i - \frac{\hat W_{\bar f_i}^T \phi_{\bar f_i}}{d_i + b_i} - \frac{\hat W_{\bar g_i}^T \phi_{\bar g_i}}{d_i + b_i}, \tag{5.69}$$

where c_i is the coupling gain, and the tuning laws are chosen as

$$\dot{\hat W}_{\bar f_i} = F_{\bar f_i} \phi_{\bar f_i} r_i - \kappa_{\bar f_i} F_{\bar f_i} \hat W_{\bar f_i}, \tag{5.70}$$

$$\dot{\hat W}_{\bar g_i} = F_{\bar g_i} \phi_{\bar g_i} r_i - \kappa_{\bar g_i} F_{\bar g_i} \hat W_{\bar g_i}, \tag{5.71}$$

where the arbitrary positive definite matrices $F_{\bar f_i} \in R^{l_{\bar f_i} \times l_{\bar f_i}}andF_{\bar g_i} \in R^{l_{\bar g_i} \times l_{\bar g_i}}$ and the coefficients $\kappa_{\bar f_i}$and$\kappa_{\bar g_i} > 0$ are design parameters. Then, Y_i is cooperative UUB with respect to Y_0 and, hence, the direct term of DG output voltages v_{odi} synchronizes to v_{ref}, if c_i is chosen as

$$c_i > \frac{\bar{\sigma}^2(P_i)}{2\beta_i(d_i + b_i)}. \tag{5.72}$$

where $\bar{\sigma}(P_i)$ denotes the maximum singular value of P_i in (5.61), and β_i is calculated from (5.61).

Proof The Lyapunov function candidate for each agent is considered as

$$V_i = \frac{1}{2}\frac{r_i^2}{g_i} + \frac{1}{2}\tilde{W}_{\bar{f}_i}^T F_{\bar{f}_i}^{-1}\tilde{W}_{\bar{f}_i} + \frac{1}{2}\tilde{W}_{\bar{g}_i}^T F_{\bar{g}_i}^{-1}\tilde{W}_{\bar{g}_i} + \frac{1}{2}E_{i1}P_iE_{i1}^T. \tag{5.73}$$

The derivative of V_i is written as

$$\begin{aligned} \dot{V}_i = {} & \frac{1}{2}\left(-g_{i0} + \frac{-\dot{g}_i}{g_i^2}\right)r_i^2 + r_i\bar{f}_i + r_i\bar{g}_i + r_i(d_i + b_i)u_i \\ & + \tilde{W}_{\bar{f}_i}^T F_{\bar{f}_i}^{-1}\dot{\hat{W}}_{\bar{f}_i} + \tilde{W}_{\bar{g}_i}^T F_{\bar{g}_i}^{-1}\dot{\hat{W}}_{\bar{g}_i} + \dot{E}_{i1}P_iE_{i1}^T. \end{aligned} \tag{5.74}$$

Placing (5.69), (5.70), (5.71), and (5.60) into (5.74) yields

$$\begin{aligned} \dot{V}_i = {} & \frac{1}{2}\left(-g_{i0} + \frac{-\dot{g}_i}{g_i^2}\right)r_i^2 - c_i(d_i + b_i)r_i^2 - \kappa_{\bar{f}_i}\tilde{W}_{\bar{f}_i}^T W_{\bar{f}_i} - \kappa_{\bar{f}_i}\left|\tilde{W}_{\bar{f}_i}\right|^2 \\ & - \kappa_{\bar{g}_i}\tilde{W}_{\bar{g}_i}^T W_{\bar{g}_i} - \kappa_{\bar{g}_i}\left|\tilde{W}_{\bar{g}_i}\right|^2 + E_{i1}\Lambda^T P_i E_{i1}^T + r_i P_i E_{i1}^T + \varepsilon_{\bar{f}_i} + \varepsilon_{\bar{g}_i}. \end{aligned} \tag{5.75}$$

Placing (5.61) into (5.75) yields

$$\begin{aligned} \dot{V}_i = {} & \frac{1}{2}\left(-g_{i0} + \frac{-\dot{g}_i}{g_i^2}\right)r_i^2 - c_i(d_i + b_i)r_i^2 - \kappa_{\bar{f}_i}\tilde{W}_{\bar{f}_i}^T W_{\bar{f}_i} - \kappa_{\bar{f}_i}\left|\tilde{W}_{\bar{f}_i}\right|^2 \\ & - \kappa_{\bar{g}_i}\tilde{W}_{\bar{g}_i}^T W_{\bar{g}_i} - \kappa_{\bar{g}_i}\left|\tilde{W}_{\bar{g}_i}\right|^2 - \frac{\beta_i}{2}E_{i1}E_{i1}^T + r_i P_i E_{i1}^T + \varepsilon_{\bar{f}_i} + \varepsilon_{\bar{g}_i}. \end{aligned} \tag{5.76}$$

According to the Remarks 5.1 and 5.2

$$\begin{aligned} \dot{V} \leq {} & -c_i(d_i + b_i)r_i^2 + \kappa_{\bar{f}_i}\left|\tilde{W}_{\bar{f}_i}\right|W_{\bar{f}_i}^M - \kappa_{\bar{f}_i}\left|\tilde{W}_{\bar{f}_i}\right|^2 + \kappa_{\bar{g}_i}\left|\tilde{W}_{\bar{g}_i}\right|^2 W_{\bar{g}_i}^M \\ & - \kappa_{\bar{g}_i}\left|\tilde{W}_{\bar{g}_i}\right|^2 - \frac{\beta_i}{2}|E_{i1}| + |r_i|\bar{\sigma}(P_i)|E_{i1}| + \varepsilon_{\bar{f}_i}^M + \varepsilon_{\bar{g}_i}^M. \end{aligned} \tag{5.77}$$

Equation (5.77) can be written as

$$\dot{V} \leq -H^T S H + G^T H, \tag{5.78}$$

where

$$H = \begin{bmatrix} |E_{i1}| & \left|\tilde{W}_{\bar{f}_i}\right| & \left|\tilde{W}_{\bar{g}_i}\right| & |r_i| \end{bmatrix}^T, \tag{5.79}$$

$$S = \begin{bmatrix} \frac{\beta_i}{2} & 0 & 0 & \frac{\bar{\sigma}(P_i)}{2} \\ 0 & \kappa_{\bar{f}_i} & 0 & 0 \\ 0 & 0 & \kappa_{\bar{g}_i} & 0 \\ \frac{\bar{\sigma}(P_i)}{2} & 0 & 0 & c_i(d_i + b_i) \end{bmatrix}, \tag{5.80}$$

$$G = \begin{bmatrix} 0 & \kappa_{\bar{f}_i} W_{\bar{f}_i}^M & \kappa_{\bar{g}_i} W_{\bar{g}_i}^M & 0 \end{bmatrix}^T. \tag{5.81}$$

If the following conditions hold,

1. S is positive definite, and
2. $\|H\| > \dfrac{\|G\|}{\underline{\sigma}(S)}$.

then $\dot{V}_i < 0$.

According to Sylvester's criterion, S is positive definite if

$$c_i > \frac{\bar{\sigma}^2(P_i)}{2\beta_i(d_i + b_i)}. \tag{5.82}$$

Since $\|G\|_1 \geq \|G\|_2 \geq \cdots \geq \|G\|_\infty$, the second condition holds if

$$\begin{cases} |E_{i1}| > \frac{\|G\|_1}{\underline{\sigma}(S)}, \\ \left|\tilde{W}_{\bar{f}_i}\right| > \frac{\|G\|_1}{\underline{\sigma}(S)}, \\ \left|\tilde{W}_{\bar{g}_i}\right| > \frac{\|G\|_1}{\underline{\sigma}(S)}, \\ |r_i| > \frac{\|G\|_1}{\underline{\sigma}(S)}. \end{cases} \tag{5.83}$$

where $\underline{\sigma}(S)$ is the minimum singular value of S.

Therefore, the sliding mode error and the NN weight approximation errors are ultimately bounded by $\frac{\|G\|_1}{\underline{\sigma}(S)}$. Since the sliding mode errors are ultimately bounded, the local neighborhood tracking errors in (5.53) are also bounded [8]. According to Lemma 4.3, δ_i are also ultimately bounded, and hence, all Y_i are cooperative UUB with respect to Y_0, and hence, the direct term of DG output voltages v_{odi} synchronizes to v_{ref}. This completes the proof.

Remark 5.3 The coupling gain affects the controller speed; the greater value of c_i increases the controller synchronization speed. Additionally, the synchronization speed is affected by λ_1 and λ_2 in (5.55). Greater value of λ_2 with respect to λ_1 forces the local neighborhood tracking error $e_{i,m}$ to converge to zero faster and, hence, increases the synchronization speed. The neural network weight estimations, $\hat{W}_{\bar{f}_i}$

and $\hat{W}_{\bar{g}_i}$, are the adaptive weights in the control law in (5.69). They are tuned adaptively online in real time, without manual intervention, using the tuning laws in (5.70) and (5.71). By contrast, $F_{\bar{f}_i} \in R^{l_{\bar{f}_i} \times l_{\bar{f}_i}}$, $F_{\bar{g}_i} \in R^{l_{\bar{g}_i} \times l_{\bar{g}_i}}$, $\kappa_{\bar{f}_i}$, and $\kappa_{\bar{g}_i}$ in the tuning laws in (5.70) and (5.71) are the fixed design constants that are selected by the designer to obtain suitable convergence properties of the adaptive tuning laws. The design constants $F_{\bar{f}_i} \in R^{l_{\bar{f}_i} \times l_{\bar{f}_i}}$, $F_{\bar{g}_i} \in R^{l_{\bar{g}_i} \times l_{\bar{g}_i}}$, $\kappa_{\bar{f}_i}$, and $\kappa_{\bar{g}_i}$ are kept fixed through all the contingencies. By contrast, the adaptive weights, namely the tunable weights $\hat{W}_{\bar{f}_i}$ and $\hat{W}_{\bar{g}_i}$, are automatically adapted online in real time using tuning laws in (5.70) and (5.71), without manual intervention, in response to changes in system operating conditions.

Remark 5.4 As shown in (5.69), the secondary control of a DG is a function of r_i, $\phi_{\bar{f}_i}$, and $\phi_{\bar{g}_i}$. r_i, the sliding mode error defined in (5.55), is a function of the output voltage magnitude of each DG and the output voltage magnitude of its neighbors on the communication digraph and their first derivatives. $\phi_{\bar{f}_i}$, the basis functions used to compensate for the nonlinearities in $\bar{f}_i$ in (5.65), are functions of state variables of each DG. $\phi_{\bar{g}_i}$, the basis functions used to compensate for the nonlinearities in $\bar{g}_i$ in (5.66), are functions of state variables of each DG and its neighbors on the communication digraph.

The block diagram of the adaptive and distributed secondary voltage control is shown in Fig. 5.26. In this figure, $\phi_{\bar{f}_i}$ and $\phi_{\bar{g}_i}$ are the NN basis functions introduced in (5.67) and (5.68). The proposed control is fully independent of the DG parameters and the connector specifications. Therefore, the performance of the secondary control does not deteriorate by the change in DG parameters (e.g., due to aging or thermal effects.). Additionally, extensive studies are not required to tune the control parameters.

5.2.2 *Case Studies*

The islanded microgrid shown in Fig. 4.5 is used to verify the effectiveness of the proposed voltage control framework. The specifications of DGs, lines, and loads are summarized in Chap. 4. Due to the adaptive nature of the proposed methodology, the specifications of DGs are not required for the controller implementation. However, these specifications are required to model DGs in the simulations. In this Appendix, K_{PV}, K_{IV}, K_{PC}, and K_{IC} are the voltage and current controller parameters based on the detailed models discussed in Chap. 4. In the following, the simulation results are presented for four different cases. In the first three cases, a fixed communication topology is assumed, while the last case deals with a time-varying communication topology. In the first case, namely *Case* 1, the proposed secondary voltage control restores the DG voltage amplitude to the nominal voltage subsequent to the islanding process. In *Case* 2, the effectiveness of the adaptive voltage control subsequent to the changes in DG parameters is studied. *Case* 3 deals with

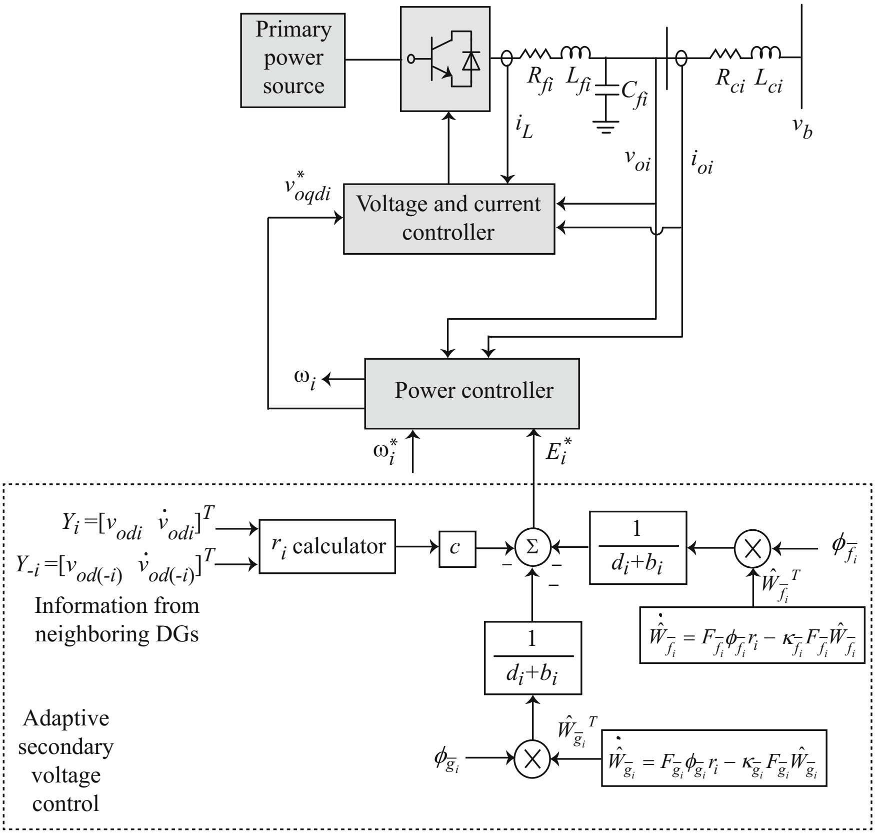

Fig. 5.26 The block diagram of the adaptive and distributed secondary control. © [2016] IEEE. Reprinted, with permission, from IEEE Transactions on Energy Conversion [5]

the voltage restoration subsequent to sudden load changes. The last case, namely *Case* 4, studies the proposed controller with a time-varying communication topology. For all cases, the NN tuning parameters are set to $F_{\bar{f}_i} = 10 \times I_{\bar{f}_i}$, $F_{\bar{g}_i} = 10 \times I_{\bar{g}_i}$ (I_N is an $N \times N$ identity matrix.), $\kappa_{\bar{f}_i} = 10$, and $\kappa_{\bar{g}_i} = 10$.

Case 1 In this case, it is assumed that the microgrid is islanded from the main grid at t = 0, and the secondary control is applied at t = 0.6 s. In practical applications, the voltage control should be applied immediately after the disturbance occurs. However, in this case, the secondary controller is intentionally delayed by 0.6 s to highlight its effectiveness. It is assumed that the DGs communicate with each other through the communication links depicted in Fig. 5.27. DGs 1 and 2 have two

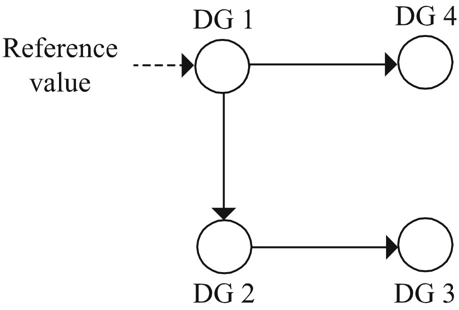

Fig. 5.27 The communication digraph for *Case* 1, *Case* 2, *and Case* 3. © [2016] IEEE. Reprinted, with permission, from IEEE Transactions on Energy Conversion [5]

communication ports: input and output ports. The associated adjacency matrix of the communication network in Fig. 5.27 is

$$A_G = \begin{bmatrix} 0 & 0 & 0 & 0 \\ 1 & 0 & 0 & 0 \\ 0 & 1 & 0 & 0 \\ 1 & 0 & 0 & 0 \end{bmatrix} \tag{5.84}$$

DG 1 is the only DG that is connected to the leader node with the pinning gain $b_1 = 1$. The coupling gain in (5.69) is $c_i = 4$ which satisfies (5.72). λ_1 and λ_2 in (5.55) are chosen as $\lambda_1 = 10$ and $\lambda_2 = 1$.

Figure 5.28 shows the simulation results when the reference voltage value v_{ref} is set to 1 pu. As shown in Fig. 5.28, while the primary control keeps the voltage stable, the secondary control returns all terminal voltage amplitudes to the pre-specified reference values in less than 0.6 s.

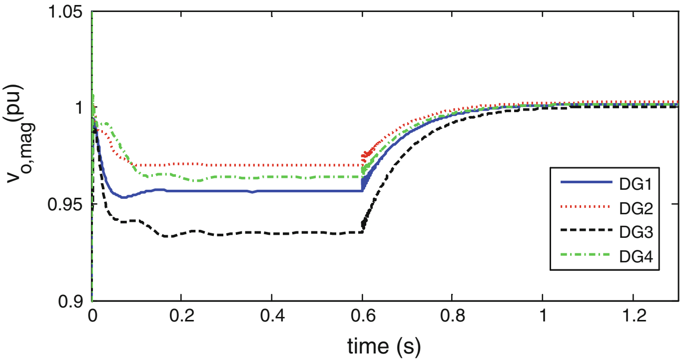

Fig. 5.28 DG output voltage magnitudes for *Case* 1 when $v_{\text{ref}} = 1$ pu. © [2016] IEEE. Reprinted, with permission, from IEEE Transactions on Energy Conversion [5]

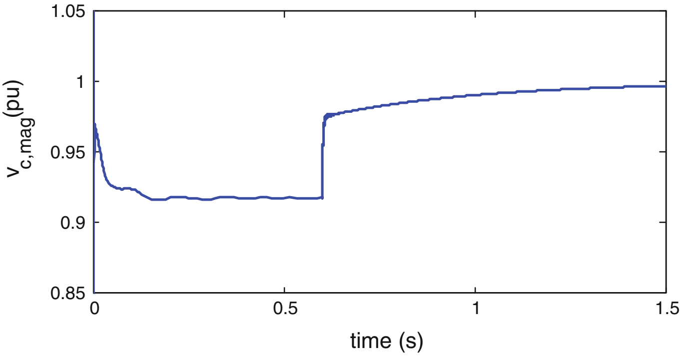

Fig. 5.29 The voltage magnitude of critical bus for *Case* 1. © [2016] IEEE. Reprinted, with permission, from IEEE Transactions on Energy Conversion [5]

The secondary voltage control can be defined to control the voltage magnitude of the critical bus shown in Fig. 4.5. As shown in Fig. 5.29, the secondary control returns the voltage magnitude of critical bus to v_{nominal} in less than 1 s.

According to Remark 5.2, the control parameters c_i, λ_1, and λ_2 have a direct impact on the synchronization speed of the secondary voltage control. Figure 5.30 shows the simulation results when $c_i = 40$, $\lambda_1 = 100$, and $\lambda_2 = 1$. As shown in this figure, the secondary control is applied at $t = 0.6$ s and returns all terminal voltage amplitudes to $v_{ref} = 1$ pu in less than 0.05 s.

Case 2 In this case, the performance of proposed distributed and adaptive voltage control is verified subsequent to the changes in DG parameters. It is assumed that the secondary voltage control is applied at $t = 0.6$ s, and the resistance and inductance of the output connector of each DG, r_c and L_c, change from 0.03 Ω and 0.35 mH to 0.06 Ω and 0.7 mH at $t = 1$ s. As shown in Fig. 5.31, the performance of the adaptive voltage control does not deteriorate as a result of the changes in r_c and L_c and the DG voltage magnitude restoration to the nominal voltage is provided.

Case 3 Fig. 5.32 shows the simulation results considering the load changes in an islanded microgrid. Initially, the secondary voltage control is applied at $t = 0.6$ s. It is assumed that the initial resistance of loads 1 and 2 is 5 Ω, and the initial inductance of loads 1 and 2 are 16 mH. At $t = 1$ s, load 1 resistance and inductance change from 5 Ω and 16 mH to 3 Ω and 6.4 mH, respectively, and load 2 resistance and inductance change from 5 Ω and 16 mH to 2 Ω and 3.2 mH, respectively. To show the effectiveness of the adaptive voltage control under load changes, it is assumed that the secondary voltage control is halted for 0.2 s. As shown in Fig. 5.32, once the voltage control is stopped at $t = 1$ s, the voltage magnitudes drop due to the sudden load changes. However, at $t = 1.2$ s, the voltage

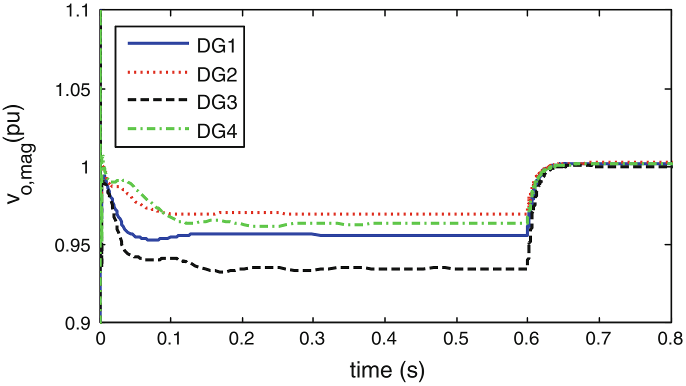

Fig. 5.30 DG output voltage magnitudes for *Case* 1 when $v_{\text{ref}} = 1$ pu, $c_i = 40$, $\lambda_1 = 100$, and $\lambda_2 = 1$. © [2016] IEEE. Reprinted, with permission, from IEEE Transactions on Energy Conversion [5]

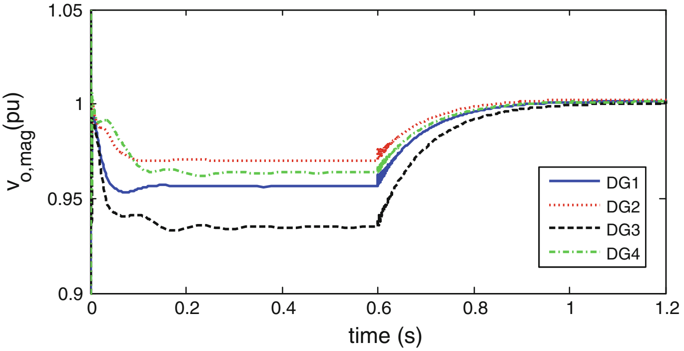

Fig. 5.31 DG output voltage magnitudes for *Case* 2. © [2016] IEEE. Reprinted, with permission, from IEEE Transactions on Energy Conversion [5]

control is applied again and returns the voltage magnitude of DGs to 1 pu, as shown in Fig. 5.32. Therefore, the performance of the adaptive voltage control does not deteriorate as a result of the load changes, and the adaptive voltage control effectively restores the output voltage magnitude of the DGs to the nominal voltage.

Case 4 In this case, it is assumed that the microgrid is islanded from the main grid at $t = 0$, and the secondary control is applied at $t = 0.6$ s. (Similar to *Case 1*, the voltage control is applied after 0.6 s to highlight the effectiveness of the proposed voltage control.) However, as opposed to *Case* 1, the voltage controller is implemented through a time-varying communication network. Figure 5.33 shows the

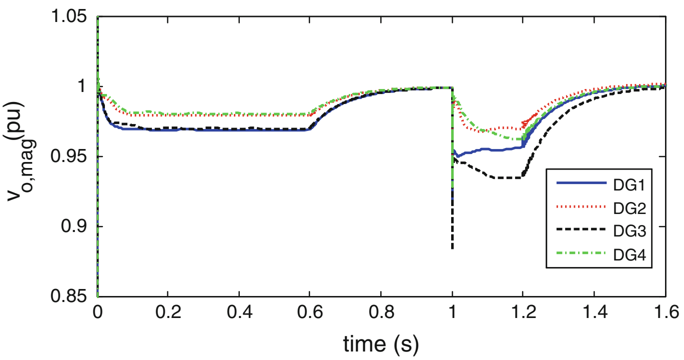

Fig. 5.32 DG output voltage magnitudes for *Case* 3. © [2016] IEEE. Reprinted, with permission, from IEEE Transactions on Energy Conversion [5]

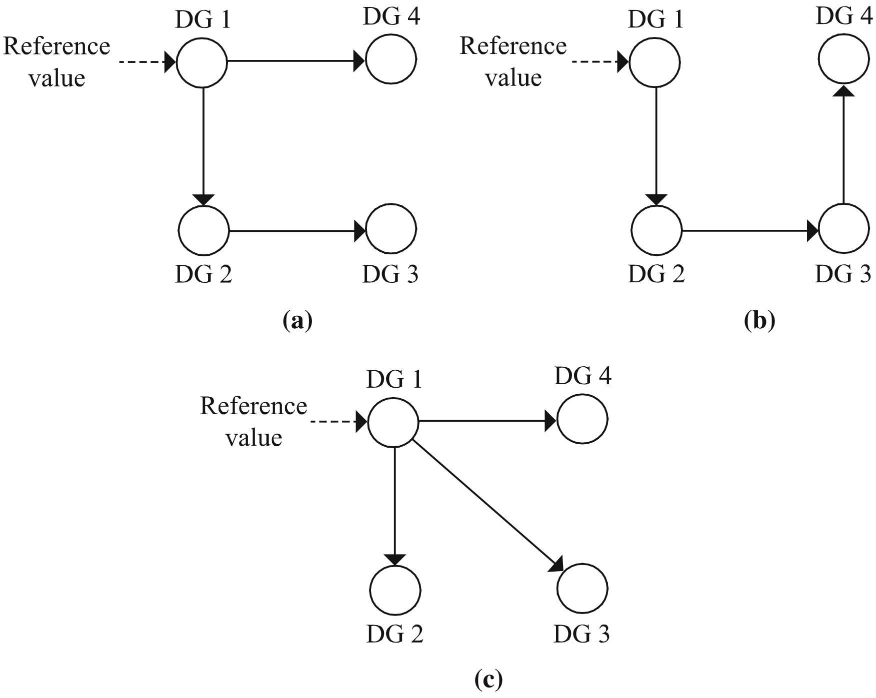

Fig. 5.33 The digraphs for modeling the time-varying communication network of *Case* 4. © [2016] IEEE. Reprinted, with permission, from IEEE Transactions on Energy Conversion [5]

three communication network structures that are used in simulation. Each structure is adopted at a specific time interval. The communication digraph in Fig. 5.33(a) models the communication network over the time interval [(0.6 + 0.15 k) s, (0.6 + 0.15 k) + 0.05 s], for k = 0,1,…. The communication digraph in Fig. 5.33b

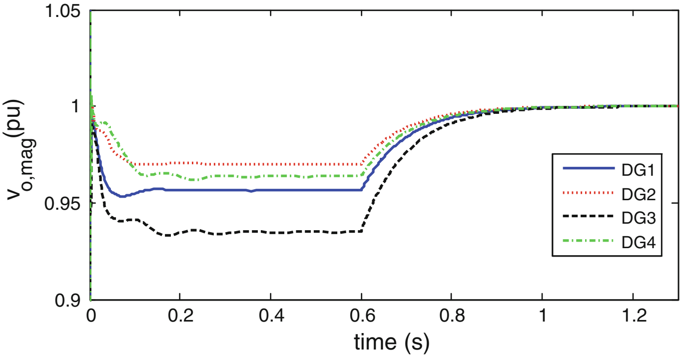

Fig. 5.34 DG output voltage magnitudes for *Case* 4. © [2016] IEEE. Reprinted, with permission, from IEEE Transactions on Energy Conversion [5]

models the communication network over the time interval [(0.65 + 0.15 k) s, (0.65 + 0.15 k) + 0.05 s], for k = 0,1,… The communication digraph in Fig. 5.33c models the communication network over the time interval [(0.7 + 0.15 k) s, (0.7 + 0.15 k) + 0.05 s], for k = 0,1,….

DG 1 is the only DG that is connected to the leader node with the pinning gain $b_1 = 1$. The coupling gain in (5.69) is $c_i = 4$ which satisfies (5.72). λ_1 and λ_2 in (5.55) are chosen as $\lambda_1 = 10$ and $\lambda_2 = 1$. Figure 5.34 shows the simulation results when the reference voltage value is set to 1 pu. As shown in Fig. 5.34, the secondary control returns all terminal voltage amplitudes to the prespecified reference value in less than half a second. Compared with the simulation results of *Case* 1, Fig. 5.34 shows that the proposed secondary control appropriately works with time-varying communication networks.

References

1. Bidram A, Davoudi A, Lewis F (2014) A multi-objective distributed control framework for islanded microgrids. IEEE Trans Ind Inform 10:1785–1798
2. Chung SK (2000) A phase tracking system for three phase utility interface inverters. IEEE Trans Power Electron 15:431–438
3. Qu Z (2009) Cooperative control of dynamical systems: applications to autonomous vehicles. Springer-Verlag, New York
4. Mwakabuta N, Sekar A (2007) Comparative study of the IEEE 34 node test feeder under practical simplications. In: Proceedings of the 39th North American Power Symposium, Sept 2007
5. Bidram A, Davoudi A, Lewis FL, Ge SS (2014) Distributed adaptive voltage control of inverter-based microgrids. IEEE Trans Energy Convers 29:862–872
6. Lewis FL, Jagannathan S, Yesildirek A (1999) Neural network control of robot manipulators and nonlinear systems. Taylor and Francis, London
7. Das A, Lewis FL (2010) Distributed adaptive control for synchronization of unknown nonlinear networked systems. Automatica 46:2014–2021

8. Zhang H, Lewis FL (2012) Adaptive cooperative tracking control of higher-order nonlinear systems with unknown dynamics. Automatica 48:1432–1439
9. Cui R, Ren B, Ge SS (2012) Synchronised tracking control of multi-agent system with high-order dynamics. IET Control Theory Appl 6:603–614
10. Stone MH (1948) The generalized Weierstrass approximation theorem. Math Mag 21 (4/5):167–184/237–254

Chapter 6
Droop-Free Distributed Control of AC Microgrids

The droop mechanism, or its variations [1–9], is a common decentralized approach to realize the primary control, although alternative methods (e.g., virtual oscillator control [10–13]) are emerging. It emulates virtual inertia for AC systems and mimics the role of governors in traditional synchronous generators [14]. Despite simplicity, the droop mechanisms suffers from (1) load-dependent frequency/voltage deviation, (2) poor performance in handling nonlinear loads [15], and (3) poor reactive power sharing in presence of unequal bus voltages [16]. Unequal bus voltages are indispensible in practical systems to perform the scheduled reactive power flow. Droop techniques cause voltage and frequency deviations, and thus, a supervisory secondary control is inevitable to update the set points of the local primary controls [17]. Such architecture requires two-way high bandwidth communication links between the central controller and each inverter. This protocol adversely affects the system reliability as failure of any communication link hinders the functionality of the central controller and, thus, the entire microgrid. The central controller itself is also a reliability risk, since it imposes a single point of failure. Scalability is another issue for that it adds to the complexity of the communication network, and it requires updating the settings of the central controller.

Spatially dispersed inverter-based microgrids naturally lend themselves to distributed control techniques to address their synchronization and coordination requirements. Distributed control architectures can discharge duties of a central controller while being resilient to faults or unknown system parameters. Distributed synchronization processes necessitate that each agent (i.e., the inverter) exchange information with other agents according to some restricted communication protocol [18, 19]. These controllers can use a sparse communication network and feature reduced computational complexity at each inverter controller [20]. Networked control of parallel inverters in [21, 22] embeds the functionality of the secondary control in all inverters, i.e., it requires a fully connected communication network.

A. Bidram et al., *Cooperative Synchronization in Distributed Microgrid Control*,
Advances in Industrial Control, DOI 10.1007/978-3-319-50808-5_6

The master node in the networked master-slave methods [23–25] is still a single point of failure. Distributed cooperative control is recently introduced for AC [26, 27] and DC microgrids [28–31]. Distributed control of AC microgrids are also discussed in [32–34] (using a ratio-consensus algorithm), [35] (a multi-objective approach), and [36–39] (using a distributed averaging proportional controller). Majority of such approaches are based on the droop mechanism (and, thus, inherit its shortcoming), require system information (e.g., number of inverters, inverter parameters and total load demand), require frequency measurement, and mainly handle active power sharing and frequency regulation (or, only reactive power sharing/voltage control). Studies in [27, 35] investigate distribution networks with negligible line impedances and, potentially, can lack satisfactory performance in practical multi-terminal distribution systems with intricate and lossy transmission networks. Moreover, the solutions focus on the islanded mode of operation and their extension to grid-connected mode is not straightforward.

This chapter provides a comprehensive distributed cooperative solution that satisfies both the secondary and the primary control objectives for an autonomous AC microgrid without relying on the droop mechanism. Herein, each inverter is considered as an agent of a multi-agent system (i.e., the microgrid); each inverter exchanges data with a few other neighbor inverters and processes the information to update its local voltage set points and synchronize their normalized power and frequencies. The controller includes three modules: voltage regulator, reactive power regulator, and active power regulator. The salient features of this control method are as follows:

- Cooperation among inverters on a communication graph provides two voltage correction terms to be added to the rated voltage and adjust the local voltage set points of individual inverters.
- Cooperation among voltage, reactive power, and active power regulators effectively carries out global voltage regulation, frequency synchronization, and proportional load sharing, particularly, in practical networks where the transmission/ distribution line impedances are not negligible.
- The voltage regulator seeks to adjust the average voltage across the microgrid, rather than the individual inverter busses, at the rated voltage value, and ensures global voltage regulation without the need to run a power flow analysis.
- The control method does not employ any droop mechanism and does not require any frequency measurement.
- The presented scheme does not require prior knowledge of system parameters or the number of inverters. Thus, it features scalability, modularity, robustness, and plug-and-play capability.
- A sparse communication graph suffices the limited message passing among inverters. This is in direct contrast with the centralized control approaches that require high-bandwidth bidirectional communication networks.

6.1 Droop-Free Cooperative Control Framework

6.1.1 *Microgrid as a Cyber-Physical System*

A distribution network is an electric network that provides the physical connection between sources and loads within a microgrid. Such a physical system can be equipped with a cyber network to exploit different control opportunities. Interaction of the sources (i.e., inverter-augmented sources) in the cyber domain offers cooperative decision making, which features scalability and improves reliability. Here, a microgrid is assumed to be a cyber-physical system with a communication network that facilitates data exchange among sources for control and monitoring purposes. Figure 6.1a illustrates physical and cyber layers of the microgrid. Each source broadcasts its information, e.g., voltage and power measurements, to a few selected sources, called its *neighbors*. As oppose to the centralized/supervisory control, this communication layout forms a sparse network; not all sources need to communicate.

From the control perspective, a multi-agent cyber-physical system can be expressed with a graphical representation with active agents (sources) modeled as nodes of the graph and communication links mapped to edges connecting nodes (see Fig. 6.1b). Communication links may not be reciprocal, forming a directed

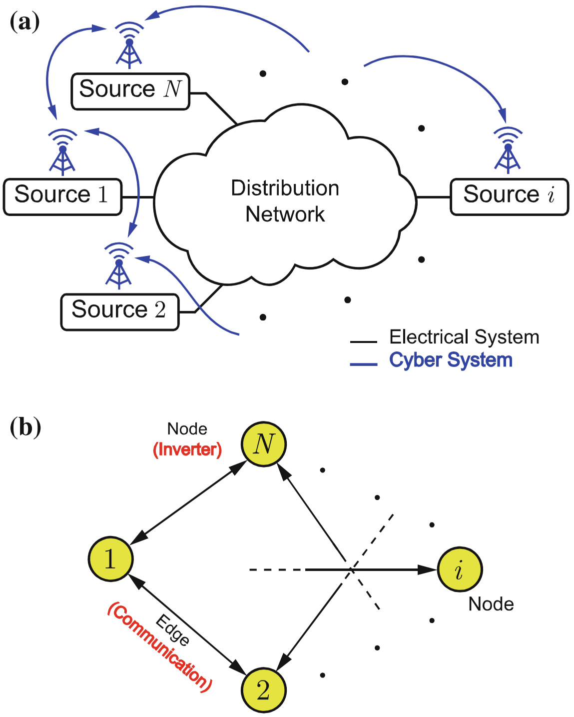

Fig. 6.1 General layout of an AC microgrid: **a** sources supplying the grid system with communication infrastructure spanned across the grid, **b** graphical representation of the cyber-physical. © [2016] IEEE. Reprinted, with permission, from IEEE Transactions on Power Electronics [54]

graph (digraph). Each node and edge inherits the dynamic model of the corresponding agent and communication channel, respectively. Information links may exchange data with different gains referred to as the *communication weights*. For example, if Node j broadcasts data x_j to Node i through a link with a designated weight of $a_{ij} > 0$, then, the information received at Node i is $a_{ij}x_j$. Generally, $a_{ij} > 0$ if Node i receives data from Node j and $a_{ij} = 0$, otherwise. This graph is represented by the adjacency matrix $\mathbf{A_G} = \left[a_{ij}\right] \in \mathbb{R}^{N \times N}$ that carries the communication weights, where N is the number of dispatchable sources. Communication weights can be time varying and may include some channel delay; however, this study assumes time-invariant and scalar adjacency matrix. N_i denotes the set of all neighbors of Node i. The in-degree and out-degree matrices, $\mathbf{D}^{\text{in}} = \text{diag}\left\{d_i^{\text{in}}\right\}$ and $\mathbf{D}^{\text{out}} = \text{diag}\left\{d_i^{\text{out}}\right\}$, are diagonal matrices with $d_i^{\text{in}} = \sum_{j \in N_i} a_{ij}$ and $d_i^{\text{out}} = \sum_{j \in N_i} a_{ji}$, respectively. The Laplacian matrix is defined as $\mathbf{L} \triangleq \mathbf{D}^{\text{in}} - \mathbf{A_G}$, whose eigenvalues determine the global dynamics of the entire system (i.e., the microgrid) [40, 41]. The Laplacian matrix is balanced if the in-degree and out-degree matrices are equal; particularly, an undirected (bidirectional) data network satisfies this requirement. A direct path from Node i to Node j is a sequence of edges that connects the two nodes. A digraph is said to have a spanning tree, if it contains a root node, from which, there exists at least a direct path to every other node. Here, a graph is called to carry the *minimum redundancy,* if it contains enough redundant links that, in the case of any single link failure, it remains connected and presents a balanced Laplacian matrix.

6.1.2 Cooperative Control Policy

The control method requires a communication graph with the adjacency matrix $\mathbf{A_G} = \left[a_{ij}\right] \in \mathbb{R}^{N \times N}$ that (1) has at least a spanning tree, (2) can be undirected or directional, yet with a balanced Laplacian matrix, and (3) the graph must carry the minimum redundancy. Communication weights, a_{ij}, are design parameters. Each source exchanges a vector of information, $\Psi_i = \left[\bar{e}_i, p_i^{\text{norm}}, q_i^{\text{norm}}\right]$, with its neighbor sources on the communication graph, where $\bar{e}_i$ is the estimation of the averaged voltage magnitude across the microgrid, calculated at Node i. $p_i^{\text{norm}} \triangleq p_i / p_i^{\text{rated}}$ and $q_i^{\text{norm}} \triangleq q_i / q_i^{\text{rated}}$ are the normalized active and reactive powers supplied by Source i. p_i and q_i are the measured active and reactive powers supplied by Source i, respectively, and p_i^{rated} and q_i^{rated} are the rated active and reactive powers of the same source. The control strategy attempts to share the total load demand among sources in proportion to their rated powers.

Objectives of the secondary/primary controller are (1) global voltage regulation, (2) frequency synchronization, (3) active power sharing, and (4) reactive power sharing. Generally, fine adjustment of the voltage magnitude and frequency can satisfy all four objectives. Particularly, active and reactive power flow can be

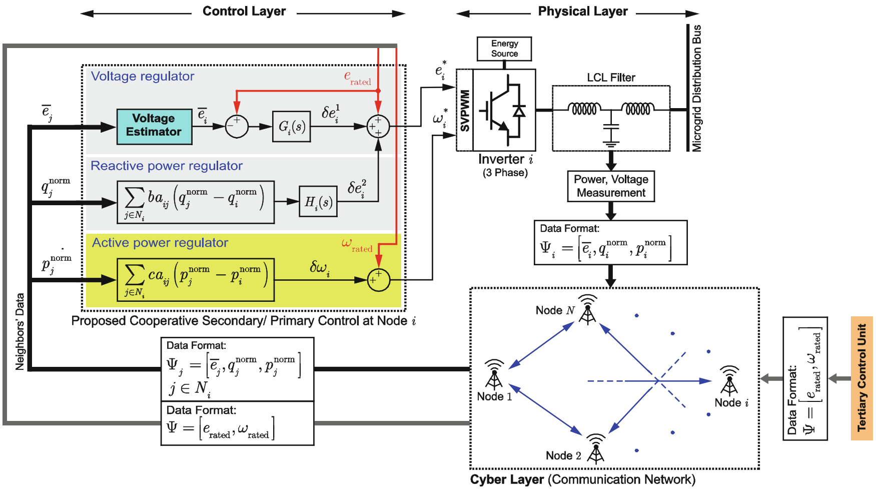

Fig. 6.2 Droop-free cooperative secondary control for the Source *i* of the AC microgrid. *Note* data exchange with the neighbor nodes. © [2016] IEEE. Reprinted, with permission, from IEEE Transactions on Power Electronics [54]

managed by tuning the frequency and voltage magnitude, respectively. The droop-free control method is established on this notion. Figure 6.2 shows the control routine for Node *i* (Source *i*). The controller consists of three separate modules: the voltage regulator, reactive power regulator, and active power regulator. The controller at Node *i* receives its neighbors' information, Ψ_js, and processes the neighbors' and local data, Ψ_i, to update its voltage set point. e_i^* and ω_i^* are the set points of the (line to neutral) voltage magnitude (rms value) and frequency, respectively. Accordingly, the Space Vector PWM module generates the actual voltage set point, v_i^*,

$$v_i^*(t) = e_i^*(t)\sqrt{2}\sin\left(\int_0^t \omega_i^*(\tau)\mathrm{d}\tau\right), \tag{6.1}$$

and assigns appropriate switching signals to drive the inverter module [42]. It should be noted that the controller is assumed activated at $t = 0$.

As seen in Fig. 6.2, each inverter is followed by an LCL filter to attenuate undesired (switching and line-frequency) harmonics. The set point in (6.1) is the reference voltage for the output terminal of the filtering module or, equivalently, the microgrid bus that corresponds to Source *i*.

The voltage and reactive power regulators adjust the set point of the voltage magnitude by producing two voltage correction terms, δe_i^1 and δe_i^2, respectively, as

$$e_i^*(t) = e_{\text{rated}} + \delta e_i^1(t) + \delta e_i^2(t), \tag{6.2}$$

where e_{rated} is the rated voltage of the microgrid. Regardless of the operating mode, i.e., islanded or grid-connected modes, the rated voltage can be safely assumed equal for all active nodes (dispatchable sources). The voltage regulator at Node i includes an estimator that finds the global averaged voltage magnitude, i.e., the averaged voltage across the microgrid. This estimation is, then, compared with the rated voltage, e_{rated}, and the difference is fed to a PI controller, G_i, to generate the first voltage correction term, δe_i^1, and, thus, handle global voltage regulation. Accordingly, the voltage regulators collectively adjust the average voltage of the microgrid on the rated value, yet individual bus voltages may slightly deviate from the rated value (typically, less than 5%). This deviation is essential in practice to navigate reactive power across the microgrid. Therefore, the reactive power regulator at Node i adjusts an additional (i.e., the second) voltage correction term, δe_i^2, to control the supplied reactive power. This module calculates the neighborhood reactive loading mismatch, mq_i,

$$mq_i = \sum_{j \in N_i} ba_{ij}(q_j^{\text{norm}} - q_i^{\text{norm}}), \tag{6.3}$$

which measures how far the normalized reactive power of the Source i is from the average of its neighbors'. The coupling gain b is a design parameter. The mismatch in (6.3) is then fed to a PI controller, H_i, (see Fig. 6.2) to adjust the second voltage correction term, δe_i^2, and, accordingly, mitigate the mismatch. Performance analysis in Sect. 6.2.5 will show that all the mismatch terms, in the steady state, converge to zero, and thus, all normalized reactive powers would synchronize. This satisfies the proportional reactive power sharing among sources.

The active power regulator at Source i controls its frequency and active power. This module calculates the neighborhood active loading mismatch to assign the frequency correction term, $\delta\omega_i$,

$$\delta\omega_i = \sum_{j \in N_i} ca_{ij}(p_j^{\text{norm}} - p_i^{\text{norm}}), \tag{6.4}$$

where the coupling gain c is a design parameter. As seen in Fig. 6.2, this correction term is added to the rated frequency, ω_{rated},

$$\omega_i^*(t) = \omega_{\text{rated}} + \delta\omega_i(t), \tag{6.5}$$

and, thus, (6.1) can be written as

$$v_i^*(t) = e_i^*(t)\sqrt{2}\sin\left(\omega_{\text{rated}}t + \int_0^t \delta\omega_i \mathrm{d}\tau\right). \tag{6.6}$$

Equation (6.6) helps to define the phase angle set point for Source i,

$$\delta_i^*(t) \triangleq c \int_0^t \sum_{j \in N_i} a_{ij}\left(p_j^{\text{norm}} - p_i^{\text{norm}}\right) \mathrm{d}\tau. \tag{6.7}$$

According to (6.6)–(6.7), the active power regulator module keeps the frequency at the rated value and fine tunes the phase angle set point, δ_i^*, to reroute the active power across the microgrid and mitigate the neighborhood active loading mismatch. It is shown in Sect. 6.2.5 that all phase angles, δ_i^*, will converge to their steady-state values, and thus, all frequency correction terms, $\delta\omega_i$, decay to zero. Therefore, the microgrid frequency synchronizes to the rated frequency, ω_{rated}, without any frequency measurement loop, while the controller stabilizes the phase angles, δ_i. Indeed, transient variations in the inverter frequency adjust its phase angle and control the active power flow; the frequency will not deviate from the rated value in the steady state. Thus, normalized active powers will synchronize, which provides the proportional active load sharing.

The droop-free controller is a general solution that can handle load sharing for variety of distribution systems; i.e., predominantly inductive, inductive-resistive, or primarily resistive networks. Indeed, the nature of the line impedances defines the role of the active and reactive power regulators for load sharing.

In particular, a predominantly inductive network naturally decouples the load sharing process; the reactive power regulator must handle the reactive load sharing by adjusting voltage magnitude while the active power regulator would handle the active load sharing through adjusting the frequency (or, equivalently, the phase angle). However, for other types of distribution network, active and reactive power flows are entangled to both voltage and phase angle adjustment. For such cases, the load sharing is a collaborative task where the two regulators (i.e., both the active and reactive power regulators) would work together to generate the desired set points.

The controller, so far, assumes fixed and known power rating for dispatchable sources. In a scenario that some sources are non-dispatchable, i.e., renewable energy sources with stochastic output power, the controller can be augmented with the methodology shown in Fig. 6.3. Supplied power by each stochastic source is measured and reported to an auxiliary control unit. This module runs optimization scenarios, e.g., Maximum Power Point Tracking (MPPT) , to decide the desired operating points. It also compares the desired generation with the actual supplied power and updates the rated powers, p_i^{rated} and q_i^{rated}, to address any mismatch. The control routine in Fig. 6.2 uses the tuned rated powers to adjust the voltage and frequency set points. With the modification in Fig. 6.3, the stochastic sources will be pushed to exploit their potentials (e.g., to produce maximum power) while the controller in Fig. 6.2 proportionally shares the remaining load demand among dispatchable sources.

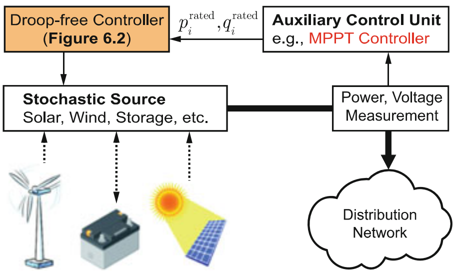

Fig. 6.3 Extension of the droop-free controller to non-dispatchable (e.g., stochastic) energy sources. © [2016] IEEE. Reprinted, with permission, from IEEE Transactions on Power Electronics [54]

In the islanded mode, the system operational autonomy requires preset (fixed) values for the rated voltage magnitude and frequency, e_{rated} and ω_{rated}, in all controllers. The voltage and frequency settings typically follow the standard ratings of the nearby electricity grid. To further extend operational availability of the droop-free controller to the grid-connected mode, one can consider adjustable voltage magnitude and frequency ratings. To this end, a tertiary controller (highlighted in Fig. 6.2) fine tunes such ratings. There is a single tertiary controller for the entire microgrid, and it uses the same communication network as the secondary controllers, to propagate updated voltage and frequency ratings to all secondary controllers across the microgrid. Functionality of the tertiary controller is elaborated in Fig. 6.4. The tertiary control unit runs cost/efficiency optimization to determine the desired active and reactive powers to be exchanged between the microgrid and the main grid, p_{d}^* and q_{d}^*, respectively.

The optimization scenarios can also account for auxiliary services such as frequency regulation or reactive power support. It is noteworthy that the power flow between the microgrid and the main grid can be bidirectional, and thus, the desired powers p_{d}^* and q_{d}^* can be either positive or negative. The controller compares the actual powers supplied to the main grid, p_{d} and q_{d}, with the desired values and, accordingly, updates voltage and frequency ratings sent to the secondary controllers. The steady-state rated voltage assignment, e_{rated}, may have slight deviation from the standard value; however, the steady-state value of the rated frequency, ω_{rated}, will always converge to the standard value (e.g., 60 Hz in the North America). In fact, it is the transient variations in the rated frequency that adjusts the phase angles across the microgrid and manages the active power flow.

6.1.3 Voltage Estimation Policy

Each node has an estimation module that develops the estimation of the averaged voltage magnitude across the microgrid, e.g., $\bar{e}_i$, for Node i, and exchanges this estimation with its neighbors. The voltage estimation policy is demonstrated in Fig. 6.5. Accordingly, the estimator at Node i updates its own output, $\bar{e}_i$, by processing the neighbors' estimates, $\bar{e}_j$s ($j \in N_i$), and the local voltage measurement, e_i,

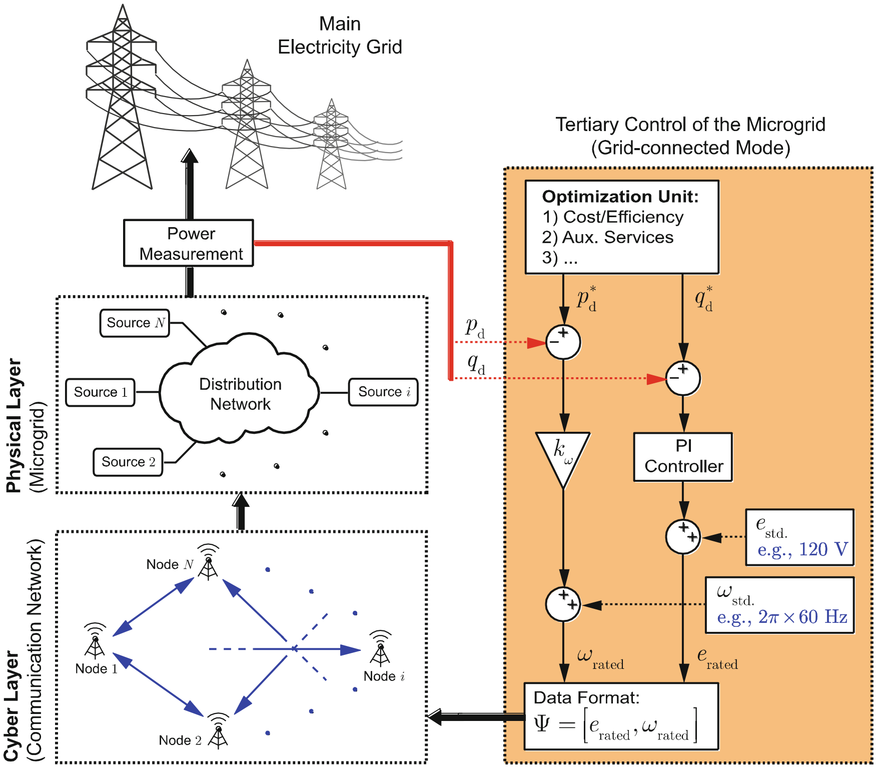

Fig. 6.4 Functionality of the tertiary controller in the grid-connected mode. © [2016] IEEE. Reprinted, with permission, from IEEE Transactions on Power Electronics [54]

$$\bar{e}_i(t) = e_i(t) + \int_0^t \sum_{j \in N_i} a_{ij}\left(\bar{e}_j(\tau) - \bar{e}_i(\tau)\right) \mathrm{d}\tau. \tag{6.8}$$

This updating policy is commonly referred to as the *dynamic consensus protocol* in the literature [43]. As seen in (6.8), the local measurement, e.g., e_i, is directly fed into the estimation protocol. Thus, in case of any voltage variation at Node i, the local estimate, $\bar{e}_i$, immediately responds. Then, the change in $\bar{e}_i$ propagates through the communication network and corrects all other estimations. Assume that $\mathbf{e} = \left[e_1, e_{2,}, \cdots, e_N\right]^{\mathrm{T}}$ and $\bar{\mathbf{e}} = \left[\bar{e}_1, \bar{e}_{2,}, \cdots, \bar{e}_N\right]^{\mathrm{T}}$ are the measured voltage and the estimated average voltage vectors, respectively. $\mathbf{E}$ and $\bar{\mathbf{E}}$ are the Laplace transforms of $\mathbf{e}$ and $\bar{\mathbf{e}}$, respectively. Accordingly, global dynamic response of the estimation policy is formulated in [29] as

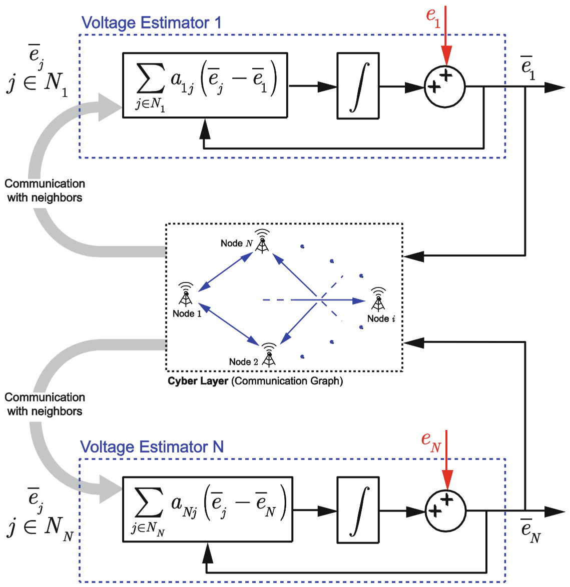

Fig. 6.5 Voltage averaging policy at each node; dynamic consensus protocol. © [2016] IEEE. Reprinted, with permission, from IEEE Transactions on Power Electronics [54]

$$\bar{\mathbf{E}} = s(s\mathbf{I}_N + \mathbf{L})^{-1}\mathbf{E} = \mathbf{H}_{\text{est}}\mathbf{E}, \tag{6.9}$$

where $\mathbf{I}_N \in \mathbb{R}^N$, $\mathbf{L}$, and $\mathbf{H}_{\text{est}}$ are the identity, Laplacian, and the estimator transfer function matrices, respectively. It is shown in [29] that if the communication graph has a spanning tree with a balanced Laplacian matrix, $\mathbf{L}$, then, all elements of $\bar{\mathbf{e}}$ converge to a consensus value that is the true average voltage, i.e., the average of all elements in $\mathbf{e}$. Equivalently,

$$\bar{\mathbf{e}}^{\text{ss}} = \mathbf{M}\mathbf{e}^{\text{ss}} = \langle \mathbf{e}^{\text{ss}} \rangle \underline{1}, \tag{6.10}$$

where $\mathbf{M} \in \mathbb{R}^{N\times N}$ is the averaging matrix, whose elements are all $1/N$. $\mathbf{x}^{\text{ss}}$ expresses the steady-state value of the vector $\mathbf{x} \in \mathbb{R}^{N\times 1}$. $\langle \mathbf{x} \rangle$ is a scalar that represents the average of all elements in the vector $\mathbf{x}$. $\underline{1} \in \mathbb{R}^{N\times 1}$ is a column vector whose elements are all one.

6.2 System-Level Modeling

System-level modeling studies the dynamic/static response of the entire microgrid with the droop-free controller in effect. The system under study encompasses interactive cyber and physical subsystems. First, the communication graph topology defines the interaction among controllers, then, functionality of the controllers determines output characteristics of the sources, and, finally, the transmission/distribution network rules the physical interaction among sources and loads. Thus, the system-level study involves mathematical modeling of each of the subsystems and establishment of a mathematical coupling between the interactive subsystems.

6.2.1 Distribution Network Model

Dispatchable sources, transmission network, and loads form the physical layer of the microgrid. This layer is shown in Fig. 6.1a, where sources are considered as controllable voltage source inverters. The controller determines the voltage set points (both magnitude, e_i^*, and phase, δ_i^*) for each source (i.e., inverter) by processing the supplied active and reactive powers. Such controller acts on the physical layer, which is a multi-input/multi-output plant with the voltage set points as the inputs, and the supplied active and reactive powers as the outputs. Herein, we express the output variables, i.e., the supplied powers, in terms of the input variables, i.e., the voltage set points.

Figure 6.1a helps to formulate the supplied current of each source. One can express the supplied current by Source i, as

$$I_i = Y_{ii}V_i + \sum_{j=1(\neq i)}^{N} Y_{ij}(V_i - V_j), \tag{6.11}$$

where I_i and V_i are the phasor representations of the supplied current and phase voltage of the Source i, respectively. Y_{ii} and Y_{ij} are the local load admittance at Bus i (Source i) and the admittance of the transmission line connecting busses i and j, respectively. With no loss of generality, the distribution network is assumed reduced (e.g., by using Kron reduction) such that all non-generating busses are removed from the network. Thus, the complex power delivered by the Source i is,

$$s_i = 3V_iI_i^* = 3|V_i|^2\sum_{j=1}^{N} Y_{ij}^* - 3\sum_{j=1(\neq i)}^{N} V_iV_j^*Y_{ij}^*. \tag{6.12}$$

Assume $V_i = e_i\angle\delta_i$ and $Y_{ij} = y_{ij}\angle\theta_{ij}$ where e_i, y_{ij}, δ_i, and θ_{ij} are the magnitude of V_i, magnitude of Y_{ij}, phase of V_i, and phase of Y_{ij}, respectively. $Y_{ij} = g_{ij} + jb_{ij}$ is the rectangular representation of the admittance Y_{ij}. One can use (6.12) to derive the active and reactive powers delivered by the Source i,

$$p_i = 3e_i^2\sum_{j=1}^{N} g_{ij} - 3\sum_{j=1(\neq i)}^{N} e_ie_jy_{ij}\cos(\delta_i - \delta_j - \theta_{ij}), \tag{6.13}$$

$$q_i = -3e_i^2 \sum_{j=1}^{N} b_{ij} - 3 \sum_{j=1(\neq i)}^{N} e_i e_j y_{ij} \sin(\delta_i - \delta_j - \theta_{ij}), \tag{6.14}$$

The secondary control typically acts slower than the dynamic of the power network (microgrid), as its objectives are voltage and power regulation in the steady state. Accordingly, one can safely neglect the transient responses of the microgrid and use the phasor analysis in (6.13)–(6.14) to model the power flow. Equations (6.13)–(6.14) express nonlinear relationships between the voltages and supplied powers. In time domain, any variable x can be represented as $x = x^q + \hat{x}$ where x^q and $\hat{x}$ are the quiescent and small-signal perturbation parts, respectively. Thus, one can write,

$$p_i = p_i^q + \hat{p}_i = p_i^q + \sum_{j=1}^{N} \frac{\partial p_i}{\partial e_j} \hat{e}_j + \sum_{j=1}^{N} \frac{\partial p_i}{\partial \delta_j} \hat{\delta}_j \Rightarrow \hat{p}_i = \sum_{j=1}^{N} k_{e,ij}^{p} \hat{e}_j + \sum_{j=1}^{N} k_{\delta,ij}^{p} \hat{\delta}_j, \tag{6.15}$$

$$q_i = q_i^q + \hat{q}_i = q_i^q + \sum_{j=1}^{N} \frac{\partial q_i}{\partial e_j} \hat{e}_j + \sum_{j=1}^{N} \frac{\partial q_i}{\partial \delta_j} \hat{\delta}_j \Rightarrow \hat{q}_i = \sum_{j=1}^{N} k_{e,ij}^{q} \hat{e}_j + \sum_{j=1}^{N} k_{\delta,ij}^{q} \hat{\delta}_j, \tag{6.16}$$

where the coefficients in (6.15)–(6.16) are formulated,

$$k_{e,ii}^{p} = \frac{p_i^q}{e_i^q} + 3e_i^q \sum_{j=1}^{N} g_{ij}, \tag{6.17}$$

$$k_{e,ij}^{p} = -3e_i^q y_{ij} \cos(\delta_i^q - \delta_j^q - \theta_{ij}), \quad j \neq i \tag{6.18}$$

$$k_{\delta,ii}^{p} = 3 \sum_{j=1(\neq i)}^{N} e_i^q e_j^q y_{ij} \sin(\delta_i^q - \delta_j^q - \theta_{ij}) = -q_i^q - 3e_i^2 \sum_{j=1}^{N} b_{ij}, \tag{6.19}$$

$$k_{\delta,ij}^{p} = -3e_i^q e_j^q y_{ij} \sin(\delta_i^q - \delta_j^q - \theta_{ij}), \quad j \neq i \tag{6.20}$$

$$k_{e,ii}^{q} = \frac{q_i^q}{e_i^q} - 3e_i^q \sum_{j=1}^{N} b_{ij}, \tag{6.21}$$

$$k_{e,ij}^{q} = -3e_i^q y_{ij} \sin(\delta_i^q - \delta_j^q - \theta_{ij}), \quad j \neq i \tag{6.22}$$

$$k_{\delta,ii}^{q} = -3 \sum_{j=1(\neq i)}^{N} e_i^q e_j^q y_{ij} \cos(\delta_i^q - \delta_j^q - \theta_{ij}) = p_i^q - 3e_i^2 \sum_{j=1}^{N} g_{ij}, \tag{6.23}$$

$$k^q_{\delta,ij} = 3e^q_i e^q_j y_{ij} \cos(\delta^q_i - \delta^q_j - \theta_{ij}), \quad j \neq i. \tag{6.24}$$

Equations (6.15)–(6.24) explain how a disturbance in any of the voltage magnitudes, $\hat{e}_i$s, or phases, $\hat{\delta}_i$s, affects the power flow in the entire microgrid. These equations can be represented in the matrix format,

$$\hat{\mathbf{p}} = \mathbf{k}^p_e \hat{\mathbf{e}} + \mathbf{k}^p_\delta \hat{\boldsymbol{\delta}} \tag{6.25}$$

$$\hat{\mathbf{q}} = \mathbf{k}^q_e \hat{\mathbf{e}} + \mathbf{k}^q_\delta \hat{\boldsymbol{\delta}} \tag{6.26}$$

where $\hat{\mathbf{p}} = [\hat{p}_1, \hat{p}_2, \ldots, \hat{p}_N]^{\mathrm{T}}$, $\hat{\mathbf{q}} = [\hat{q}_1, \hat{q}_2, \ldots, \hat{q}_N]^{\mathrm{T}}$, $\hat{\mathbf{e}} = [\hat{e}_1, \hat{e}_2, \ldots, \hat{e}_N]^{\mathrm{T}}$, and $\hat{\boldsymbol{\delta}} = \left[\hat{\delta}_1, \hat{\delta}_2, \ldots, \hat{\delta}_N\right]^{\mathrm{T}}$ are column vectors carrying small-signal portions of the active powers, reactive powers, voltage magnitudes, and voltage phases, respectively. $\mathbf{k}^p_e = \left[k^p_{e,ij}\right]$, $\mathbf{k}^p_\delta = \left[k^p_{\delta,ij}\right]$, $\mathbf{k}^q_e = \left[k^q_{e,ij}\right]$, and $\mathbf{k}^q_\delta = [k^q_{\delta,ij}]$ are all matrices in $\mathbb{R}^{N\times N}$ that contain coefficients in (6.17)–(6.24). $\mathbf{k}^p_\delta$ and $\mathbf{k}^q_e$ are referred to here as the $p - \delta$ and $q - e$ transfer matrices, respectively.

6.2.2 Dynamic Model of the Control and Cyber Subsystems

The cyber domain is where the controllers exchange measurements, process information, and update the voltage set points. Interactions and functionality of the controllers are shown in Fig. 6.2. One can see how the voltage and reactive power regulators cooperate to adjust the voltage magnitude set points, e^*_i. In the frequency domain,

$$G_i(s)(E_{\text{rated}} - \bar{E}_i) = \Delta E^1_i, \tag{6.27}$$

$$H_i(s)\left(\sum_{j\in N_i} ba_{ij}(Q^{\text{norm}}_j - Q^{\text{norm}}_i)\right) = \Delta E^2_i, \tag{6.28}$$

$$E_{\text{rated}} + \Delta E^1_i + \Delta E^2_i = E^*_i, \tag{6.29}$$

where E_{rated}, $\bar{E}_i$, ΔE^1_i, Q^{norm}_i, ΔE^2_i, and E^*_i are the Laplace transforms of e_{rated}, $\bar{e}_i$, Δe^1_i, q^{norm}_i, Δe^2_i, and e^*_i, respectively. Equations (6.27)–(6.29) can be represented in the matrix format,

$$\mathbf{G}(\mathbf{E}_{\text{rated}} - \bar{\mathbf{E}}) = \mathbf{G}(\mathbf{E}_{\text{rated}} - \mathbf{H}_{\text{est}}\mathbf{E}) = \Delta\mathbf{E}^1, \tag{6.30}$$

$$-b\mathbf{HLQ}^{\text{norm}} = -b\mathbf{HLq}_{\text{rated}}^{-1}\mathbf{Q} = \Delta\mathbf{E}^2, \tag{6.31}$$

$$\mathbf{E}_{\text{rated}} + \Delta\mathbf{E}^1 + \Delta\mathbf{E}^2 = \mathbf{E}^*, \tag{6.32}$$

where $\mathbf{G} = \text{diag}\{G_i\}$ and $\mathbf{H} = \text{diag}\{H_i\}$ are diagonal matrices containing voltage and reactive power controllers, respectively. $\mathbf{G}$ and $\mathbf{H}$ are referred to as the voltage-controller and Q-controller matrices, respectively. $\mathbf{q}_{\text{rated}} = \text{diag}\{q_i^{\text{rated}}\}$ is a diagonal matrix that carries the rated reactive powers of the sources. $\mathbf{E}_{\text{rated}} = E_{\text{rated}}\underline{1}$, $\Delta\mathbf{E}^1 = \left[\Delta E_1^1, \Delta E_2^1, \ldots, \Delta E_N^1\right]^{\text{T}}$, $\Delta\mathbf{E}^2 = \left[\Delta E_1^2, \Delta E_2^2, \ldots, \Delta E_N^2\right]^{\text{T}}$, $\mathbf{E}^* = \left[E_1^*, E_2^*, \ldots, E_N^*\right]^{\text{T}}$, and $\mathbf{Q}^{\text{norm}} = \left[Q_1^{\text{norm}}, Q_2^{\text{norm}}, \ldots, Q_N^{\text{norm}}\right]^{\text{T}}$ are column vectors carrying input and control variables.

It is assumed that for $t < 0$, all sources of the microgrid operate with identical voltage set points, i.e., for all $1 \le i \le N$, $e_i^* = e_{\text{rated}}$, and $\omega_i^* = \omega_{\text{rated}}$, and thus, $v_i(t) = e_{\text{rated}} \sin(\omega_{\text{rated}} t)$. Then, the droop-free controller is activated at $t = 0$. Thus, the quiescent value of any variable x, x^q, represents its steady-state value for $t < 0$, i.e., before activating the controller, and the small-signal part, $\hat{x}$, captures the variable response to the controller activation for $t \ge 0$. Therefore, one can safely write $\delta\mathbf{e}^{1,\text{q}} = \left[\delta e_1^{1,\text{q}}, \delta e_2^{1,\text{q}}, \ldots, \delta e_N^{1,\text{q}}\right]^{\text{T}} = 0$, $\delta\mathbf{e}^{2,\text{q}} = \left[\delta e_1^{2,\text{q}}, \delta e_2^{2,\text{q}}, \ldots, \delta e_N^{2,\text{q}}\right]^{\text{T}} = 0$, and $\mathbf{e}_{\text{rated}}^q = e_{\text{rated}}\underline{1}$, and accordingly, simplify (6.30)–(6.31),

$$\mathbf{G}\left(\hat{\mathbf{E}}_{\text{rated}} - \mathbf{H}_{\text{est}}\hat{\mathbf{E}}\right) = \Delta\widehat{\mathbf{E}}^1, \tag{6.33}$$

$$-b\mathbf{HLq}_{\text{rated}}^{-1}\left(\frac{\mathbf{q}^q}{s} + \hat{\mathbf{Q}}\right) = \Delta\widehat{\mathbf{E}}^2, \tag{6.34}$$

where $\mathbf{q}^q = \left[q_1^q, q_2^q, \ldots, q_N^q\right]^{\text{T}}$ carries the reactive powers supplied by individual sources for $t < 0$. Since the rated voltage does not change before and after activating the controller, $\hat{\mathbf{E}}_{\text{rated}} = \mathbf{0}$. The voltage set points dynamics can now be found by substituting (6.33)–(6.34) into (6.32),

$$\hat{\mathbf{E}}^* = -\mathbf{GH}_{\text{est}}\hat{\mathbf{E}} - b\mathbf{HLq}_{\text{rated}}^{-1}\left(\frac{\mathbf{q}^q}{s} + \hat{\mathbf{Q}}\right). \tag{6.35}$$

As seen, (6.35) has two terms. The first term, $-\mathbf{GH}_{\text{est}}\hat{\mathbf{E}}$, represents the controller effort to achieve the global voltage regulation, and the second term, $-b\mathbf{HLQ}_{\text{rated}}^{-1}\left(\mathbf{q}^q/s + \hat{\mathbf{Q}}\right)$, explains how the controller balances reactive load sharing across the microgrid.

Active power regulators (see Fig. 6.2) adjust the active power flow by tuning the phase angles. The controller at each source, e.g., Source i, compares its normalized active power with those of its neighbors and, accordingly, updates the phase angle set point as in (6.7). Controller activation at $t = 0$ implies that $\omega_i^*(t<0) = \omega_{\text{rated}}$ and, thus, $\delta_i^q = \delta_i^{\text{ss}}(t<0) = 0$. Accordingly,

$$\hat{\delta}_i^*(t \geq 0) = \int_0^t \sum_{j \in N_i} c a_{ij} (p_j^{\text{norm}} - p_i^{\text{norm}})\, \mathrm{d}\tau. \tag{6.36}$$

Equivalently, in the frequency domain,

$$\hat{\Delta}_i^* = \frac{1}{s} \left(\sum_{j \in N_i} c a_{ij} (P_j^{\text{norm}} - P_i^{\text{norm}}) \right), \tag{6.37}$$

where $\hat{\Delta}_i^*$ is the Laplace transform of $\hat{\delta}_i^*$. One can write (6.37) in the matrix format,

$$\hat{\mathbf{\Delta}}^* = -\frac{c}{s} \mathbf{L} \mathbf{p}_{\text{rated}}^{-1} \mathbf{P} = -\frac{c}{s} \mathbf{L} \mathbf{p}_{\text{rated}}^{-1} \left(\frac{\mathbf{p}^q}{s} + \hat{\mathbf{P}} \right), \tag{6.38}$$

where $\hat{\mathbf{\Delta}}^* = \left[\hat{\Delta}_1^*, \hat{\Delta}_2^*, \ldots, \hat{\Delta}_N^* \right]^{\mathrm{T}}$ and $\mathbf{p}_{\text{rated}} = \operatorname{diag}\{p_i^{\text{rated}}\}$ is a diagonal matrix that includes the rated active powers of the sources. $\mathbf{p}^q = \left[\mathbf{p}_1^q, \mathbf{p}_2^q, \ldots, \mathbf{p}_N^q \right]^{\mathrm{T}}$ carries the active powers supplied by individual sources before the controller activation, i.e., for $t<0$. Equation (6.38) represents the phase angles' dynamic response to mitigate and, eventually, eliminate the active load sharing mismatch.

6.2.3 Dynamic Model of the Entire Microgrid

Figure 6.6 represents the model of the entire microgrid, which is separated into two submodels: the quiescent model and the small-signal model. The entire system in the small-signal model can be treated as a multi-input/multi-output plant, where $\mathbf{p}^q/s$ and $\mathbf{q}^q/s$ are the inputs, and $\hat{\mathbf{E}}$, $\hat{\mathbf{P}}$, and $\hat{\mathbf{Q}}$ are the outputs. Equations (6.35) and (6.38) show how the controller adjusts the voltage set points by processing the load sharing mismatches. Dynamic model of the inverters are studied in [44–46]. Accordingly, for the inverter driving the Source i, one can write,

$$\hat{\Delta}_i = G_i^{\Delta} \hat{\Delta}_i^*, \tag{6.39}$$

$$\hat{E}_i = G_i^E \hat{E}_i^*, \tag{6.40}$$

where G_i^E and G_i^{Δ} are the magnitude and phase transfer functions, respectively. Each inverter accommodates an output filter to eliminate the switching harmonics,

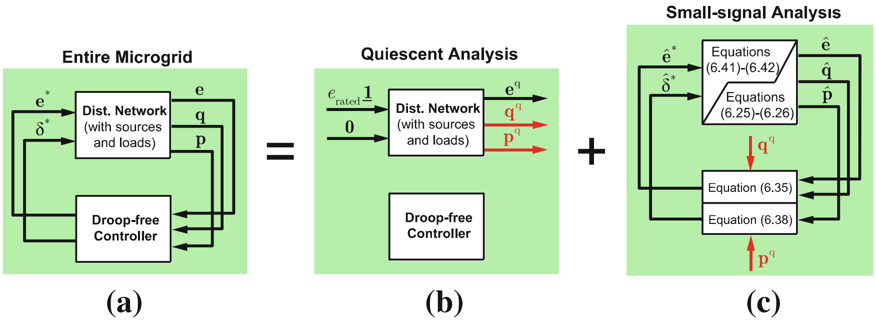

Fig. 6.6 Model of the entire microgrid: **a** interaction between the physical layer and the control/cyber layer, **b** quiescent analysis, **c** small-signal analysis. © [2016] IEEE. Reprinted, with permission, from IEEE Transactions on Power Electronics [54]

whose dynamic is included in the transfer functions G_i^E and G_i^{Δ}. Equivalently, in the matrix format,

$$\hat{\boldsymbol{\Delta}} = \mathbf{G}^{\Delta}\hat{\boldsymbol{\Delta}}^*, \tag{6.41}$$

$$\hat{\mathbf{E}} = \mathbf{G}^{E}\hat{\mathbf{E}}^*, \tag{6.42}$$

where $\mathbf{G}^E = \text{diag}\{G_i^E\}$ and $\mathbf{G}^{\Delta} = \text{diag}\{G_i^{\Delta}\}$ are diagonal matrices of the inverter transfer functions. By substituting (6.35) and (6.38) in (6.25)–(6.26), and also using (6.41)–(6.42), one can formulate the entire microgrid.

It is commonly assumed that the transmission/distribution network is predominantly inductive, and thus, active and reactive powers are mainly controlled by adjusting the voltage phases and magnitudes, respectively [47]. This assumption implies that in (6.25) and (6.26), $\mathbf{k}_e^p \simeq \mathbf{0}$ and $\mathbf{k}_\delta^q \simeq \mathbf{0}$, respectively, which helps to find the reduced-order dynamic model of the entire system. Substituting (6.41) in (6.38) and (6.42) in (6.35) yields

$$\left(\mathbf{G}^{\Delta}\right)^{-1}\hat{\boldsymbol{\Delta}} = -\frac{c}{s}\mathbf{L}\mathbf{p}_{\text{rated}}^{-1}\left(\frac{\mathbf{p}^q}{s}+\hat{\mathbf{P}}\right), \tag{6.43}$$

$$\left(\left(\mathbf{G}^{E}\right)^{-1}+\mathbf{G}\mathbf{H}_{\text{est}}\right)\hat{\mathbf{E}} = -b\mathbf{H}\mathbf{L}\mathbf{q}_{\text{rated}}^{-1}\left(\frac{\mathbf{q}^q}{s}+\hat{\mathbf{Q}}\right). \tag{6.44}$$

Substituting the reduced form of (6.25)–(6.26) in (6.43)–(6.44) yields

$$\hat{\mathbf{P}} = -\mathbf{T}_P\mathbf{L}\mathbf{p}_{\text{rated}}^{-1}\frac{\mathbf{p}^q}{s}, \tag{6.45}$$

$$\hat{\mathbf{Q}} = -\mathbf{T}_Q \mathbf{L} \mathbf{q}_{\text{rated}}^{-1} \frac{\mathbf{q}^q}{s}, \tag{6.46}$$

where $\mathbf{T}_P$ and $\mathbf{T}_Q$ are the P—balancing and Q—balancing matrices and are defined as,

$$\mathbf{T}_P \triangleq \left(s\left(c\mathbf{k}_\delta^p \mathbf{G}^\Delta \right)^{-1} + \mathbf{L}\mathbf{p}_{\text{rated}}^{-1} \right)^{-1}, \tag{6.47}$$

$$\mathbf{T}_Q \triangleq \left(\left(b\mathbf{k}_e^q \mathbf{G}^E \mathbf{H} \right)^{-1} + b^{-1}\mathbf{H}^{-1}\mathbf{G}\mathbf{H}_{\text{est}} \left(\mathbf{k}_e^q \right)^{-1} + \mathbf{L}\mathbf{q}_{\text{rated}}^{-1} \right)^{-1}. \tag{6.48}$$

Equations (6.43)–(6.48) describe dynamic response of the entire microgrid with the droop-free controller in effect. Equations (6.45)–(6.46) show that if the power (either active or reactive) was proportionally shared prior to activating the controller, i.e., $\mathbf{p}_{\text{rated}}^{-1}\mathbf{p}^q = n\underline{1}$ or $\mathbf{q}_{\text{rated}}^{-1}\mathbf{q}^q = m\underline{1}$, the power flow would remain intact after the controller activation, i.e., $\hat{\mathbf{p}} = \mathbf{0}$ or $\hat{\mathbf{q}} = \mathbf{0}$.

6.2.4 Controller Design Guideline

Appropriate selection of the control parameters is essential for proper operation of the droop-free control methodology. For a given microgird, converter transfer function matrices, $\mathbf{G}^\Delta$ and $\mathbf{G}^E$, rated active and reactive power matrices, $\mathbf{p}_{\text{rated}}$ and $\mathbf{q}_{\text{rated}}$, respectively, and $p - \delta$ and $q - e$ transfer matrices, $\mathbf{k}_\delta^p$ and $\mathbf{k}_e^q$, respectively, are known. Alternative communication networks may be chosen to exchange information; they, however, must satisfy three requirements; it should be a sparse graph with (1) at least a spanning tree, (2) balanced Laplacian matrix, and (3) minimum communication redundancy. Communication weights of the graph, a_{ij}, and, thus, the Laplacian matrix, $\mathbf{L}$, directly determine the voltage estimator dynamic, $\mathbf{H}_{\text{est}}$. One may tune the weights and examine the estimators' dynamic through (6.9) to achieve a fast enough response. More details and insightful guidelines for optimal design of communication weights in cooperative systems can be found in [48].

Next, the designer may adjust the controller matrices $\mathbf{G} = \text{diag}\{G_i\}$ and $\mathbf{H} = \text{diag}\{H_i\}$ and the coupling gain b by evaluating (6.48) to place all poles of $\mathbf{T}_Q$ in the open left-hand plane (OLHP) . Intuitively, smaller gains help to stabilize the entire system while larger gains provide a faster dynamic response. Accordingly, the designer may decide the parameters by making a trade-off between relative stability and settling time. The estimator dynamic should be considerably faster than the microgrid dynamics. Therefore, to evaluate (6.48), one can safely assume $\mathbf{H}_{\text{est}} \simeq \mathbf{M}$. Moreover, inverter switching frequency can be assumed high enough to provide a prompt response to the voltage command, i.e., $\mathbf{G}^E \simeq \mathbf{I}_N$.

As can be seen in Fig. 6.2, two separate modules, i.e., the voltage and the reactive power regulators, adjust the voltage magnitude, e_i^*, by generating two voltage correction terms, δe_i^1 and δe_i^2, respectively. As discussed in Sect. 6.1.2, the voltage regulator is tasked to maintain average voltage across the microgrid at the rated value. Per such assignment, the voltage regulator must act fast to ensure voltage stability/regulation. On the other hand, the reactive power regulator is accountable for reactive load sharing in the steady state, and its transient performance has less significance. Accordingly, the voltage control loops (including voltage estimators, controllers G_is, and voltage measurement filters) must be designed for a higher bandwidth compared to the reactive power control loops (involving controllers H_is and reactive power measurement filters). Typically, voltage measurement filters have a relatively high bandwidth as they only need to filter the switching harmonics. On the contrary, besides damping the switching harmonics, the active and reactive measurement units should filter out much lower frequency terms of the line-frequency harmonics and other undesired contents caused by load nonlinearity or unbalance. Such design requirement slows down the power measurements process and, thus, the overall active/reactive load sharing control loops. Accordingly, as a design guideline, it is sufficient to choose the reactive power controllers H_is to be slightly slower than the voltage controllers G_i s; low bandwidth power measurement filters automatically set the frequency response of the power regulators to be quite slower than the voltage regulator module.

Next step in the design procedure considers active power regulators. Equations (6.45) and (6.47) provide dynamic response of the active load sharing mechanism. Given the fast response of the inverters, one may assume $\mathbf{G}^{\Delta} \simeq \mathbf{I}_N$, which simplifies (6.47). The designer may sweep the coupling gain c and assess the stability and dynamic response through (6.47) to find an appropriate choice for c.

6.2.5 Steady-State Performance Analysis

The design guideline in Sect. 6.2.4 ensures stable operation of the microgrid; physical variables such as voltages (magnitude and phase), system frequency, and supplied active and reactive powers would converge to steady-state values. This performance analysis investigates load sharing and voltage regulation quality in the steady state. To this end, assume that the system operates in the steady state for $t \geq t_0$. It should be noted that although the controller stabilizes voltages across the microgrid, one cannot simply deduce that the voltage and reactive power mismatches are zero. In other words, the inputs to the PI controllers G_i and H_i in Fig. 6.2 may be nonzero in the steady state, yet the two voltage correction terms δe_i^1 and δe_i^2 continuously vary with opposite rates such that sum of the two terms leaves a constant value, and thus, the voltage magnitude set point converges to a steady-state value. The following discussion shows that such a scenario never happens; i.e., the mismatch inputs to both controllers decay to zero in the steady state, resulting in successful global voltage regulation and reactive load sharing. It also explains that the active power mismatch terms would all decay to zero, which provides the desired active load sharing while maintaining the rated frequency.

Voltage regulation and reactive load sharing is first to study. In the steady state, the voltage estimators converge to the true average voltage of the microgrid. Equivalently, $\bar{\mathbf{e}}^{\mathrm{ss}} = \mathbf{M}\mathbf{e}^{\mathrm{ss}} = \langle \mathbf{e}^{\mathrm{ss}} \rangle \underline{\mathbf{1}}$. Thus, based on the control methodology in Fig. 6.2, one can write

$$\begin{cases} \boldsymbol{\delta} e^1 = \boldsymbol{\delta} e_0^1 + \big(G_{\mathrm{p}} + G_{\mathrm{I}}(t - t_0)\big)\big(e_{\mathrm{rated}}\underline{1} - \mathbf{M}\mathbf{e}^{\mathrm{ss}}\big) \\ \boldsymbol{\delta} e^2 = \boldsymbol{\delta} e_0^2 + \big(H_{\mathrm{p}} + H_{\mathrm{I}}(t - t_0)\big)\big(-b\mathbf{L}\mathbf{q}_{\mathrm{rated}}^{-1} q^{\mathrm{ss}}\big) \end{cases}, \tag{6.49}$$

where $\boldsymbol{\delta}\mathbf{e}_0^1$ and $\boldsymbol{\delta}\mathbf{e}_0^2$ are column vectors that carry the integrator outputs in G_is and H_is at $t = t_0$, respectively. Accordingly,

$$\begin{aligned} \mathbf{e}^{*\mathrm{ss}} &= \mathbf{e}_{\mathrm{rated}} + \boldsymbol{\delta}\mathbf{e}^1 + \boldsymbol{\delta}\mathbf{e}^2 \\ &= e_{\mathrm{rated}}\underline{\mathbf{1}} + \boldsymbol{\delta}\mathbf{e}_0^1 + \boldsymbol{\delta}\mathbf{e}_0^2 + \mathbf{G}_{\mathrm{P}}(e_{\mathrm{rated}} - \langle \mathbf{e}^{\mathrm{ss}} \rangle)\underline{\mathbf{1}} - b\mathbf{H}_{\mathrm{P}}\mathbf{L}\mathbf{q}_{\mathrm{rated}}^{-1}\mathbf{q}^{\mathrm{ss}} \\ &\quad + \big(\mathbf{G}_{\mathrm{I}}(e_{\mathrm{rated}} - \langle \mathbf{e}^{\mathrm{ss}} \rangle)\underline{\mathbf{1}} - b\mathbf{H}_{\mathrm{I}}\mathbf{L}\mathbf{q}_{\mathrm{rated}}^{-1}\mathbf{q}^{\mathrm{ss}}\big)(t - t_0), \end{aligned} \tag{6.50}$$

where $\mathbf{G}_{\mathrm{I}}$ and $\mathbf{G}_{\mathrm{P}}$ are the diagonal matrices carrying the integral and proportional gains of the voltage-controller matrix $\mathbf{G}$ such that $\mathbf{G}_{\mathrm{P}} + \mathbf{G}_{\mathrm{I}}/s = \mathbf{G}$. Similarly, $\mathbf{H}_{\mathrm{I}}$ and $\mathbf{H}_{\mathrm{P}}$ are the diagonal matrices carrying the integral and proportional gains of the Q-controller matrix $\mathbf{H}$. Equation (6.50) holds for all $t \geq t_0$ and provides a constant voltage set point vector, $\mathbf{e}^{*\mathrm{ss}}$. Thus, the time-varying part of (6.50) is zero or, equivalently,

$$(e_{\mathrm{rated}} - \langle \mathbf{e}^{\mathrm{ss}} \rangle)\mathbf{U}\underline{\mathbf{1}} = \mathbf{L}\mathbf{q}_{\mathrm{rated}}^{-1}\mathbf{q}^{\mathrm{ss}}, \tag{6.51}$$

where $\mathbf{U} = b^{-1}\mathbf{G}_{\mathrm{I}}\mathbf{H}_{\mathrm{I}}^{-1} = \mathrm{diag}\{u_i\}$ is a diagonal matrix. Multiplying both sides of (6.51) from the left by $\underline{\mathbf{1}}$,$^{\mathrm{T}}$,

$$(e_{\mathrm{rated}} - \langle \mathbf{e}^{\mathrm{ss}} \rangle)\underline{\mathbf{1}}^{\mathrm{T}}\mathbf{U}\underline{\mathbf{1}} = \underline{\mathbf{1}}^{\mathrm{T}}\mathbf{L}\mathbf{q}_{\mathrm{rated}}^{-1}\mathbf{q}^{\mathrm{ss}}. \tag{6.52}$$

Given the balanced Laplacian matrix, $\underline{\mathbf{1}}^{T}\mathbf{L} = \mathbf{0}$ [30], which simplifies (6.52),

$$(e_{\mathrm{rated}} - \langle \mathbf{e}^{\mathrm{ss}} \rangle)\sum_{i=1}^{N} u_i = 0. \tag{6.53}$$

Since all entries of the matrix $\mathbf{U}$ are positive, (6.53) yields $e_{\mathrm{rated}} = \langle \mathbf{e}^{\mathrm{ss}} \rangle$, which implies that the controllers successfully regulates the averaged voltage magnitude of the microgrid, $\langle \mathbf{e}^{\mathrm{ss}} \rangle$, at the rated value, e_{rated}. Moreover, by substituting $e_{\mathrm{rated}} - \langle \mathbf{e}^{\mathrm{ss}} \rangle = 0$ in (6.51),

$$\mathbf{L}\mathbf{q}_{\mathrm{rated}}^{-1}\mathbf{q}^{\mathrm{ss}} = \mathbf{0}. \tag{6.54}$$

If $\mathbf{L}$ is the Laplacian matrix associated with a graph that contains a spanning tree, the only nonzero solution to $\mathbf{L}\mathbf{x} = \mathbf{0}$ is $\mathbf{x} = n\underline{\mathbf{1}}$, where n is a real number [29]. Thus, (6.54) implies $\mathbf{q}^{\mathrm{ss}} = n\mathbf{q}_{\mathrm{rated}}\underline{\mathbf{1}}$, which assures that the controller shares the total reactive load among the sources in proportion to their ratings.

Frequency regulation and active load sharing is the next to study. The controller guarantees the convergence of the voltage magnitude vector, $\mathbf{e}$, and phase angle vector, $\boldsymbol{\delta}$, to steady-state values. Thus, (6.6)–(6.7) suggest that all sources would synchronize to the rated frequency, ω_{rated}. Moreover, based on (6.7), stabilizing the phase angles across the microgrid implies that all the frequency correction terms in (6.4) should decay to zero. Equivalently,

$$c\mathbf{L}\mathbf{p}_{\mathrm{rated}}^{-1}\mathbf{p}^{\mathrm{ss}} = \mathbf{0}, \tag{6.55}$$

which offers, $\mathbf{p}^{\mathrm{ss}} = m\mathbf{p}_{\mathrm{rated}}\underline{\mathbf{1}}$, where m is a positive real number. Thus, the controller successfully handles the proportional active load sharing.

6.3 Experimental Verification

A 120/208 V, 60 Hz three-phase AC microgrid prototype is shown in Fig. 6.7. System schematic is described in Fig. 6.8, where four inverter-driven sources are placed in a radial connection to supply two loads, Z_1 and Z_4. The inverters (sources) have similar topologies but different ratings, i.e., the ratings of the inverters 1 and 2 are twice those for the inverters 3 and 4. Each inverter is augmented with an LCL filter to eliminate switching and line-frequency harmonics. *RL*-circuit model is used

Fig. 6.7 AC microgrid prototype, courtesy of the Intelligent Microgrid Laboratory at Aalborg University: **a** inverter modules, **b** dSAPCE processor board (DS1006), **c** programming and monitoring PC, **d** *RL* loads. © [2016] IEEE. Reprinted, with permission, from IEEE Transactions on Power Electronics [54]

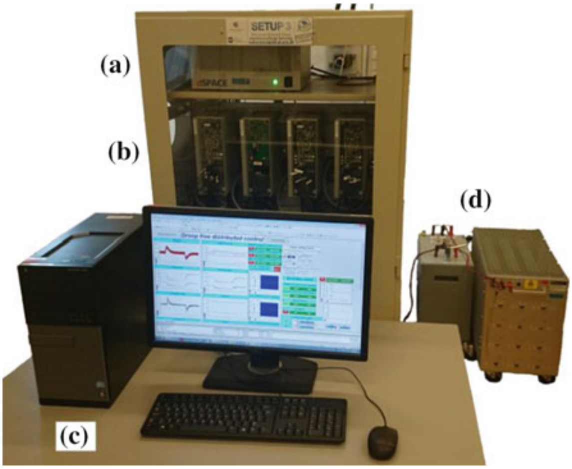

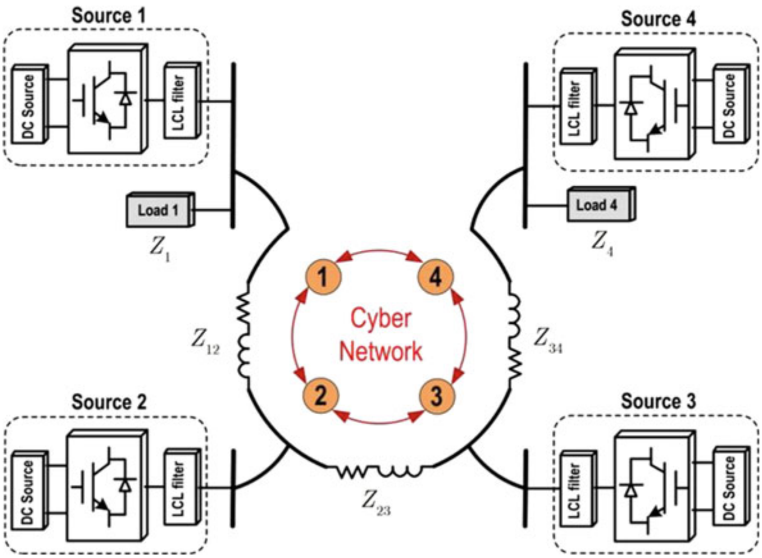

Fig. 6.8 Schematic of the microgrid prototype; radial electrical connection and ring cyber network. © [2016] IEEE. Reprinted, with permission, from IEEE Transactions on Power Electronics [54]

for each transmission line. An inductive-resistive distribution network is adopted to investigate collaborative interaction of the active and reactive power regulators in load sharing. Structure of the cyber network is highlighted in Fig. 6.8. Alternative cyber networks for a set of four agents are discussed in [29, 30] where the ring structure is shown to be the most effective option and, thus, is considered here. It can be seen that the ring connection provides a sparse network that carries the required minimum redundancy where no single communication link failure would hinder the connectivity of the graph. Communication links are bidirectional to feature a balanced Laplacian matrix. A dSPACE processor board (DS1006) models the communication channels and implements the control routines. Electrical and control parameters of the microgrid are provided in Appendix.

6.3.1 Performance Assessment

Figure 6.9 evaluates performance of the droop-free controller. Inverters are initially driven with fixed voltage command, i.e., $e_i^* = 120$ V and $\omega_i^* = 120\pi$ rad/s. It should be noted that no voltage feedback control had been initially in action to compensate the voltage drop across the LCL filters, and thus, the resulting bus voltages in Fig. 6.9a are less than the desired set point, i.e., $e_i^* = 120$ V. It can also

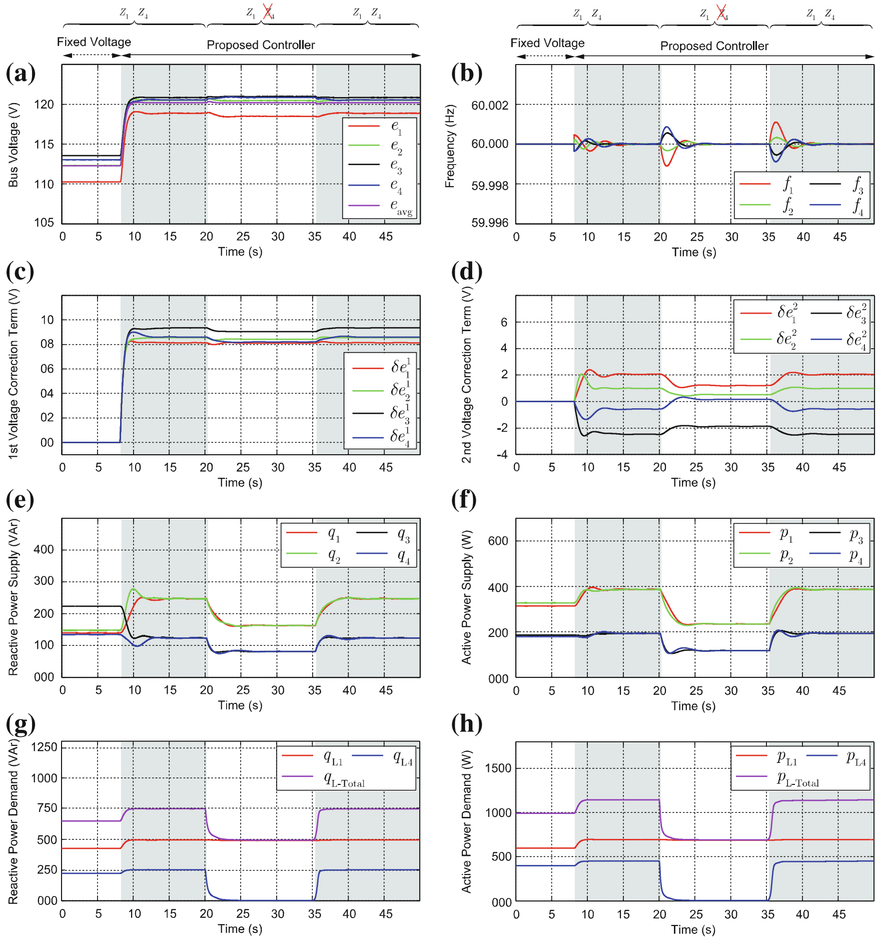

Fig. 6.9 Performance evaluation of the droop-free controller: **a** bus voltage (phase-to-neutral), **b** inverter frequency set points, **c** first voltage correction term, **d** second voltage correction term, **e** supplied reactive power, **f** supplied active power, **g** load reactive power, **h** load active power. Power ratings of the inverters 1 and 2 are twice those of inverters 3 and 4. © [2016] IEEE. Reprinted, with permission, from IEEE Transactions on Power Electronics [54]

be seen in Figs. 6.9e and 6.8f that the total load is not shared among sources in proportion to their power ratings.

It can be seen in the Appendix that the voltage controllers G_is are designed slightly faster than the reactive power controllers H_is. Cut-off frequencies of the power measurement filters are as low as 3 Hz to damp all undesired low-frequency harmonics. These design considerations set the dynamic responses of the two voltage and reactive power regulators apart enough to dynamically separate the two resulting voltage correction terms, i.e., δe_i^1 and δe_i^2. The controller is activated at

$t = 8$ s. The voltage correction terms have been added to the voltage set points to help with the global voltage regulation and reactive load sharing. Figure 6.9(a) demonstrates that the controllers have boosted the bus voltages across the microgrid to satisfy the global voltage regulation; i.e., for $t > 8$ s, the average voltage across the microgrid is successfully regulated at the desired value of 120 V. As seen in Fig. 6.9b, c, the first and the second voltage correction terms respond at two different time scales; the first correction term δe_i^1 (output of the voltage regulator) responds four times faster than the second correction term δe_i^2 (output of the reactive power regulator). Figure 6.9b shows that the controllers have varied the frequency set points in transients to adjust individual phase angles and provide the desired active load sharing. This figure supports the discussions in Sect. 6.2.5, where the active power regulator is proven to only enforce transient deviations in frequency and that imposes no steady-state deviation. It can be seen that all inverter frequencies synchronize to the rated frequency of 60 Hz in the steady state. Figure 6.9e, f show the filtered power measurements and explain how the controllers have effectively rerouted the power flow to provide proportional load sharing.

Individual and total reactive and active load demands are plotted in Fig. 6.9g, h, respectively. It should be noted that the loads have drawn more power once the controller is activated, since the voltages are boosted across the entire microgrid.

Next, the controller performance is studied in response to the load change. The load at Bus 4, Z_4, has been unplugged at $t = 20$ s and plugged back in at $t = 35$ s. As seen in Fig. 6.9, the controller has successfully maintained global voltage regulation, frequency synchronization, and proportional load sharing, despite the change in load. It can also be observed in Fig. 6.9e, f that the inverters 3 and 4 respond faster to the load change than the other two inverters as they are in closer vicinity of Z_4. Soft load change is performed in this study for safety purposes. In fact, the load inductor at Bus 4 features an air-gap control knob. Using this control opportunity, at $t = 20$ s, the load inductance is manually increased to its maximum value to provide an ultimate current damping feature. Then, the load is physically unplugged. A reverse procedure is followed at $t = 35$ s to plug the load, Z_4, back in. This soft load change procedure, besides the damping effect of the power measurement filters, explains why the supplied powers in Fig. 6.9e, f and the load demands in Fig. 6.9g, h show a slow and gradual profile rather than sudden changes.

6.3.2 Communication Delay and Channel Bandwidth

Communication is indispensable to access neighbor data and, thus, to the operation of distributed systems. Accordingly, channel non-idealities, e.g., transmission/propagation delay and limited bandwidth, and channel deficiencies such as packet loss may compromise the overall system performance. Thus, low delay and high-bandwidth communication protocols are of paramount value for distributed control structures. For example, Wi-fi and Ultra Wide Band (UWB) protocols offer bandwidths up to 5 and 7.5 GHz, respectively, with delays less than 1 μs. It should be noted that the length of the communication link directly affects the channel delay. Channel non-ideality effects on the controller performance has been studied in [49] for distributed systems and, particularly, for microgrids in [50–52]. It is shown that such non-idealities have a negligible impact on the overall system performance if the channel delay is negligible compared to the controller dynamics. For the underlying microgrid, results in Fig. 6.9 clearly show that the controller dynamics are in the orders of hundreds of milliseconds (or longer); the system dynamics exhibit different time constants for the voltage, active, and reactive power regulation. Therefore, the controller is expected to operate safely with most of the existing communication protocols. To further study the effect of communication delay and limited bandwidth, a detailed model of the underlying microgrid is

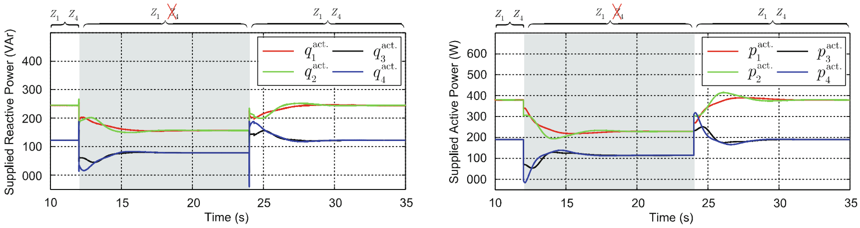

(a) Maximum Delay = 1 ms, Minimum Channel Bandwidth = 100 kHz

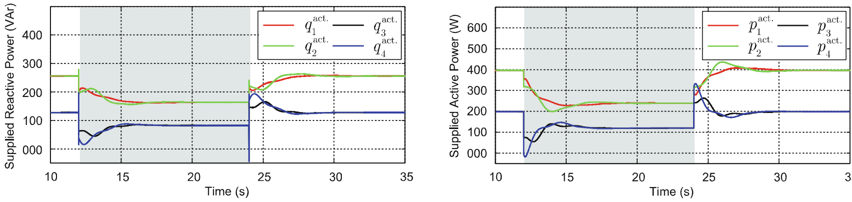

(b) Maximum Delay = 50 ms, Minimum Channel Bandwidth = 10 kHz

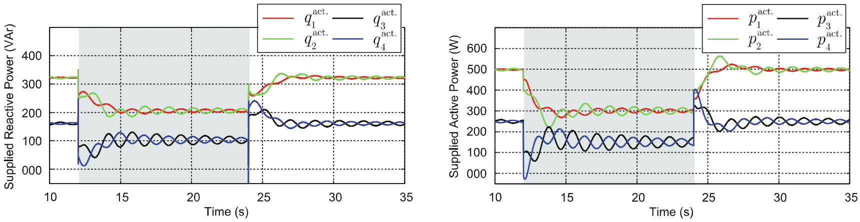

(c) Maximum Delay = 150 ms, Minimum Channel Bandwidth = 1 kHz

Fig. 6.10 Controller performance with non-ideal communication channel. Supplied active and reactive powers for **a** delay = 1 ms and BW = 100 kHz, **b** delay = 50 ms and BW = 10 kHz, **c** delay = 150 ms and BW = 1 kHz. © [2016] IEEE. Reprinted, with permission, from IEEE Transactions on Power Electronics [54] simulated in MATLAB/SIMULINK. Figure 6.10 shows the transient load sharing performance in response to the step load change for a variety of communication delays and bandwidths. It should be noted that the results in this figure present *instantaneous* active and reactive powers, not the filtered measurements. However, the controller still processes the filtered quantities. Comparison of studies in Fig. 6.10 shows how long delays can compromise system stability (see Fig. 6.10c).

Analysis of distributed control protocols in [53] demonstrates that large communication delays impose DC errors on the voltage estimations and cause drift from a consensus. One can see such effect in Fig. 6.10, where longer delays introduce larger errors in voltage estimations and lead to bus voltages regulated at higher values than the desired rated voltage. This undesired voltage increment explains elevated supplied powers in Fig. 6.10b, c in comparison to Fig. 6.10a. Simulation studies ensure immunity of the controller performance to delays as long as 10 ms and channel bandwidths as low as 100 kHz, which makes communication protocols such as Wi-fi and UWB very suitable for the field implementation.

6.3.3 Plug-and-Play Study

Figure 6.11 studies the plug-and-play capability of the control method. Inverter 3 has intentionally been unplugged at $t = 10$ s. Although this inverter is turned off instantly, the power measurements exponential decay to zero because of the existing low-pass filters.

It should be noted that a source failure also implies loss of all communication links connected to that particular source. Accordingly, when Source 3 fails, it automatically renders the links 2–3 (between Nodes 2 and 3) and 3–4 inoperable. However, as seen in Fig. 6.11, the remaining links still form a connected graph with balanced Laplacian matrix, and thus, the control methodology should remain functional. As seen in Fig. 6.11c, d, the controllers have successfully responded to the inverter loss and shared the excess power among the remaining inverters in proportion to their power ratings. After the loss of Inverter 3, the voltage measurement for Bus 3 would be unavailable. Thus, the controllers collectively regulate the new average voltage, i.e., the average voltage of the remaining three inverters, at the rated value of 120 V. However, the actual average voltage across the microgrid is seen to be slightly less than the rated voltage.

As seen in Fig. 6.11a, Bus 3 experiences voltage sag due to the loss of generation. It should be noted that although inverter 3 is disconnected from Bus 3, the bus voltage is still available. Inverter 3 is plugged back in at $t = 20$ s; however, the synchronization procedure delays inverter engagement.

After successful synchronization, the controller is activated at $t = 31$ s and has shown excellent performance in the global voltage regulation and readjusting the load sharing to account for the latest plugged-in inverter.

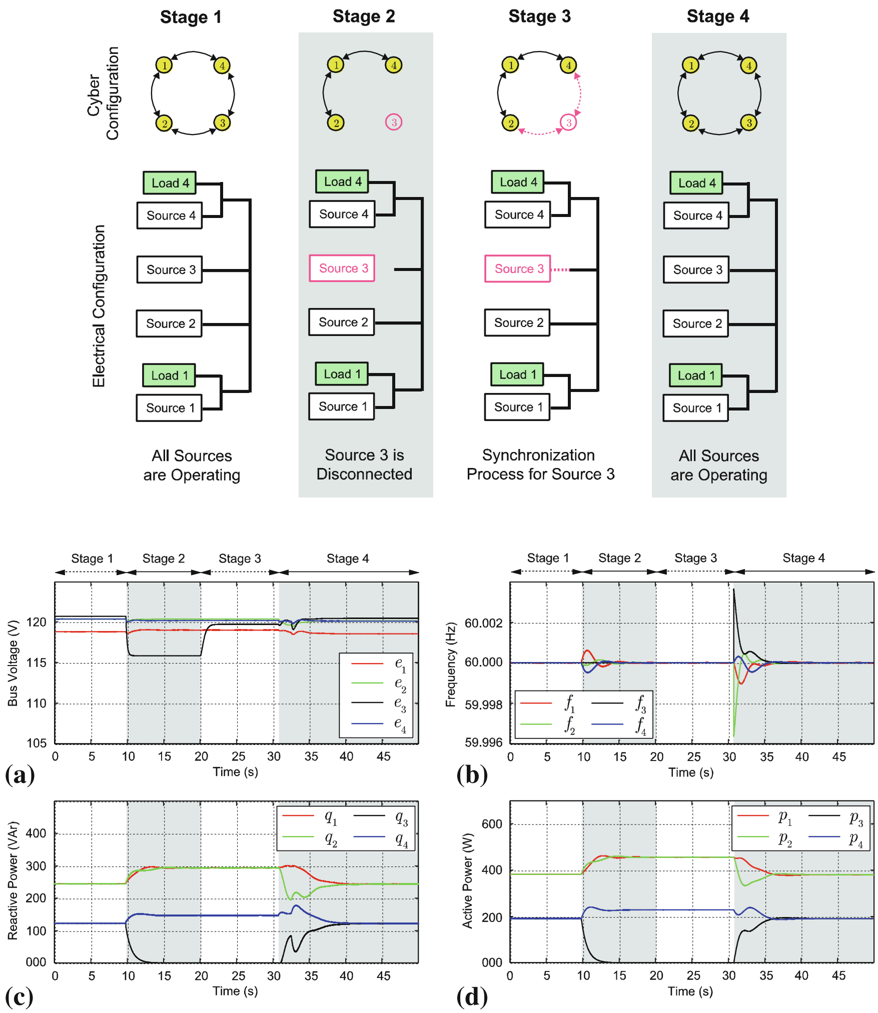

Fig. 6.11 Plug-and-play study for Inverter 3: **a** bus voltage (phase-to-neutral), **b** inverter frequency, **c** supplied reactive power, **d** supplied active power. © [2016] IEEE. Reprinted, with permission, from IEEE Transactions on Power Electronics [54]

6.3.4 *Failure Resiliency in Cyber Domain*

Resiliency to a single link failure is studied in Fig. 6.12. The original communication graph is designed to carry a minimum redundancy, such that no single communication link failure can compromise the connectivity of the cyber network.

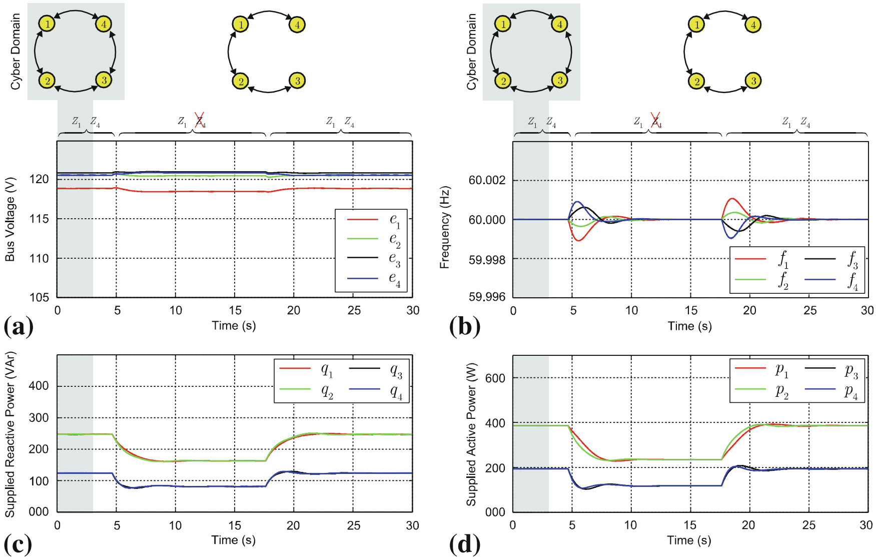

Fig. 6.12 Resiliency to failure in Link 3–4: **a** bus voltage (phase-to-neutral), **b** inverter frequency, **c** supplied reactive power, **d** supplied active power. © [2016] IEEE. Reprinted, with permission, from IEEE Transactions on Power Electronics [54]

As seen in Fig. 6.12, the Link 3–4 has been disabled at $t = 3$ s; yet, it does not have any impact on the voltage regulation or load sharing, as the new graph is still connected and has a balanced Laplacian matrix. It should be noted that, by practicing error detection/control protocols in the communication modules, any link failure can be immediately detected at the receiving end. Accordingly, the receiving end controller updates its set of neighbors by ruling out the node on the transmitting end of the failed link. This reconfiguration ensures that the misleading zero-valued data associated to the failed link (e.g., zero active and reactive power measurements) will not be processed by the receiving end controller, and thus, the system remains functional.

The controller response to load change is then studied in Fig. 6.12 with the failed link, where a satisfactory performance is reported. In this study, the load at Bus 4, i.e., Z_4, has been unplugged and plugged back in at $t = 5$ s and $t = 17.5$ s, respectively. It should be noted that although the link failure does not affect the steady-state performance, it slows down the system dynamics as it limits the information flow.

It should be noted that any reconfiguration in the cyber domain, e.g., communication link failure, affects the Laplacian matrix and, thus, the whole system dynamic. However, it will not compromise the steady-state performance of the control methodology, as long as the cyber network remains connected and presents a balanced Laplacian matrix. Connectivity of the cyber network plays a key role in the functionality of the entire microgrid. Including redundant cyber links, as discussed in Sects. 6.1.1 and 6.1.2, ensures network connectivity for the most probable contingencies. However, any communication link failure requires immediate attention/maintenance before another cyber incident takes place. It should be noted that it is very unlikely to lose connectivity due to simultaneous failures of several communication links.

6.4 Summary

A distributed secondary/primary controller is presented for AC microgrids. The controller embedded on each inverter has three modules: the voltage, reactive power, and the active power regulators. The voltage regulator estimates the global average voltage across the microgrid. This estimation is then further used to adjust the local voltage set point. The reactive power regulator also adjusts the voltage set point by comparing the local normalized reactive power with the neighbors'. The active power regulator compares the local normalized active power with the neighbors' and, accordingly, adjusts the frequency (or, phase angle) set point to carry out the proportional active power sharing. This control paradigm does not rely on the droop mechanism, yet it is fully distributed, i.e., it uses a sparse communication network for data exchange among inverters. Experimental results show that the cooperative controller provides a precise global voltage regulation and proportional load sharing. Controller performance, plug-and-play capability, and resiliency to single communication link failure are also verified through experiments.

Appendix

DC bus voltages that supply the inverter modules are all 650 V. The filter inductors are identical and $L_{\mathrm{F1}} = L_{\mathrm{F2}} = 1.8$ mH, and the intermediate capacitor is $C_{\mathrm{F}} = 25\,\mu\mathrm{F}$. The line impedance connecting busses i and j can be expressed as $Z_{ij} = R_{ij} + sL_{ij}$ where,

$$\begin{cases} R_{12} = 0.8\,\Omega, & L_{12} = 3.6\ \mathrm{mH} \\ R_{23} = 0.4\,\Omega, & L_{23} = 1.8\ \mathrm{mH}\,. \\ R_{34} = 0.7\,\Omega, & L_{34} = 1.5\ \mathrm{mH} \end{cases} \tag{6.56}$$

The control parameters are,

$$\begin{cases} \mathbf{p}_{\mathrm{rated}} = 1\ \mathrm{kW} \times \mathrm{diag}\{1.6, 1.6, 0.8, 0.8\} \\ \mathbf{q}_{\mathrm{rated}} = 1\ \mathrm{kVAr} \times \mathrm{diag}\{0.6, 0.6, 0.3, 0.3\} \end{cases}, \tag{6.57}$$

$$\mathbf{A}_{\mathrm{G}} = \begin{bmatrix} 0 & 1.5 & 0 & 1.5 \\ 1.5 & 0 & 1.5 & 0 \\ 0 & 1.5 & 0 & 1.5 \\ 1.5 & 0 & 1.5 & 0 \end{bmatrix}, \tag{6.58}$$

$$b = 2, \quad c = 0.02, \tag{6.59}$$

$$\begin{cases} \mathbf{G}_{\mathrm{P}} = 0.01 \times \mathbf{I}_4, & \mathbf{G}_{\mathrm{I}} = 3 \times \mathbf{I}_4 \\ \mathbf{H}_{\mathrm{P}} = 0.005 \times \mathbf{I}_4, & \mathbf{H}_{\mathrm{I}} = 2 \times \mathbf{I}_4 \end{cases}. \tag{6.60}$$

References

1. Wu D, Tang F, Guerrero JM, Vasquez JC (2014) Autonomous control of distributed generation and storage to coordinate P/Q sharing in islanded microgrids—an approach beyond droop control. In: Proceedings of IEEE international energy conference, pp 983–988
2. Ashabani SM, Mohamed YARI (2013) General interface for power management of micro-grids using nonlinear cooperative droop control. IEEE Trans Power Syst 28:2929–2941
3. Hu J, Zhu J, Dorrell DG, Guerrero JM (2014) Virtual flux droop method—a new control strategy of inverters in microgrids. IEEE Trans Power Electron 29:4704–4711
4. Mohamed YAI, El-Saadany EF (2008) Adaptive decentralized droop controller to preserve power sharing stability of paralleled inverters in distributed generation microgrids. IEEE Trans Power Electron 23:2806–2816
5. He J, Li YW (2011) Analysis, design, and implementation of virtual impedance for power electronics interfaced distributed generation. IEEE Trans Ind Appl 41:2525–2538
6. Simpson-Porco JW, Dorfler F, Bullo F (2013) Voltage stabilization in microgrids via quadratic droop control. In: IEEE 52nd Annual conference decision and control, pp 7582–7589
7. Mahmood H, Michaelson D, Jiang J (2015) Accurate reactive power sharing in an islanded microgrid using adaptive virtual impedances. IEEE Trans Power Electron 30(3):1605–1617
8. Han H, Liu Y, Sun Y, Su M, Guerrero JM (2015) An improved droop control strategy for reactive power sharing in islanded microgrid. IEEE Trans Power Electron 30(6):3133–3141
9. Lee CT, Chu CC, Cheng PT (2013) A new droop control method for the autonomous operation for distribute energy resource interface converters. IEEE Trans Power Electron 28:1980–1993
10. Dhople SV, Johnson BB, Hamadeh AO (2013) Virtual oscillator control for voltage source inverters. In: Proceedings of 51st annual Allerton conference, pp 1359–1363
11. Johnson BB, Dhople SV, Hamadeh AO, Krein PT (2014) Synchronization of nonlinear oscillators in an LTI electrical power network. In: IEEE transaction no circuits system I: regular papers, vol 61, pp 834–844
12. Johnson BB, Dhople SV, Hamadeh AO, Krein PT (2014) Synchronization of parallel single-phase inverters with virtual oscillator control. IEEE Trans Power Electron 29 (11):6124–6138
13. Johnson BB, Dhople SV, Cale JL, Hamadeh AO, Krein PT (2014) Oscillator-based inverter control for islanded three-phase microgrids. IEEE J Photovoltaics 4(1):387–395
14. Vandon TL, Meersman B, De Koonig JDM, Vandevelde L (2012) Analogy between conventional grid control and islanded microgrid control based on a global dc-link voltage droop. IEEE Trans Power Del 27:1405–1414

15. Etemadi AH, Davison EJ, Iravani R (2012) A decentralized robust strategy for multi-DER microgrids—part I: fundamental concepts. IEEE Trans Power Del 27:1843–1853
16. Shafiee Q, Nasirian V, Guerrero JM, Lewis FL, Davoudi A (2014) Team-oriented adaptive droop control for autonomous AC microgrids. In: Proceedings of 40th industrial electronics conference (IECON), pp 1861–1867
17. Etemadi AH, Davison EJ, Iravani R (2014) A generalized decentralized robust control of islanded microgrids. IEEE Trans Power Syst 29(6):3102–3113
18. Hui Q, Haddad W (2008) Distributed nonlinear control algorithms for network consensus. Automatica 42:2375–2381
19. Fax J, Murray R (2004) Information flow and cooperative control of vehicle formations. IEEE Trans Automat Control 49:1465–1476
20. Qu Z (2009) Cooperative control of dynamical systems: applications to autonomous vehicles. Springer, New York
21. Shafiee Q, Guerrero JM, Vasquez JC (2014) Distributed secondary control for islanded microgrids—a novel approach. IEEE Trans Power Electron 29:1018–1031
22. Shafiee Q, Stefanovic C, Dragicevic T, Popovski P, Vasquez JC, Guerrero JM (2014) Robust networked control scheme for distributed secondary control of islanded microgrids. IEEE Trans Ind Electron 61:5363–5374
23. Zhang Y, Ma H (2012) Theoretical and experimental investigation of networked control for parallel operation of inverters. IEEE Trans Ind Electron 59:1961–1970
24. Marwali MN, Keyhani A (2004) Control of distributed generation systems—part I: voltages and currents control. IEEE Trans Power Electron 19:1541–1550
25. Marwali MN, Jung JW, Keyhani A (2004) Stability analysis of load sharing control for distributed generation systems. IEEE Trans Energy Convers 22:737–745
26. McArthur SDJ, Davidson EM, Catterson VM, Dimeas AL, Hatziargyriou ND, Ponci F, Funabashi T (2007) Multi-agent systems for power engineering applications—part I: concepts, approaches, and technical challenges. IEEE Trans Power Syst 22:1743–1752
27. Bidram A, Davoudi A, Lewis FL, Qu Z (2013) Secondary control of microgrids based on distributed cooperative control of multi-agent systems. IET Gener Transm Dist 7:822–831
28. Nasirian V, Davoudi A, Lewis FL (2014) Distributed adaptive droop control for dc microgrids. In: Proceedings of 29th IEEE applied power electronics conference and exposition (APEC), pp 1147–1152
29. Nasirian V, Moayedi S, Davoudi A, Lewis FL (2015) Distributed cooperative control of dc microgrids. IEEE Trans Power Electron 30:2288–2303
30. Nasirian V, Davoudi A, Lewis FL, Guerrero JM (2014) Distributed adaptive droop control for dc distribution systems. IEEE Trans Energy Convers 29:944–956
31. Moayedi S, Nasirian V, Lewis FL, Davoudi A (2015) Team-oriented load sharing in parallel dc-dc converters. IEEE Trans Ind Appl 51(1):479–490
32. Robbins BA, Hadjicostis CN, Dominguez-Garcia AD (2013) A two-stage distributed architecture for voltage control in power distribution systems. IEEE Trans Power Syst 28:1470–1482
33. Dominguez-Garcia AD, Hadjicostis CN, Vaidya NF (2012) Resilient networked control of distributed energy resources. IEEE J Sel Areas Commun 30:113–1148
34. Cady ST, Dominguez-Garcia AD (2012) Distributed generation control of small-footprint power systems. In: Proceedings of North American power symposium, pp 1–6
35. Bidram A, Davoudi A, Lewis FL (2014) A multi-objective distributed control framework for islanded microgrids. IEEE Trans Ind Inform 10(3):1785–1798
36. Dorfler F, Simpson-Porco JW, Bullo F (2014) Breaking the hierarchy: distributed control and economic optimality in microgrids. Available on arXiv:1401.1767v1
37. Bouattour H, Simpson-Porco JW, Dorfler F, Bullo F (2013) Further results on distribute secondary control in microgrids. In: IEEE conference on decision and control, pp 1514–1519
38. Simpson-Porco JW, Dorfler F, Bullo F, Shafiee Q, Guerrero JM (2013) Stability, power sharing, and distributed secondary control in droop-controlled microgrids. In: IEEE smart grid communications symposium, pp 672–677

39. Simpson-Porco JW, Dorfler F, Bullo F (2013) Synchronization and power sharing for droop-controlled inverters in islanded microgrids. Automatica 49:2603–2611
40. Olfati-saber R, Fax JA, Murray RM (2007) Consensus and cooperation in networked multi-agent systems. Proc IEEE 95(1):215–233
41. Olfati-Saber R, Murray RM (2004) Consensus problems in networks of agents with switching topology and time-delays. IEEE Trans Automat Control 49(9):1520–1533
42. Erickson RW, Maksimovic D (2001) Fundamental of power electronics, 2nd edn. Kluwer, Norwell
43. Spanos DP, Olfati-Saber R, Murray RM (2005) Dynamic consensus for mobile networks. In: Proceedings of 16th international federation of automatic control (IFAC), pp 1–6
44. Chen L, Hu C, Zhang Q, Zhang K, Batarseh I (2015) Modeling and triple-loop control of ZVS grid-connected dc/ac converters for three-phase balanced micro-inverter application. IEEE Trans Power Electron 30(4):2010–2023
45. Sozer Y, Torrey DA (2009) Modeling and control of utility interactive inverters. IEEE Trans Power Electron 24(11):2475–2483
46. Pogaku N, Prodanovic M, Green TC (2007) Modeling, analysis and testing of autonomous operation of an inverter-based microgrid. IEEE Trans Power Electron 22(2):613–625
47. Guo X, Lu Z, Wang B, Sun X, Wang L, Guerrero JM (2014) Dynamic phasors-based modeling and stability analysis of droop-controlled inverters for microgrid applications. IEEE Trans Smart Grid 5(6):2980–2987
48. Zhang H, Lewis FL, Qu Z (2012) Lyapunov, adaptive, and optimal design techniques for cooperative systems on directed communication graphs. IEEE Trans Ind Electron 59 (7):3026–3041
49. Xiao F, Wang L (2008) Asynchronous consensus in continuous-time multi-agent systems with switching topology and time-varying delays. IEEE Trans Automat Control 53(8):1804–1816
50. Kahrobaeian A, Mohamed YARI (2015) Networked-based hybrid distributed power sharing and control of islanded micro-grid systems. IEEE Trans Power Electron 30(2):603–617
51. Ci S, Qian J, Wu D, Keyhani A (2012) Impact of wireless communication delay on load sharing among distributed generation systems through smart microgrids. IEEE Wireless Commun 19(3):24–29
52. Liu S, Wang X, Liu PX, Impact of communication delays on secondary frequency control in an islanded microgrid. IEEE Trans Ind Electron (to be published). doi:10.1109/TIE.2014.2367456
53. Behjati H, Davoudi A, Lewis FL (2014) Modular DC-DC converters on graphs: cooperative control. IEEE Trans Power Electron 29(12):6725–6741
54. Nasirian V, Shafiee Q, Guerrero J, Lewis F, Davoudi A, (2016) Droop-free distributed control for AC microgrids. IEEE Trans Power Electronics 31(2):1600–1617

Chapter 7
Cooperative Control for DC Microgrids

Similar to the control hierarchy of the AC systems, a hierarchical control structure is conventionally adopted for DC microgrid operation [1, 2]. The highest hierarchy, the tertiary control, is in charge of economical operation and coordination with the distribution system operator. It assigns the microgrid voltage to carry out the scheduled power exchange between the microgrid and the main grid [3–6]. To satisfy voltage demand of the tertiary control, the secondary control measures voltages across the microgrid and, accordingly, updates the voltage set points for the primary controllers. The primary control, typically implemented locally with a droop mechanism, regulates the output voltage of individual converters that supply microgrid.

The secondary and tertiary controls are typically implemented in a centralized fashion [7, 8], which communicates with converters through communication links with high connectivity. Loss of any link in such a topology can lead to the failure of the corresponding unit and, thus, overstressing other units, leading to system-level instability and cascaded failures [9]. Since future extensions add to the complexity of the controller, scalability of central controllers is not straightforward. Distributed control has emerged as an attractive alternative as it offers improved reliability, simpler communication network, and easier scalability [8]. For example, distributed tertiary control via DC bus signaling is studied in [10–12]. Structurally, it is desired to extend the distributed control paradigm to the secondary/primary controls. Categorically, such a controller shall satisfy two main control objectives of DC microgrids, namely voltage regulation [13] and proportional load sharing [14].

Proper load sharing assigns the load among participating converters in proportion to their rated power. This equalizes the per-unit currents of all sources and prevents circulating currents [14] and overstressing of any source [15–18]. The droop control is widely adopted for load sharing by imposing virtual output impedance on each converter [18–20]. Static/dynamic performance and stability assessment of droop controllers are investigated in [21–25]. Despite simplicity and ease of implementation, the conventional droop method suffers from poor voltage regulation and load sharing, particularly when the transmission line impedances are

A. Bidram et al., *Cooperative Synchronization in Distributed Microgrid Control*,
Advances in Industrial Control, DOI 10.1007/978-3-319-50808-5_7

not negligible [26–29]. The primary reason for this poor voltage regulation is the voltage drop caused by the virtual impedance. Another factor is the output voltage mismatch among different converters, which is crucial for the natural power flow in DC systems, but further exacerbates the voltage regulation issue.

Possible solutions to the aforementioned issues have been reviewed in [8]. These solutions are either centralized [1] or require establishment of a fully connected communication network throughout the microgrid, where any two nodes are directly connected [30–32]. For example, a centralized secondary control in [1] measures the microgrid voltage, calculates a voltage restoration term, and sends the restoration term to all sources. It assumes equal voltages for all converters across the microgrid, which is not a viable assumption for practical DC microgrids. Adaptive droop control in [33, 34] further improves performance, but the transmission line impedance is neglected. High droop gains in [8] mitigate power-sharing discrepancy caused by the line impedances. In [35], a communication network is spread all over the microgrid and the functionality of the centralized secondary controller is embedded in each converter. Point-to-point communication links are required for all sources, and any link failure renders the whole microgrid inoperable. The line impedance effect is taken into account in [26], with a fully connected communication network. Despite improved accuracy, systems with a fully connected communication network are susceptible to failure as any link failure impairs the whole control functionality. Future extension is another challenge; after any structural/electrical upgrade, some control settings, e.g., the number of sources, need to be updated and embedded in all converters. Voltage regulation requirement is redefined in [36] to incorporate the line impedance effect. Accordingly, it is required that the average voltage across the microgrid (and only not a specific bus voltage) is regulated at the global voltage set point determined by the tertiary control. This is called the global voltage regulation and is considered in this chapter. This chapter focuses on the cooperative secondary/primary controls for DC microgrids. The salient features of these control methods are as follows:

- Cooperation among converters on a communication graph is used to provide neighbors' data and, accordingly, fine-tune the local voltage set point for each converter.
- Each converter is augmented with a voltage regulator. This regulator uses the estimation made by the voltage observer to adjust the local voltage set point and provide global voltage regulation.
- A current regulator is also added that compares the actual per-unit current of a converter with a weighted average of its neighbors' and, accordingly, generates a voltage correction term to provide proportional load sharing. As an alternative control solution, the current regulator can tune the droop coefficient in an adaptive droop mechanism to balance load sharing.
- Cooperation of the voltage and current regulators is shown to effectively carry out both global voltage regulation and proportional load sharing, particularly, when the transmission line impedances are not negligible.

- A noise-resilient voltage observer is introduced that processes local and neighbors' voltage approximation to estimate the global average voltage across the microgrid.
- The control scheme does not require a priori knowledge of the global parameters such as the number of sources. Thus, it is scalable and truly features plug-and-play capability.
- A sparse communication network is spanned across the microgrid that enables limited message passing among converters; each converter only exchanges data with its neighbors. This is in direct contrast to the centralized control approaches which require communication networks with high-bandwidth communication links and a high level of connectivity.

7.1 Distributed Cooperative Controller for DC Microgrids

7.1.1 Graphical Representation of DC Microgrids

Figure 7.1 shows the mapping of a cyber network to a physical microgrid. The nodes represent converters, and edges represent communication links for data exchange. The communication graph does not need to have the same topology as the underlying physical microgrid. This cyber connection lays the groundwork for the cooperative control paradigm, where neighbors' interactions can lead to a global consensus. Accordingly, not all agents (converters) in a large-scale dynamic system need to be in a direct contact. Instead, each agent only exchanges control variables with its neighbors. Then, using the neighbors' data and its local measurements, the agent updates its control variables. The cooperative control offers global consensus of the desired variables, provided that the communication graph is properly designed.

Figure 7.1b shows a directed graph (digraph) associated with the cyber layer connecting the microgrid converters in Fig. 7.1a. Such a graph is represented as a set of nodes $\mathbf{V_G} = \{v_1^{\mathrm{g}}, v_2^{\mathrm{g}}, \ldots, v_N^{\mathrm{g}}\}$ connected through a set of edges $\mathbf{E_G} \subset \mathbf{V_G} \times \mathbf{V_G}$, and an associated adjacency matrix $\mathbf{A_G} = [a_{ij}] \in \mathbb{R}^{N \times N}$, where N is the number of nodes. The adjacency matrix $\mathbf{A_G}$ contains the communication weights, where $a_{ij} > 0$ if $(v_j^{\mathrm{g}}, v_i^{\mathrm{g}}) \in \mathbf{E_G}$ and $a_{ij} = 0$, otherwise. a_{ij} is the communication weight for data transfer from Node j to Node i. Here, the adjacency matrix is assumed to be time invariant. $N_i = \{j | (v_j^{\mathrm{g}}, v_i^{\mathrm{g}}) \in \mathbf{E_G}\}$ denotes the set of all neighbors of Node i; i.e., if $j \in N_i$, then v_i^{g} receives information from v_j^{g}. However, in a digraph, the link is not necessarily reciprocal; i.e., v_j^{g} might not receive information from v_i^{g}. The in-degree matrix $\mathbf{D_G^{in}} = \mathrm{diag}\{d_i^{\mathrm{in}}\}$ is a diagonal matrix with $d_i^{\mathrm{in}} = \sum_{j \in N_i} a_{ij}$. Similarly, the out-degree matrix is $\mathbf{D_G^{out}} = \mathrm{diag}\{d_i^{\mathrm{out}}\}$, where $d_i^{\mathrm{out}} = \sum_{i \in N_j} a_{ji}$. The Laplacian matrix is defined as $\mathbf{L} = \mathbf{D_G^{in}} - \mathbf{A_G}$, whose eigenvalues affect the global dynamics of the entire microgird [37].

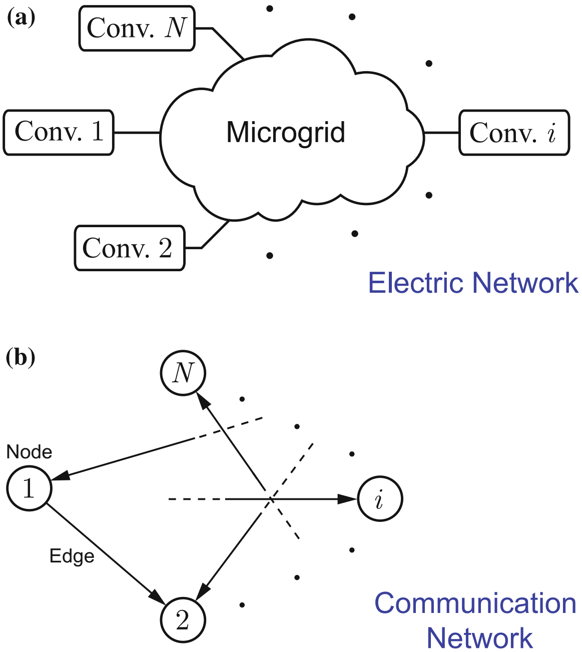

Fig. 7.1 General layout of a DC microgrid: **a** converters supplying the grid and **b** communication network spanned among sources for data exchange. © [2016] IEEE. Reprinted, with permission, from IEEE Transactions on Power Electronics [36]

The Laplacian matrix is balanced if the in-degree of each node matches its out-degree, i.e., $\mathbf{D}_{\mathbf{G}}^{\text{in}} = \mathbf{D}_{\mathbf{G}}^{\text{out}}$. In particular, if the graph is undirected, i.e., all links are bidirectional then, the Laplacian matrix is balanced. A direct path from v_i^{g} to v_j^{g} is a sequence of edges that connects the two nodes. A digraph is said to have a spanning tree if it contains a root node, from which there exists at least a direct path to every other node.

7.1.2 *Cooperative Secondary Control Framework*

Figure 7.2 shows the layout of a typical DC microgrid, where the physical, cyber, and control layers are all illustrated. The physical layer consists of the dispatchable sources (including the power electronics converters), transmission lines, and loads. A cyber layer, comprised of all communication links, is spanned across the microgrid to facilitate data exchange. This is a sparse communication network with at least a spanning tree and is also chosen such that in case of any cyber-link failure, the remaining network still contains a spanning tree. Although the graph shown in Fig. 7.2 is undirected (bidirectional), directed graphs can be used in a general case. Each converter transmits a set of data, $\Psi_i = [\bar{v}_i, v_i, i_i^{\text{pu}}]$, to its neighbors that consist of three elements: its estimate of the average voltage across the microgrid, $\bar{v}_i$, its actual local voltage measurement, v_i, and the measured per-unit current, i_i^{pu}. At the other end of the communication links, each converter j receives data from all its neighbors, Ψ_k, $k \in N_j$, with communication weights, a_{jk}. These communication weights are design parameters and can be considered as data transfer gains.

The per-unit term here refers to the current provided by the converter divided by its rated current, i.e., $i_i^{\mathrm{pu}} \triangleq i_i / I_i^{\mathrm{rated}}$, where I_i^{rated} is the rated current of the ith converter. Thus, individual converters may use different values as their base currents (i.e., their rated currents), unlike the conventional per-unit terminology, where converters in the same voltage zone share identical values for base currents. This terminology of the per-unit current is used here to represent loading percentage of each converter.

The global voltage regulation and proportional load sharing are the two objectives of the secondary/primary control, which require proper voltage set point assignment for the individual converters. The cooperative secondary controller is highlighted in Fig. 7.2, where local and neighbors' information are processed to adjust the local voltage set point, v_i^*. The starting point is the conventional droop mechanism that characterizes the converter output impedance using a virtual impedance r_i. The droop controller, at a primary control level, acts on local information. When operating conditions vary, the droop mechanism promptly

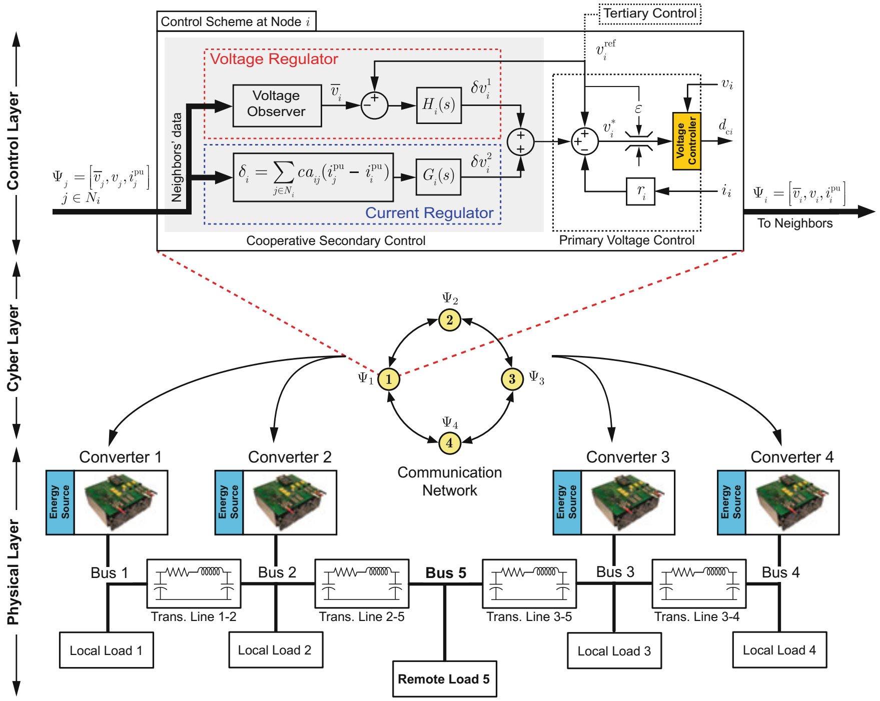

Fig. 7.2 Distributed cooperative control for DC microgrids. © [2016] IEEE. Reprinted, with permission, from IEEE Transactions on Power Electronics [36]

initiates the voltage adjustment. However, this local control has a limited performance. Cooperation among converters, at the secondary control level, can help properly fine-tune the voltage set points, v_i^*, and mitigate the current and voltage residuals.

The voltage set point for the droop control is augmented with two correction terms. These correction terms are provided through cooperation among converters. They are resulted from voltage and current regulators that help fine adjustment of the local voltage set points, i.e., v_i^*s, to provide global voltage regulation and proportional load sharing. Based on Fig. 7.2, the local voltage set point for an individual converter can be expressed as

$$v_i^* = v_i^{\mathrm{ref}} - r_i i_i + \delta v_i^1 + \delta v_i^2. \tag{7.1}$$

This set point is further adjusted by a voltage limiter (see Fig. 7.2) to maintain the bus voltages within an acceptable range.

The voltage regulator consists of a voltage observer and a PI controller, H_i. The voltage observer at each node estimates the average voltage across the microgrid, where $\bar{v}_i$ is the estimation at Node i. This estimation is then compared with the global reference voltage, v_i^{ref}, to generate the first voltage correction term, δv_i^1. In case of any mismatch between $\bar{v}_i$ and v_i^{ref}, the controller adjusts δv_i^1 to eliminate the discrepancy. In the islanded mode of operation, the global reference voltage, v_i^{ref}, are typically all equal to the rated voltage of the microgrid. However, in the grid-connected mode, where the microgrid exchanges power with the main grid, the tertiary control sets a new voltage level for the microgrid and relays the new reference value to individual converters. A cooperative observer will process the local voltage measurement and the neighbors' estimates to evaluate the average voltage across the microgrid. Functionality of the observer is discussed in detail in Sect. 7.1.3. The line impedances might incapacitate the droop mechanism to proportionally share the load. Herein, a cooperative current regulator generates the second voltage correction term, δv_i^2. The regulator at Node i compares the local per-unit current, i_i^{pu}, with a weighted average of the neighbors' per-unit currents to find the current mismatch, δ_i,

$$\delta_i = \sum_{j \in N_i} c a_{ij} \left(i_j^{\mathrm{pu}} - i_i^{\mathrm{pu}} \right), \tag{7.2}$$

where c is the coupling gain between the voltage and current regulators. The current mismatch, δ_i, is fed to a PI controller, G_i, which calculates the second voltage correction term, δv_i^2. If the per-unit currents of any two neighbors differ, the current regulators of the corresponding converters respond and adjust their second voltage correction terms to gain balance.

The current regulator itself (without the droop mechanism shown in Fig. 7.2) can accurately carry out the proportional load sharing. The droop mechanism, however, is typically a part of the primary controller and might be already embedded with the power electronic converter without any deactivation flexibility. Therefore, it is included in the primary controller of Fig. 7.2 to show that the current regulator can handle the load sharing even in the presence of the droop mechanism.

The primary voltage controller typically includes a voltage limiter (see Fig. 7.2). These limiters carry out two tasks: They limit voltage variations at the source terminals and also limit transmission line loading. According to Fig. 7.2, each output voltage is limited to $v_i^{\mathrm{ref}} - \varepsilon \le v_i \le v_i^{\mathrm{ref}} + \varepsilon$. With no loss of generality, one can assume that all converters use identical reference voltages, i.e., $v_i^{\mathrm{ref}} = v_{\mathrm{ref}}$ for all $1 \le i \le N$. Accordingly, voltage difference between every two nodes does not exceed the voltage limit band, i.e., $\left|v_i - v_j\right| \le 2\varepsilon$. Equivalently, the transmission line current will be limited to $i_{ij} \le 2\varepsilon / r_{ij}$, where r_{ij} is the series resistance of the transmission line between nodes i and j.

7.1.3 Voltage Observer

The observer module is a part of the voltage regulator module, as shown in Fig. 7.2. It uses a dynamic cooperative framework to process neighbors' information and estimate the average voltage across the microgrid.

7.1.3.1 Dynamic Consensus Algorithm

Figure 7.3a shows the cooperative distributed approach for the global averaging. The observer at Node i receives its neighbors' estimates, $\bar{v}_j$s ($j \in N_i$). Then, the

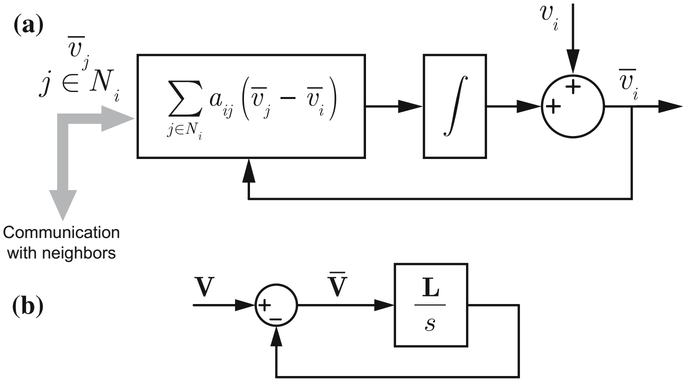

Fig. 7.3 Dynamic consensus protocol: **a** averaging policy at each node and **b** global model of the averaging technique in the frequency domain. © [2016] IEEE. Reprinted, with permission, from IEEE Transactions on Power Electronics [36]

observer updates its own estimate, $\bar{v}_i$, by processing the neighbors' estimates and the local voltage measurement, v_i,

$$\bar{v}_i(t) = v_i(t) + \int_0^t \sum_{j \in N_i} a_{ij} \big(\bar{v}_j(\tau) - \bar{v}_i(\tau) \big) \mathrm{d}\tau. \tag{7.3}$$

This updating protocol is commonly referred to as *dynamic consensus* in the literature [38]. As shown in (7.3), the local measurement, e.g., v_i, is directly fed into the estimation protocol. Thus, in case of any voltage variation at Node i, the local estimate, $\bar{v}_i$, immediately responds. Then, the change in $\bar{v}_i$ propagates through the communication network and affects all other estimations. By differentiating (7.3)

$$\dot{\bar{v}}_i = \dot{v}_i + \sum_{j \in N_i} a_{ij} \big(\bar{v}_j - \bar{v}_i \big) = \dot{v}_i + \sum_{j \in N_i} a_{ij} \bar{v}_j - d_i^{\mathrm{in}} \bar{v}_i. \tag{7.4}$$

Accordingly, one can formulate the global observer dynamic as

$$\dot{\bar{\mathbf{v}}} = \dot{\mathbf{v}} + \mathbf{A_G} \bar{\mathbf{v}} - \mathbf{D}_{\mathbf{G}}^{\mathrm{in}} \bar{\mathbf{v}} = \dot{\mathbf{v}} - \big(\mathbf{D}_{\mathbf{G}}^{\mathrm{in}} - \mathbf{A_G} \big) \bar{\mathbf{v}} = \dot{\mathbf{v}} - \mathbf{L} \bar{\mathbf{v}}, \tag{7.5}$$

where $\mathbf{v} = [v_1, v_2, \ldots, v_N]^{\mathrm{T}}$ is the voltage measurement vector, which carries measured voltage of all nodes. Also, $\bar{\mathbf{v}} = [\bar{v}_1, \bar{v}_2, \ldots, \bar{v}_N]^{\mathrm{T}}$ denotes the voltage estimation vector, which contains the global average voltage estimated by all nodes. Equivalently, in the frequency domain,

$$s\overline{\mathbf{V}} - \bar{\mathbf{v}}(0) = s\mathbf{V} - \mathbf{v}(0) - \mathbf{L}\overline{\mathbf{V}}, \tag{7.6}$$

where $\mathbf{V}$ and $\overline{\mathbf{V}}$ are the Laplace transforms of $\mathbf{V}$ and $\bar{\mathbf{v}}$, respectively. Equation (7.3) implies that $\mathbf{v}(0) = \bar{\mathbf{v}}(0)$. Therefore,

$$\overline{\mathbf{V}} = s(s\mathbf{I}_N + \mathbf{L})^{-1} \mathbf{V} = \mathbf{H}_{\mathrm{obs}} \mathbf{V}, \tag{7.7}$$

where $\mathbf{I}_N \in \mathbb{R}^{N \times N}$ and $\mathbf{H}_{\mathrm{obs}}$ are the identity matrix and the observer transfer function, respectively. Equation (7.7) expresses the global dynamics of the voltage observers, whose block diagram is shown in Fig. 7.3b. It is shown in Appendix that if $\mathbf{L}$ is balanced, then all elements of $\bar{\mathbf{v}}$ converge to a consensus value, which is the true average voltage, i.e., the average of all elements in $\mathbf{V}$. In other words,

$$\bar{\mathbf{v}}^{\mathrm{ss}} = \lim_{t \to \infty} \bar{\mathbf{v}}(t) = \mathbf{Q} \times \lim_{t \to \infty} \mathbf{v}(t) = \mathbf{Q}\mathbf{v}^{\mathrm{ss}} = \langle \mathbf{v}^{\mathrm{ss}} \rangle \underline{\mathbf{1}}, \tag{7.8}$$

where $\mathbf{Q} \in \mathbb{R}^{N \times N}$ is the averaging matrix, whose elements are all equal to $1/N$. $\mathbf{x}^{\mathrm{ss}}$ expresses the steady-state value of the vector $\mathbf{x} \in \mathbb{R}^{N \times 1}$. $\langle \mathbf{x} \rangle$ represents the average of all elements in the vector $\mathbf{X}$. $\underline{\mathbf{1}} \in \mathbb{R}^{N \times 1}$ is a vector whose elements are all equal to one.

7.1.3.2 Noise Cancelation Module

Disturbances may degrade the efficacy and accuracy of the voltage observers. Nonzero initial value of the integrator in Fig. 7.3a or read/write errors in digital storage devices are common disturbance sources in digital processing [39, 40]. For example, a nonzero initial value of any observer's integrator yields to an identical DC error in all estimations. Therefore, a noise cancelation module is essential to identify and cancel such disturbance/noises. Figure 7.4a shows the noise cancelation (NC) module incorporated in the voltage observer. A disturbance source, d_i, highlighted in red, is assumed for the observer at Node i. This source represents the aggregated effect of all possible disturbance/noises. The primary stage of the NC module is an observer similar to that of Fig. 7.3a that estimates average of the voltage deviations, w_is, where $w_i = \bar{v}_i - v_i$. This stage is followed by an integrator to ensure disturbance tracking for DC and exponentially damping disturbances, e.g., a nonzero initial value for any integrator.

At each node, the NC module estimates $\langle \mathbf{w} \rangle$ as a noise indicator, where $\mathbf{w} = [w_1, w_2, \ldots, w_N]^{\mathrm{T}}$ is the voltage deviation vector. If the noise cancelation term, $\hat{d}_i$, is disabled for all nodes, with no noise corrupting the signals, i.e., $d_i = 0$ for all nodes, the voltage observers converge to the true average voltage. Thus,

$$\mathbf{w} = \bar{\mathbf{v}} - \mathbf{v} \Rightarrow \langle \mathbf{w}^{\mathrm{ss}} \rangle = \langle \bar{\mathbf{v}}^{\mathrm{ss}} \rangle - \langle \mathbf{v}^{\mathrm{ss}} \rangle = \mathbf{0}. \tag{7.9}$$

However, if any noise pollutes any observation, the voltage observations no longer converge to the global average, i.e., $\langle \bar{\mathbf{v}}^{\mathrm{ss}} \rangle \neq \langle \mathbf{v}^{\mathrm{ss}} \rangle$. Accordingly, $\langle \mathbf{w}^{\mathrm{ss}} \rangle \neq \mathbf{0}$. Thus, $\langle \mathbf{w} \rangle$ is a suitable noise indicator. Accordingly, with activated NC module, it estimates $\langle \mathbf{w} \rangle$ and feeds the result into the integrator. If $\langle \mathbf{w} \rangle \neq \mathbf{0}$, the integrator adjusts the noise cancelation term, $\hat{d}_i$, until it matches the noise, i.e., $\hat{d}_i = d_i$, and cancels its effect on the voltage estimations.

Similar to (7.5), the total voltage observer dynamics can be derived by analyzing the policy explained in Fig. 7.4a. Herein, the total observer is referred to as the observer in Fig. 7.4a, which incorporates the NC module. According to this figure,

$$\dot{\bar{\mathbf{v}}} = -\mathbf{L}\bar{\mathbf{v}} + \dot{\mathbf{v}} + \dot{\mathbf{d}} - \dot{\hat{\mathbf{d}}}, \tag{7.10}$$

$$\dot{\hat{\mathbf{d}}} = \mathbf{K}\bar{\mathbf{w}}, \tag{7.11}$$

$$\dot{\bar{\mathbf{w}}} = -b\mathbf{L}\bar{\mathbf{w}} + \dot{\mathbf{w}} = -b\mathbf{L}\bar{\mathbf{w}} + \dot{\bar{\mathbf{v}}} - \dot{\mathbf{v}}, \tag{7.12}$$

where $\mathbf{d} = [d_1, d_2, \ldots, d_N]^{\mathrm{T}}$ and $\hat{\mathbf{d}} = \left[\hat{d}_1, \hat{d}_2, \ldots, \hat{d}_N\right]^{\mathrm{T}}$ are the actual and estimated disturbance vectors, respectively. $\bar{\mathbf{w}} = [\bar{w}_1, \bar{w}_2, \ldots, \bar{w}_N]^{\mathrm{T}}$ is the estimated voltage deviation vector. $\mathbf{K} = \mathrm{diag}\{k_i\}$ is the NC integrator gain matrix. b is the coupling gain between the main observer and the NC module. Equivalently, in the frequency domain,

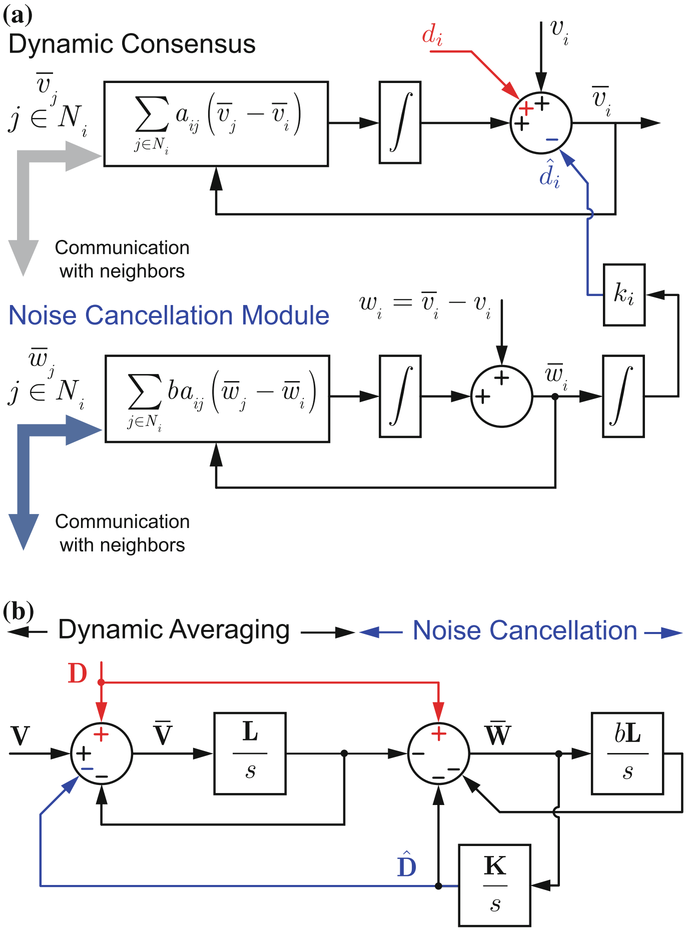

Fig. 7.4 Dynamic consensus protocol with noise cancelation: **a** averaging and noise cancelation policies at each node and **b** global model of the averaging technique in the frequency domain. © [2016] IEEE. Reprinted, with permission, from IEEE Transactions on Power Electronics [36]

$$(s\mathbf{I}_N + \mathbf{L})\bar{\mathbf{V}} - \bar{\mathbf{v}}(0) = s\mathbf{V} - \mathbf{v}(0) + s\mathbf{D} - \mathbf{d}(0) - s\hat{\mathbf{D}} + \hat{\mathbf{d}}(0), \tag{7.13}$$

$$s\widehat{\mathbf{D}} - \hat{\mathbf{d}}(0) = \mathbf{K}\overline{\mathbf{W}}, \tag{7.14}$$

$$(s\mathbf{I}_N + b\mathbf{L})\overline{\mathbf{W}} - \bar{\mathbf{w}}(0) = s\bar{\mathbf{V}} - \bar{\mathbf{v}}(0) - s\mathbf{V} + \mathbf{v}(0), \tag{7.15}$$

where $\mathbf{D}$, $\hat{\mathbf{D}}$, and $\overline{\mathbf{W}}$ are the Laplace transforms of $\mathbf{d}$, $\hat{\mathbf{d}}$, and $\bar{\mathbf{w}}$, respectively. The initial conditions of the vectors involved in the total observer can be determined using Fig. 7.4a. Accordingly,

$$\hat{\mathbf{d}}(0) = \mathbf{0}, \quad \bar{\mathbf{v}}(0) = \mathbf{v}(0) + \mathbf{d}(0), \tag{7.16}$$

$$\bar{\mathbf{w}}(0) = \bar{\mathbf{v}}(0) - \mathbf{v}(0) = \mathbf{d}(0). \tag{7.17}$$

Each disturbance source, d_i, represents the aggregated effect of all possible disturbances at the corresponding node. Thus, the initial conditions of all the integrators in Fig. 7.4a can be safely assumed zero. Based on (7.13)–(7.17), the global block diagram of the total observer is shown in Fig. 7.4b. One can simplify (7.13)–(7.15) using (7.16) and (7.17),

$$(s\mathbf{I}_N + \mathbf{L})\overline{\mathbf{V}} = s\mathbf{V} + s\mathbf{D} - \mathbf{K}\overline{\mathbf{W}}, \tag{7.18}$$

$$(s\mathbf{I}_N + b\mathbf{L})\overline{\mathbf{W}} = s(\overline{\mathbf{V}} - \mathbf{V}). \tag{7.19}$$

Therefore,

$$\left((s\mathbf{I}_N + \mathbf{L}) + s\mathbf{K}(s\mathbf{I}_N + b\mathbf{L})^{-1}\right)\overline{\mathbf{V}} = \left(s\mathbf{I}_N + s\mathbf{K}(s\mathbf{I}_N + b\mathbf{L})^{-1}\right)\mathbf{V} + s\mathbf{D}, \tag{7.20}$$

which can be written as

$$\bar{\mathbf{V}} = \mathbf{H}_{\text{obs}}^{\text{F}}\mathbf{V} + \mathbf{H}_{\text{NC}}\mathbf{D}, \tag{7.21}$$

$$\mathbf{H}_{\text{obs}}^{\text{F}} = \left((s\mathbf{I}_N + \mathbf{L}) + s\mathbf{K}(s\mathbf{I}_N + b\mathbf{L})^{-1}\right)^{-1} \times \left(s\mathbf{I}_N + s\mathbf{K}(s\mathbf{I}_N + b\mathbf{L})^{-1}\right), \tag{7.22}$$

$$\mathbf{H}_{\text{NC}} = s\left((s\mathbf{I}_N + \mathbf{L}) + s\mathbf{K}(s\mathbf{I}_N + b\mathbf{L})^{-1}\right)^{-1}, \tag{7.23}$$

where $\mathbf{H}_{\text{obs}}^{\text{F}}$ and $\mathbf{H}_{\text{NC}}$ are the total observer and NC transfer functions, respectively. It should be noted that for $\mathbf{K} = \mathbf{0}$, (7.22) and (7.7) provide the same functions. Basically, (7.7) presents the observer transfer function with a disabled NC module, where (7.22) expresses the function with an activated NC module. Appendix shows that $\lim_{s \to 0} \mathbf{H}_{\text{obs}}^{\text{F}} = \mathbf{Q}$, which guarantees convergence of all estimations to the global average voltage. It should also be noted that $\mathbf{H}_{\text{NC}}$ has a zero at the origin, and thus, for DC and exponentially damping disturbances, the second term in (7.21) decays to zero. Accordingly, the noise cancelation module successfully cancels any DC disturbance and attenuates any other disturbance according to its fundamental frequency. This is a satisfactory performance since most common disturbance sources in digital signal processing, such as nonzero integrator initial condition and read/write errors, have a DC or very-low-frequency nature [40].

7.2 Analytical Model Development for DC Microgrids

7.2.1 Global Dynamic Model

Let $\mathbf{v}_{\text{ref}} = [v_1^{\text{ref}}, v_2^{\text{ref}}, \ldots, v_N^{\text{ref}}]^{\text{T}}$ and $\mathbf{i} = [i_1, i_2, \ldots, i_N]^{\text{T}}$ be the global reference voltage and the actual supplied current vectors, respectively. $\mathbf{V}_{\text{ref}}$ and $\mathbf{I}$ are the Laplace transforms of $\mathbf{v}_{\text{ref}}$ and $\mathbf{i}$, respectively. Systematically, $\mathbf{V}_{\text{ref}}$ is the input to the entire microgrid, where $\mathbf{V}$ and $\mathbf{I}$ are the outputs. A global dynamic model formulates the transfer functions from the input, $\mathbf{V}_{\text{ref}}$, to any outputs $\mathbf{V}$ and $\mathbf{I}$.

The cooperative distributed control of Fig. 7.2 introduces two voltage correction terms at each node, δv_i^1 and δv_i^2. Accordingly,

$$\Delta\mathbf{V}^1 = \mathbf{H}\left(\mathbf{V}_{\text{ref}} - \overline{\mathbf{V}}\right), \tag{7.24}$$

$$\Delta\mathbf{V}^2 = -c\mathbf{GLI}^{\text{pu}}. \tag{7.25}$$

$\Delta\mathbf{v}^1 = [\delta v_1^1, \delta v_2^1, \ldots, \delta v_N^1]^{\text{T}}$ and $\Delta\mathbf{v}^2 = [\delta v_1^2, \delta v_2^2, \ldots, \delta v_N^2]^{\text{T}}$ are the first and the second voltage correction vectors, respectively. $\Delta\mathbf{V}^1$ and $\Delta\mathbf{V}^2$ are the Laplace transforms of $\Delta\mathbf{v}^1$ and $\Delta\mathbf{v}^2$, respectively. $\mathbf{H} = \text{diag}\{H_i\}$ and $\mathbf{G} = \text{diag}\{G_i\}$ are the voltage and current controller matrices, respectively. $\mathbf{i}^{\text{pu}} = [i_1^{\text{pu}}, i_2^{\text{pu}}, \ldots, i_N^{\text{pu}}]^{\text{T}}$ is the per-unit current vector with the Laplace transform of $\mathbf{I}^{\text{pu}}$. One can write

$$\mathbf{I}^{\text{pu}} = \mathbf{I}_{\text{rated}}^{-1}\mathbf{I}, \tag{7.26}$$

where $\mathbf{I}_{\text{rated}} = \text{diag}\{I_i^{\text{rated}}\}$ and I_i^{rated} are the current rating matrix and the current rating of the converter at Node i, respectively. Thus, by substituting (7.26) in (7.25),

$$\Delta\mathbf{V}^2 = -c\mathbf{GLI}_{\text{rated}}^{-1}\mathbf{I}. \tag{7.27}$$

Let $\mathbf{v}^* = [v_1^*, v_2^*, \ldots, v_N^*]^{\text{T}}$ be the vector of local voltage set points with the Laplace transform of $\mathbf{V}^*$. The cooperative controller finds the local voltage set points according to,

$$\mathbf{V}^* = \mathbf{V}_{\text{ref}} + \Delta\mathbf{V}^1 + \Delta\mathbf{V}^2 - \mathbf{rI}, \tag{7.28}$$

where $\mathbf{r} = \text{diag}\{r_i\}$ is the virtual impedance matrix. By substituting (7.24) and (7.27) in (7.28),

$$\mathbf{V}^* = (\mathbf{I}_N + \mathbf{H})\mathbf{V}_{\text{ref}} - \mathbf{H}\overline{\mathbf{V}} - \left(c\mathbf{GLI}_{\text{rated}}^{-1} + \mathbf{r}\right)\mathbf{I}. \tag{7.29}$$

On the other hand, dynamic behavior of any converter with a closed-loop voltage regulator can be modeled as

$$V_i = G_i^{\mathrm{c}}(s)V_i^*, \tag{7.30}$$

where V_i and V_i^* are the Laplace transforms of v_i and v_i^*, respectively. G_i^{c} is the closed-loop transfer function of the converter at Node i. The closed-loop transfer functions are formulated in [41, 42] for a wide variety of converters. Global dynamic of the converters can be found as

$$\mathbf{V} = \mathbf{G}_{\mathrm{c}}\mathbf{V}^*, \tag{7.31}$$

where $\mathbf{G}_{\mathrm{c}} = \mathrm{diag}\{G_i^{\mathrm{c}}\}$ is the transfer function matrix. Substituting (7.29) in (7.31) yields

$$\mathbf{V} = \mathbf{G}_{\mathrm{c}}\big((\mathbf{I}_N + \mathbf{H})\mathbf{V}_{\mathrm{ref}} - \mathbf{H}\overline{\mathbf{V}} - \big(c\mathbf{G}\mathbf{L}\mathbf{I}_{\mathrm{rated}}^{-1} + \mathbf{r}\big)\mathbf{I}\big). \tag{7.32}$$

The voltage observer dynamics are formulated in (7.21)–(7.23). By neglecting the disturbance in the observers, one can write $\overline{\mathbf{V}} = \mathbf{H}_{\mathrm{obs}}^{\mathrm{F}}\mathbf{V}$. The microgrid admittance matrix, $\mathbf{Y}_{\mathrm{bus}}$, relates the supplied currents to the bus voltages as

$$\mathbf{I} = \mathbf{Y}_{\mathrm{bus}}\mathbf{V}. \tag{7.33}$$

The admittance matrix carries all the details of the distribution grid. For example, π-circuit model of any line can be considered by including the line series resistance, series inductance, and parallel capacitance in the admittance matrix, $\mathbf{Y}_{\mathrm{bus}}$. Therefore, (7.32) can be written as

$$\begin{cases} \mathbf{V} = \big(\mathbf{G}_{\mathrm{c}}^{-1} + \mathbf{H}\mathbf{H}_{\mathrm{obs}}^{\mathrm{F}} + \big(c\mathbf{G}\mathbf{L}\mathbf{I}_{\mathrm{rated}}^{-1} + \mathbf{r}\big)\mathbf{Y}_{\mathrm{bus}}\big)^{-1}(\mathbf{I}_N + \mathbf{H})\mathbf{V}_{\mathrm{ref}} \\ \mathbf{I} = \Big((\mathbf{Y}_{\mathrm{bus}}\mathbf{G}_{\mathrm{c}})^{-1} + \mathbf{H}\mathbf{H}_{\mathrm{obs}}^{\mathrm{F}}\mathbf{Y}_{\mathrm{bus}}^{-1} + c\mathbf{G}\mathbf{L}\mathbf{I}_{\mathrm{rated}}^{-1} + \mathbf{r}\Big)^{-1}(\mathbf{I}_N + \mathbf{H})\mathbf{V}_{\mathrm{ref}} \end{cases}. \tag{7.34}$$

Equation (7.34) represents the global microgrid dynamics with the cooperative controller in effect.

7.2.2 Guidelines for Controller Design

For a given microgrid, the matrix of converters' closed-loop transfer functions, $\mathbf{G}_{\mathrm{c}}$, the current rating matrix, $\mathbf{I}_{\mathrm{rated}}$, and the admittance matrix, $\mathbf{Y}_{\mathrm{bus}}$, are known. The communication graph needs to contain at least a spanning tree. Weights of the communication links, a_{ij}, and, thus, the Laplacian matrix, $\mathbf{L}$, may, then, be chosen to provide the desired dynamic for the voltage observers by evaluating (7.7). It should be noted that the selection of the communication weights must satisfy a balanced Laplacian matrix. Equation (7.23) helps to design the coupling gain, b, and the integrator gain matrix, $\mathbf{K}$, to achieve a satisfactory noise cancelation dynamic. Given the Laplacian matrix, $\mathbf{L}$, and the total observer transfer function,

$\mathbf{H}_{\mathrm{obs}}^{\mathrm{F}}$ (or the reduced-order function $\mathbf{H}_{\mathrm{obs}}$), one can use (7.34) to design the voltage and current controller matrices (**H** and **G**, respectively), the virtual impedance matrix, **r**, and the coupling gain, c, to provide any desired asymptotically stable dynamic response, where all poles of (7.34) lie in the open left-hand plane (OLHP). The current regulator surpasses the droop mechanism in providing the proportional load sharing, and thus, the virtual impedance matrix, **r**, can be freely designed. However, the designer may still use the traditional approach to tune the virtual impedances as

$$\mathbf{r} = m\mathbf{I}_{\mathrm{rated}}^{-1}, \tag{7.35}$$

where m is a positive scalar design parameter.

7.2.3 *Steady-State Analysis*

Steady-state analysis is essential to ensure that the cooperative controller satisfies both operational requirements: the global voltage regulation and the proportional load sharing. With no loss of generality, one can assume

$$\mathbf{V}_{\mathrm{ref}} = \frac{v_{\mathrm{ref}}}{s}\underline{\mathbf{1}}, \tag{7.36}$$

where v_{ref} is the reference voltage for the entire microgrid. Voltage stabilization, throughout the microgrid, is also assumed. Accordingly, the voltage vector, **V**, is a type 1 vector; i.e., it has a single pole at the origin and all other poles lie in the OLHP. Thus, one may safely use the final value theorem to find the steady-state voltage vector, $\mathbf{v}^{\mathrm{ss}}$,

$$\begin{aligned}\mathbf{v}^{\mathrm{ss}} &= \lim_{t\to\infty}\mathbf{v}(t) = \lim_{s\to 0} s\mathbf{V}(s)\\ &= \lim_{s\to 0}\left(s\mathbf{G}_{\mathrm{c}}^{-1} + s\mathbf{H}\mathbf{H}_{\mathrm{obs}}^{\mathrm{F}} + s\left(c\mathbf{G}\mathbf{L}\mathbf{I}_{\mathrm{rated}}^{-1} + \mathbf{r}\right)\mathbf{Y}_{\mathrm{bus}}\right)^{-1} \times s v_{\mathrm{ref}}(\mathbf{I}_N + \mathbf{H})\underline{\mathbf{1}}.\end{aligned} \tag{7.37}$$

The voltage and current controllers (H_is and G_is, respectively) are PI controllers, and thus, one can write $\mathbf{H} = \mathbf{H}_{\mathrm{P}} + \mathbf{H}_{\mathrm{I}}/s$, where $\mathbf{H}_{\mathrm{P}}$ and $\mathbf{H}_{\mathrm{I}}$ are diagonal matrices carrying proportional and integral gains of the voltage controllers. Similarly, $\mathbf{G} = \mathbf{G}_{\mathrm{P}} + \mathbf{G}_{\mathrm{I}}/s$, where $\mathbf{G}_{\mathrm{P}}$ and $\mathbf{G}_{\mathrm{I}}$ are diagonal matrices that contain proportional and integral gains of the current controllers. It is also known that the DC gain of the closed-loop converters is equal to one, i.e., $\mathbf{G}_{\mathrm{c}}(0) = \mathbf{I}_N = \mathbf{G}_{\mathrm{c}}^{-1}(0)$ [41]. In addition, based on Theorem 7.2 (see Appendix), $\lim_{s\to 0}\mathbf{H}_{\mathrm{obs}}^{\mathrm{F}} = \mathbf{Q}$. Thus, (7.37) can be written as

$$\mathbf{v}^{\mathrm{ss}} = v_{\mathrm{ref}}\left(\mathbf{H}_{\mathrm{I}}\mathbf{Q} + c\mathbf{G}_{\mathrm{I}}\mathbf{L}\mathbf{I}_{\mathrm{rated}}^{-1}\mathbf{Y}_{\mathrm{dc}}\right)^{-1}\mathbf{H}_{\mathrm{I}}\underline{\mathbf{1}}, \tag{7.38}$$

or, equivalently,

$$\left(\mathbf{U}\mathbf{Q} + c\mathbf{L}\mathbf{I}_{\mathrm{rated}}^{-1}\mathbf{Y}_{\mathrm{dc}}\right)\mathbf{v}^{\mathrm{ss}} = v_{\mathrm{ref}}\mathbf{U}\underline{\mathbf{1}}, \tag{7.39}$$

where $\mathbf{Y}_{\mathrm{dc}}{=}\mathbf{Y}_{\mathrm{bus}}(0)$ is the DC admittance matrix, and $\mathbf{U} = \mathbf{G}_{\mathrm{I}}^{-1}\mathbf{H}_{\mathrm{I}} = \mathrm{diag}\{u_i\}$ is a diagonal matrix with $u_i = \mathbf{H}_{\mathrm{I}}(i,i)/\mathbf{G}_{\mathrm{I}}(i,i)$. All the integrator gains for the current controllers are assumed to be positive, and thus, $\mathbf{G}_{\mathrm{I}}^{-1}$ exists. Since the Laplacian matrix is designed to be balanced (see Sect. 7.1.3), one can write $\mathbf{QL} = \mathbf{0}$. Therefore, by multiplying both sides of (7.39) by the averaging matrix, $\mathbf{Q}$,

$$\mathbf{Q}(\mathbf{U}(\mathbf{Q}\mathbf{v}^{\mathrm{ss}})) = v_{\mathrm{ref}}\mathbf{Q}(\mathbf{U}\underline{\mathbf{1}}). \tag{7.40}$$

Based on the definition of the averaging matrix, $\mathbf{Q}$, $\mathbf{Qx} = \langle\mathbf{x}\rangle\underline{\mathbf{1}}$, for any vector $\mathbf{x} \in \mathbb{R}^{N\times 1}$. Accordingly, (7.40) is equivalent to

$$\langle\mathbf{v}^{\mathrm{ss}}\rangle\langle\mathbf{U}\underline{\mathbf{1}}\rangle\underline{\mathbf{1}} = v_{\mathrm{ref}}\langle\mathbf{U}\underline{\mathbf{1}}\rangle\underline{\mathbf{1}}, \tag{7.41}$$

or, equivalently, $\langle\mathbf{v}^{\mathrm{ss}}\rangle = v_{\mathrm{ref}}$. This analysis shows that the cooperative controller provides global voltage regulation; i.e., it successfully regulates the average voltage at the desired value. On the other hand, (7.39) can be written as

$$\mathbf{U}(\mathbf{Q}\mathbf{v}^{\mathrm{ss}}) + c\mathbf{L}\mathbf{I}_{\mathrm{rated}}^{-1}\mathbf{i}^{\mathrm{ss}} = v_{\mathrm{ref}}\mathbf{U}\underline{\mathbf{1}}, \tag{7.42}$$

or, equivalently,

$$\mathbf{L}\left(\mathbf{I}_{\mathrm{rated}}^{-1}\mathbf{i}^{\mathrm{ss}}\right) = c^{-1}(v_{\mathrm{ref}} - \langle\mathbf{v}^{\mathrm{ss}}\rangle)\mathbf{U}\underline{\mathbf{1}} = \mathbf{0}. \tag{7.43}$$

The Lemma 7.1 (see Appendix) ensures that the Laplacian matrix $\mathbf{L}$ has a simple eigenvalue at the origin, i.e., $\lambda_1 = 0$. Thus, based on (7.43), $\mathbf{I}_{\mathrm{rated}}^{-1}\mathbf{i}^{\mathrm{ss}}$ is the right eigenvector of $\mathbf{L}$ associated with $\lambda_1 = 0$. It is mentioned in the Proof of Lemma 7.2 (see Appendix) that $w_r = \underline{\mathbf{1}}$ is the right eigenvector of the Laplacian matrix, $\mathbf{L}$, associated with $\lambda_1 = 0$. Thus,

$$\mathbf{I}_{\mathrm{rated}}^{-1}\mathbf{i}^{\mathrm{ss}} = n\underline{\mathbf{1}}, \tag{7.44}$$

where n is a positive scalar. Equation (7.44) concludes the proportional load sharing. Equations (7.41) and (7.44) show that the cooperative controller successfully carries out both global voltage regulation and proportional load sharing.

7.3 Distributed Adaptive Droop Control for DC Microgrids: An Alternative Solution

This section presents an alternative solution for controlling DC microgrids. Let us assume that the data package transmitted by Node i, $\Psi_i = [\bar{v}_i, i_i^{\text{pu}}]$, consists of two elements: its estimate of the average voltage across the microgrid, $\bar{v}_i$, and the measured per-unit current, i_i^{pu}; you may note this data format is different than the one used in Sect. 7.1.2. At the receiving ends of the communication links, each converter k receives data from all its neighbors, Ψ_j, $j \in N_k$, with associated communication weights, a_{kj}. These weights are design parameters and can be considered as data transfer gains.

The global voltage regulation and proportional load sharing are the two objectives of the secondary control, which require proper voltage set point assignment for individual converters. The distributed adaptive droop controller is elaborated in Fig. 7.5a, where local and neighbors' information are processed to adjust the local voltage set point, v_i^*. Cooperation among converters, at the secondary control level, helps to fine-tune the voltage set points, v_i^*, and mitigate the current and voltage residues.

The voltage set point for each converter is augmented with two terms provided through cooperation among converters. They are resulted from voltage and current regulators. Based on Fig. 7.5a, the local voltage set point for an individual converter can be expressed as

$$v_i^* = v_i^{\text{ref}} - v_i^{\text{d}} + \delta v_i = v_i^{\text{ref}} - r_i i_i + \delta v_i, \tag{7.45}$$

where v_i^{ref}, v_i^{d}, δv_i, and r_i are the global reference voltage, droop voltage, voltage correction term, and the virtual impedance of the ith converter, respectively. This set point is further adjusted by a voltage limiter (see Fig. 7.5a) to maintain the bus voltages within an acceptable range. Figure 7.5b elaborates how adjustable voltage correction term, δv_i, and virtual impedance, r_i, can navigate operating point of the

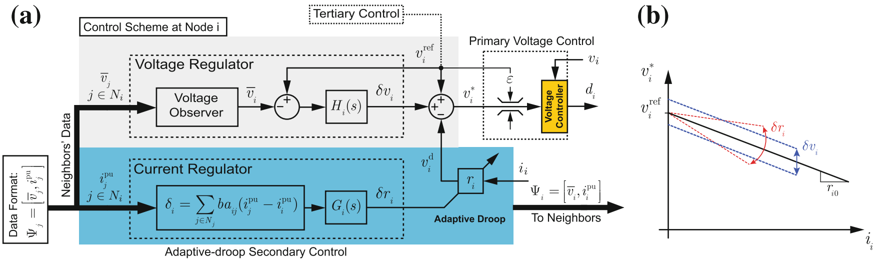

Fig. 7.5 Distributed control policy: **a** cooperative adaptive droop control for a single agent (converter) and **b** effect of adjustable voltage correction and virtual impedance on the droop characterization. © [2016] IEEE. Reprinted, with permission, from IEEE Transactions on Energy Conversion [47]

converter. The droop mechanism, which generates the term $r_i i_i$ in (7.45), characterizes output impedance of the converters and helps to share load, which leads to the voltage drop across the microgrid. The voltage correction terms, δv_is, are augmented to the local reference voltages to boost the voltage across the microgrid. Accordingly, the controller contains two modules: a voltage regulator and a current regulator.

The voltage regulator at Node i consists of a voltage observer and a PI controller, $H_i(s)$. The voltage observer at each node estimates the average voltage across the microgrid, where $\bar{v}_i$ is the estimation at Node i. This estimation is then compared with the global reference voltage, v_i^{ref}, to generate the voltage correction term, δv_i. In case of any mismatch between $\bar{v}_i$ and v_i^{ref}, the controller adjusts δv_i to eliminate the discrepancy. In the islanded mode of operation, the global reference voltages, v_i^{ref}s, are typically identical and equal to the rated voltage of the microgrid. However, in the grid-tied mode, the tertiary control sets a new voltage level for the microgrid and relays the new reference values to individual converters. The voltage observer (discussed in Sect. 7.1.3) processes the local voltage measurement and the neighbors' estimates to evaluate the average voltage across the microgrid.

The current regulator at Node i provides the input to the droop mechanism. The droop mechanism characterizes the converter output impedance using the virtual impedance r_i. Virtual impedances are conventionally initialized in reciprocal to the converters' rated current, i.e., $r_{i0} = m/I_i^{\mathrm{rated}}$, where m is a design parameter and is identical for all converters. However, the distribution line impedances compromise performance of the droop controller. Thus, the droop gains are suggested to adapt according to the microgrid loading condition. To this end, a cooperative current regulator is included in the secondary control of any converter, e.g., converter i, which compares the local per-unit current, i_i^{pu}, with the weighted average of the neighbors' per-unit currents and finds the current mismatch, δ_i,

$$\delta_i = \sum_{j \in N_i} b a_{ij} \left(i_j^{\mathrm{pu}} - i_i^{\mathrm{pu}} \right). \tag{7.46}$$

where b is the coupling gain between the voltage and current regulators. This mismatch is then fed to a PI controller, $G_i(s)$, to generate an impedance correction term, δr_i, which updates the virtual impedance

$$r_i(t) = r_{i0} - \delta r_i(t). \tag{7.47}$$

If the per-unit currents of any two neighbors differ, the current regulators of the corresponding converters respond and adjust their impedance correction terms to achieve balance.

7.4 Experimental Performance Evaluation

A low-voltage DC microgrid, with a structure shown in Fig. 7.2, is prototyped to study the control methodology of Sect. 7.1.2. Figure 7.6 shows the experimental setup. Four adjustable isolated AC sources are used as the energy sources. Each source is driven by a buck converter augmented with an input rectifier. The converters have similar topologies but different ratings; i.e., the rated currents of the first and the fourth converters are twice those for the other two converters. A π-circuit model is used for each transmission line. There are four local loads and one remote load, as shown in Fig. 7.2.

Alternative graphical connections are shown in Fig. 7.7. Communication links are assumed bidirectional to feature a balanced Laplacian matrix and help with the sparsity of the resulting communication graph. Although all alternative graphs include spanning trees, some are susceptible to lose connectivity in the case of a single link failure. For example, if any of the links highlighted in red in Fig. 7.7a, b is lost, the corresponding graph losses its connectivity, which hinders the functionality of the control mechanism. However, for the set of four agents, the circular communication flow in Fig. 7.7c is the sparsest network where the failure of a single link does not compromise the graphical connectivity. Figure 7.7d shows a fully connected graph, but it lacks sparsity. Therefore, the graphical structure in Fig. 7.7c is chosen for data exchange in the cyber layer.

A dSPACE control board (DS1103) implements the control routines. Electrical parameters of the microgrid are provided in Appendix. Although different voltage

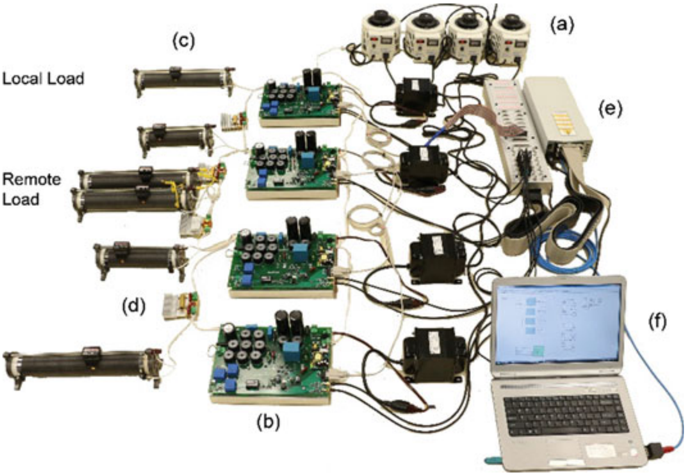

Fig. 7.6 DC microgrid prototype: **a** input AC sources, **b** buck converters driving each source, **c** local and remote loads, **d** transmission lines, **e** dSAPCE control board (DS1103), and **f** programming and monitoring PC. © [2016] IEEE. Reprinted, with permission, from IEEE Transactions on Power Electronics [36]

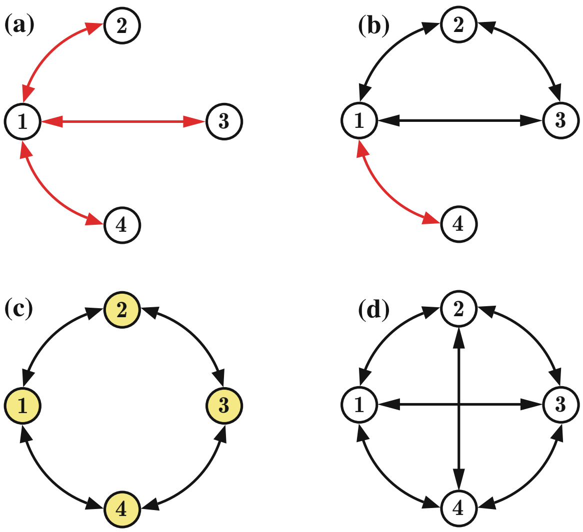

Fig. 7.7 Alternative connections forming a connected graph with: **a** no redundant link, **b** suboptimal link redundancy, **c** optimal link redundancy, and **d** full connection. © [2016] IEEE. Reprinted, with permission, from IEEE Transactions on Power Electronics [36]

levels are possible [43, 44], a 48 V system is considered here. The typical acceptable voltage deviation is about 5% of the rated voltage [19], and thus, the voltage limiters are set accordingly with $\varepsilon = 2.5$ V.

7.4.1 Design Procedure

Prior knowledge of converters' frequency response is essential to the design procedure in Sect. 7.1.3. Dynamic modeling of power electronics converters for microgrid applications is discussed in detail in the literature [45]. Analytical approaches do not consider practical limitations such as constraints on the duty cycles of switching converters. Alternatively, the transfer functions of the underlying converters are extracted experimentally using perturbation injection and frequency sweep techniques. For a wide range of loading conditions and input voltages, the reference point of each converter is augmented with a sinusoidal signal with an adjustable frequency. For any given frequency point, the sinusoidal content of the converter's output voltage is then compared with the injected sinusoidal signal to extract the converter's frequency response for that given frequency.

This procedure is repeated for the frequency range of interest. Output impedances are chosen in the study to cover light load ($R = 24\ \Omega$) to full load ($R = 12\ \Omega$) conditions. Measured transfer functions are shown in Fig. 7.8. Accordingly, the converter's transfer function can be formulated as a second-order function

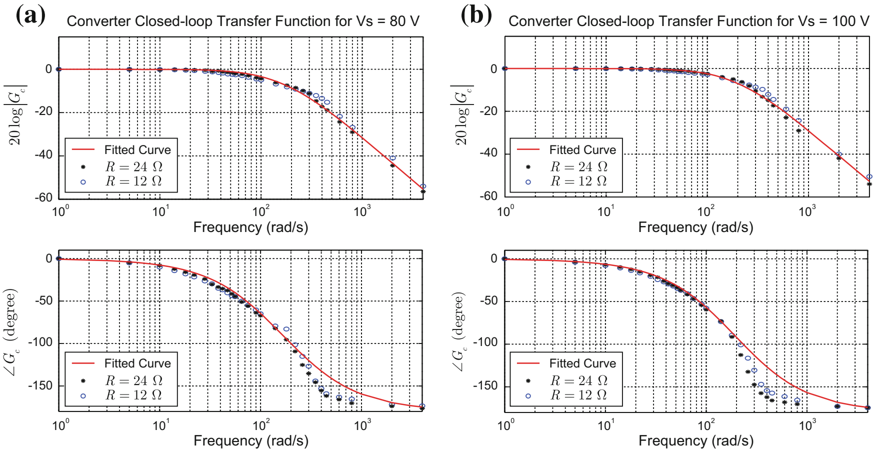

Fig. 7.8 Measured frequency response of the buck converters for various operating conditions: **a** $V_s = 80$ V and **b** $V_s = 100$ V. © [2016] IEEE. Reprinted, with permission, from IEEE Transactions on Power Electronics [36]

$$G_i^c = \frac{|p_1||p_2|}{(s-p_1)(s-p_2)}, \tag{7.48}$$

where p_1 and p_2 ($|p_2| > |p_1|$) can be found by curve-fitting techniques. Fitted frequency response is highlighted in red in Fig. 7.8, where an good agreement is reported between the empirical and fitted data. The transfer function in (7.48) is further used in the design procedure.

Following the guideline in Sect. 7.1.3, knowledge of the microgrid admittance matrix is also required. The underlying microgrid is a five-bus system (see Fig. 7.2) and has a five-by-five admittance matrix. However, the admittance matrix, $\mathbf{Y}_{\text{bus}}$, in (7.33) only represents the interaction between the voltages and currents of the generating buses and, thus, is a four-by-four matrix. This matrix can be found by reducing the original five-by-five admittance matrix though the Kron's reduction technique.

Design of the communication weights, a_{ij}s, which are stored in the adjacency matrix, $\mathbf{A_G}$ (or, equivalently, the Laplacian matrix, $\mathbf{L}$), is tightly linked to the voltage observers' dynamic in (7.7). The weights can be designed to adjust the convergence speed of the estimated voltages.

Proper functioning of the voltage regulator in Fig. 7.2 requires a fast estimation of the global average voltage, particularly faster than the converters' dynamic. Here, it is desired that the eigenvalues of the adjacency matrix (or, equivalently, poles of $\mathbf{H}_{\text{obs}}$) provide a dynamic estimation response at least twice as fast as that of the converters. A scaling factor, a, is defined to scale the adjacency matrix as

$$\mathbf{A_G} = a \times \begin{bmatrix} 0 & 90 & 0 & 110 \\ 90 & 0 & 100 & 0 \\ 0 & 100 & 0 & 120 \\ 110 & 0 & 120 & 0 \end{bmatrix}. \tag{7.49}$$

Figure 7.9 shows how the eigenvalues of the adjacency matrix vary as the scaling coefficient, a, changes from 0.5 to 1.5. The dominant pole of the converters' transfer function is $p_1 = -106$. Eigenvalues of $\mathbf{A_G}$, λ_ks, are highlighted in Fig. 7.9 in black for $a = 1$, where $\forall k \leq 3, |\text{real}(\lambda_k)| > 2 \times |\text{real}(p_1)|$. Therefore, $a = 1$ provides an appropriate scaling coefficient for the adjacency matrix in (7.49). It should be noted that the nonzero matrix entries in (7.49) are arbitrarily chosen and other selections are viable; however, they might result in a different optimal scaling factor.

The performance of the noise cancelation module is evaluated numerically using (7.23). The coupling gain, b, and the NC integrator gain matrix, $\mathbf{K}$, are chosen (see Appendix) to provide higher than 65% attenuation for disturbances with $f_{\text{noise}} < 5$ Hz. The noise cancelation transfer function, $\mathbf{H}_{\text{NC}}$, is plotted in Fig. 7.10 for the first node. As seen, all terms of $\mathbf{H}_{\text{NC}}$ are stable functions and exhibit satisfactory attenuations as demonstrated by the low gain at low frequencies. This implies successful noise rejection for DC and low-frequency disturbances. Similar performance is observed for the NC modules at other nodes.

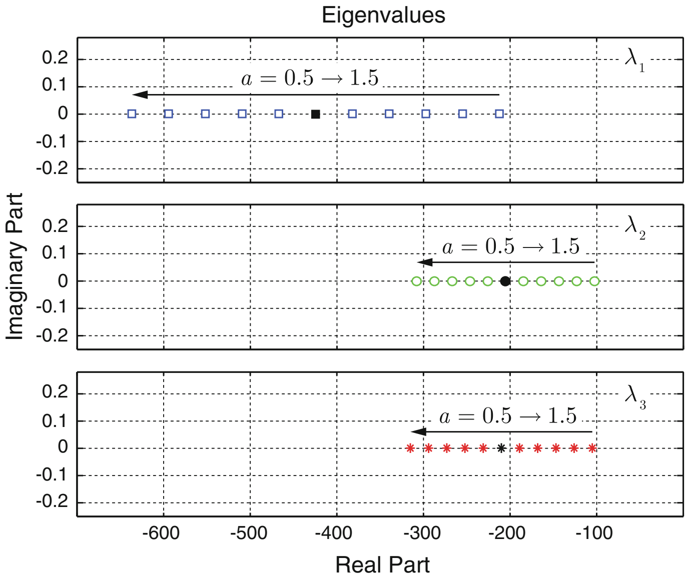

Fig. 7.9 Movement of the eigenvalues of the adjacency matrix as the scaling coefficient changes. © [2016] IEEE. Reprinted, with permission, from IEEE Transactions on Power Electronics [36]

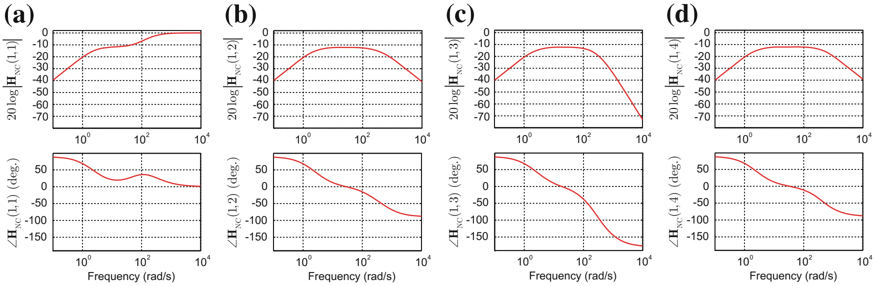

Fig. 7.10 Frequency response of the noise cancelation module at the first node: **a** $\mathbf{H}_{\mathrm{NC}}(1,1)$, **b** $\mathbf{H}_{\mathrm{NC}}(1,2)$, **c** $\mathbf{H}_{\mathrm{NC}}(1,3)$, and **d** $\mathbf{H}_{\mathrm{NC}}(1,4)$. © (2016) IEEE. Reprinted, with permission, from IEEE Transactions on Power Electronics

Comparison between (7.7) and (7.22) shows that NC modules can affect the observers' transfer function. Proper selection of the coupling gain, b, and the matrix $\mathbf{K}$ can significantly suppress this impact. Figure 7.11 compares the first entry, $(1,1)$, of the total observers' transfer function, $\mathbf{H}_{\mathrm{obs}}^{\mathrm{F}}$, with the reduced-order function, $\mathbf{H}_{\mathrm{obs}}$, where it can be seen that the NC module has a negligible impact on observers' the frequency response. A similar match is observed between other entries of $\mathbf{H}_{\mathrm{obs}}^{\mathrm{F}}$ and corresponding entries of $\mathbf{H}_{\mathrm{obs}}$. Accordingly, one can safely assume $\mathbf{H}_{\mathrm{obs}}^{\mathrm{F}} = \mathbf{H}_{\mathrm{obs}}$.

The current regulator module carries out the load sharing regardless of the selection of the droop coefficients. However, the choice of the coefficients based on (7.35) improves the load sharing dynamics. Accordingly, $m = 3$ is chosen here, which results in the virtual impedance matrix, $\mathbf{r}$, provided in Appendix.

The coupling gain between the current and the voltage regulators, c, determines load sharing dynamics. Figure 7.12 compares the measured dynamic response of the microgrid for two different values of c. Small coupling gain c can slow down the system, while a large coupling gain can lead to resonance or even make the system unstable. A medium value is adopted here, i.e., $c = 0.075$. Satisfactory system performance is verified empirically. Although (7.34) provides analytical evaluation of system dynamic, it does not consider limitations such as constraint on the duty cycle of the switching converters, and thus, empirical performance evaluation is preferred instead. Design parameters are summarized in Appendix. As seen, dissimilar control parameters are selected for different converters to verify controller performance in the case of heterogeneous agents (sources).

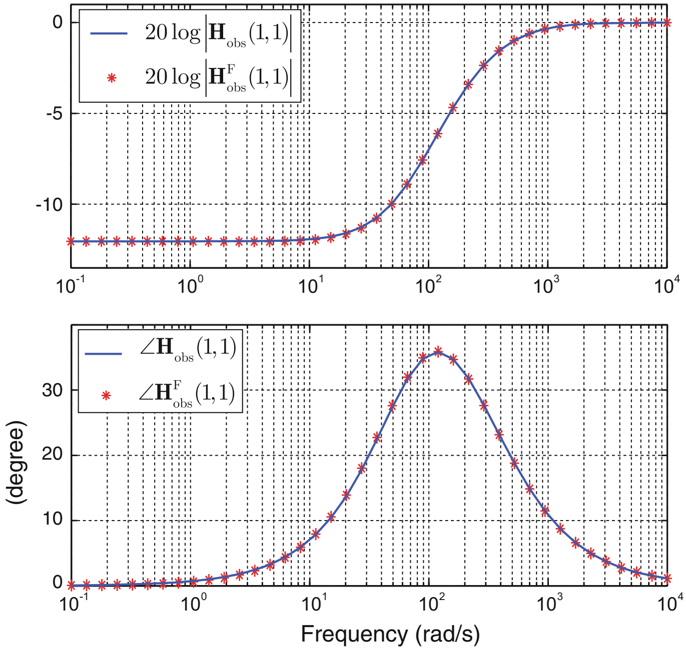

Fig. 7.11 Comparison of the reduced-order observers' dynamic, $\mathbf{H}_{\text{obs}}(1,1)$, and the total observers' dynamic, $\mathbf{H}^{\text{F}}_{\text{obs}}(1,1)$. © [2016] IEEE. Reprinted, with permission, from IEEE Transactions on Power Electronics [36]

7.4.2 Droop Controller Versus Cooperative Controller

Figure 7.13 comparatively studies the performance of the cooperative control methodology. The microgrid is initially controlled using the conventional droop controller. It leads to voltages less than the desired value, i.e., $v_{\text{ref}} = 48$ V. In addition, although the droop gains are designed reciprocal to the converters' rated currents, the transmission line effects have clearly incapacitated the droop mechanism resulting in a poor load sharing. The cooperative controller is engaged at $t = 5.18$ s. Consequently, the voltages are all boosted across the microgrid, and the average voltage is finely regulated at the set point, i.e., $v_{\text{ref}} = 48$ V. Figure 7.13b shows that the proportional load sharing is also carried out, where the first and the fourth converters carry twice the current as the other two converters. Performance of the voltage observers is shown in Fig. 7.13c, where a good agreement is seen between the true average voltage, $\bar{v}$, and the individual estimated voltages, $\bar{v}_i$s.

The efficacy of the noise cancelation module is studied in Fig. 7.14, where a step disturbance, i.e., $d_1(t) = 2u(t - 3.35\text{ s})$, is intentionally applied to the estimation at

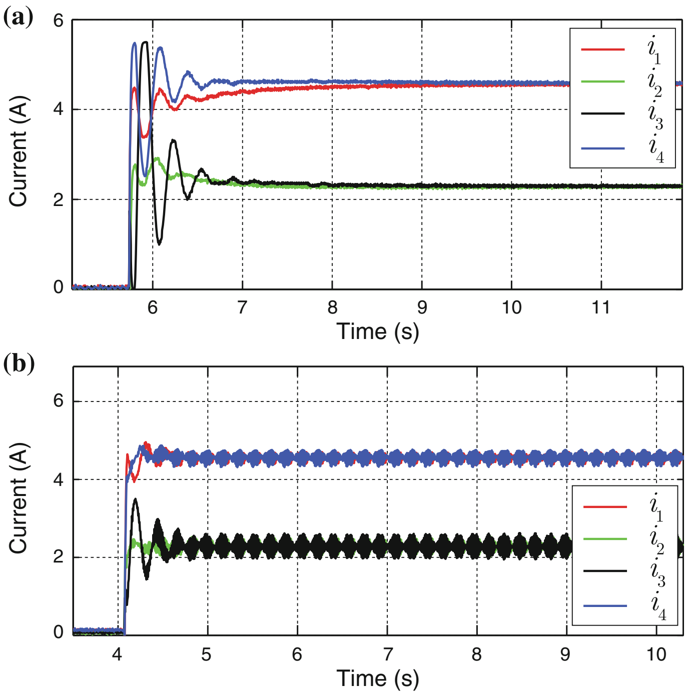

Fig. 7.12 Current regulating performance for small and large coupling gains; measured output currents for: **a** $c = 0.005$ stable and very slow and **b** $c = 0.15$ fast and resonating. © [2016] IEEE. Reprinted, with permission, from IEEE Transactions on Power Electronics [36]

Node one. It is shown in Fig. 7.14c that the disturbance causes sudden increase in all estimations. Accordingly, the controller has slightly decreased the duty ratios. Simultaneously, the NC module has identified the noise and adjusted the cancelation term, $\hat{d}_1$, to neutralize the noise impact. Consequently, all estimations are recovered in less than 1 s and continue tracking the true average voltage, $\bar{v}$. Figure 7.14a, b shows that the NC module has effectively eliminated the noise impact on the voltage regulation and the load sharing.

7.4.3 Load Change Performance Assessment

The controller performance in case of load change is studied in Fig. 7.15, where the remote load at bus five, R_5, is changed in step between 10 and 20 Ω. Tight voltage regulation and load sharing can be observed in this figure. Excellent transient load sharing is also noticeable in Fig. 7.15b.

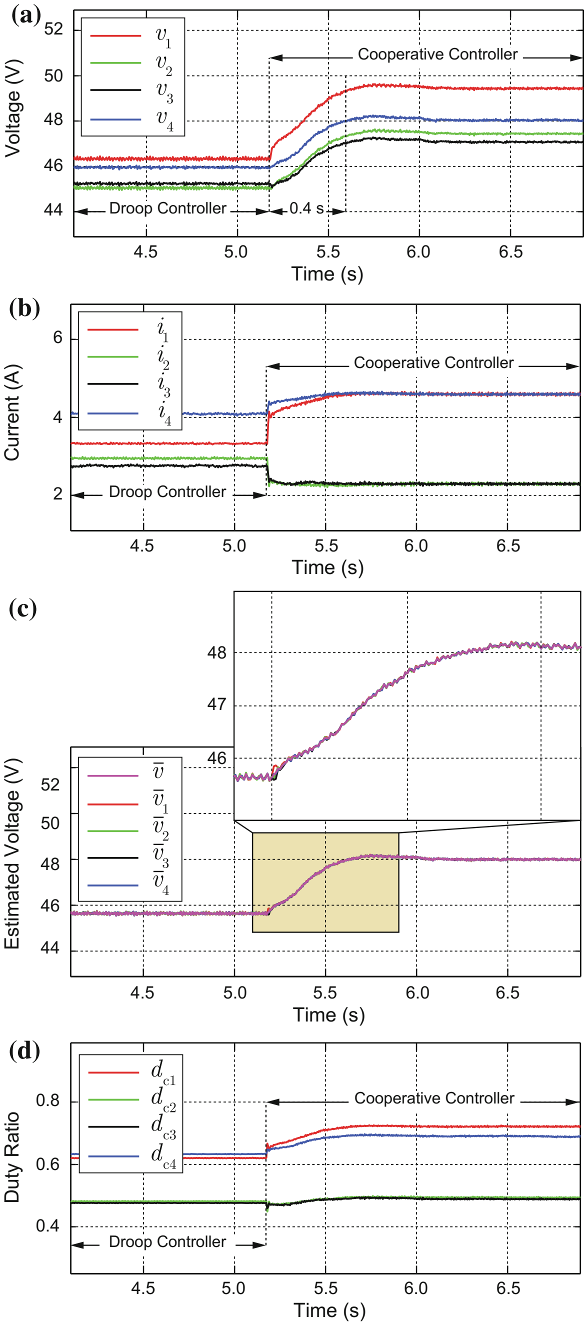

Fig. 7.13 Comparative studies of the conventional droop control and the cooperative controller: **a** terminal voltages, **b** supplied currents, **c** estimations of the average voltage, and **d** converters' duty ratios. © [2016] IEEE. Reprinted, with permission, from IEEE Transactions on Power Electronics [36]

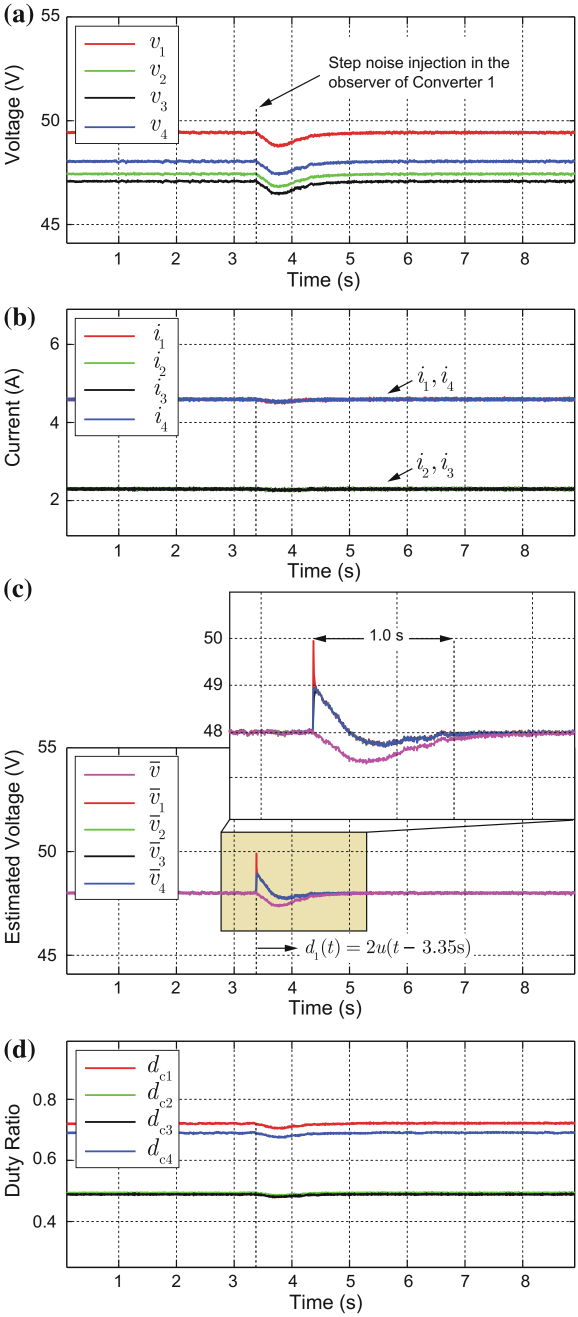

Fig. 7.14 Performance of the noise cancelation mechanism: **a** terminal voltages, **b** supplied currents, **c** estimations of the average voltage, and **d** converters' duty ratios. © [2016] IEEE. Reprinted, with permission, from IEEE Transactions on Power Electronics [36]

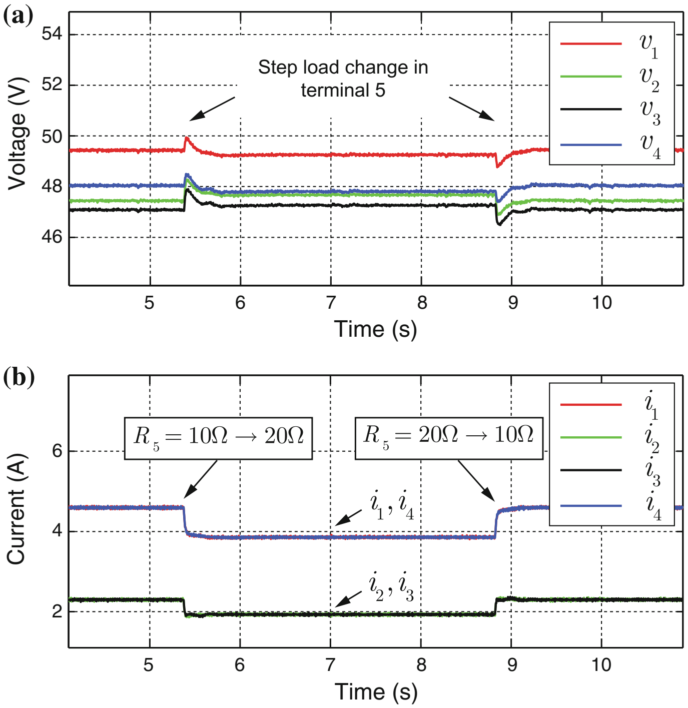

Fig. 7.15 Performance of the cooperative distributed controller in a case of load change: **a** terminal voltages and **b** supplied currents. © [2016] IEEE. Reprinted, with permission, from IEEE Transactions on Power Electronics [36]

7.4.4 Plug-and-Play Capability

Figure 7.16 studies plug-and-play capability of the cooperative controller and its performance in case of a converter failure. As seen, when the second converter fails, the controller readjusts the voltages to satisfy the global voltage regulation. It also readjusts the load sharing among the remaining converters. It should be noted that a converter failure also implies loss of all communication links connected to that particular converter. Accordingly, when the second converter fails, it automatically renders the links 1–2 (between nodes 1 and 2) and 2–3 inoperable. However, the remaining links still form a connected graph with balanced Laplacian matrix (see Fig. 7.7c).

Then, the second converter is plugged back in at $t = 12.1$ s. As seen, the controller has properly updated the load sharing and global voltage regulation, after the second converter is plugged in.

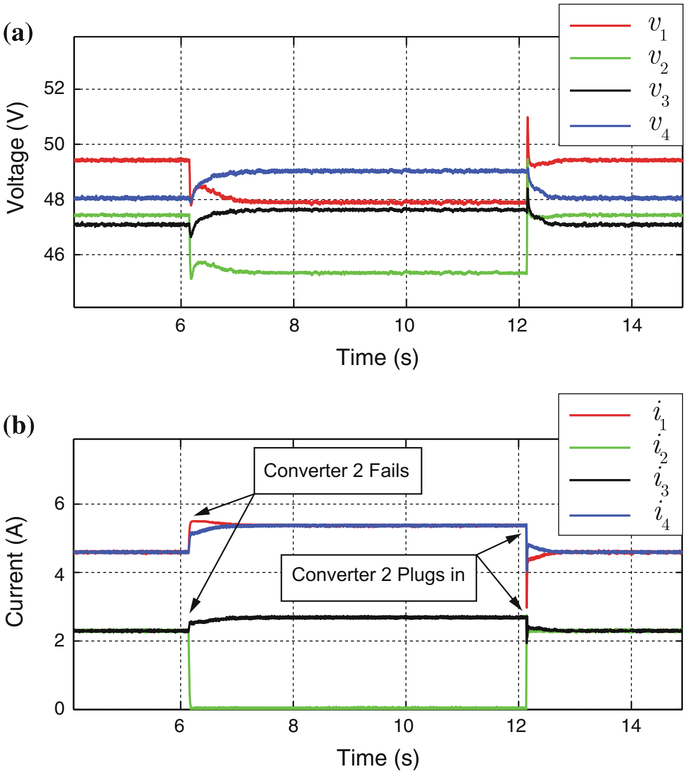

Fig. 7.16 Converter failure and plug-and-play studies: **a** terminal voltages and **b** supplied currents. © [2016] IEEE. Reprinted, with permission, from IEEE Transactions on Power Electronics [36]

7.4.5 *Cyber-Link Failure Resiliency*

Resiliency to a single link failure is studied next in Fig. 7.17. The original communication graph is designed to carry a minimum redundancy, so no single link failure can cause loss of graphical connectivity. Thus, the control system shall remain operational. As shown in Fig. 7.17, the link 1–2 has failed at $t = 11$ s, but it does not have any impact on voltage regulation or load sharing.

Response of the controller to the step load change in the remote load is also studied with the failed link, where a satisfactory performance can be seen. It should be noted that the reconfiguration caused by the link failure affects the Laplacian matrix and, thus, the whole system dynamic. Comparing Figs. 7.15b and 7.17b, one can see that the link failure slightly slows the controller transient response.

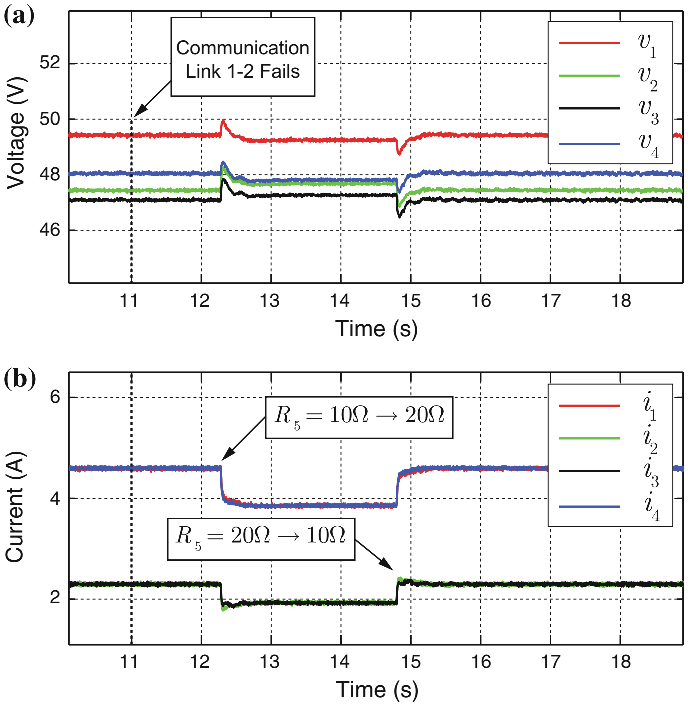

Fig. 7.17 Link failure resiliency: **a** terminal voltages and **b** supplied currents. © [2016] IEEE. Reprinted, with permission, from IEEE Transactions on Power Electronics [36]

7.5 Summary

Distributed and cooperative secondary/primary controllers are discussed for DC microgrids. The controller on each converter has two modules: the voltage regulator and the current regulator. The voltage regulator uses a noise-resilient voltage observer to estimate the global average voltage. This estimation is then further used to adjust the local voltage set point to provide global voltage regulation.

The current regulator compares local per-unit current with its neighbors' per-unit currents and, accordingly, adjusts the voltage set point (or, alternatively, the droop coefficient) to carry out proportional load sharing. The control paradigms use sparse communication networks for data exchange. Studies show that they provide precise global voltage regulation and proportional load sharing.

Appendix

Dynamic Consensus

Following lemmas need to be studied before studying the dynamic consensus:

Lemma 7.1 [37]: *Assume that the digraph* $\mathbf{G}$ *has a spanning tree. Then, the Laplacian matrix* $\mathbf{L}$ *has a simple eigen-value at the origin, i.e.,* $\lambda_1 = 0$, *and other eigen-values lie in the Open Right Hand Plane (ORHP). In addition,*

$$\lim_{t\to\infty} e^{-\mathbf{L}t} = w_r w_l^{\mathrm{T}}, \tag{7.50}$$

where $w_r \in \mathbb{R}^{N\times 1}$ *and* $w_l^{\mathrm{T}} \in \mathbb{R}^{N\times 1}$ *are the right and left eigen-vectors of* $\mathbf{L}$ *associated with* $\lambda_1 = 0$, *respectively. It should be noted that* w_l^{T} *should be normalized with respect to* w_r, *i.e.,* $w_l^{\mathrm{T}} w_r = 1$.

Lemma 7.2 *Assume that the digraph* $\mathbf{G}$ *has a spanning tree and the Laplacian matrix,* $\mathbf{L}$, *is balanced. Then,*

$$\lim_{s\to 0} s(s\mathbf{I}_N + \mathbf{L})^{-1} = \mathbf{Q}. \tag{7.51}$$

$$\lim_{s\to 0} \mathbf{L}(s\mathbf{I}_N + \mathbf{L})^{-1} = \lim_{s\to 0} (s\mathbf{I}_N + \mathbf{L})^{-1}\mathbf{L} = \mathbf{I}_N - \mathbf{Q}. \tag{7.52}$$

where $\boldsymbol{Q}$ *is the averaging matrix defined in Sect. 7.1.3*

Proof of Lemma 7.2: Assume a linear system of $\dot{\mathbf{x}} = -\mathbf{L}\mathbf{x}$ with $\mathbf{x}(0) \neq 0$ and $\mathbf{x} \in \mathbb{R}^{N\times 1}$. One can write

$$\mathbf{x}(t) = e^{-\mathbf{L}t}\mathbf{x}(0). \tag{7.53}$$

Or, equivalently, in the frequency domain,

$$\mathbf{X} = (s\mathbf{I}_N + \mathbf{L})^{-1}\mathbf{x}(0). \tag{7.54}$$

Lemma 7.1 ensures that $\mathbf{X}$ is a type 1 vector; i.e., it has a single pole at the origin and all other poles lie in the OLHP. Thus, using the final value theorem,

$$\lim_{t\to\infty} \mathbf{x}(t) = \lim_{s\to 0} s\mathbf{X} = \left(\lim_{s\to 0} s(s\mathbf{I}_N + \mathbf{L})^{-1}\right)\mathbf{x}(0). \tag{7.55}$$

On the other hand, by using Lemma 7.1, (7.53) yields to

$$\lim_{t\to\infty}\mathbf{x}(t) = \left(\lim_{t\to\infty} e^{-\mathbf{L}t}\right)\mathbf{x}(0) = w_r w_l^{\mathrm{T}}\mathbf{x}(0). \tag{7.56}$$

For any Laplacian matrix **L,** all row sums are equal to zero. Thus, $w_r = \underline{\mathbf{1}}$. In addition, for any balanced **L**, all column sums are also equal to zero. Thus, $w_l = (1/N)\underline{\mathbf{1}}$. Accordingly, (7.56) implies that

$$\lim_{t\to\infty}\mathbf{x}(t) = \mathbf{Q}\mathbf{x}(0). \tag{7.57}$$

Comparing (7.55)–(7.57),

$$\left(\lim_{s\to 0} s(s\mathbf{I}_N + \mathbf{L})^{-1}\right)\mathbf{x}(0) = \mathbf{Q}\mathbf{x}(0). \tag{7.58}$$

Since (7.58) holds for all $\mathbf{x}(0) \neq 0$, one may conclude (7.51). In addition,

$$\mathbf{I}_N = \lim_{s\to 0}(s\mathbf{I}_N + \mathbf{L})(s\mathbf{I}_N + \mathbf{L})^{-1} = \lim_{s\to 0} s(s\mathbf{I}_N + \mathbf{L})^{-1} + \lim_{s\to 0}\mathbf{L}(s\mathbf{I}_N + \mathbf{L})^{-1}. \tag{7.59}$$

Comparing (7.51) with (7.59) concludes (7.52).

Theorem 7.1 *Assume that the communication graph* **G**, *used in a cooperative control system, has a spanning tree and the associated Laplacian matrix,* **L**, *is balanced. Then, using the observer in* (7.7), *all the estimated averages in* $\bar{\mathbf{v}}$ *converge to the true global average voltage.*

Proof of Theorem 7.1: Equation (7.34) shows the global dynamic of the microgrid, when the cooperative controller is effective. It is assumed that the system parameters are, accordingly, designed to stabilize the microgrid. Thus, the resulting voltage vector, **V**, is a type 1 vector. Based on Lemma 7.1, all poles of the term $s(s\mathbf{I}_N + \mathbf{L})^{-1}$ lie in the OLHP. It should be noted that if λ_i is an eigenvalue of **L,** then $s = -\lambda_i$ is a pole of $s(s\mathbf{I}_N + \mathbf{L})^{-1}$. The term s in $s(s\mathbf{I}_N + \mathbf{L})^{-1}$ cancels the pole of $(s\mathbf{I}_N + \mathbf{L})^{-1}$ at the origin. Thus, (7.7) implies that $\overline{\mathbf{V}}$ is also a type 1 vector. Since both **V** and $\overline{\mathbf{V}}$ are type 1, one may use the final value theorem

$$\lim_{t\to\infty}\bar{\mathbf{v}}(t) = \lim_{s\to 0} s\bar{\mathbf{V}} = \lim_{s\to 0} s(s\mathbf{I}_N + \mathbf{L})^{-1}(s\mathbf{V}). \tag{7.60}$$

Using Lemma 7.2,

$$\lim_{t\to\infty}\bar{\mathbf{v}}(t) = \lim_{s\to 0} s(s\mathbf{I}_N + \mathbf{L})^{-1} \times \lim_{s\to 0}(s\mathbf{V}) = \mathbf{Q} \times \lim_{t\to\infty}\mathbf{v} = \mathbf{Q}\mathbf{v}^{\mathrm{ss}} = \langle\mathbf{v}^{\mathrm{ss}}\rangle\underline{\mathbf{1}}. \tag{7.61}$$

Equation (7.61) implies that all estimations converge to the true global average voltage. In other words,

$$\forall i : 0 \leq i \leq N, \quad \lim_{t \to \infty} \bar{v}_i(t) = \frac{1}{N}\sum_{i=1}^{N} v_i(t). \tag{7.62}$$

Analysis of the Noise Cancelation Module

Following lemmas need to be studied before analyzing the noise cancelation module:

Lemma 7.3 *For a given matrix* $\mathbf{A} \in \mathbb{R}^{N \times N}$, *if* $\mathbf{I}_N + \mathbf{A}$ *is invertible then,*

$$(\mathbf{I}_N + \mathbf{A})^{-1} = \mathbf{I}_N - \mathbf{A}(\mathbf{I}_N + \mathbf{A})^{-1} = \mathbf{I}_N - (\mathbf{I}_N + \mathbf{A})^{-1}\mathbf{A}. \tag{7.63}$$

Proof of Lemma 7.3: For a given matrix $\mathbf{A} \in \mathbb{R}^{N \times N}$,

$$(\mathbf{I}_N + \mathbf{A})^{-1} = (\mathbf{I}_N + \mathbf{A})^{-1}(\mathbf{I}_N + \mathbf{A}) - (\mathbf{I}_N + \mathbf{A})^{-1}\mathbf{A} = \mathbf{I}_N - (\mathbf{I}_N + \mathbf{A})^{-1}\mathbf{A}.$$

Lemma 7.4 *For a given invertible matrix* $\mathbf{A} \in \mathbb{R}^{N \times N}$ *if* $\mathbf{I}_N + \mathbf{A}$ *is invertible then,*

$$(\mathbf{I}_N + \mathbf{A}^{-1})^{-1} = \mathbf{A}(\mathbf{I}_N + \mathbf{A})^{-1} = (\mathbf{I}_N + \mathbf{A})^{-1}\mathbf{A}. \tag{7.64}$$

Proof of Lemma 7.4: For a given invertible matrix $\mathbf{A}$,

$$(\mathbf{I}_N + \mathbf{A}^{-1})^{-1} = (\mathbf{A}\mathbf{A}^{-1} + \mathbf{A}^{-1})^{-1} = \left((\mathbf{I}_N + \mathbf{A})\mathbf{A}^{-1}\right)^{-1} = \mathbf{A}(\mathbf{I}_N + \mathbf{A})^{-1}.$$

Lemma 7.5 *If* $\mathbf{L}$ *is a balanced Laplacian matrix,* $b > 0$, *and* $\mathbf{K} = \mathrm{diag}\{k_i\}$ *has positive diagonal elements then,* $\mathbf{L}' = b\mathbf{L}\mathbf{K}^{-1}\mathbf{L}$ *is a balanced Laplacian matrix.*

Proof of Lemma 7.5: The matrix $\mathbf{L}$ is said to be a Laplacian matrix if a communication graph exists with the associated Laplacian matrix $\mathbf{L}$. Equivalently, a matrix is a Laplacian matrix if and only if $\mathbf{L}\underline{\mathbf{1}} = \mathbf{0}$. A Laplacian matrix is balanced if it has all column sums of zero, i.e., $\underline{\mathbf{1}}^{\mathrm{T}}\mathbf{L} = \mathbf{0}$. Let $\mathbf{L}$ be a balanced Laplacian matrix and $\mathbf{L}' = b\mathbf{L}\mathbf{K}^{-1}\mathbf{L}$, then

$$\mathbf{L}'\underline{\mathbf{1}} = b\mathbf{L}\mathbf{K}^{-1}(\mathbf{L}\underline{\mathbf{1}}) = \mathbf{0}, \tag{7.65}$$

which implies that $\mathbf{L}'$ is a Laplacian matrix. On the other hand,

$$\underline{\mathbf{1}}^{\mathrm{T}}\mathbf{L}' = b\left(\underline{\mathbf{1}}^{\mathrm{T}}\mathbf{L}\right)\mathbf{K}^{-1}\mathbf{L} = \mathbf{0}, \tag{7.66}$$

which shows that $\mathbf{L}'$ is also balanced.

Lemma 7.6 *If* $\mathbf{L}$ *is a balanced Laplacian matrix,* $b > 0$, *and* $\mathbf{K} = \mathrm{diag}\{k_i\}$ *has positive diagonal elements then,*

$$\lim_{s\to\infty} s\big(s\mathbf{I}_N + (s\mathbf{I}_N + b\mathbf{L})\mathbf{K}^{-1}(s\mathbf{I}_N + \mathbf{L})\big)^{-1} = \mathbf{Q}. \tag{7.67}$$

$$\lim_{s\to\infty} s\Big(\mathbf{I}_N + s(s\mathbf{I}_N + \mathbf{L})^{-1}\mathbf{K}(s\mathbf{I}_N + b\mathbf{L})^{-1}\Big)^{-1} = \mathbf{I}_N - \mathbf{Q}. \tag{7.68}$$

Proof of Lemma 7.6: Let $\mathbf{L}$ be a balanced Laplacian matrix, $b > 0$, and $\mathbf{K} = \mathrm{diag}\{k_i\}$ has positive diagonal elements. Then,

$$\lim_{s\to\infty} \big((s\mathbf{I}_N + b\mathbf{L})\mathbf{K}^{-1}(s\mathbf{I}_N + \mathbf{L})\big) = b\mathbf{L}\mathbf{K}^{-1}\mathbf{L}. \tag{7.69}$$

Let us define $\mathbf{L}' = b\mathbf{L}\mathbf{K}^{-1}\mathbf{L}$. Then, using (7.69),

$$\lim_{s\to 0} s\big(s\mathbf{I}_N + (s\mathbf{I}_N + b\mathbf{L})\mathbf{K}^{-1}(s\mathbf{I}_N + \mathbf{L})\big)^{-1} = \lim_{s\to 0} s(s\mathbf{I}_N + \mathbf{L}')^{-1}. \tag{7.70}$$

Lemma 7.5 ensures that $\mathbf{L}'$ is a balanced Laplacian matrix. Therefore, by applying Lemma 7.2 (7.51), one can write $\lim_{s\to 0} s(s\mathbf{I}_N + \mathbf{L}')^{-1} = \mathbf{Q}$, which, together with (7.70), proves (7.67).

To study the second part of the Lemma, (7.68), one may note that for $s \neq 0$, $s\mathbf{I}_N + b\mathbf{L}$ is invertible [46]. $\mathbf{K}$ is also invertible, and $\mathbf{K}^{-1} = \mathrm{diag}\{k_i^{-1}\}$. Let us define

$$\Gamma \triangleq \Big(\mathbf{I}_N + s(s\mathbf{I}_N + \mathbf{L})^{-1}\mathbf{K}(s\mathbf{I}_N + b\mathbf{L})^{-1}\Big)^{-1}. \tag{7.71}$$

Using Lemma 7.3,

$$\Gamma = \mathbf{I}_N - s(s\mathbf{I}_N + \mathbf{L})^{-1}\mathbf{K}(s\mathbf{I}_N + b\mathbf{L})^{-1}\Big(\mathbf{I}_N + s(s\mathbf{I}_N + \mathbf{L})^{-1}\mathbf{K}(s\mathbf{I}_N + b\mathbf{L})^{-1}\Big)^{-1}. \tag{7.72}$$

Lemma 7.4 offers to further expand (7.72)

$$\begin{aligned}\Gamma &= \mathbf{I}_N - s(s\mathbf{I}_N + \mathbf{L})^{-1}\mathbf{K}(s\mathbf{I}_N + b\mathbf{L})^{-1}\frac{1}{s}(s\mathbf{I}_N + b\mathbf{L})\mathbf{K}^{-1}(s\mathbf{I}_N + \mathbf{L}) \\ &\quad \times \Big(\mathbf{I}_N + \frac{1}{s}(s\mathbf{I}_N + b\mathbf{L})\mathbf{K}^{-1}(s\mathbf{I}_N + \mathbf{L})\Big)^{-1} \\ &= \mathbf{I}_N - s\big(s\mathbf{I}_N + (s\mathbf{I}_N + b\mathbf{L})\mathbf{K}^{-1}(s\mathbf{I}_N + \mathbf{L})\big)^{-1}.\end{aligned} \tag{7.73}$$

By applying Lemma 7.6 (7.67)–(7.73), one can conclude $\lim_{s\to 0}\Gamma = \mathbf{I}_N - \mathbf{Q}$.

Theorem 7.2 *Assume that the communication graph* $\mathbf{G}$*, used in a distributed control system, has a spanning tree, and the associated Laplacian matrix,* $\mathbf{L}$*, is balanced. Then, using the total observer in* (7.21)–(7.23)*, all the estimated averages in* $\overline{\mathrm{v}}$ *converge to the true global average voltage average.*

Proof of Theorem 7.2: For any $s \neq 0$, $s\mathbf{I}_N + b\mathbf{L}$ is invertible [46]. The integrator gain matrix, $\mathbf{K}$, is also invertible, and $\mathbf{K}^{-1} = \mathrm{diag}\{k_i^{-1}\}$. Thus, one can safely reformulate the total observer transfer function as

$$\begin{aligned}\mathbf{H}_{\mathrm{obs}}^{\mathrm{F}} &= \left((s\mathbf{I}_N + \mathbf{L}) + s\mathbf{K}(s\mathbf{I}_N + b\mathbf{L})^{-1}\right)^{-1}\left((s\mathbf{I}_N + \mathbf{L}) + s\mathbf{K}(s\mathbf{I}_N + b\mathbf{L})^{-1}\right) - \mathbf{L}\\ &= \mathbf{I}_N - \left((s\mathbf{I}_N + \mathbf{L}) + s\mathbf{K}(s\mathbf{I}_N + b\mathbf{L})^{-1}\right)^{-1}\mathbf{L}\\ &= \mathbf{I}_N - \left((s\mathbf{I}_N + \mathbf{L})\left(\mathbf{I}_N + s(s\mathbf{I}_N + \mathbf{L})^{-1}\mathbf{K}(s\mathbf{I}_N + b\mathbf{L})^{-1}\right)\right)^{-1}\mathbf{L}\\ &= \mathbf{I}_N - \left(\mathbf{I}_N + s(s\mathbf{I}_N + \mathbf{L})^{-1}\mathbf{K}(s\mathbf{I}_N + b\mathbf{L})^{-1}\right)^{-1}(s\mathbf{I}_N + \mathbf{L})^{-1}\mathbf{L}.\end{aligned} \tag{7.74}$$

Using Lemma 7.2 (7.52) and Lemma 7.6 (7.68), the total observer DC gain can be found

$$\lim_{s \to 0} H_{\mathrm{obs}}^{\mathrm{F}} = \mathbf{I}_N - (\mathbf{I}_N - \mathbf{Q})^2 = 2\mathbf{Q} - \mathbf{Q}^2 = \mathbf{Q}. \tag{7.75}$$

Therefore, for type 1 (DC and exponentially damping) disturbances, (7.21) yields to

$$\begin{aligned}\lim_{t \to \infty} \overline{\mathbf{v}}(t) &= \lim_{s \to 0} \mathbf{H}_{\mathrm{obs}}^{\mathrm{F}} \times \lim_{s \to 0}(s\overline{\mathbf{V}}) \times \lim_{s \to 0} \mathbf{H}_{\mathrm{NC}} \times \lim_{s \to 0}(s\mathbf{D})\\ &= \mathbf{Q} \times \lim_{t \to \infty} \mathbf{v} + 0 = \mathbf{Qv} = \langle \mathbf{v}^{\mathrm{ss}} \rangle \underline{1},\end{aligned} \tag{7.76}$$

which proves the Theorem 7.2.

Microgrid Parameters

Each of the underlying buck converters has $L = 2.64$ mH and $C = 2.2$ mF and works with the switching frequency of $F_s = 60$ kHz. Transmission lines series impedances are $Z_{12} = Z_{34} = Z_b$ and $Z_{25} = Z_{35} = Z_b$, where the base impedance is $Z_b = 0.5 + (50\ \mu\mathrm{H})s$. The circuit model of the line includes 22 nF of capacitance on either end. Impedances of the local loads are $R = 30\ \Omega$ and $R_2 = R_3 = R_4 = 20\ \Omega$. Voltages of the (rectified) input DC sources are $V_{\mathrm{s}1} = V_{\mathrm{s}4} = 80$ V and $V_{\mathrm{s}2} = V_{\mathrm{s}3} = 100$ V. The control parameters are as follow:

$$\mathbf{I}_{\mathrm{rated}} = \mathrm{diag}\{6, 3, 3, 6\}, \tag{7.77}$$

$$\mathbf{A}_{\mathrm{G}} = \begin{bmatrix} 0 & 90 & 0 & 110 \\ 90 & 0 & 100 & 0 \\ 0 & 100 & 0 & 120 \\ 110 & 0 & 120 & 0 \end{bmatrix}, \quad \mathbf{r} \begin{bmatrix} 0.5 & 0 & 0 & 0 \\ 0 & 1.0 & 0 & 0 \\ 0 & 0 & 1.0 & 0 \\ 0 & 0 & 0 & 0.5 \end{bmatrix}, \tag{7.78}$$

$$b = 1, \quad c = 0.075, \tag{7.79}$$

$$\mathbf{H}_{\mathrm{p}} = \begin{bmatrix} 0.1 & 0 & 0 & 0 \\ 0 & 0.09 & 0 & 0 \\ 0 & 0 & 0.08 & 0 \\ 0 & 0 & 0 & 0.11 \end{bmatrix}, \quad \mathbf{H}_{\mathrm{I}} = \begin{bmatrix} 6 & 0 & 0 & 0 \\ 0 & 5 & 0 & 0 \\ 0 & 0 & 5.4 & 0 \\ 0 & 0 & 0 & 5.6 \end{bmatrix}, \tag{7.80}$$

$$\mathbf{G}_{\mathrm{p}} = \begin{bmatrix} 1.1 & 0 & 0 & 0 \\ 0 & 1 & 0 & 0 \\ 0 & 0 & 1.2 & 0 \\ 0 & 0 & 0 & 1.1 \end{bmatrix}, \quad \mathbf{G}_{\mathrm{I}} = \begin{bmatrix} 7 & 0 & 0 & 0 \\ 0 & 7.4 & 0 & 0 \\ 0 & 0 & 6.6 & 0 \\ 0 & 0 & 0 & 7 \end{bmatrix}, \tag{7.81}$$

$$\mathbf{K}_{\mathrm{p}} = \begin{bmatrix} 1 & 0 & 0 & 0 \\ 0 & 2 & 0 & 0 \\ 0 & 0 & 3 & 0 \\ 0 & 0 & 0 & 4 \end{bmatrix}. \tag{7.82}$$

References

1. Guerrero JM, Vasquez JC, Matas J, de Vincuña LG, Castilla M (2011) Hierarchical control of droop-controlled AC and DC microgrids—a general approach toward standardization. IEEE Trans Ind Electron 58:158–172
2. Zhang L, Wang Y, Li H, Sun P (2012) Hierarchical coordinated control of DC microgrid with wind turbines. In: Proceedings of 38th annual conference IEEE Industrial Electronics Society (IECON), 2012, pp 3547–3552
3. Xu L, Chen D (2011) Control and operation of a DC microgrid with variable generation and energy storage. IEEE Trans Power Del 26(4):2513–2522
4. Yuen C, Oudalov A, Timbus A (2011) The provision of frequency control reserves from multiple microgrids. IEEE Trans Ind Electron 58(1):173–183
5. Kanchev H, Lu D, Colas F, Lazarov V, Francois B (2011) Energy management and operational planning of a microgrid with a PV-based active generator for smart grid applications. IEEE Trans Ind Electron 58(10):4583–4592
6. Chen C, Duan S, Cai T, Liu B, Hu G (2011) Optimal allocation and economic analysis of energy storage system in microgrids. IEEE Trans Power Electron 26(10):2762–2773
7. Zhou T, Francois B (2011) Energy management and power control of a hybrid active wind generator for distributed power generation and grid integration. IEEE Trans Ind Electron 58 (1):95–104

8. Anand S, Fernandes BG, Guerrero JM (2013) Distributed control to ensure proportional load sharing and improve voltage regulation in low-voltage DC microgrids. IEEE Trans Power Electron 28(4):1900–1913
9. Loh PC, Li D, Chai YK, Blaabjerg F (2013) Autonomous control of interlinking converter with energy storage in hybrid ac–dc microgrid. IEEE Trans Ind Appl 49(3):1374–1382
10. Schönberger J, Duke R, Round SD (2006) DC-bus signaling: a distributed control strategy for a hybrid renewable Nanogrid. IEEE Trans Ind Electron 53(5):1453–1460
11. Sun K, Zhang L, Xing Y, Guerrero JM (2011) A distributed control strategy based on DC bus signaling for modular photovoltaic generation systems with battery energy storage. IEEE Trans Power Electron 26(10):3032–3045
12. Chen D, Xu L, Yao L (2013) DC voltage variation based autonomous control of DC microgrids. IEEE Trans Power Del 28(2):637–648
13. Karlsson P, Svensson J (2003) DC bus voltage control for a distributed power system. IEEE Trans Power Electron 18(6):1405–1412
14. Ito Y, Zhongqing Y, Akagi H (2004) DC microgrid based distribution power generation system. In: Proceedings of 4th international power electronics and motion control conference (IPEMC), 2004, pp 1740–1745
15. Loh PC, Li D, Chai YK, Blaabjerg F (2013) Autonomous operation of hybrid microgrid with AC and DC subgrids. IEEE Trans Power Electron 28(5):2214–2223
16. Qiu W, Liang Z (2005) Practical design considerations of current sharing control for parallel VRM applications. In: Proceedings of 20th annual applied power electronics conference and exposition, 2005, pp 281–286
17. Guerrero JM, Hang L, Uceda J (2008) Control of distributed uninterruptible power supply systems. IEEE Trans Ind Electron 55(8):2845–2859
18. Lu X, Sun K, Guerrero JM, Vasquez JC, Huang L (2014) State-of-charge balance using adaptive droop control for distributed energy storage systems in DC microgrid applications. IEEE Trans Ind Electron 61(6):2804–2815
19. Ferreira RAF, Braga HAC, Ferreira AA, Barbosa PG (2012) Analysis of voltage droop control method for DC microgrids with Simulink: modeling and simulation. In: Proceedings of 10th IEEE/IAS international conference on industry applications (INDUSCON), 2012, pp 1–6
20. Lopes JAP, Moreira CL, Madureira AG (2006) Defining control strategies for microgrids islanded operation. IEEE Trans Power Syst 21(2):916–924
21. Tuladhar A, Jin H, Unger T, Mauch K (2000) Control of parallel inverters in distributed AC power systems with consideration of line impedance effect. IEEE Trans Ind Appl 36(1):131–138
22. Guerrero JM, Vicuña LG, Matas J, Castilla M, Miret J (2005) Output impedance design of parallel-connected UPS inverters with wireless load sharing control. IEEE Trans Ind Electron 52(4):1126–1135
23. Marwali MN, Jung JW, Keyhani A (2004) Control of distributed generation systems—Part II: load sharing control. IEEE Trans Power Electron 19(6):1551–1561
24. De Brabandere K, Bolsens B, Van Den Keybus J, Woyte A, Driesen J, Belmans R (2007) A voltage and frequency droop control method for parallel inverters. IEEE Trans Power Electron 22(4):1107–1115
25. Mohamed Y, El-Saadany EF (2008) Adaptive decentralized droop controller to preserve power sharing stability of paralleled inverters in distributed generation microgrids. IEEE Trans Power Electron 23(6):2806–2816
26. Lu X, Guerrero JM, Sun K, Vasquez JC (2014) An improved droop control method for DC microgrids based on low bandwidth communication with DC bus voltage restoration and enhanced current sharing accuracy. IEEE Trans Power Electron 29(4):1800–1812
27. Anand S, Fernandes BG (2011) Steady state performance analysis for load sharing in DC distributed generation system. In: Proceedings of 10th international conference on environment and electrical engineering (EEEIC), 2011, pp 1–4

28. Li YW, Kao CN (2009) An accurate power control strategy for power-electronics-interfaced distributed generation units operation in a low voltage multi-bus microgrid. IEEE Trans Power Electron 24(12):2977–2988
29. He J, Li YW (2011) Analysis, design and implementation of virtual impedance for power electronics interfaced distributed generation. IEEE Trans Ind Appl 47(6):2525–2538
30. Qiu W, Liang Z (2005) Practical design considerations of current sharing control for parallel VRM applications. In: Proceedings of 20th annual applied power electronics conference and exposition, 2005, pp 281–286
31. Laaksonen H, Saari P, Komulainen R (2005) Voltage and frequency control of inverter based weak LV network microgrid. In: Proceedings of the international conference on future power systems, 2005, pp 1–6
32. Vandoorn TL, Meersman B, Degroote L, Renders B, Vandevelde L (2011) A control strategy for islanded microgrids with dc-link voltage control. IEEE Trans Power Del 26(2):703–713
33. Meng L, Dragicevic T, Guerrero JM, Vasquez JC (2013) Optimization with system damping restoration for droop controlled dc-dc converters. In: Proceedings of IEEE energy conversion congress and exposition (ECCE), 2013, pp 65–72
34. Dragicevic T, Guerrero JM, Vasquez JC, Skrlec D (2014) Supervisory control of an adaptive-droop regulated DC microgrid with battery management capability. IEEE Trans Power Electron 29(2):695–706
35. Shafiee Q, Guerrero JM, Vasquez JC (2014) Distributed secondary control for islanded microgrids—a novel approach. IEEE Trans Power Electron 29(2):1018–1031
36. Nasirian V, Moayedi S, Davoudi A, Lewis FL (2015) Distributed cooperative control of DC microgrids. IEEE Trans Power Electron 30:2288–2303
37. Olfati-Saber R, Murray RM (2004) Consensus problems in networks of agents with switching topology and time-delays. IEEE Trans Autom Control 49(9):1520–1533
38. Spanos DP, Olfati-Saber R, Murray RM (2005) Dynamic consensus for mobile networks. In: Proceedings of 16th International Federation of Automatic Control (IFAC), 2005, pp 1–6
39. Furukawa M, Xu J, Shimizu Y, Kato Y (2008) Scratch-induced demagnetization of perpendicular magnetic disk. IEEE Trans Magn 44(11):3633–3636
40. Sridharan V, Asadi H, Tahoori MB, Kaeli D (2006) Reducing data cache susceptibility to soft errors. IEEE Trans Dependable Secure Comput 3(4):353–364
41. Erickson RW, Maksimovic D (2001) Fundamental of power electronics, 2nd edn. Kluwer, Norwell
42. Nasirian V, Karimi Y, Davoudi A, Zolghadri MR, Ahmadian M, Moayedi S (2013) Dynamic model development and variable switching-frequency control for DCVM Cúk converters in PFC applications. IEEE Trans Ind Appl 49(6):2636–2650
43. Nilsson D, Sannino A (2004) Efficiency analysis of low- and medium voltage DC distribution systems. In: Proceedings of IEEE Power Engineering Society general meeting, 2004, pp 2315–2321
44. Anand S, Fernandes BG (2010) Optimal voltage level for DC microgrids. In: Proceedings of 36th annual conference on IEEE Industrial Electronics Society (IECON), 2010, pp 3034–3039
45. Pavlovic T, Bjazic T, Ban Z (2013) Simplified averaged models of dc–dc power converters suitable for controller design and microgrid simulation. IEEE Trans Power Electron 28 (7):3266–3275
46. Qu Z (2009) Cooperative control of dynamical systems: applications to autonomous vehicles. Springer, New York
47. Nasirian V, Davoudi A, Lewis F, Guerrero J (2014) Distributed adaptive droop control for DC distribution systems. IEEE Trans Energy Conversion 29(4):944–956

Chapter 8

Distributed Assistive Control of DC Microgrids

Proliferation of power electronics loads in DC distribution networks shifts the load consumption profiles from the traditional constant impedance loads to electronically driven loads with potentially volatile power profiles. Such fast-acting consumption patterns can destabilize the entire distribution network, given their weak nature due to the lack of damping and generational inertia [1, 2]. Hardware-centric approaches focus on placement of energy storage devices to decouple the source, load, and distribution network dynamics (e.g., [3–6]). However, widespread utilization of these devices can be costly. Control-centric approaches, either linear controllers based on average-value models of the underlying switching converters (e.g., [7–9]) or nonlinear control paradigms based on the hybrid system representation of power electronics converters (e.g., [10–13]), are the alternative methods found in the literature.

The concept of power buffer is introduced in [14, 15] to shield the power distribution network from abrupt changes in load, and the sensitive loads from the transients in distribution network, by modifying the effective loading impedance seen by the distribution network. Power buffers are power electronic converters with two prominent features. From the hardware perspective, power buffers have relatively large storage components. From the control perspective, they are mainly concerned with buffering, storing, and managing energy rather than voltage regulation. The latter task is usually performed with a point-of-load converter that follows the power buffer. Therefore, power buffers can provide a holistic approach between the hardware- and control-centric approaches to help minimize the effects of transients on the DC distribution networks [16–18]. The challenge in the control of power buffers stems from the trade-off between demands of the final loads and the power network, which can be properly formulated in a game-theoretic framework and the limited generational capacity in microgrids, which calls for the optimal utilization of energy stored in the power buffers.

A geometric manifold is derived from the optimal state trajectories based on the energy–impedance state-space representation in [19]. Game-theoretic solutions for steady-state conditions [20] or trajectory formation [21, 22] are provided in a decentralized fashion. Team formation and player-by-player optimization to find the

A. Bidram et al., *Cooperative Synchronization in Distributed Microgrid Control*,
Advances in Industrial Control, DOI 10.1007/978-3-319-50808-5_8

Nash equilibrium is discussed in [23]. Non-cooperative game-theoretic control frameworks extract geometric manifolds based on the a priori computation of state trajectories in [24]. Majority of these endeavors neglect the role of the distribution network in problem formulation, leading to a suboptimal trajectory. However, the transmission line impedances practically limit the effective range of a buffer to assist only its physical neighbors. Therefore, it is of paramount value to develop a game-theoretic framework that accounts for the transmission line effect. Moreover, the existing literature lacks a feedback solution to control the buffers; optimal trajectories are usually numerically calculated for the most probable load change/fault scenarios and, then, saved in lookup tables for further use, i.e., when a load transient occurs.

Information exchange, even limited, can help the power buffers optimally share a common objective and appropriately respond to global (system-level) changes. This chapter uses a limited information exchange among active loads and establishes a game-theoretic coordination of these entities in a DC microgrid. It offers an analytical solution that accounts for the distribution network effect. Salient features of this work are as follows:

- Power buffers add a degree of freedom in addressing the transient mismatch between the power supplied by the distribution network and the power delivered to the final load.
- A communication network is spanned across the active loads. This network spatially extends the effective range of a power buffer to assist its neighboring loads.
- A game-theoretic performance function is introduced for each active load. Optimization of this function ensures proper respond to abrupt local and neighbors' load changes.
- Active loads and their physical coupling though the distribution network are properly modeled using the small-signal analysis.
- A policy iteration algorithm is offered to solve algebraic Riccati equations (AREs) and find the optimal solutions to minimize system's performance functions.

8.1 Introductory of Power Buffer and Distributed Control

8.1.1 Operational Principle of Power Buffer

A power buffer is connected in series to a power electronics load and shapes the power profile drawn from the distribution line of the microgrid, as illustrated in Fig. 8.1. Here, *final load* collectively refers to the point-of-load converter and its load. The *active load* refers to the series connection of a power buffer and a final load. As shown in Fig. 8.1, the final load abruptly changes its load, p_{out}, at $t = t_1$.

To handle the extra power demand, the power buffer gently ramps up its input power, p_{in}, and thus, there would be a mismatch between the supplied and the

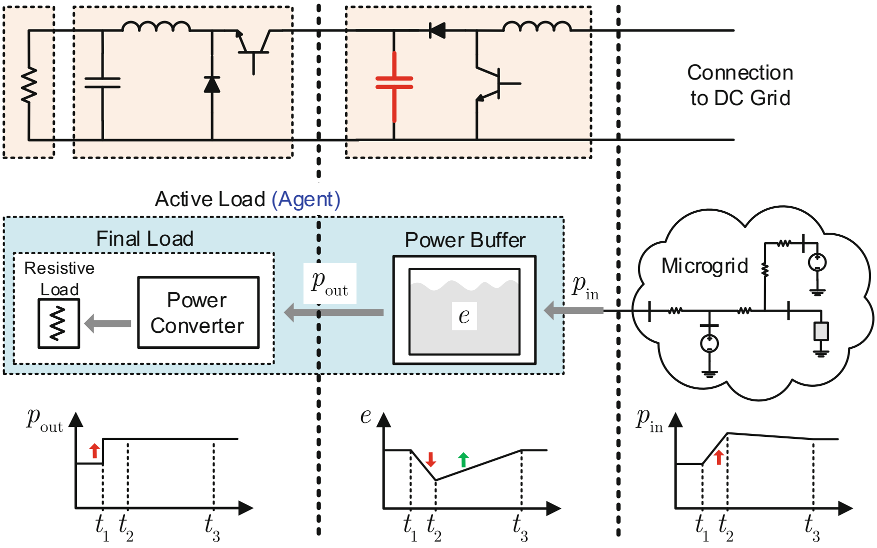

Fig. 8.1 Power buffer operation during a step change in power demand. © [2016] IEEE. Reprinted, with permission, from IEEE Transactions on Energy Conversion [35]

demanded powers. The buffer uses its stored energy, e, to compensate for this mismatch. At $t = t_2$, the input power reaches the load demand, and thus, the buffering mode ends. Then, the controller triggers the energy restoration procedure. In this stage, i.e., $t_2 < t < t_3$, the buffer slightly draws extra power from the microgrid to restore its energy. At $t = t_3$, the buffer regains its initial energy level and ends the energy restoration mode. For $t > t_3$, the input power to the buffer equals the load power, i.e., $p_{in} = p_{out}$, and the stored energy, e, remains intact until the next load change occurs. It is noteworthy that the buffering interval $[t_1, t_2]$ is significantly shorter than the energy restoration interval $[t_2, t_3]$.

8.1.2 Distributed Control

Active loads can be individually controlled by processing their local measurements, e.g., the final load power or the input bus voltage. However, such a localized approach limits the effectiveness of the power buffer to its local load. Alternatively, nearby active loads can collectively respond to load changes. Here, any active load in the physical vicinity of the load i would be called its *neighbor*. In case of a load change at the active load i, the stored energy of all its neighbor buffers can collectively smoothen the power demand from the microgrid. It is noteworthy that due to the loss of energy on the transmission lines, seeking assistance from remote buffers is not recommended.

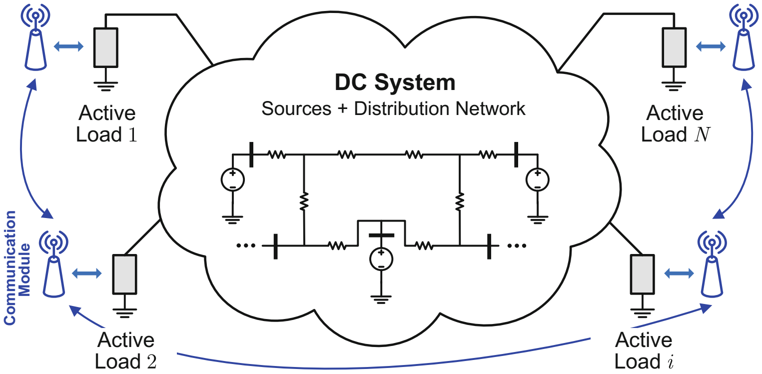

Fig. 8.2 Communication modules facilitate data exchange among active loads to perform distributed control routines. © [2016] IEEE. Reprinted, with permission, from IEEE Transactions on Energy Conversion [35]

Distributed coordination of active loads requires communication with neighbors. To this end, each active load is equipped with a communication module (see Fig. 8.2) that facilitates data exchange with its physical neighbors. This communication network transforms the DC microgrid into a multi-agent dynamic system where each active load is an *agent*. The set of all neighbors of the agent i is denote by N_i.

Each agent i relays an information vector $\mathbf{x}_i(t) = [e_\mathrm{i}, r_\mathrm{i}, p_\mathrm{i}]^\mathrm{T}$, which carries its states to its neighbors and receives their data $\mathbf{X}_j, j \in N_i$. e_i, r_i, and p_i represent the stored energy, input impedance, and the output power of the buffer of the active load i. The controller at agent i will process its local data, $\mathbf{x}_i$, as well as the neighbors', $\mathbf{x}_j s$, to appropriately control the energy stored in buffer i and provide assistance during transients.

8.2 System-Level Modeling of DC Microgrid with Power Buffers

A DC microgrid, as shown in Fig. 8.3a, is the interconnection of DC sources and loads through a distribution network. Typically, sources and some load types are controllable. The focus of this work is on coordinating active loads. Figure 8.3b demonstrates the internal architecture of an active load wherein a power buffer drives the final load. Active loads are physically coupled through the power distribution network. Therefore, to study the group behavior of the active loads, it is essential to develop a dynamic model that accounts for both the load and the distribution network dynamics. This model will be used to develop an optimal control strategy to coordinate active loads.

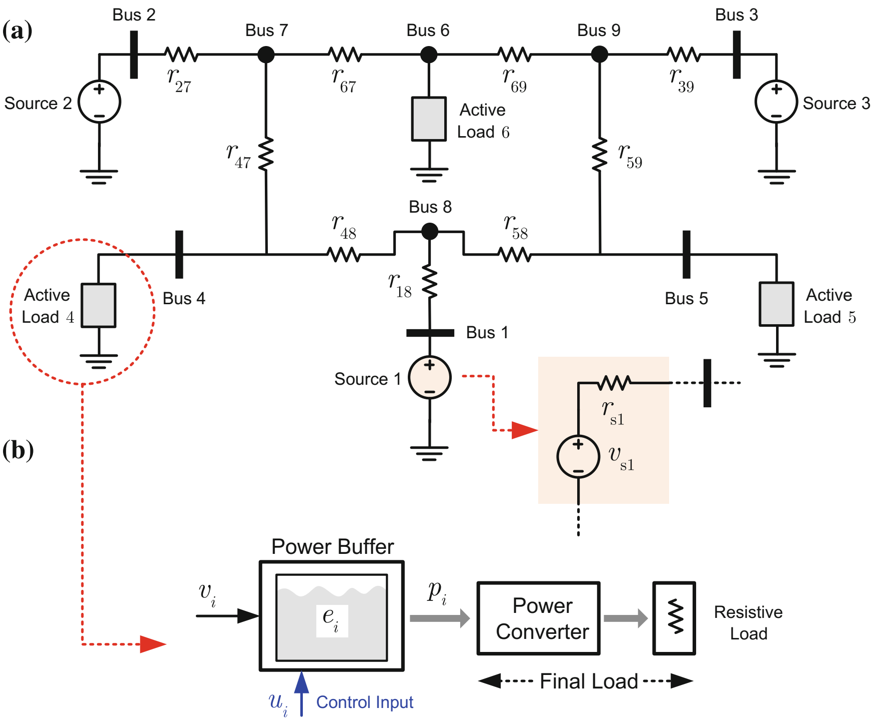

Fig. 8.3 DC microgrid layout: **a** physical components including sources, distribution network, and active loads and **b** architecture of an active load. © [2016] IEEE. Reprinted, with permission, from IEEE Transactions on Energy Conversion [35]

The energy stored in buffer i, e_i, and its input impedance, r_i, are used as the state variables to represent buffer dynamics and, consequently, the active load i. As shown in Fig. 8.3b, p_i is the output power of the buffer i. It should be noted that the power converter, which drives the resistive load in Fig. 8.3b, features a fast voltage tracker and thus maintains its stored energy steadily. Accordingly, one can safely conclude that p_i also equals the power delivered to the resistive load. Energy balance equation for buffer i implies that

$$\begin{cases} \dot{e}_i = \frac{v_i^2}{r_i} - p_i \\ \dot{r}_i = u_i \end{cases}, \tag{8.1}$$

where v_i is the buffer input voltage (the bus voltage) and u_i is the control input that adjusts the input impedance of the buffer. As the model in (8.1) is nonlinear, it can be linearized to capture the system response to small changes in state variables.

Let us express any variable x as

$$x = x^{\mathrm{q}} + \hat{x}, \tag{8.2}$$

where x^q and $\hat{x}$ are the quiescent and small-signal portions of the variable x, respectively. Accordingly, one can linearize (8.1) as

$$\begin{cases} \dot{\hat{e}}_i = -\left(i_i^q\right)^2 \hat{r}_i + 2 i_i^q \hat{v}_i - \hat{p}_i \\ \dot{\hat{r}}_i = \hat{u}_i \end{cases} \tag{8.3}$$

where $i_i^q = v_i^q / r_i^q$. Equation (8.3) explains how the stored energy of the buffer i, e_i, changes in response to the load variation $\hat{p}_i$ and the control input $\hat{u}_i$. The voltage variation $\hat{v}_i$ depends not only on the local load change $\hat{p}_i$ but also on the response of all loads and sources in the microgrid. Modeling the interaction between the loads and sources through the transmission network sheds light on how the voltage varies across the entire microgrid in response to any load change.

The transmission/distribution network couples the load dynamics, i.e., as one load's power demand changes, it changes the current flow in the entire and, thus, affects the voltages globally. Assume there exist M sources numbered 1 to M and N loads numbered $M + 1$ to $M + N$, where each source or load represents an individual bus in the microgrid.

There may be other intermediate buses in the distribution network that solely distribute power to other buses; no source or load is attached to such buses. They, however, add to the dimension and complexity of the network. Reduction methods help to find a dynamically equivalent model of the distribution network, a so-called *reduced-order* model [25]. This model captures interaction of the source/load buses, while it relaxes that of the intermediate buses. Accordingly, it reduces the computational complexity of the model and makes it suitable for dynamic/static analysis. Kron reduction method is commonly used in the circuit theory to find the reduced-order model of a circuit [26]. Particularly, for a microgrid with M sources and N loads, one can write

$$\mathbf{i}_{\mathrm{MG}} = \mathbf{Y}_{\mathrm{MG}} \mathbf{v}_{\mathrm{MG}} \Rightarrow \left[\begin{array}{c} \mathbf{i} \\ \hdashline \mathbf{0} \end{array}\right] = \left[\begin{array}{c:c} \mathbf{Y}_{11} & \mathbf{Y}_{12} \\ \hdashline \mathbf{Y}_{21} & \mathbf{Y}_{22} \end{array}\right] \left[\begin{array}{c} \mathbf{v} \\ \hdashline \mathbf{v}_{\mathrm{int}} \end{array}\right] \tag{8.4}$$

where $\mathbf{i}_{\mathrm{MG}}$, $\mathbf{Y}_{\mathrm{MG}}$, and $\mathbf{v}_{\mathrm{MG}}$ are the injected current vector, admittance matrix, and the bus voltage vector, respectively. $\mathbf{i}$ and $\mathbf{v}$ are the current and voltage vectors for the source/load buses, respectively. It is noteworthy that the injected currents to the intermediate buses are all zero, and thus, . $\mathbf{v}_{\mathrm{int}}$ is the intermediate bus voltage vector. The Kron reduction offers a reduced-order equivalent of (8.4),

$$\mathbf{i} = \mathbf{Y}\mathbf{v} \tag{8.5}$$

where

$$\mathbf{Y}{=}\mathbf{Y}_{11}-\mathbf{Y}_{12}\mathbf{Y}_{22}^{-1}\mathbf{Y}_{21} \tag{8.6}$$

is the reduced-order admittance matrix that models the interaction between the loads and sources.

For a system of M sources and N loads, one can write

$$\underbrace{\left[v_{\mathrm{s}1}/r_{\mathrm{s}1} \quad \cdots \quad v_{\mathrm{s}M}/r_{\mathrm{s}M} \;\vdots\; 0 \quad \cdots \quad 0\right]^{\mathrm{T}}}_{\mathbf{i}}=\mathbf{Y}\underbrace{\left[v_1 \quad \cdots \quad v_M \;\vdots\; v_{M+1} \quad \cdots \quad v_{M+N}\right]^{\mathrm{T}}}_{\mathbf{v}}, \tag{8.7}$$

where each source i is modeled as the series connection of a regulated voltage source, $v_{\mathrm{s}i}$, and a resistor, r_{s}, as shown in Fig. 8.3a. Entries of the admittance matrix, $\mathbf{Y}$, are determined by the admittance of the sources, the loads, and the distribution lines. Small-signal analysis of (8.7) results in

$$\mathbf{i}^{\mathrm{q}}+\hat{\mathbf{i}}=\left(\mathbf{Y}^{\mathrm{q}}+\hat{\mathbf{Y}}\right)\left(\mathbf{v}^{\mathrm{q}}+\hat{\mathbf{v}}\right)\Rightarrow\hat{\mathbf{i}}=\mathbf{Y}^{\mathrm{q}}\hat{\mathbf{v}}+\hat{\mathbf{Y}}\mathbf{v}^{\mathrm{q}}. \tag{8.8}$$

Given the regulated internal voltages of all sources, entries of the current vector $\mathbf{i}$ are constant, and thus, $\hat{\mathbf{i}}=\mathbf{0}$. Therefore, (8.8) yields

$$\hat{\mathbf{v}}=-\left(\mathbf{Y}^{\mathrm{q}}\right)^{-1}\hat{\mathbf{Y}}\mathbf{v}^{\mathrm{q}}=-\mathbf{Z}^{\mathrm{q}}\hat{\mathbf{Y}}\mathbf{v}^{\mathrm{q}}. \tag{8.9}$$

Intuitively, the load change at any active load i affects the power flow and, consequently, the voltage regulation across the microgrid. Accordingly, all other active loads would adjust their input impedances, $\hat{r}_j$s, to maintain their desired power delivery. Therefore, $\hat{\mathbf{Y}}$ can be generally written as

$$\hat{\mathbf{Y}}=\left[\begin{array}{ccc:ccc} 0 & \cdots & 0 & 0 & \cdots & 0 \\ \vdots & \ddots & \vdots & \vdots & \ddots & \vdots \\ 0 & \cdots & 0 & 0 & \cdots & 0 \\ \hdashline 0 & \cdots & 0 & \frac{-\hat{r}_{M+1}}{{r^{\mathrm{q}}_{M+1}}^{2}} & \cdots & 0 \\ \vdots & \ddots & \vdots & \vdots & \ddots & \vdots \\ 0 & \cdots & 0 & 0 & \cdots & \frac{-\hat{r}_{M+N}}{{r^{\mathrm{q}}_{M+N}}^{2}} \end{array}\right], \tag{8.10}$$

which captures the effect of all impedance variations, i.e., $\hat{r}_j$s. Plugging (8.10) in (8.9) gives

$$\hat{\mathbf{v}}=\mathbf{Z}^{\mathrm{q}}\left[0 \quad \cdots \quad 0 \;\vdots\; \frac{\hat{r}_{M+1}v^{\mathrm{q}}_{M+1}}{{r^{\mathrm{q}}_{M+1}}^{2}} \quad \cdots \quad \frac{\hat{r}_{M+N}v^{\mathrm{q}}_{M+N}}{{r^{\mathrm{q}}_{M+N}}^{2}}\right]^{\mathrm{T}}=\Gamma\left[0 \quad \cdots \quad 0 \;\vdots\; \hat{r}_{M+1} \quad \cdots \quad \hat{r}_{M+N}\right]^{\mathrm{T}}, \tag{8.11}$$

where $\Gamma = \left[\gamma_{ij}\right] \in \mathbb{R}^{(N+M)\times(N+M)}$. Particularly, (8.11) implies that each load voltage variation, $\hat{v}_i$, can be expressed as a linear function of the impedance variations, $\hat{r}_j$s, i.e.,

$$\hat{v}_i = \sum_{j=M+1}^{M+N} \gamma_{ij}\hat{r}_j, \quad i = M+1, \ldots M+N. \tag{8.12}$$

Equation (8.12) models the physical coupling among the active loads and, together with (8.3), forms the dynamic model of the entire microgrid. This model is further used in the next section to design an optimal control paradigm to adjust the load impedances.

8.3 Multi-player Game for Optimal Control

Game theory is the study of strategic interactions among multiple decision makers, called *players*. In such game-theoretic environments, an objective function is defined for each player to capture its preference ordering among multiple alternatives. The objective function of a player depends on the decisions made by others, as well as itself, which introduces a coupling between the actions of the players and binds them together in the decision making [27]. In general, game-theoretic approaches are categorized into *cooperative* and *non-cooperative* games. As opposed to cooperative games, each player in non-cooperative game tries to find an optimal strategy by optimizing its own objective function.

To develop a game-theoretic solution to the control of active loads in DC systems, the microgrid is first modeled as a set of players or agents with coupled dynamics in (8.3) and (8.12). Here, a distributed control protocol is developed to coordinate active loads. First, a performance function is defined for each agent which penalizes its own control input, u_i, as well as its states and its neighbors'. Incorporating the neighbors' states in the performance function transforms the load coordination into a graphical game. An optimal control assignment, u_i^*, is then designed for each agent that minimizes its performance function. This helps mitigate load transients by using not only its local stored energy but also its neighbors'. It should be noted that the control assignments, developed in this section, act upon the small-signal variations of the state variables, $\hat{x}_i$s. For notational simplicity, the small-signal notation, $^\wedge$, is dropped in the following derivations.

8.3.1 Microgrid Loads as Players in a Differential Game

Coordination of active loads is formulated as an optimal control problem. Then, coupled algebraic Riccati equations provide a distributed solution. The physical vicinity helps define the neighborhood in the cyber domain, i.e., nearby loads (e.g., those connected through a short transmission line) are chosen to exchange data. The information vector of each load contains energy, input impedance, and the final load power as in $\mathrm{x}_i(t) = [e_i, r_i, p_i]^{\mathrm{T}} \in \mathbb{R}^3$.

One can rewrite the single agent dynamic (8.3) with the physical coupling (8.12) in the matrix representation format

$$\underbrace{\begin{bmatrix} \dot{e}_i \\ \dot{r}_i \\ \dot{p}_i \end{bmatrix}}_{\dot{\mathrm{x}}_i} = \underbrace{\begin{bmatrix} 0 & 2i_i^{\mathrm{q}}\gamma_{ii} - (i_i^{\mathrm{q}})^2 & -1 \\ 0 & 0 & 0 \\ 0 & 0 & 0 \end{bmatrix}}_{\mathrm{A}_i} \underbrace{\begin{bmatrix} e_i \\ r_i \\ p_i \end{bmatrix}}_{\mathrm{x}_i} + \underbrace{\begin{bmatrix} 0 \\ 1 \\ 0 \end{bmatrix}}_{\mathrm{B}_i} u_i$$

$$+ \underbrace{\begin{bmatrix} 0 \\ 0 \\ 1 \end{bmatrix}}_{\mathrm{D}_i} w_i + 2i_i^{\mathrm{q}} \begin{bmatrix} \sum\limits_{j=M+1(\neq i)}^{M+N} \gamma_{ij} r_j \\ 0 \\ 0 \end{bmatrix}, \quad i = M+1, \ldots, M+N, \qquad (8.13)$$

where $w_i = \dot{p}_i$ is the disturbance that captures load transient behaviors. This disturbance is added to include p_i as one of the state variables. With no loss of generality, one can assume that any agent's dynamic is predominantly affected by its own states and its neighbors, i.e., the $\gamma_{ij} r_j$ terms in (8.13) that $j \notin N_i$ has negligible impact on the dynamic of the agent i and can be safely neglected in (8.13), which simplifies (8.13) into

$$\dot{\mathrm{x}}_i = \mathbf{A}_i \mathrm{x}_i + \mathbf{B}_i u_i + \mathbf{D}_i w_i + \begin{bmatrix} 2i_i^{\mathrm{q}} & 0 & 0 \end{bmatrix}^{\mathrm{T}} \sum_{j \in N_i} \mathit{\Gamma}_{ij} \mathrm{x}_j, \quad i = M+1, \ldots, M+N, \qquad (8.14)$$

where

$$\Gamma_{ij} = \begin{bmatrix} 0 & \gamma_{ij} & 0 \end{bmatrix}. \qquad (8.15)$$

Equation (8.14) shows that each agent is a linear system coupled with other agents through their dynamics.

Denote the neighborhood state vector for agent i, $\bar{\mathbf{x}}_i$,

$$\bar{\mathbf{x}}_i = \left(\mathbf{x}_i^{\mathrm{T}}, \{\mathbf{x}_{\mathrm{j}}^{\mathrm{T}}\}_{j \in N_i} \right)^{\mathrm{T}}, \qquad (8.16)$$

which contains states of the agent i and all its neighbors'. The objective is to design a distributed control protocol for the system in (8.14) that minimizes the following distributed performance function for agent i,

$$J_i = \int_0^\infty \left(\sum_{j \in \bar{N}_i} \mathbf{x}_j^{\mathrm{T}} \mathbf{Q}_{ij} \mathbf{x}_j + \rho_i u_i^2 \right) \mathrm{d}t, \quad i = M+1, \ldots, M+N, \tag{8.17}$$

where $\bar{N}_i = N_i \cup \{i\}$. $\mathbf{Q}_{ij} \in \mathbb{R}^{3\times 3}$ is a symmetric performance weighting matrix, and ρ_{i} is a positive performance weighting scalar. The function in (8.17) includes quadratic terms of the local and neighbor states, as well as the local control input, u_i. Intuitively, optimization of (8.17) minimizes and limits the control effort, u_i, as well as the change of local and neighbors' impedance, r_j, and energy, e_j, during a load transient.

Minimizing (8.17) introduces a multi-player game among the active loads in a DC microgrid. Performance weighting matrix and scalar, $\mathbf{Q}_{ij}$ and ρ_i, are design parameters and can be tuned to achieve a desired performance. The first term of the performance function in (8.17) penalizes the states of agent i and its neighbors', and the second term penalizes the control input for agent i.

Remark 8.1 Similar to [28], one can write the performance function (8.17) as

$$Js_i = \frac{1}{N} \sum_{j=M+1}^{M+N} J_j + \frac{1}{N} \sum_{j=M+1}^{M+N} \left(J_i - J_j \right) = \bar{J} + \tilde{J}_i, \quad i = M+1, \ldots, M+N, \tag{8.18}$$

where $\bar{\boldsymbol{J}}$ is the *overall aligned team cost* and $\widetilde{J}_i$ is the *conflict cost* for player i. That is, this game allows for players to have an aligned team component $\bar{\boldsymbol{J}}$ and an individual selfish component of strategy $\widetilde{J}_i$.

Define the multi-player game by

$$\min_{u_i} J_i, \quad i = M+1, \ldots, M+N. \tag{8.19}$$

The system in (8.14) is linear. Thus, the optimal solution to (8.19) is in the general form of [29]

$$u_i = -\mathbf{k}_i \bar{\mathbf{x}}_i, \quad i = M+1, \ldots, M+N, \tag{8.20}$$

where $\mathbf{k}_i$ is the control gain vector for agent i. The performance function (8.17) can be written in terms of $\bar{\mathbf{x}}_i$ as

$$J_i(\bar{\mathbf{x}}_i) = \int_0^\infty \left(\bar{\mathrm{x}}_i^{\mathrm{T}} \mathbf{Q}_i \bar{\mathbf{x}}_i + \rho_i u_i^2 \right) \mathrm{d}t, \quad i = M+1, \ldots, M+N, \tag{8.21}$$

where

$$\mathbf{Q}_i = \operatorname{diag}\{\mathbf{Q}_{ij}\}_{j\in\bar{N}_i}. \tag{8.22}$$

The performance function (8.21) with the general solution form in (8.20) is quadratic in $\bar{\mathbf{x}}_i$ [29]. That is,

$$J_i(\bar{\mathbf{x}}_i) = \bar{\mathbf{x}}_i^{\mathrm{T}}\mathbf{P}_i\bar{\mathbf{x}}_i, \quad i = M+1,\ldots,M+N. \tag{8.23}$$

for some kernel matrix $\mathbf{P}_i = \mathbf{P}_i^{\mathrm{T}} > \mathbf{0}$.

A differential equivalent to (8.21) is given by the Bellman equation

$$\begin{aligned} H_i &\equiv \frac{\partial J_i^{\mathrm{T}}}{\partial \bar{\mathbf{x}}_i}\left(\overline{\mathbf{A}}_i\bar{\mathbf{x}}_i + \overline{\mathbf{B}}_i\bar{\mathbf{u}}_i + \overline{\mathbf{D}}_i\bar{\mathbf{w}}_i + \Psi(\bar{\mathbf{x}}_i)\right) + \bar{\mathbf{x}}_i^{\mathrm{T}}\mathbf{Q}_i\mathbf{x}_i^{\mathrm{T}} + \rho_i u_i^2 \\ &= \mathbf{0}, \quad i = M+1,\ldots,M+N \end{aligned} \tag{8.24}$$

where

$$\overline{\mathbf{A}}_i = \operatorname{diag}\{\mathbf{A}_j\}_{j\in\bar{N}_i},\ \overline{\mathbf{B}}_i = \operatorname{diag}\{\mathbf{B}_j\}_{j\in\bar{N}_i}, \tag{8.25}$$

$$\bar{\mathbf{D}}_i = \operatorname{diag}\{\mathbf{D}_j\}_{j\in\bar{N}_i},\ \bar{\mathbf{w}}_i = \left(w_i, \{w_j\}_{j\in N_i}\right)^{\mathrm{T}}, \tag{8.26}$$

$$\bar{\mathbf{u}}_{\mathrm{i}} = \left(u_i, \{u_j\}_{j\in N_i}\right)^{\mathrm{T}}, \tag{8.27}$$

and

$$\Psi(\bar{\mathbf{x}}_i) = \operatorname{vec}\left\{\begin{bmatrix} 2i_i^{\mathrm{q}} & 0 & 0\end{bmatrix}\sum_{j\in N_l}\Gamma_{lj}\mathbf{x}_j\right\}_{l\in\bar{N}_i}, \tag{8.28}$$

is the interconnection vector. $\operatorname{vec}\{\mathbf{y}_l\}_{l\in S}$ represents a column vector that concatenates elements $\mathbf{y}_l$, $l\in S$. Substituting J_i, expressed in (8.23), in the Bellman Eq. (8.24) for agent i yields

$$\begin{aligned} H_i = \bar{\mathbf{x}}_i^{\mathrm{T}}\mathbf{Q}_i\mathbf{x}_i^{\mathrm{T}} + \rho_i u_i^2 + \bar{\mathbf{x}}_i^{\mathrm{T}}\mathbf{P}_i\left(\bar{\mathbf{A}}_i\bar{\mathbf{x}}_i + \bar{\mathbf{B}}_i\bar{\mathbf{u}}_i + \bar{\mathbf{D}}_i\bar{\mathbf{w}}_i + \Psi(\bar{\mathbf{x}}_i)\right) \\ + \left(\bar{\mathbf{A}}_i\bar{\mathbf{x}}_i + \bar{\mathbf{B}}_i\bar{\mathbf{u}}_i + \bar{\mathbf{D}}_i\bar{\mathbf{w}}_i + \Psi(\bar{\mathbf{x}}_i)\right)^{\mathrm{T}}\mathbf{P}_i\bar{\mathbf{x}}_i = \mathbf{0}, \qquad i = M+1,\ldots,M+N. \end{aligned} \tag{8.29}$$

A necessary condition that provides the optimal solution for minimizing (8.21) is the *stationarity condition* [29]

$$\frac{\partial H_i}{\partial u_i} = 2\left(\bar{\mathbf{B}}_{ii}^{\mathrm{T}}\mathbf{P}_i\bar{\mathbf{x}}_i + \rho_i u_i\right) = 0, \tag{8.30}$$

where $\bar{\mathbf{B}}_{ii} = \begin{bmatrix} \mathbf{B}_i^{\mathrm{T}} & \mathbf{0}^{\mathrm{T}} & \cdots & \mathbf{0}^{\mathrm{T}} \end{bmatrix}^{\mathrm{T}}$ is in fact the first column of $\bar{\mathbf{B}}_i$ defined in (8.25). Equation (8.30) results in the optimal distributed control input,

$$u_i^* = -\frac{\bar{\mathbf{B}}_{ii}^{\mathrm{T}} \mathbf{P}_i \bar{\mathbf{x}}_i}{\rho_i}, \quad i = M+1, \ldots, M+N. \tag{8.31}$$

Note that (8.31) is of the desired distributed form (8.20).

Substituting the optimal distributed control input (8.31) into the Bellman Eq. (8.29) gives the following coupled algebraic Riccati equation (ARE)

$$\begin{aligned} H_i = \bar{\mathbf{x}}_i^{\mathrm{T}} \mathbf{Q}_i \mathrm{x}_i^{\mathrm{T}} + \rho_i (u_i^*)^2 + \bar{\mathbf{x}}_i^{\mathrm{T}} \mathbf{P}_i \big(\bar{\mathbf{A}}_i \bar{\mathbf{x}}_i + \bar{\mathbf{B}}_i \bar{\mathbf{u}}_i^* + \bar{\mathbf{D}}_i \bar{\mathbf{w}}_i + \Psi(\bar{\mathbf{x}}_i) \big) \\ + \big(\bar{\mathbf{A}}_i \bar{\mathbf{x}}_i + \bar{\mathbf{B}}_i \bar{\mathbf{u}}_i^* + \bar{\mathbf{D}}_i \bar{\mathbf{w}}_i + \Psi(\bar{\mathbf{x}}_i) \big)^{\mathrm{T}} \mathbf{P}_i \bar{\mathbf{x}}_i = \mathbf{0}, \quad i = M+1, \ldots, M+N. \end{aligned} \tag{8.32}$$

where

$$\bar{\mathbf{u}}_i^* = \left(\mathrm{u}_i^*, \left\{ \mathrm{u}_j^* \right\}_{j \in N_i} \right)^{\mathrm{T}}. \tag{8.33}$$

To find the optimal distributed control input (8.31) for all agents, the AREs (8.32) must be first solved for $\mathbf{P}_i$s for a given DC microgrid. Then, for the implementation, the $\mathbf{P}_i$ can be plugged into the feedback solution (8.31). *Policy iteration* is an off-line computation algorithm that is commonly used to solve the AREs (8.32).

8.3.2 *Policy Iteration to Solve the Coupled AREs*

A policy iteration algorithm is presented here to solve the AREs in (8.32) and, consequently, find the optimal distributed control policies in (8.31). The policy iteration technique is a class of *reinforcement learning* methods commonly used to solve optimal control problems. This technique repeatedly performs two computational steps, namely *policy evaluation* and *policy improvement*. In the first step, policy evaluation, the performance of a given control policy in the form of (8.31) is evaluated using the Bellman Eq. (8.29). That is, for the given control policies u_i, $i = M+1, \ldots, M+N$, the kernel matrices $\mathbf{P}_i$, $i = M+1, \ldots, M+N$, are found from (8.29). In the next step, policy improvement, an improved control policy is found for each agent, using (8.31) and the kernel matrices $\mathbf{P}_i$ found in the first step. These two steps are, then, repeated until no improvement in control policies of all agents is observed, and hence, an optimal control policy is reached. The following algorithm summarizes the policy iteration:

Algorithm: Multi-player learning policy iteration for solving coupled AREs (8.32)

Initialization: Let u_i^0, $i = M+1, \cdots, M+N$ be any stabilizing initial policy. Repeat the following two steps until a convergence is achieved,

Initialization: Let u_i^0, $i = M+1, \cdots, M+N$ be any stabilizing initial policy. Repeat the following two steps until a convergence is achieved,

Policy improvement: Update the control policies using (8.31).

The kernel matrices, $\mathbf{P}_i$s, are solved using the small-signal model developed in Sect. 8.2. This model provides a dynamic model that captures small state variations about a quiescent operating point. The designer is encouraged to choose half-load operation as the quiescent condition and find the kernel matrices, $\mathbf{P}_i$s, accordingly. This model may not be accurate for large load variations; however, the discrepancy does not render this feedback solution inoperable. In fact, for operations near the half-load condition, the controller offers the optimal solution, while the solution is suboptimal for larger variations in load.

8.4 Case Studies

A 48-V DC distribution network, which collectively supplies three active loads through three sources, is adopted to study the assistive control methodology. This is the standard voltage for communication supply networks. Schematic of the DC microgrid is shown in Fig. 8.4a, where the resistive distribution system spans among sources and loads. Figure 8.4b elaborates the design of an active load incorporating the power buffer and the point-of-load converter. Accordingly, each active load consists of three modules: (1) an adjustable resistive load, (2) a buck converter, and (3) a boost converter. The buck converter features a fast proportional–integral (PI) controller and drives the resistive load at fixed voltage set point of 48 V. The boost converter features large storage elements, particularly a large output capacitor. It drives the final load at the rated voltage of 100 V; however, this voltage set point is subject to vary in load transients as the buffer varies its stored energy to perform the assistive control routine and smoothen the system transients. A high-frequency *LC* filter is placed in the design between the buck and the boost converters to eliminate high-frequency contents of the current drawn by the buck converter. Each load carries a communication module to exchange information with neighbor loads. Cyber neighborhood assignment in this study is inspired by physical vicinity: a load exchange information with those loads that are in its physical vicinity. Figure 8.4c exhibits the communication network. Control and physical parameters of the underlying system are provided in detail in Appendix.

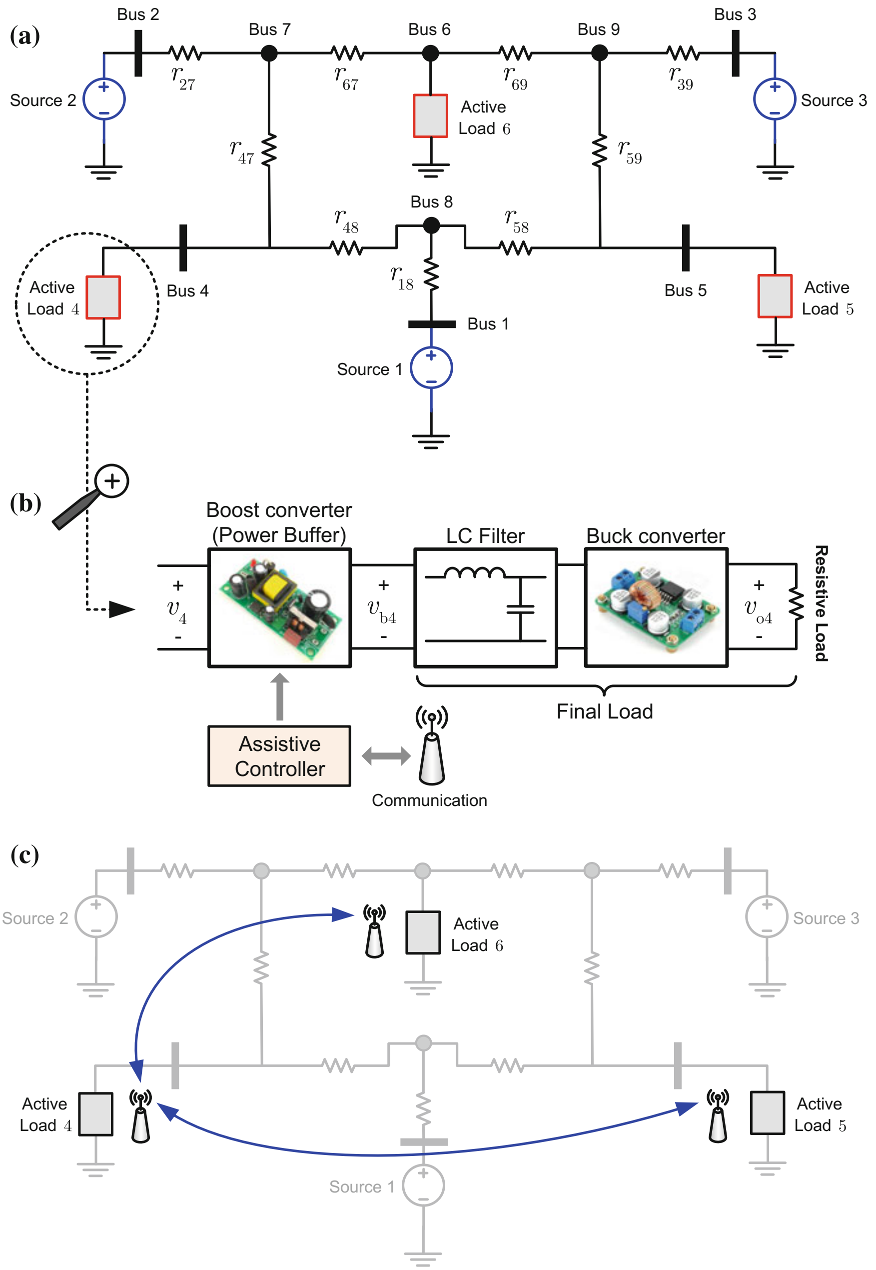

Fig. 8.4 DC microgrid layout: **a** physical layer that includes sources, distribution network, and active loads, **b** structure of an active load, and **c** communication network among active loads. © [2016] IEEE. Reprinted, with permission, from IEEE Transactions on Energy Conversion [35]

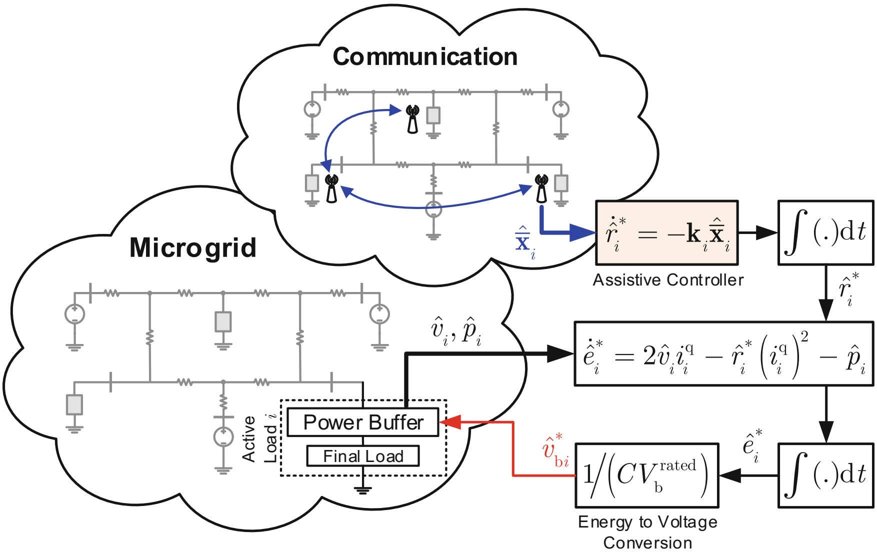

Fig. 8.5 Transient impedance adjustment by tuning the voltage set point of power buffer. © [2016] IEEE. Reprinted, with permission, from IEEE Transactions on Energy Conversion [35]

8.4.1 Impedance Adjustment by Tuning Buffer Voltage

Typically, a power buffer is a power electronic converter that controls the power flow by controlling a single solid-state switch. Thus, it offers a single degree of freedom, i.e., the switching duty ratio, which can discharge a single control objective. For instance, it can operate in either the output voltage, input current, or input impedance regulation modes; it cannot handle any two control modes at the same time.

This study demands maintaining the buffer voltage, in the steady state, on the rated value of $V_{\mathrm{b}}^{\mathrm{rated}} = 100\,\mathrm{V}$, while shaping the input impedance profile of the buffer in load transient instants. Here, a variable voltage set point is considered to handle both control objectives of the power buffer. Each buffer operates in output voltage control mode; the voltage set point, however, will not be fixed. The quiescent value of the voltage set point for buffer *i*, $v_{\mathrm{b}\,\mathrm{i}}^*$, is the rated value, $V_{\mathrm{b}}^{\mathrm{rated}}$. However, this set point varies in transients to help shape a desired input impedance profile.

Figure 8.5 demonstrates the voltage controller for the buffer *i*. The communication at load *i* provides neighbor states, and accordingly, the controller calculates the desired impedance profile for the buffer *i* as

$$\dot{\hat{r}}_{\mathrm{i}}^* = -\mathbf{k}_i\hat{\mathbf{x}}_i \Rightarrow \hat{r}_{\mathrm{i}}^* = -\int \mathbf{k}_i\hat{\mathbf{x}}_i \mathrm{d}\,t. \tag{8.34}$$

The control vectors, $\mathbf{k}_i$s, are provided in Appendix. These vectors are found based on the policy iteration algorithm in Sect. 8.3.2 and for the performance matrices, $\mathbf{Q}_i$s, given in Appendix. Small-signal analysis of the stored energy in (8.3) yields

$$\dot{\hat{e}}_i^* = 2\hat{v}_i i_\mathrm{i}^\mathrm{q} - \hat{r}_i^* \left(i_\mathrm{i}^\mathrm{q}\right)^2 - \hat{p}_i \Rightarrow \hat{e}_i^* = \int \left(2\hat{v}_i i_\mathrm{i}^\mathrm{q} - \hat{r}_i^* \left(i_\mathrm{i}^\mathrm{q}\right)^2 - \hat{p}_i\right) \mathrm{d}t. \tag{8.35}$$

Plugging the input voltage and output power small-signal measurements, $\hat{v}_i$ and $\hat{p}_i$, respectively, in (8.35) evaluates the desired energy profile, $\hat{e}_i^*$. On the other hand, as the capacitor in each buffer contains the most energy stored in that buffer, one can safely assume,

$$e_i \approx \frac{1}{2} C v_{\mathrm{b}i}^2 \Rightarrow \hat{e}_i \approx C V_\mathrm{b}^\mathrm{rated} \hat{v}_{\mathrm{b}i}. \tag{8.36}$$

Therefore, the desired energy profile can be translated into a desired voltage profile

$$\hat{v}_{\mathrm{b}i}^* = \hat{e}_i^* / \left(C V_\mathrm{b}^\mathrm{rated}\right). \tag{8.37}$$

The adjustment in (8.37) will be added to the rated voltage, $V_\mathrm{b}^\mathrm{rated}$, to form the voltage set point for the buffer i,

$$v_{\mathrm{b}i}^* = V_\mathrm{b}^\mathrm{rated} + \hat{v}_{\mathrm{b}i}^*. \tag{8.38}$$

The voltage controller on each buffer responds fast enough to ensure the reference tracking. Tracking the desired voltage in (8.38), equivalently, yields the desired input impedance profile in (8.34), which exploits the assistive nature of the power buffer.

8.4.2 Steady-State and Small-Signal Decomposition

The controller at load i, as in (8.38), processes and acts upon small-signal variations of the local and neighbor state variables, $\hat{\mathbf{x}}_i$. Thus, the controller implementation requires a mechanism that decomposes quiescent and small-signal portions of the state variables. As shown in Fig. 8.6, an ultralow-frequency (e.g., < 1 Hz) filter is

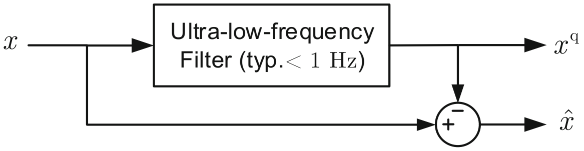

Fig. 8.6 Signal decomposition into steady-state and small-signal terms using an ultralow-frequency filter. © [2016] IEEE. Reprinted, with permission, from IEEE Transactions on Energy Conversion [35]

used for signal decomposition. In case of any transient variations in signal x, the filter maintains preincident steady-state value of the signal, x^q, and thus, the transient variations can be captured through

$$\hat{x} = x - x^q, \tag{8.39}$$

and be further used in the controller.

Controller development in Sect. 8.3 uses an ideal converter model. However, parasitic elements and component tolerances may affect the controller performance. Particularly, the controller neglects the power loss due to parasitic elements, and therefore, it assigns a higher impedance set point than what can sufficiently meet the load power demand. This mismatch limits the required power flow, gradually decreases the buffer voltage, and, consequently, renders the controller inoperable. From this perspective, another advantage of the decomposition mechanism in Fig. 8.6 is to handle the impedance mismatch. In fact, after the system reaches the steady state, the decomposition mechanism damps all small-signal values to zero and updates the quiescent values for the next load change. Therefore, $\hat{e}_i^*$ or, equivalently, $\hat{v}_{\mathrm{b}i}^*$ decays to zero, which ensures maintaining the rated buffer voltage and its energy reserve during the steady-state operation.

8.4.3 Conventional Approach: Deactivated Power Buffers

The first study replicates conventional control approach. The voltage controller of the load converters works with fixed set points. In this study, all buffers are deactivated, i.e., the buffers work as a converter with a fixed voltage set point of $\hat{v}_{\mathrm{b}i}^* = 100\,\mathrm{V}$, and do not use their stored energy to assist load transients. Resistive loads connected to terminals 4, 5, and 6 are 30 Ω, 30 Ω, and 20 Ω, respectively. Figure 8.7 shows the simulation results.

At $t = 2.5\,\mathrm{s}$, the load at bus 4 is changed in step from 30 Ω to 15 Ω, which doubles the power demand, as shown in Fig. 8.7g. A step change in the bus voltages, source currents, and input resistances of the converters, v_is, $i_{\mathrm{s}i}$s, and r_is, respectively, can be observed. It is noteworthy that such abrupt power demand may cause instability when renewable (e.g., PV and wind turbines) and slow dynamic sources (e.g., fuel cells) widely supply the network.

It is shown in Figs. 8.7b, c that the voltage controllers on the boost and buck converters respond sufficiently fast to the load change and preserve regulated voltages. Figure 8.7f exhibits the input impedance of the active loads, i.e., the input impedance of the boost converters.

Figure 8.7h represents the energy–impedance trajectory of the boost converters during the load change. As shown, only the converter supplying the varied load, i.e., load 4, shows a trajectory, while other converters do not change their energy or impedance. It can also be seen that the converter 4 reduces its impedance while keeping its stored energy almost intact as the trajectory moves straightly from point

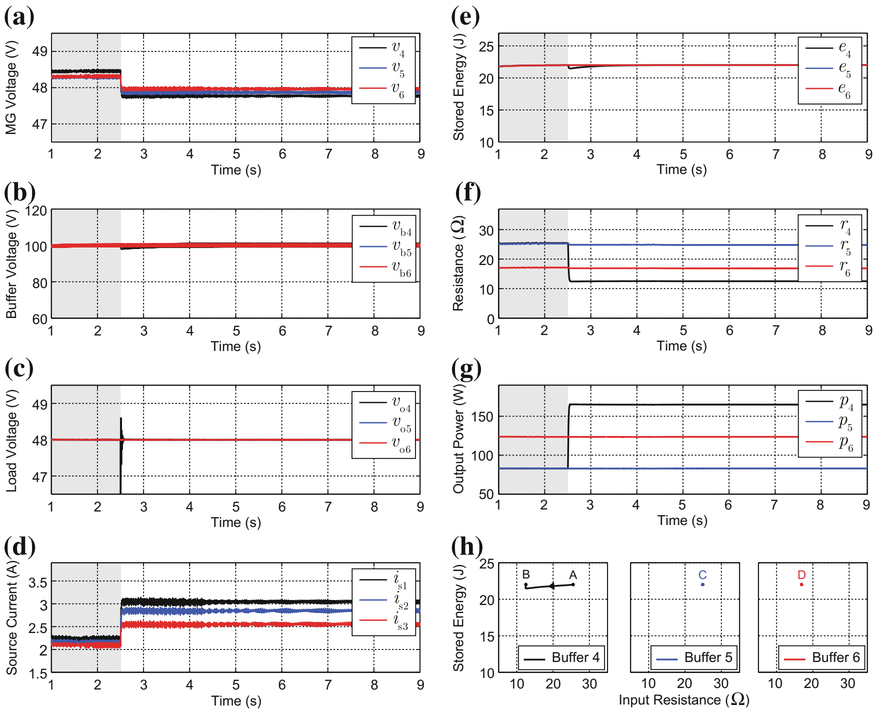

Fig. 8.7 Microgrid performance in response to the load change at Terminal 4 with deactivated power buffers: **a** microgrid bus voltages at the load terminals, **b** output voltage of the power buffers, **c** output voltage across the resistive loads, **d** source currents, **e** stored energy in power buffers, **f** input impedance of the power buffers, **g** output of the active loads, and **h** energy–impedance trajectory of the power buffers during the load transient. © [2016] IEEE. Reprinted, with permission, from IEEE Transactions on Energy Conversion [35]

A to point B. Such observation implies that the boost converter is not in the buffering mode and maintains a steady energy reserve throughout its operation.

8.4.4 Assistive Controller: Single Assisting Neighbor

The power buffers are activated to perform the assistive control methodology using the implementation technique explained in Subsection 8.4.1. The load at bus 5 experiences a step change from 30 Ω to 15 Ω at $t = 2.5$ s. As shown in Fig. 8.4c, load 4 is the only neighbor of load 5 and engages in supporting the load transient with its stored energy. Figure 8.8 exhibits the state variables during this study. Fast voltage regulation can be observed in Fig. 8.8c. It is shown in Figs. 8.8a, d, f that

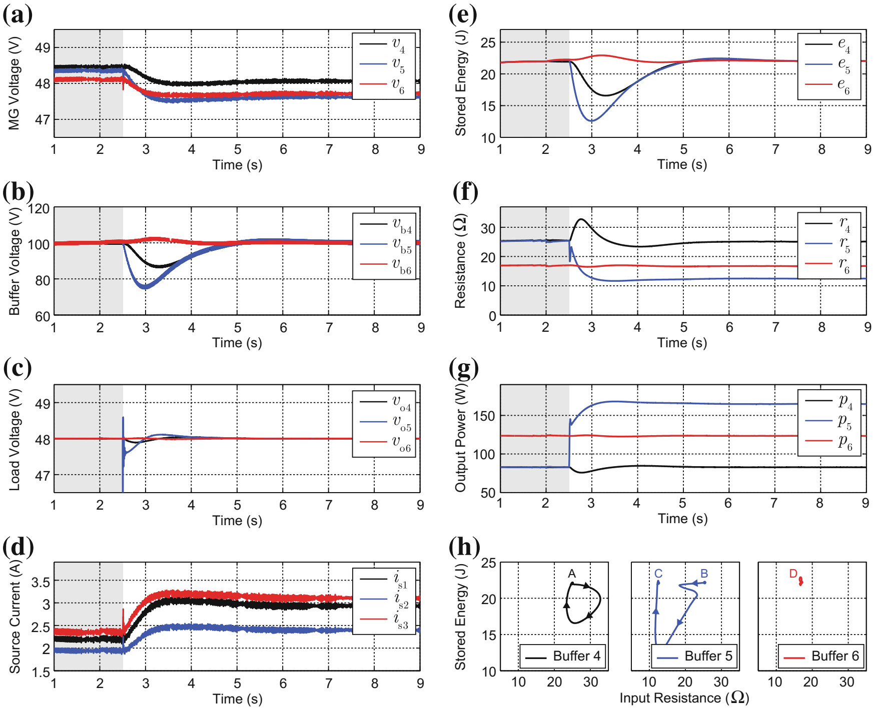

Fig. 8.8 Microgrid performance in response to the load change at Terminal 4 with deactivated power buffers: **a** microgrid bus voltages at the load terminals, **b** output voltage of the power buffers, **c** output voltage across the resistive loads, **d** source currents, **e** stored energy in power buffers, **f** input impedance of the power buffers, **g** output of the active loads, and **h** energy–impedance trajectory of the power buffers during the load transient. © (2016) IEEE. Reprinted, with permission, from IEEE Transactions on Energy Conversion [35]

the controller has successfully smoothen the bus voltages, source currents, and buffer impedances in response to the load transient (see Fig. 8.8g).

Buffers 4 and 5 use their stored energy to smoothen the impedance profile. Load 6 is not a neighbor of load 5 and, thus, has taken no action; it maintains its energy and impedance steady at point D. Figure 8.8b, e shows how buffers 4 and 5 spend their stored energy during the load transient. For an alternative discussion, the energy–impedance trajectories in Fig. 8.8h exhibit movements only in buffers 4 and 5. During the load transient, buffer 4 starts from point A in Fig. 8.8h and triggers assisting buffer 5 by dropping its energy and increasing its impedance. It then regains its stored energy and moves back to the starting condition, i.e., point A. Buffer 5 drops its energy and, at the same time, decreases its impedance to respond to the load transient. After reaching the desired impedance level, it slightly absorbs more power to regain its initial energy level. By comparison, with no buffering effect, the trajectory would go straight from points B to C.

8.4.5 Assistive Controller: Multiple Assisting Neighbors

The load at bus 4 changes from 30 Ω to 15 Ω at $t = 2.5$ s. As shown in Fig. 8.4c, load 4 has two neighbors, loads 5 and 6, which are expected to assist with the load transient. Figure 8.9 exhibits the state variables during this study. Figure 8.9a, d, f clearly shows that the controller has successfully smoothen the bus voltages, source currents, and buffer impedances in response to the load transient. All buffers contribute by using their stored energy to smoothen the impedance profile. Figure 8.9b, e shows how the buffers spend their energy asset during the load transient. The energy–impedance trajectories in Fig. 8.9h exhibit movements for all buffers. During the load transient, buffers 5 and 6 start from points C and D in Fig. 8.9h, respectively, and assist buffer 4 by losing their energy and elevating their impedance. They regain their energy shortly and move back to the starting condition,

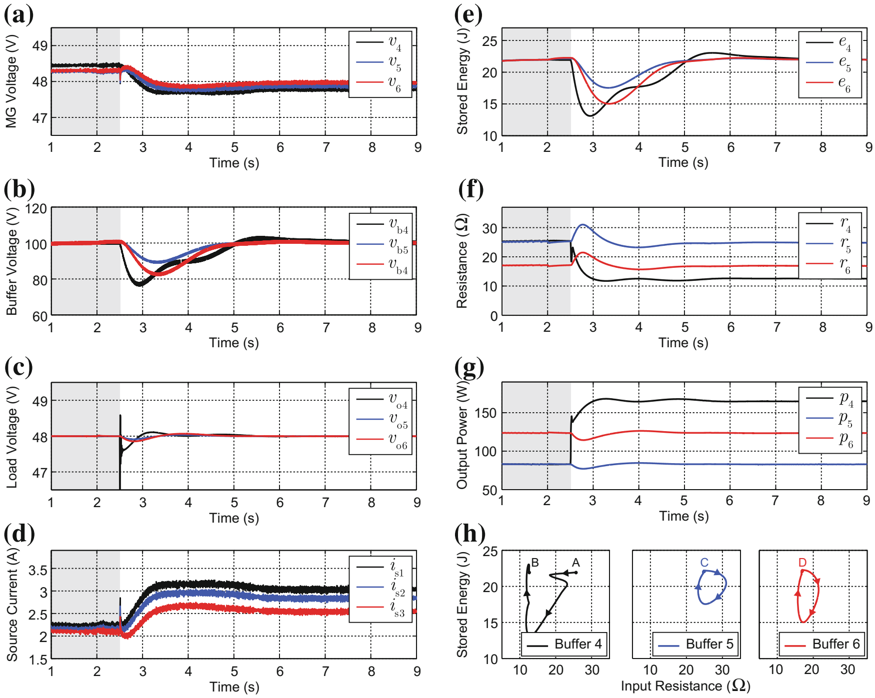

Fig. 8.9 Controller performance in response to the load change at Terminal 4; multiple assisting neighbors: **a** microgrid bus voltages at the load terminals, **b** output voltage of the power buffers, **c** output voltage across the resistive loads, **d** source currents, **e** stored energy in power buffers, **f** input impedance of the power buffers, **g** output of the active loads, and **h** energy–impedance trajectory of the power buffers during the load transient. © [2016] IEEE. Reprinted, with permission, from IEEE Transactions on Energy Conversion [35]

i.e., points C and D. Buffer 4, which is the primary buffer in handling the load, drops its energy and, at the same time, reduces its impedance to respond to the load transient. After reaching the desired impedance level, it slightly absorbs more power to restore its initial energy level. In contrast, with no buffering effect, buffer 4 trajectory would have traveled a straight path from point A to point B.

8.4.6 Communication Delay and Channel Bandwidth

Communication plays a vital role in accessing neighbor data and, therefore, in the functionality of a distributed system. Accordingly, cyber deficiencies, e.g., communication delay or limited bandwidth, may compromise the system performance. Therefore, distributed control protocols must be tested against probable channel non-idealities to ensure satisfactory field performance. Effect of channel non-idealities on the performance of distributed systems has been investigated in [30] and, particularly, for microgrids in [31–33]. Accordingly, channel deficiencies have a negligible impact on the system performance so long as the communication system is significantly faster than the controller dynamics.

Distributed control structures commonly feature low-delay and wide-bandwidth communication protocols. For example, Wi-fi and ultrawideband (UWB) protocols typically offer bandwidths up to 5 GHz and 7.5 GHz, respectively, with delays less than 1 μs; the length of the communication link directly affects the channel delay. On the other hand, power electronics typically have significantly slower dynamics compared to the communication systems. Thus, considering wide-bandwidth communications is expected to ensure satisfactory controller performance. Particularly, for the underlying control methodology, each controller is linked to its neighbors in a close physical vicinity. Therefore, field implementation features short communication links with negligible delays. Figures 8.7 through 8.9 clearly show that the controller dynamics are in the orders of 500 ms (or longer). Thus, the controller will operate safely with wide-bandwidth communication systems.

To further study the effect of cyber deficiencies, the entire system is simulated with non-ideal communication links. Figure 8.10 shows the system performance in response to a step load change at bus 4 for a variety of channel delays and bandwidths.

The load has changed from 30 Ω to 15 Ω at $t = 2.5$ s. It can be observed in Fig. 8.10 that as the communication delay increases, it takes longer for the neighbors, i.e., buffers 5 and 6, to respond and help in supplying the additional load demand. This latency led to undesired oscillations on the source currents and buffer voltages for delays longer than 250 ms. However, simulation studies ensure immunity of the controller performance to delays as long as 100 ms and channel bandwidths as low as 5 kHz, which makes Wi-fi and UWB protocols very suitable for the field implementation.

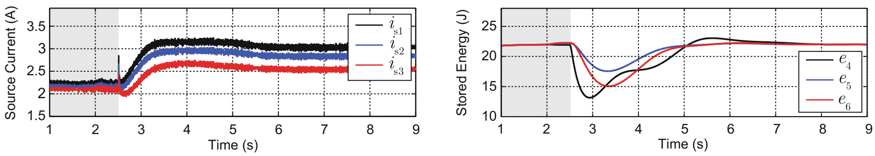

(a) Maximum Delay = **0 ms**, Minimum Channel Bandwidth = **infinity**

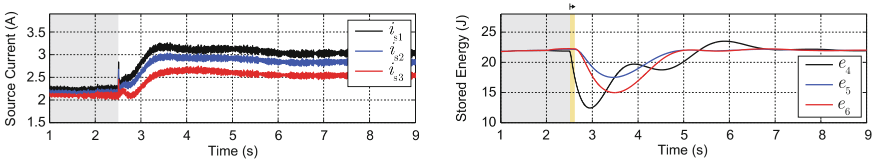

(b) Maximum Delay = **100 ms**, Minimum Channel Bandwidth = **5 kHz**

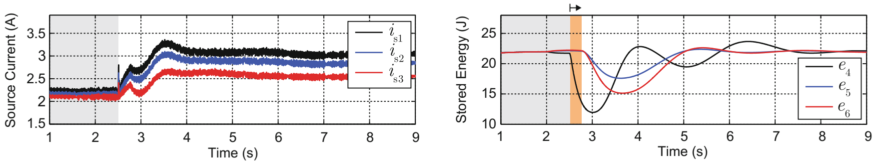

(c) Maximum Delay = **250 ms**, Minimum Channel Bandwidth = **2 kHz**

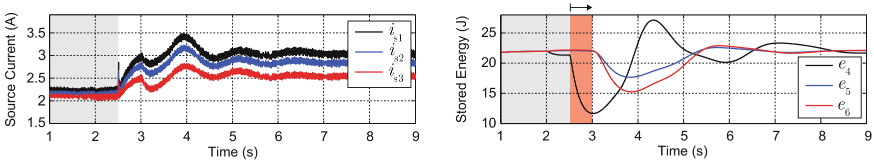

(d) Maximum Delay = **500 ms**, Minimum Channel Bandwidth = **1 kHz**

Fig. 8.10 Effect of channel deficiency on controller performance in response to a step load change at Terminal 4: **a** ideal channel, **b** delay = 100 ms and BW = 5 kHz, **c** delay = 250 ms and BW = 2 kHz, and **d** delay = 500 ms and BW = 1 kHz. © [2016] IEEE. Reprinted, with permission, from IEEE Transactions on Energy Conversion [35]

8.5 Summary

Loads within a DC microgrid can be augmented with power buffers. A communication network is also included to facilitate information exchange among neighbor active loads. A dynamic model of the active loads is derived that accounts for the physical coupling throughout the power distribution system. Then, a performance function is defined for each load, which forms a game-theoretic coordination framework. A distributed control policy is then introduced that minimizes all performance functions. A policy iteration algorithm solves the algebraic Riccati equations that provide the weighting factors to adjust the control inputs. A low-voltage DC microgrid is simulated in MATLAB/Simulink environment and used to verify efficacy of the control methodology.

Appendix

Power System Parameters

The underlying microgrid has three DC sources. Each source is modeled as a series connection of a voltage source and an internal resistance,

$$V_{s1} = V_{s2} = V_{s3} = 50\,\mathrm{V}, \tag{8.40}$$

$$r_{s1} = r_{s2} = r_{s3} = 0.1\,\Omega. \tag{8.41}$$

Transmission line impedances are chosen as follows:

$$r_{48} = 0.2\,\Omega, \tag{8.42}$$

$$r_{58} = r_{47} = r_{67} = r_{69} = 0.3\,\Omega, \tag{8.43}$$

$$r_{18} = r_{27} = r_{39} = 0.5\,\Omega, \tag{8.44}$$

$$r_{59} = 0.7\,\Omega. \tag{8.45}$$

Identical converters are used for the three active loads; they share identical power buffer designs and also identical buck converters. The converter, filtering components, and parasitic elements are listed in Tables 8.1 and 8.2. It should be noted that the simulation of power electronics accounts for the switching components and parasitic elements to carefully capture nonlinear behavior of the underlying system.

It is typical for power buffers to carry large passive components because they mainly involve in storing energy and buffering power. Particularly, in the

Table 8.1 Boost converter (power buffer) component values

	Symbol	Quantity	Unit
Component description			
Input inductor	L	2.65	mH
Output capacitor	C	4.4	mF
Parasitic element			
MOSFET on-state resistor	r_{on}	40	mΩ
Diode forward voltage	V_{D}	1	V
Input inductor ESR	r_L	520	mΩ
Output capacitor ESR	r_C	25	mΩ
Control parameter			
Proportional gain (voltage controller)	k_{P}	0.01	–
Integral gain (voltage controller)	k_{I}	1.5	–
Rated output voltage	$V_{\mathrm{b}}^{\mathrm{rated}}$	100	V
Hysteresis band (current controller)	Δi_L	0.2	A

Table 8.2 Buck converter and LC filter component values

	Symbol	Quantity	Unit
Component description			
LC filter inductor	L_{filter}	300	μH
LC filter capacitor	C_{filter}	2.2	mF
Output inductor	L	2.65	mH
Output capacitor	C	2.2	mF
Parasitic element			
MOSFET on-state resistor	r_{on}	40	mΩ
Diode forward voltage	V_{D}	1	V
LC filter inductor ESR	$r_{L,\mathrm{filter}}$	100	mΩ
LC filter capacitor ESR	$r_{C,\mathrm{filter}}$	50	mΩ
Output inductor ESR	r_L	520	mΩ
Output capacitor ESR	r_C	50	mΩ
Control parameter			
Switching frequency	F_{aw}	60	kHz
Proportional gain	k_{P}	0.01	–
Integral gain	k_{I}	1.5	–
Output voltage set point	V_{o}^{*}	48	V

underlying network, each buffer is assisted by one or two neighbor buffers. This few number of neighbor buffers demands significant local buffering capacity to handle load transients (see Table 8.1). However, for larger networks with more number of active loads, smaller buffer designs suffice due to the availability of significant neighbor buffering power. Furthermore, the buck converters simulate supplying sensitive loads and, thus, are required to provide fast voltage regulation.

Despite fast voltage controllers on buck converters, they cannot offer satisfactory transient voltage regulation since their input voltages (output voltage of the buffers) drastically change in load transients. Alternatively, to tackle the voltage regulation issue, the buck converters are also designed with large passive components.

It should be noted that the power buffers use cascaded voltage–current regulators. In such design, a voltage (PI) controller processes the difference between the desired and actual voltages and produces the current set point. A hysteresis current regulator is, then, used to regulate the output current. This design does not feature a fixed switching frequency. However, the buck converters use voltage controller with a fixed switching frequency.

Control Parameters

The performance weighting matrices $\mathbf{Q}_{ij}$ are selected to guarantee the desired steady-state behavior and also improve transient response. Entries $\mathbf{Q}_{ij}(1,1) > 0$ are chosen to ensure that $\hat{e}_i(t) \to 0$. Entries $\mathbf{Q}_{ij}(2,2) = \mathbf{Q}(3,3) = 0$ are chosen because one does not necessarily desire for $\hat{r}_i(t)$ or $\hat{p}_i(t)$ to go to zero. To improve the transient response and encourage the stored energy to support load transients, the cross products $\hat{e}_i\hat{r}_j$ and $\hat{e}_i\hat{p}_j$ are weighted by the positive $\mathbf{Q}_{ij}(1,2)$ and $\mathbf{Q}_{ij}(1,3)$ terms in $\mathbf{Q}_{ij}$ [34]. The performance weighting matrices and scalars are selected specifically as follows:

$$\mathbf{Q}_{44} = \begin{bmatrix} 0.43 & 0.35 & 3.65 \\ 0.35 & 0 & 0 \\ 3.65 & 0 & 0 \end{bmatrix}, \quad \mathbf{Q}_{45} = \begin{bmatrix} 8.50 & 12.1 & 91.8 \\ 12.1 & 0 & 0 \\ 91.8 & 0 & 0 \end{bmatrix}, \quad \mathbf{Q}_{46} = \begin{bmatrix} 7.00 & 10.9 & 75.6 \\ 10.9 & 0 & 0 \\ 75.6 & 0 & 0 \end{bmatrix}, \tag{8.46}$$

$$\mathbf{Q}_{54} = \begin{bmatrix} 8.38 & 12.1 & 23.8 \\ 12.1 & 0 & 0 \\ 23.8 & 0 & 0 \end{bmatrix}, \quad \mathbf{Q}_{55} = \begin{bmatrix} 0.43 & 0.35 & 3.67 \\ 0.35 & 0 & 0 \\ 3.67 & 0 & 0 \end{bmatrix}, \tag{8.47}$$

$$\mathbf{Q}_{64} = \begin{bmatrix} 8.00 & 8.87 & 13.8 \\ 8.87 & 0 & 0 \\ 13.8 & 0 & 0 \end{bmatrix}, \mathbf{Q}_{66} = \begin{bmatrix} 0.15 & 0.04 & 0.64 \\ 0.04 & 0 & 0 \\ 0.64 & 0 & 0 \end{bmatrix}, \tag{8.48}$$

$$\rho_4 = \rho_5 = \rho_6 = 1. \tag{8.49}$$

Accordingly, one can solve the AREs (8.32) through the policy iteration method, described in Sect. 8.3.2, to find the control gain vectors,

$$\begin{aligned} \mathbf{k}_4 &= \left[0.3 \quad 0.3 \quad 0.12 \;\vdots\; -0.2 \quad 0.1 \quad -0.9 \;\vdots\; -0.2 \quad 0.1 \quad -0.9 \right], \\ \bar{\mathbf{x}}_4 &= \left[\mathbf{x}_4^{\mathrm{T}} \;\vdots\; \mathbf{x}_5^{\mathrm{T}} \;\vdots\; \mathbf{x}_6^{\mathrm{T}} \right]^{\mathrm{T}}, \end{aligned} \tag{8.50}$$

$$\begin{aligned} \mathbf{k}_5 &= \left[-0.2 \quad 0.1 \quad -0.7 \;\vdots\; 0.3 \quad 0.3 \quad 0.12 \right], \\ \bar{\mathbf{x}}_5 &= \left[\mathbf{x}_4^{\mathrm{T}} \;\vdots\; \mathbf{x}_5^{\mathrm{T}} \right]^{\mathrm{T}}, \end{aligned} \tag{8.51}$$

$$\begin{aligned} \mathbf{k}_6 &= \left[-0.2 \quad 0.1 \quad -0.5 \;\vdots\; 0.3 \quad 0.3 \quad 0.12 \right], \\ \bar{\mathbf{x}}_6 &= \left[\mathbf{x}_4^{\mathrm{T}} \;\vdots\; \mathbf{x}_6^{\mathrm{T}} \right]^{\mathrm{T}}. \end{aligned} \tag{8.52}$$

References

1. Sanchez S, Molinas M (2014) Degree of influence of system state transition on the stability of a DC microgrid. IEEE Trans Smart Grid 30:2535–2542
2. Farhadi M, Mohammed O (2015) Adaptive energy management in redundant hybrid DC microgrid for pulse load mitigation. IEEE Trans Smart Grid 6:54–62

3. Patterson M, Macia NF, Kannan AM (2015) Hybrid microgrid model based on solar photovoltaic battery fuel cell system for intermittent load applications. IEEE Trans Energy Convers 30:359–366
4. Inthamoussou FA, Queralt JP, Bianchi FD (2013) Control of a supercapacitor energy storage system for microgrid applications. IEEE Trans Energy Convers 28:690–697
5. Xu G, Xu L, Morrow DJ, Chen D (2012) Coordinated DC voltage control of wind turbine with embedded energy storage system. IEEE Trans Energy Convers 27:1036–1045
6. Tummuru NR, Mishra MK, Srinivas S (2015) Dynamic energy management of hybrid energy storage system with high-gain PV converter. IEEE Trans Energy Convers 30:150–160
7. Sanchez S, Molinas M (2015) Large signal stability analysis at the common coupling point of a DC microgrid: A grid impedance estimation approach based on a recursive method. IEEE Trans Energy Convers 30:122–131
8. Ahmadi R, Ferdowsi M (2014) Improving the performance of a line regulating converter in a converter-dominated DC microgrid system. IEEE Trans Smart Grid 5:2553–2563
9. Kim M, Kwasinski A (2014) Decentralized hierarchical control of active power distribution nodes. IEEE Trans Energy Convers 29:934–943
10. Kazemlou S, Mehraeen S (2014) Novel decentralized control of power systems with penetration of renewable energy sources in small-scale power systems. IEEE Trans Energy Convers 29:851–861
11. Kwasinski A, Onwuchekwa CN (2011) Dynamic behavior and stabilization of DC microgrids with instantaneous constant-power loads. IEEE Trans Power Electron 26:822–834
12. Magne P, Nahid-Mobarakeh B, Pierfederici S (2012) General active global stabilization of multi-loads DC power networks. IEEE Trans Power Electron 27:1788–1798
13. Magne P, Nahid-Mobarakeh B, Pierfederici S (2013) Active stabilization of DC microgrids without remote sensors for more electric aircraft. IEEE Transactions on Industry Applications 49(5):2352–2360
14. Logue D, Krein PT (2000) The power buffer concept for utility load decoupling. In: Proceedings of 31st Annual Conference on Power Electronics Specialists PESC 00, IEEE, p 973–978
15. Logue DL, Krein PT (2001) Preventing instability in DC distribution systems by using power buffering. In: Proceedings of 32nd Annual Conference on Power Electronics Specialists Conference PESC, IEEE pp 33–37
16. Weaver WW, Krein PT (2004) Mitigation of power system collapse through active dynamic buffers. In Proceedings of 35th Annual Conference on Power Electronics Specialists PESC 04, IEEE, pp 1080–1084
17. Shan Z, Krein PT, Chi KT, Tan SC (2013) Pre-energized compact auxiliary circuit to buffer loads from fast transients with the goal of managing load-informed power. In: Proceedings of IEEE 14th Workshop on control and modeling for power electronics (COMPEL), IEEE, pp. 1–4
18. Balog RS, Weaver WW, Krein PT (2012) The load as an energy asset in s distributed DC smartgrid architecture. IEEE Trans Smart Grid 3:253–260
19. Weaver WW, Krein PT (2009) Optimal geometric control of power buffers. IEEE Trans Power Electron 24:1248–1258
20. Weaver WW, Krein PT (2009) Game-theoretic control of small-scale power systems. IEEE Trans Power Del 24:1560–1567
21. Weaver WW (2011) Dynamic energy resource control of power electronics in local area power networks. IEEE Trans Power Electron 26:852–859
22. Ekneligoda NC, Weaver WW (2014) Game-theoretic cold-start transient optimization in DC microgrids. IEEE Trans Ind Electron 61:6681–6690
23. Ekneligoda NC, Weaver WW (2012) Game-theoretic communication structures in microgrids. IEEE Trans Power Del 27:2334–2341
24. Banerjee B, Weaver WW (2014) Generalized geometric control manifolds of power converters in a DC microgrid. IEEE Trans Energy Convers 29:904–912
25. Wood AJ, Wollenberg B (1996) Power generation operation and control. 2nd edn. Wiley

26. Dorfler F, Bullo F (2013) Kron reduction of graphs with applications to electrical networks. IEEE Trans Circuits Syst I Reg Papers 60(1):150–163
27. Basar T, Olsder GJ (1999) Dynamic Non-cooperative game theory. 2nd edn. SIAM Classics
28. Vamvoudakis KG, Lewis FL (2011) Multi-player non-zero sum games: Online adaptive learning solution of coupled Hamilton-Jacobi equations. Automatica 47(8):1556–1569
29. Lewis FL, Vrabie D, Syrmos VL (2012) Optimal control 3rd edn. Wiley
30. Xiao F, Wang L (2008) Asynchronous consensus in continuous-time multi-agent systems with switching topology and time-varying delays. IEEE Trans Automat Control 53(8):1804–1816
31. Kahrobaeian A, Mohamed YARI (2015) Networked-based hybrid distributed power sharing and control of islanded micro-grid systems. IEEE Trans Power Electron 30(2):603–617
32. Nasirian V, Shafiee Q, Guerrero JM, Lewis F, Davoudi A (2016) Droop-free distributed control for AC microgrids. IEEE Trans Power Electron 31(2):1600–1617
33. Liu X, Wang, Liu PX (2015) Impact of communication delays on secondary frequency control in an islanded microgrid. IEEE Trans Ind Electron 62(4):2021–2031
34. Al-Sunni FM, Stevens BL, Lewis FL (1992) Negative state weighting in the linear quadratic regulator for aircraft control. J Guidance Control Dyn 15(5):1279–1281
35. Fan L, Nasirian V, Modares H, Lewis F, Song Y, Davoudi A (2016) Game-theoretic control of active loads in DC microgrids. IEEE Trans Energy Conversion 31(3):882–895

Index

A. Bidram et al., *Cooperative Synchronization in Distributed Microgrid Control*,
Advances in Industrial Control, DOI 10.1007/978-3-319-50808-5